

Technische Universität München

Fakultät für Chemie

Investigation of Structural and Chemical Stability of Selected Li-Ion Systems

*New Insights into the Formation and the Properties
of the Solid Electrolyte Interphase*

Byron Konstantinos Antonopoulos

Vollständiger Abdruck der von der Fakultät für Chemie der Technischen Universität
München zur Erlangung des akademischen Grades eines

Doktors der Naturwissenschaften (Dr. rer. nat.)

genehmigten Dissertation.

Vorsitzender: Prof. Dr. Sebastian Günther

Prüfer der Dissertation: 1. Prof. Dr. Harry E. Hoster
2. Prof. Dr. Hubert A. Gasteiger

Diese Dissertation wurde am 01.08.2018 bei der Technischen Universität München eingereicht und
durch die Fakultät für Chemie am 01.10.2018 angenommen.

*„Ein Experte ist ein Mann, der hinterher genau sagen kann,
warum seine Prognose nicht gestimmt hat.“*

Winston Churchill

Für meine Tante Clio, die trotz aller Hürden im Leben, stets
voller Freude war und positiv in die Zukunft blickte.

Danksagung

Zuallererst möchte ich meinem Doktorvater Harry Hoster danken, der mir damals spontan eine wissenschaftliche Heimat geboten hat und bei unseren sehr intensiven Treffen immer nur so vor Ideen sprudelte. Harry, dass unsere Gespräche stets auf Augenhöhe verliefen und du mit mir völlig unkonventionell kommuniziert und zusammengearbeitet hast (z.B. bis tief in die Nacht hinein), ist alles andere als selbstverständlich, ich schätze das sehr. Wie gerne würde ich einige unserer vielen Ideen weitertreiben; wer weiß, was die Zukunft noch bringt...

Vielen Dank auch an Hubert Gasteiger, mit dem ich im Laufe der Jahre immer enger zusammenarbeiten durfte und ihn nach und nach doch noch von meiner Arbeit als Wissenschaftler überzeugen konnte. Hubert, es freut mich ganz besonders, dass du dich als Zweitgutachter zur Verfügung gestellt hast und ich möchte dir dafür danken.

Besonderer Dank gilt meiner ehemaligen Führungskraft Peter Lamp, der mir die für die Wissenschaft notwendigen Freiräume gegeben hat und mir Entscheidungskompetenzen übertragen hat, die andere in ähnlicher Situation gewiss nicht hatten. Danke dir Peter für das Vertrauen, das du mir entgegengebracht hast.

Ein großer Dank gilt Claudia Lintz und Filippo Maglia, die mich nicht nur wissenschaftlich, sondern auch menschlich begleitet haben und die einen erheblichen Beitrag zur außergewöhnlichen Atmosphäre im Büro hatten.

Vielen Dank an meine Kollaborationspartner an der TU München, am Argonne National Lab, in Kopenhagen und am MIT für die stets sehr intensiven und zugleich amüsanten Projekttreffen und natürlich für das umfassende und unbezahlbare Feedback zu meiner eigenen Arbeit.

Ich danke Odysseas Paschos, Sandra Zugmann, Barbara Stiaszny und allen weiteren Kolleginnen und Kollegen in meiner Abteilung, die immer Lust auf kleine Diskussionen links und rechts hatten, mir immer ausgeholfen haben, wenn ich mich mal wieder in einer Sackgasse befunden habe, und die ständig kritisch meine Aussagen hinterfragten. Vielen Dank für die gute und kollegiale Arbeitsatmosphäre.

Zu guter Letzt gilt der größte Dank meiner Familie und meinen Freunden, die von meiner Arbeit zwar inhaltlich nichts verstanden oder teilweise sogar eine gewisse Abneigung für die Elektrochemie empfunden haben, aber meinen Erzählungen stets sehr interessiert lauschten und bei allen Entscheidungen hinter mir standen. Insbesondere die Zielstrebigkeit meiner lieben Frau trieb mich immer und immer wieder an, sodass kein Tag zu lang und kein Fall zu tief war, sondern – ganz im Gegenteil – am Ende alles doch nur wie ein kleiner Hopser in Erinnerung bleibt.

Abstract

Li-ion batteries are believed to be a key for the transformation of several industrial and private sectors towards a sustainable future, particularly in the fields of decentralized energy production and supply as well as electromobility. While high power components like chargers and transistors are anything but easy to provide, the actual bottleneck in the development of new storage generations are the Li-ion cells and their limitation in terms of power, energy capacity, lifetime, safety and cost. Since the early days of the Li-ion electrochemistry, scientists struggled with finding electrolytes, that fulfilled the huge set of requirements. The best compromise since decades is an electrolyte consisting of organic solvents which allows a reversible Li-ion insertion into the electrode materials and at the same time is only slightly decomposed on the negative electrode (anode). Due to the very low thermodynamical potential of the anode (one of the reasons of the high power und high energy properties of Li-ion cells) a reduction of solvent is unavoidable – the electrolyte was simply found to passivate the surface by the formation of a thick “solid electrolyte interphase” (SEI). The properties of this SEI (e.g. ionic conductivity, stability, involvement in irreversible side reactions and many more) depend strongly on the conditions it is formed. In this work the formation and subsequent processes of the SEI was studied using model experimental setups and the results were combined with fundamental simulation techniques. The developed knowledge was then used to further understand the influence of impurities (e.g. water and transition metals) during and after the formation of the SEI and was transferred to applied experimental setups for validation. Additionally, parts of the results and developed tools were even transferred to the positive electrode (cathode), so that oxidative decomposition of the electrolyte could be investigated.

This work demonstrates, how simplified model experiments can support the progress of understanding complicated commercial-like systems. While often in doubt, model systems, experimental and theoretical, can provide helpful trends, so that the chemical and physical mechanisms on the electrodes can be understood and thus steered. Furthermore, in this study significant similarities between aqueous and carbonate solvent-based environments are identified, which should encourage the research community to respectively transfer know-how and experiences from decades of aqueous electrochemistry to Li-ion chemistry. In Summary, the several results of this work supplement the existing literature in many ways and serve as a springboard not only for further fundamental studies, but also for optimization of industrial processes.

Zusammenfassung

Li-Ionen-Batterien gelten als Schlüssel für die nachhaltige und zukunftsorientierte Transformation zahlreicher Segmente von Industrie und Privatwirtschaft, insbesondere im Bereich der dezentralen Energieproduktion und -versorgung sowie auch der Elektromobilität. Während Hochleistungs-Komponenten wie Ladegeräte und Transistoren alles andere als leicht zu entwickeln sind, liegt der eigentliche Flaschenhals der Entwicklung neue Speichergenerationen bei den Li-Ionen-Zellen und ihrer Limitierungen hinsichtlich Leistung, Energiekapazität, Lebensdauer, Sicherheit und Kosten. Seit den frühen Jahren der Li-Ionen-Elektrochemie hatten Wissenschaftler große Mühen bei der Suche nach Elektrolyten, die die lange Anforderungsliste erfüllen. Der beste Kompromiss seit Jahrzenten ist ein Elektrolyt mit Karbonat-basierten Elektrolyten, der die reversible Aufnahme von Li-Ionen in die Elektrodenmaterialien erlaubt und gleichzeitig nur geringe Zersetzung an der negativen Elektrode, der Anode, aufweist. Aufgrund des thermodynamisch sehr geringen Potentials der Anode (einer der Gründe für die hohe Leistungs- und Kapazitätsfähigkeit von Li-Ionen-Zellen) ist eine Reduktion von Lösungsmitteln unvermeidbar – der genutzte Elektrolyt passiviert schlicht die Elektrodenoberfläche durch die Formierung einer dicken „solid electrolyte interphase“ (SEI). Die Eigenschaften dieser SEI (z.B. ionische Leitfähigkeit, Stabilität, Rolle bei irreversiblen Nebenreaktionen und viele weitere) hängt stark von den Formierungsbedingungen ab. In dieser Arbeit wurden die Formierung der SEI und einige Folgeprozesse mithilfe von modellhaften experimentellen Versuchsaufbauten untersucht und die Ergebnisse mit Simulationsmethoden kombiniert. Das entwickelte Wissen wurde in der Folge genutzt, um den Einfluss von Verunreinigungen (z.B. Wasser und Übergangsmetalle) während und nach der Formierung zu verstehen und zur Validierung in angewandte Versuchsaufbauten übertragen. Zusätzlich wurde ein Teil der Ergebnisse auch zur positiven Elektrode, der Kathode, transferiert, um dort die oxidative Zersetzung des Elektrolyten zu untersuchen.

Diese Arbeit demonstriert, wie vereinfachte Modellversuche den Verständnis-Fortschritt komplizierter anwendungsnaher Systeme unterstützen können. Obwohl oft bezweifelt, können Modellsysteme, ob experimentell oder theoretisch, hilfreiche Trends zur Verfügung stellen, sodass chemische und physikalische Mechanismen an Elektroden verstanden und folglich auch gesteuert werden können. Des Weiteren hat diese Arbeit signifikante Parallelen zwischen wässriger und Karbonat-basierter Elektrolyte identifiziert, die die Forschungsgemeinschaft dazu motivieren sollten, entsprechendes Wissen aus jahrzehntelanger wässriger Elektrochemie in die Welt der Li-Ionen zu übertragen. Zusammenfassend ergänzen die Ergebnisse dieser Arbeit die bestehende Literatur auf vielerlei Art und bietet ein Sprungbrett sowohl für weitere Grundlagenforschung als auch für die Optimierung industrieller Prozesse.

Content

1. Introduction	1
1.1. Motivation.....	1
1.2. Objective & Goals.....	3
1.3. Basic Research Approach	3
2. Literature Review	5
2.1. The Solid Electrolyte Interphase.....	5
2.1.1. Formation.....	5
2.1.2. Stability and Aging	8
2.1.3. The SEI on Model Electrode Surfaces.....	10
2.2. Transition Metal Dissolution at the Cathode	14
2.3. Transition Metal Deposition at the Anode.....	15
2.4. Open Questions & Motivation	18
3. Methodology & Design of Experiments.....	19
3.1. Automotive Framework Requirements.....	19
3.2. Experimental Simplifications.....	20
3.2.1. Model Electrode Surfaces	21
3.2.2. Three-Electrode Setup	22
3.2.3. Water Contamination.....	23
3.2.4. Cation Deposition Simulation.....	23
3.3. Experimental Approach	24
3.3.1. Methods on Model Electrode Surfaces.....	24
3.3.2. Methods on Composite Carbon Electrodes.....	25
3.4. Suitability of Glassy Carbon as Model Electrode in Li-Ion Research.....	27
4. Results and Discussion Section 1 – Model Electrode Surfaces.....	31
4.1. Formation of the Solid Electrolyte Interphase at Constant Potentials: a Model Study on Highly Oriented Pyrolytic Graphite.....	31
4.2. The Dynamic Impedance Properties of Solid Electrolyte Interphase on HOPG	57
4.3. The Role of Interface in Stabilizing Reaction Intermediates for Hydrogen Evolution and SEI Formation in Aprotic Electrolyte	68

5. Results and Discussion Section 2 – Transfer to Real Electrodes – Solid Electrolyte Interphase: Can faster formation at lower potentials yield better performance?	87
6. Results and Discussion Section 3 – Influence of Electrolyte Contaminations	101
6.1. The Deposition Mechanism of Transition Metal Cations on the Negative Electrodes of Li-Ion Batteries	101
6.2. Electrocatalytic Transformation of HF Impurity to H ₂ and LiF in Lithium-Ion Batteries ..	114
7. Results and Discussion Section 4 – Cathode Surface Layers – Oxidation of Ethylene Carbonate on Li Metal Oxide Surfaces	143
8. General Conclusions	169
9. Outlook	171
10. References	173
11. Publication Overview	179
11.1. Journal Publications	179
11.2. Conference Contributions	179
11.3. Patent Applications	179
11.4. Other	180
11.5. In Preparation/Unpublished	180

Table of Abbreviations

AC	alternating current
BET	Brunauer-Emmett-Teller
CE	counter electrode
CMC	carboxymethyl cellulose
CV	cyclic voltammetry
DBDMB	2,5-di- <i>tert</i> -butyl-1,4-dimethoxybenzene
DMC	dimethyl carbonate
DRT	distribution of relaxation times
EC	ethylene carbonate
EDX	energy dispersive x-ray
EIS	electrochemical impedance spectroscopy
EMC	ethyl methyl carbonate
EPR	paramagnetic resonance spectroscopy
Fc/Fc ⁺	ferrocene/ferrocenium
FEC	fluoroethylene carbonate
GC	glassy carbon
HF	hydrofluoric acid
HOPG	highly oriented pyrolytic graphite
LIB	lithium ion battery
LiBOB	lithium bis(oxalato)borate
M ²⁺	transition metal cations
MCMB	mesocarbon microbead
Mn-Tf	Manganese(II) bis(trifluoromethanesulfonate)

Ni(AcAc) ₂	Nickel(II) acetylacetonate
NMC	LiNi _x Mn _y Co _z O ₂
NMC111	Li _x Ni _{1/3} Mn _{1/3} Co _{1/3} O ₂
NMCXYZ	See NMC111, respectively
NMP	<i>N</i> -methyl-2-pyrrolidone
OCP	open circuit potential
PE/PP	polyethylene/polypropylene
PGAA	prompt-gamma-activation-analysis
PVDF	polyvinylidene fluoride
RE	reference electrode
SBR	styrene-butadiene rubber
SEI	solid electrolyte interphase
STM	scanning tunneling microscopy
VC	vinylene carbonate
WE	working electrode
XANES	X-ray absorption near edge spectroscopy
XAS	X-ray absorption spectroscopy
XPS	X-ray photoemission spectroscopy

1. Introduction

1.1. Motivation

An increased lifetime of lithium ion batteries is known to be fundamental for an economically reasonable implementation in both mobile and stationary electrified systems in a plurality of applications. Commercially available batteries mostly contain carbon or graphite as negative electrode (anode) material and transition metal olivines, oxides or spinel materials as positive electrode (cathode) material. The electrodes are held apart by a separator soaked with an organic liquid electrolyte as Li-ion solvent. Mainly used transition metals for cathodes are Ni, Mn, Co, Al and Fe [1]. In particular, automotive cells, which have high gravimetric and volumetric energy and power density requirements, are nowadays composed of the following [1]:

- Advanced graphite materials (e.g. natural or synthetic graphite flakes) on the anode side, adulterated with a binder and a conductive agent, coated on a copper foil (current collector)
- An electrolyte consisting of LiPF_6 solved in ethylene carbonate (EC) mixed with dimethyl carbonate (DMC) and/or ethyl methyl carbonate (EMC), enriched with small amounts of additives like vinylene carbonate (VC).
- A layered polymer separator (e.g. polyethylene/polypropylene, PE/PP) to electronically separate the two electrodes and store the electrolyte.
- A $\text{LiNi}_x\text{Mn}_y\text{Co}_z\text{O}_2$ (NMC) cathode, adulterated with a binder and a conductive agent, coated on aluminum foil (current collector).

The conductive agent in both electrodes is usually a carbon powder with minimal particle size and therefore high Brunauer-Emmett-Teller (BET) surface area, thus filling the gaps between the active materials and providing a good electronic connection between the active material particles. While polyvinylidene fluoride (PVDF) successfully served as a binder in the last generations of cells, the PVDF-containing electrode slurry must be processed with toxic *N*-methyl-2-pyrrolidone (NMP) before being coated on a current collector sheet. For a safer and cheaper electrode manufacturing, water based binders like carboxymethyl cellulose (CMC) and/or styrene-butadiene rubber (SBR) are implemented more and more, particularly on the anode side. The separator ideally is a passive component only serving as a soaked electrolyte reservoir and excludes direct electrode contact. The electrodes or rather the active material undergo the desired reversible electrochemical reactions involving Li^+ -ions, which are pushed from one electrode to the other when the cell is in operation. The single half-cell reactions provide significantly differing open circuit potential (OCP) values, allowing the cell to be charged and discharged with voltages $> 3\text{V}$, thus providing high energy and power capabilities [1–3].

For several reasons the cell is assembled in fully discharged state, meaning that the anode is completely delithiated. Before applying any voltage or current, the potential of both electrodes (anode & cathode)

is similar at ~ 3 V vs. Li/Li⁺. During the first cycle of the cell, the anodic potential drops to very low values, at whichsoever the electrolyte is below its electrochemical stability window. This facilitates the reduction of solvent leading to a Li-ion consuming formation of the so called *solid electrolyte interphase* (SEI). The SEI consists of numerous species including polymers, ethers, esters, oxides, carbonates and fluorides. Its physical and chemical properties depend on the anode surface, the exact electrolyte composition (including possible additives), the formation parameters as well as several other influences. At the best it is a perfect electronic insulator and Li⁺-ion conductor, so that further SEI formation is suppressed and Li⁺-ions are unhindered when diffusing or migrating to or from the anode surface [4–6]. The SEI formation and further growth is one of the least controllable fragments in Li-ion cells and has therefore been the focus of countless investigation since the beginning of Li-ion battery research. A selection can be found in references [5,7–20].

During cycling as well as storage of a Li-ion cell a large number of physico-chemical degradation mechanisms take place leading to a reduced battery lifetime and safety. Battery aging in general is defined as the sum of effects leading to capacity and power fade. Destabilizing a battery in terms of safety includes the reduction of exothermic reaction onset temperatures as well as safety affecting side reactions (e.g. gas evolution). The presence of degradation mechanisms and their significance strongly depend on various operating parameters.

One of the major aging effects of Li-ion batteries is the degradation of the SEI due to mechanical cracking, impurity catalyzed side reactions, dissolution etc. Those lead to a continuous SEI decomposition and reformation and therefore to further Li⁺-ion and solvent consumption and rise of cell impedance. The macroscopic result is a decrease of capacity and power capability [3]. A second major aging reason in lithium ion batteries was found to be the metal dissolution from the cathode. It mainly arises from impurities, which attack the cathode in partly autocatalytic reaction chains [21–26]. Particularly water and hydrofluoric acid (HF) were found to be harmful to the cathode by degenerating the active material particles [15,27,28]. On the one hand, the cathode active material loss by means of transition metal dissolution immediately causes a loss of cathodic and therefore full cell capacity. On the other hand, the dissolved transition metal cations contaminate the electrolyte and can cause an acceleration of undesired lifetime-decreasing side reactions on the anode surface. The positively charged transition metal cations are attracted by the low potential of the anode leading to a strong migration towards the anode surface, where they are expected to be reduced and plated. The immediate result is a consumption of electrons leading to a decreased overall coulombic efficiency. The location of the formed metal particles within the SEI as well as their active effect on the chemical and physical SEI stability are unknown. Although their presence is expected to generally affect the chemical and physical properties of the anode thus leading to issues in terms of lifetime, rate capability and safety, no deeper knowledge on this aging phenomenon is acquired [21,29–37].

The future trends in Li-ion cell development consist of increasing the cathode potential window and to utilize nickel-rich NMC materials [1], both leading to an increase of transition metal dissolution as well as an oxidation of the electrolyte on the cathode surface [38]. Therefore, it is indispensable from the future cell generation point of view to develop a deep understanding of the processes and reaction mechanisms on both the anode and cathode surfaces and within the SEIs in general, so that measures against unfavorable processes can be developed and the cell performance can be maintained or even increased.

1.2. Objective & Goals

The present work's goal is to supplement the fundamental understanding of the SEI properties provided by the research society. This understanding is then used to generally optimize the SEI formation as well as decrypt the mechanism of transition metal cation deposition on the anode, so that scattered published phenomena can be explained and consolidated. The major focus is in particular investigating the properties of the SEIs and their stability in terms of physical quality and chemical composition. In order to make the results applicable, the used framework requirements are derived from the automotive sector. This is for instance achieved by considering only state-of-the-art as well as medium-term possible cell chemistries. Understanding the mechanisms fundamentally and particularly stating the responsible reaction mechanisms can lead to recommendations regarding the cell composition or manufacturing. More precisely, these recommendations can point out how to utilize possible beneficial findings or avoid negative ones, respectively. Furthermore, derived mechanistic models can provide assistance to understand, simulate and reduce ageing of future generation lithium ion batteries and similar electrochemical energy storage systems. All results derived from model experiments are discussed from the application point of view, thus they can be transferred and implemented into industrial threads.

1.3. Basic Research Approach

To understand both the formation of the SEI and its physical and chemical properties as well as the short and long time behavior of anodes suffering from cathodic metal deposition, it is necessary to exclude uncertainties in the experimental procedures, so that findings can easily be assigned. For that, the experimental setup has to be simplified as much as possible bearing in mind only the influencing parameters derived from automotive applications. The general structure of this work can be separated into four sections and is schematically represented in Figure 1.

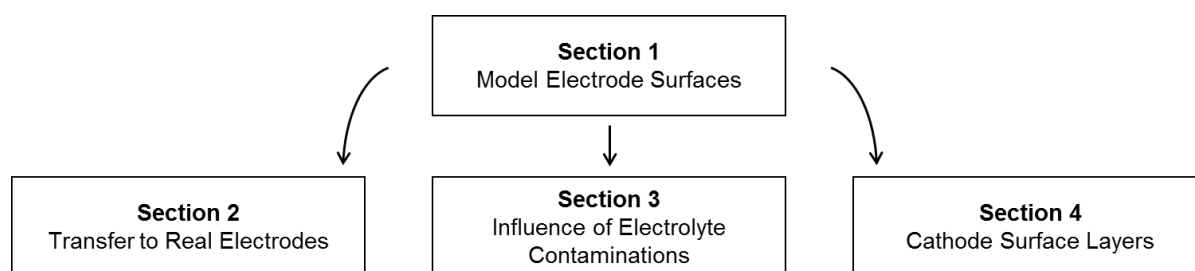


Figure 1: Structure of the work.

Section 1 is the first step towards generally achieving the objective of this work. It includes the characterization of several differently formed SEIs in neat electrolyte on model electrode surfaces (single crystals and defect-poor surfaces). The use of a simplified setup including flat model electrodes and purified electrolytes avoids possible overlaps of irreversible electrolyte reduction currents and other poorly controllable reactions during SEI formation. Additionally, fundamental simulations and experimental (electrochemical) techniques can be applied in order to characterize surface layers (after injection of a surface sensitive model redox couple). Section 1 allows the derivation of advanced models describing the potential-dependent evolution of the SEI during the first polarization. The results are presented and discussed in chapter 3.4. The derived SEI formation models serve as intermediate results in this work and allow the continuation of research towards three directions, which are assigned as sections 2-4 in Figure 1, respectively. In Section 2 the transferability of the designed models and concepts to commercial-like systems consisting of composite carbon electrodes is discussed and the applicability verified. The transfer is done by applying alternative formation protocols to the electrodes, which actually translate the models derived from section 1 to the language of galvanostatic formation of composite electrodes. The electrodes are investigated using cycling and high rate tests and compared to a baseline in terms of aging stability and SEI resistivity. The successful prediction of the effects of the alternative formation protocols on the electrodes suggests the applicability of the original model derived from section 1. Respective results are presented and discussed in chapter 5. Additionally, the developed methods and SEI characteristics of section 1 in simplified model systems are used as a springboard to further understand the evolution of the SEI in electrolyte contaminated with selected transition metal cations or water (section 3). The respective mechanisms (cation deposition and $\text{H}_2\text{O}/\text{HF}$ reduction) are discussed in chapter 6. The work is rounded out by a theoretical study on the oxidation of electrolyte on cathode active material surfaces, which utilizes the methodology developed and discussed in section 1.

2. Literature Review

This review gives a short introduction into the Li-ion battery specific literature, so that the fundamental topics of this work are elucidated to the reader. It covers the basics of the SEI and its formation, the dependencies of cell performance (e.g. power and capacity, lifetime etc.) on the SEI and emphasizes on a major but yet not well understood ageing mechanism of the SEI. The literature review is summarized by a short discussion on open questions, which lead to the motivation of this work.

2.1. The Solid Electrolyte Interphase

2.1.1. Formation

The electrolyte solvent of state-of-the-art Li-ion batteries is a mixture of cyclic and linear carbonates. While most of the electrolytes contain ethylene carbonate (EC), which is a good Li salt solvent, linear carbonates like dimethyl carbonate (DMC), ethyl methyl carbonate (EMC) or respective combinations thereof are added to improve the low EC viscosity. Already in the early days of Li-ion batteries it was noticed, that carbonate containing electrolytes are electrochemically unstable in the potential regions at which graphite negative electrodes are operated (Figure 2). Though, the scientific community noticed that, under certain conditions, the electrolyte is reduced to a three dimensional layer, which passivates any further electrolyte reduction and thus enables a long cycle life. This layer, which consists of both inorganic minerals like Li_2CO_3 , LiF , Li_2O and several organic species, was named *solid electrolyte interphase* (SEI). SEIs on graphite or Li-metal anodes were found to be similar [2,3,13,15,27,39–42]. The reduction of electrolyte causes the loss of Li charge carriers due to trapping in the SEI species, which reduces the available capacity of a Li-ion cell.

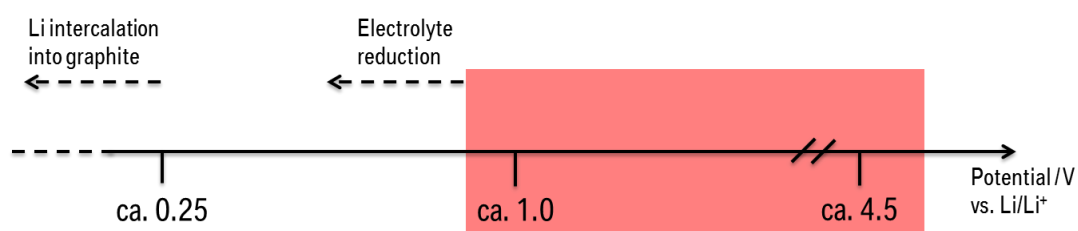


Figure 2: The electrochemical stability window of carbonate containing electrolytes in Li-ion batteries (red box) does not cover the full potential range of the full cell (ca. 0.1-4.4 V vs. Li/Li⁺).

Since cells are assembled in fully discharged state, the graphite anode is at first fully delithiated. In such a state, the electrochemical potential of the anode is not well defined and lies around the level of a fully lithiated NMC cathode [1,5]. Therefore the full cell voltage is close to 0 V. Once you apply a current, the anode potential quickly drops to values < 1 V vs. Li/Li^+ , thus leading to electrolyte reduction. In a full cell, the reduction reaction on the anode and oxidation reaction at the cathode are equilibrated. If only parts of the delithiated charge carriers of the cathode are inserted into the anode and are available for reversible reactions, the cathode has to be oversized in order to balance the Li^+ -ion loss during the SEI formation. Due to its passivation abilities, the SEI is nearly fully formed in the first and at worst

rounded off in the first subsequent cycles. Therefore, these first cycles are also called the formation cycles, out of which the very first is the most influential one in terms of passivation and Li^+ -ion conduction properties.

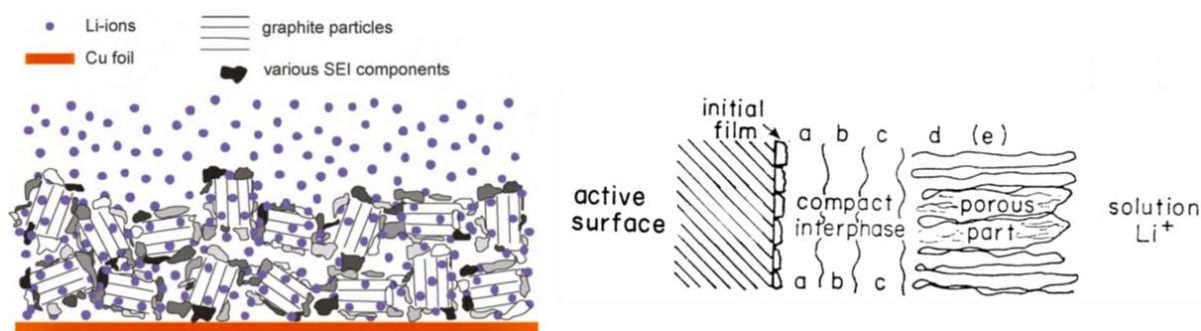


Figure 3: Left: The SEI fully covers graphite particles forming sectors of various species (modified from [39] with permission from Elsevier). Right: Schematical representation of the multilayer SEI, which can be simplified to a two-layer model consisting of compact and porous SEI layers (reproduced from [15] with permission from Elsevier).

The electrolyte reduction products fully cover the electrode graphite particles forming a multi-layer macroscopically thick interface layer, which is why the term interphase is used. As represented by the various grey beads in the left part of Figure 3, Peled *et al.* found the SEI to consist of several small segments, which is contradictory to the simple picture of a homogeneously reduced electrolyte forming a uniform SEI [43]. Furthermore, the SEI was found to be significantly thicker on edge planes than on the basal planes of graphite [44,45]. From a macroscopic point of view the SEI can be simplified into a two-layer model (Figure 3 right), consisting of a compact layer on the electrode surface, covered by a porous SEI on the electrolyte side [45–57]. This model, which homogenizes the segmented nature of the SEI, is particularly important from the reaction kinetic point of view. While electrolyte and therefore solved Li^+ -ions can penetrate the porous SEI, the ions have to lose their solvation shell at the compact SEI surface and migrate via solid state diffusion to the graphite for intercalation. While the porous SEI might influence the ion movement properties in the SEI, the compact SEI thickness is a major impediment for Li^+ -ions on their way to the electrode. Furthermore, the research community claims that the major activation barrier is not the Li^+ -ion intercalation at the electrode surface itself, but the desolvation of the ion at the compact layer surface [18,56,58–63]. Therefore the compact layer can cause significant resistances both in terms of reaction kinetics and ion movement.

While the growth of an SEI is independent of the exact cell chemistry, the chemical and physical properties of the (by means of composition, thickness, conductivity, flexibility, passivation degree etc.) are strongly dependent on several parameters. The main influences are the electrolyte composition (e.g. carbonate mixture, purity), the graphite type (e.g. natural/synthetic graphite, pretreatment) and the formation conditions (e.g. current rate, temperature), amongst others [2,39,64–66]. In particular, the electrolyte composition has been topic of extensive studies in the past, leading to the state-of-the-art commercialized electrolyte composition [12,14]. Apart from the major solvent components, the SEI is

strongly affected by electrolyte additives, which are (for either kinetical or thermodynamical reasons) preferably reduced during the formation cycles, leading to beneficial SEI properties. Since the most known additive is vinylene carbonate (VC), which is also contained in the electrolyte used in the experiments of the present work, the VC influences on the SEI are depicted in more detail in the context of Figure 4.

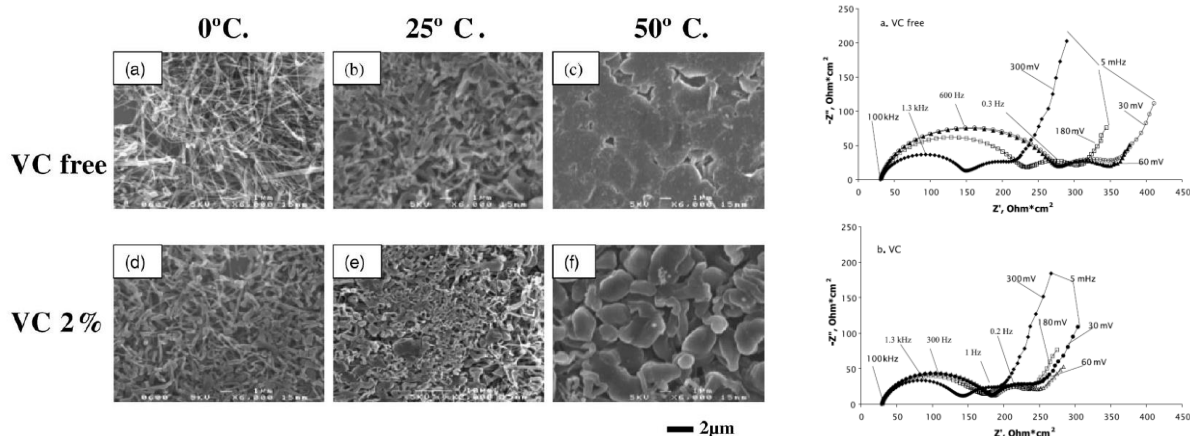


Figure 4: Left: SEM images for Li deposited on nickel substrate at indicated temperatures in electrolyte without or including VC (reproduced from [12] with permission from Elsevier). Right: EIS Nyquist plots of anodes in a three-electrode setup at different lithiation states (indicated by electrode OCP) in VC free or VC containing electrolyte (reproduced from [14] with permission from Elsevier).

The left part of Figure 4 shows SEM images of Lithium electrochemically plated on a nickel substrate in a VC free and VC containing electrolyte. The experiments were performed at 0, 25 and 50°C, as indicated in the figure. Li is not plated homogeneously but instead grows dendrites which form a mesh due to the pressurized cell setup. While the core experimental conditions were identical (apart from the temperature), the images provide insights into differing final situations. The dendrites in the VC-free electrolyte appear to be covered by a thick coating which even closes the mesh pores at higher temperatures. On the other hand, the VC-containing electrolyte leads to a thinner dendrite covering [12]. The right part of Figure 4 shows Electrochemical Impedance Spectroscopy (EIS) Nyquist plots of graphite anodes in VC-containing or VC-free electrolyte after several cycles by Aurbach *et al.* [14]. The electrodes were brought to different lithiation degrees indicated by the electrode OCP. Independent of the lithiation and the electrolyte, the half cycle in the middle frequency regions appear to be stable, which is not the case for the high frequency semicircle. The authors claim for that and similar reasons in several publications, that the high frequency semicircle can be attributed to Li⁺-ion migration through the SEI, whilst the middle frequency response is related to the charge transfer. The SEI impedance increases significantly with increasing lithiation in the VC-free electrolyte. On the other hand, when the SEI is formed in VC containing electrolyte, the impedance remains low. This behavior was attributed to a higher flexibility of the SEI, which allows the SEI to sustain the high ion conductivity even when being stretched by the “breathing” anode during lithiation. These two experiments are representative for the

general trend found in VC-containing electrolytes that VC is a helpful additive prolonging cell lifetime while keeping the SEI resistance minimal. While it is not unusual to vary the electrolyte composition, particularly by using different additives, this work was performed on a constant cell chemistry. The focus of this work is not the identification of the best SEI formers, but to understand the formation and evolution of SEIs coming from a fixed chemical baseline.

2.1.2. Stability and Aging

The instability of carbonate containing electrolytes at the anode is considered to be a general drawback of electrolytes of this kind, that can only be condoned under the following two premises: The formed reduction products are fully passivating in terms of further electrolyte decomposition, while Li^+ -ions can move unhindered through the SEI for intercalation/deintercalation at the graphite surface. The principle is illustrated in Figure 5.

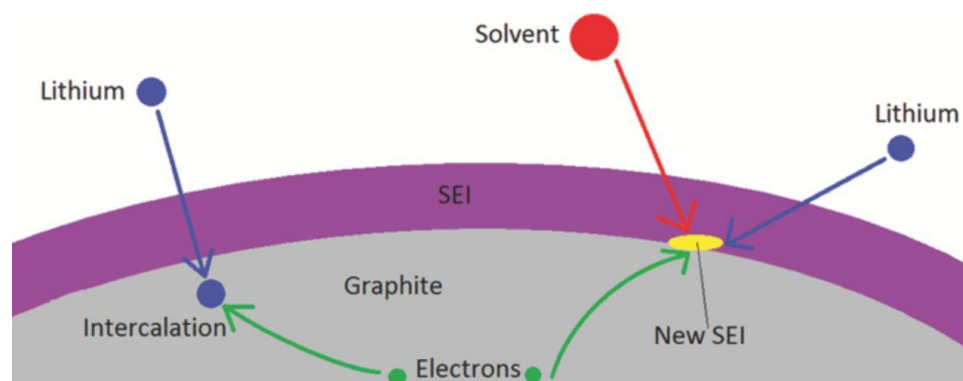


Figure 5: Illustration of the two key SEI properties: Li^+ -ion conduction and passivation of further electrolyte reduction reactions (reproduced from [64] with permission from The Electrochemical Society).

Generally, wet chemistry products can only fulfil their task to a limited degree. Therefore, no SEI can provide unhindered Li^+ -ion movement or a full passivation. In order to passivate the electrode, species formed on the electrode must be insulating and inhibit further electrolyte to approach the surface. The earlier mentioned compact SEI provides this passivating ability, but affects the ion movement properties. On the other hand, being insulating, the compact SEI layer should grow at the best only by tunneling electrons, which is physically limited [45]. Though, the graphite anode undergoes complicated changes if its physical and chemical states are altered upon lithiation. The graphite lattice's "breathing", which results from the additional foreign atoms in between the single graphene lattices, leads to a graphite volume expansion by around 10% [67,68]. This mechanical transformation causes the SEI to break and partially dissolve¹. These mechanically induced SEI damages and reformation reactions as well as reactions resulting from impurity attacks (e.g. HF) lead to further electrolyte decomposition. This does not

¹ It is noteworthy that in pristine Silicon electrodes the volume change is $\gg 100\%$ [69], which makes Silicon hard to be established as anode material for long-life applications.

only cause further Li^+ -ion consumption, but also increases the SEI impedance. Both effects are key aging reasons of Li-ion batteries reducing capacity and power capability [3].

The electrolyte reduction and SEI are related to several more microscopic aging mechanisms in Li-ion cells. Figure 6 gives an overview of all the mechanisms whereas apart from the described SEI growth (nr. 9) also the mechanisms 4, 6, 10, 11, 13 and 15 are SEI related.

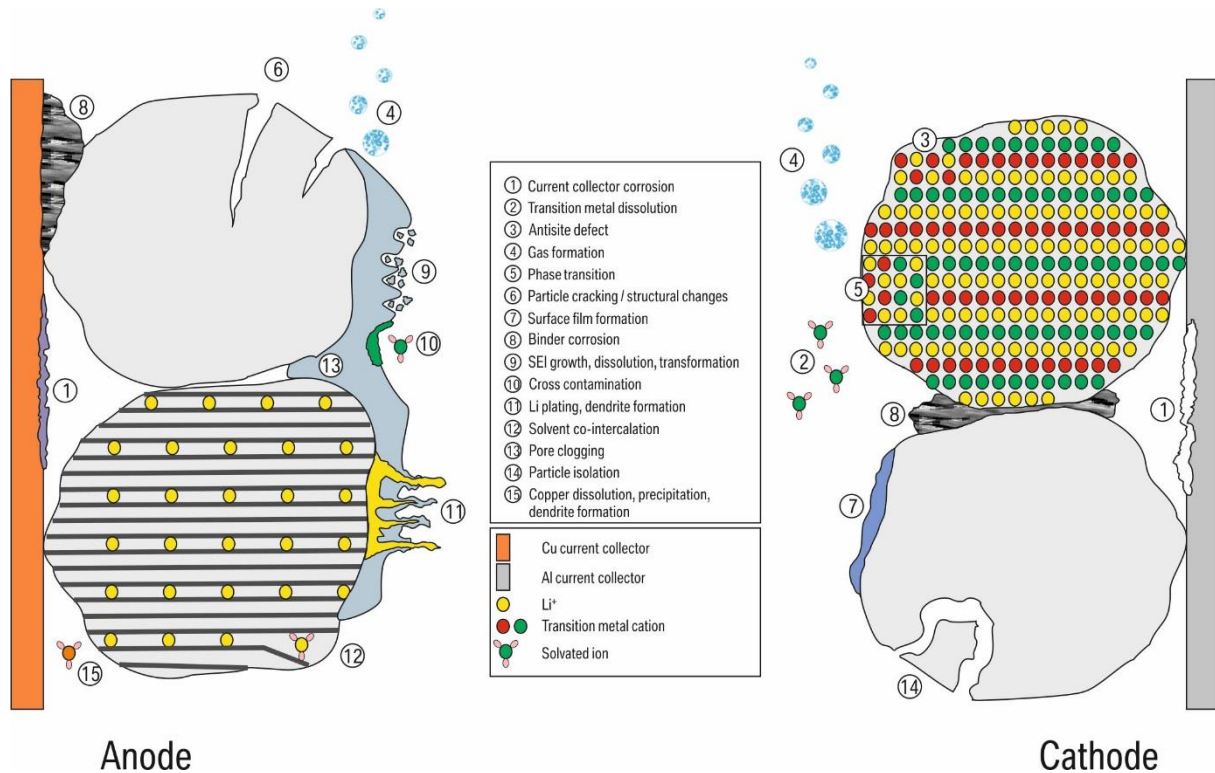


Figure 6: Overview of the aging mechanisms in a Li-ion cell on the microscopic level. Numbers 4, 6, 9, 10, 11, 13 and 15 are related to electrolyte reduction and SEI formation (reproduced from [70] with permission from Elsevier).

In many electrolyte reduction reactions paths gas evolution is involved, which is illustrated by Figure 6 (nr. 4) [8,13,15]. Even though, the gas might not be the reason for further irreversible (electro-)chemical reactions, though in porous composite carbon electrodes gas bubbles can remain adsorbed on particle surfaces, physically limiting the electroactive surface area and thus the power capability of the electrode. Furthermore, evolving gases can be a safety matter. In bigger commercial cells (all formats) the gas evolution particularly in the first formation cycle can be a serious issue, which is why the cells are degassed with advanced methods and only sealed after the evolved formation gases have been removed. If the electrode active material cracks or Li is plated and forms dendrites, new unpassivated electronically conducting surface area is created or exposed (Figure 6, nr. 6 and 11). Just like in the first cycle, the uncovered surface area allows new SEI formation reactions leading to an additional capacity loss. If the SEI becomes too thick, it might even close pores between electrode particles (Figure 6 nr. 13). This effect, which in principle is also presented in Figure 4 (left), reduces porosity and increases tortuosity. Apart from a reduced electrolyte conductivity the closing of pores may lead to more significant gradients

in the electrode through-plane direction (e.g. Li^+ -ion concentration, local temperature, overpotential and current distribution etc.), thus causing inhomogeneous electrode aging [70]. The last SEI related aging mechanism is the deposition of transition metal cations on the anode, which is depicted as nr. 10 in Figure 6. Since this mechanism is a major topic of this work, the cation origin (Figure 6 nr. 2) and the deposition mechanism and consequences are discussed in more detail later.

2.1.3. The SEI on Model Electrode Surfaces

Commercial-like carbon composite electrodes consist of graphite particles connected to each other by binder and conductive agent, which cover some of the graphite particle surface. The spherical or flake-like active material particles have typical sizes of 10-20 μm , the surface can be rough and amorphous. For those reasons the electrochemically active surface area is unknown, which is why battery community uses other current normalizations like the C-rate. Though, an exact knowledge of the free surface area is inevitable for fundamental electrochemical methods, where currents are compared as areal current densities [71,72]. Flat model electrode surfaces, which ideally consist of the same material as commercial-like electrodes, can provide assistance in applying fundamental electrochemical techniques to battery materials and at the same time exclude several side dependencies resulting from the complex undefined composition and three dimensions of a commercial-like electrode. Lucht *et al.* studied the SEI formation on a binder-free electrode in order to exclude parts of the overlapping reaction [73–75]. Since their work included surface spectroscopy methods, the exclusion of binder helped avoiding respective overlaps which are usually found when using a binder [76–78]. However, the binder-free electrodes neither provide a well-defined surface area, which is why those electrodes are not suitable for fundamental electrochemical techniques.

Well known and characterized carbon model electrode surfaces are provided by glassy carbon (GC) and Highly Oriented Pyrolytic Graphite (HOPG). While originally this work considered both, in the early experiments glassy carbon was found to not be necessarily suitable for SEI research, which is why this chapter focuses on basal plane HOPG only. The details of the early glassy carbon experiments and why it was abandoned as a substrate choice are discussed separately in chapter 3.4. A base of this work is to investigate the SEI formation and evolution in a fixed commercial-like electrolyte. Therefore, the electrolyte reduction and the subsequent evolution of an SEI is particularly to be investigated from the formation conditions point of view.

Ma *et al.* performed *in-situ* scanning tunneling microscopy (STM) during potential sweeps on pristine HOPG. The electrolyte composition was similar to the one used in this work (no VC), which is why the results are to be considered. Figure 7 pictures the STM response as a function of time and potential. During one experiment a 500 x 500 frame is scanned three times with the middle part being scanned in reverse STM tip direction.

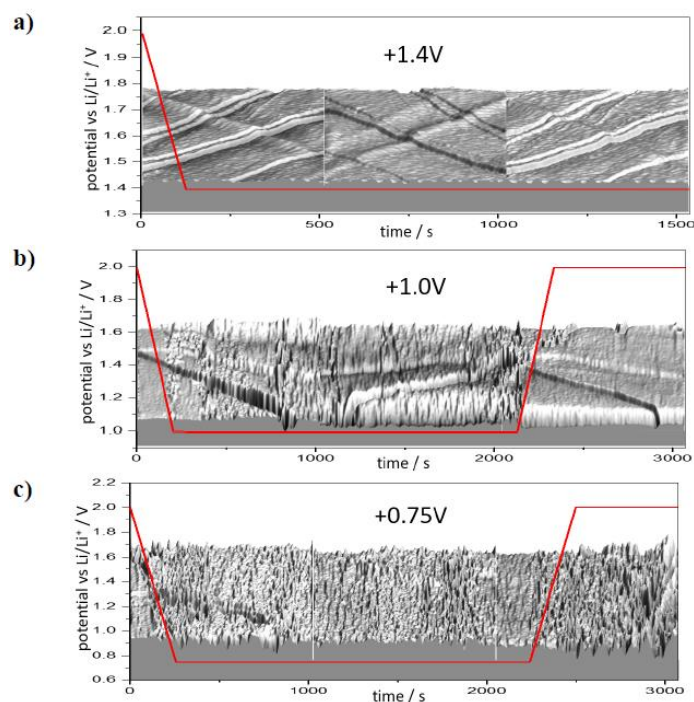


Figure 7: Change in three-dimensional Surface Morphology of HOPG in 1 M LiPF₆ in EC/DMC (1:1) *in-situ* during potential scans and potential holding. The applied potential profile is shown as a solid line (reproduced from [48] with permission from The Electrochemical Society).

In Figure 7a the potential is swept down to 1.4 V vs. Li/Li⁺, which appears to have no effect on the surface. Without sweeping the potential back to higher values, the final frame looks identical to the first, which indicates that no electrolyte decomposition took place. In b) the potential was swept down to 1 V vs. Li/Li⁺, which lead to a significant affection of the tree-dimensional surface structure. Though, when sweeping back to higher potentials, the formed layer seems to disappear. Those results indicate, that at 1 V vs. Li/Li⁺ the electrolyte is being reduced and forms a surface layer, though the formed species are either reoxidized or dissolve when reincreasing the potential. In a third experiment, which is presented in Figure 7c, the potential was swept down to 0.75 V vs. Li/Li⁺. Again, the STM shows a significant surface film formation, which remains on the HOPG surface even after sweeping back to higher potentials. These experiments visualize evidentially, that an adequately thick SEI, which is stable and therefore provides one of the inevitable properties for passivation, is formed on HOPG basal plane not earlier than at 0.8 V vs. Li/Li⁺.

While it is well known, that the SEI on commercial-like electrodes is formed by several electrolyte reduction reaction pathways resulting in a variety of products, the SEI dependencies on the formation potential has been investigated only roughly. The reason for that is, that the potential of a composite anode is pushed to < 100 mV vs. Li/Li⁺ as this is the potential range the anode is operated in. Therefore, characterizing in detail the SEI formed at higher potentials was so far of little interest as it never repre-

sents a reasonable situation. One approach performed by two groups separately was measuring formation cyclic voltammetry (CV) data in order to separate single reaction steps [51,49]. The results obtained on basal plane HOPG at similar sweep rates are presented in Figure 8.

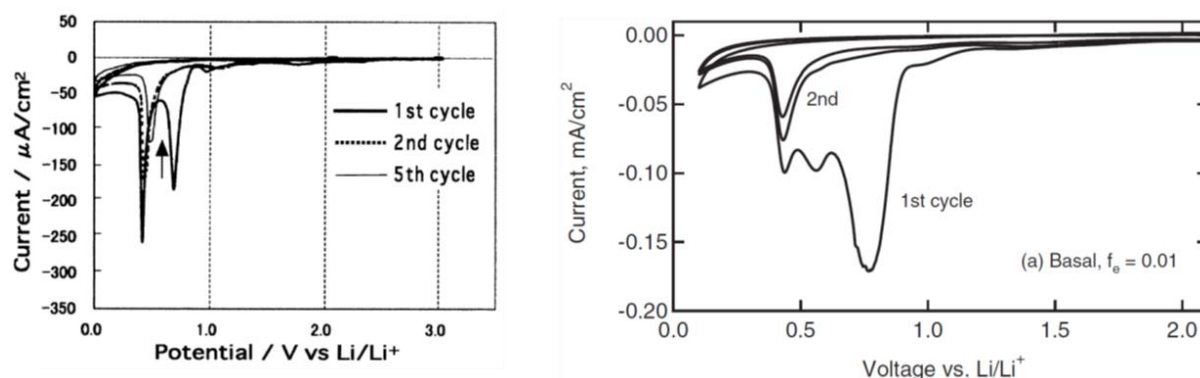


Figure 8: Formation CVs on basal plane HOPG. Left: with 10 mV s^{-1} in VC containing electrolyte (reproduced from [51] with permission from Elsevier); right: with 20 mV s^{-1} in VC free electrolyte (reproduced from [49] with permission from The Electrochemical Society).

The experiment on the left side of Figure 8 was performed in VC containing electrolyte, the one on the right side of Figure 8 was performed in a similar VC free electrolyte. Focusing in both experiments on the first cycle, a major reduction peak starts at $\sim 800 \text{ mV vs. Li/Li}^+$, which is saturated at $\sim 600 \text{ mV vs. Li/Li}^+$. The right plot in Figure 8 includes a second reduction maximum at $\sim 550 \text{ mV vs. Li/Li}^+$, which is not obtained by the research team measuring the left data. However, both experiments share again a common reduction peak at $\sim 400 \text{ mV vs. Li/Li}^+$, which remains present even in subsequent cycles. A common feature that both experiments share as well is a slight current increase at potentials $< 200 \text{ mV vs. Li/Li}^+$, indicating that even at elevated potential scan rates low amounts of Li⁺-ions might be intercalated at step edges of the HOPG basal plane. While the right plot in Figure 8 nearly reproduces the left plot, the additional peak at $\sim 550 \text{ mV vs. Li/Li}^+$ might be induced by electrolyte impurities or the slightly differing solvent composition. The experiments presented in Figure 8 serve as a springboard for the SEI formation experiments in chapter 4.1, which considers two formation potentials in the CV peak valley indicated by the arrow in Figure 8 and two potentials lower than the last CV peak.

A question that legitimately arises when simplifying experiments e.g. by using model electrodes is, whether the results can be transferred to a much more complicated or even commercial-like system. While this work does not only discuss this problem but considers it experimentally, there are already published indications that under carefully defined circumstances HOPG results can be transferred. One example, that indicates the transferability, is presented in Figure 9.

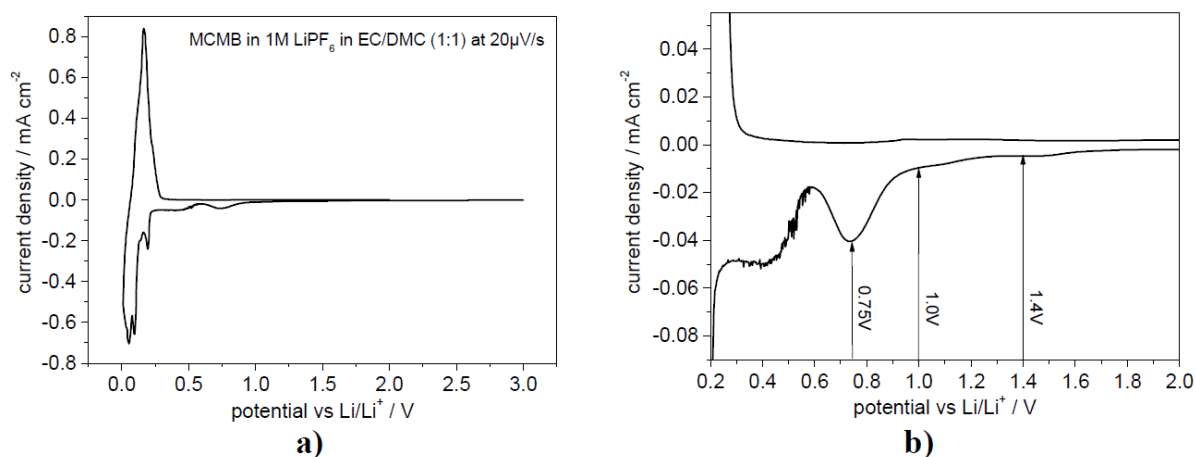


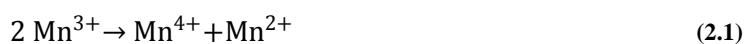
Figure 9: CV formation cycle on an MCMB electrode with $20 \mu\text{V s}^{-1}$. b) is a zoom of a) (both reproduced from [48] with permission from The Electrochemical Society).

Figure 9a shows a CV formation cycle with $20 \mu\text{V s}^{-1}$ (again in VC free electrolyte) of a mesocarbon microbead (MCMB) composite electrode. The potential region $< 250 \text{ mV vs. Li/Li}^+$ three distinct and one shoulder-like peaks, which correspond to the lithiation stages of graphite [79,80]. Figure 9b, which is a zoom of Figure 9a, includes two more distinct peaks with maxima at 750 and 400 mV vs. Li/Li⁺. Since those peaks do not correspond to lithiation reactions, they can be attributed to SEI formation. In comparison to the SEI formation peaks in Figure 8 the MCMB formation peaks are broader, which is particularly noticeable due to the small scan rate, which should actually cause a tightening of the peaks. While on one hand the peak broadness indicates an inhomogeneity of the surface and the respective SEI formation reactions, the clear separation of the two peaks indicates the similarity of the basal plane HOPG surface to a commercial-like MCMB electrode from the thermodynamic point of view. However, there are numerous pieces of information that one should take into consideration when transferring results from HOPG to composite electrodes. It is for instance known, that the SEI is generally thinner on the HOPG basal plane than on the edge plane [44]. Furthermore, even at commercial like electrodes the carbon surface plays an important role on the SEI chemical and physical properties as well as its passivation abilities [44,46,57]. The more heterogeneous the carbon surface is, the more parallel SEI formation paths are favorable. The broad spectrum is well represented by the broad SEI formation peak in Figure 9b.

To summarize this subchapter, the chemical composition of the SEI on HOPG might differ from SEIs on commercial-like carbon surfaces, though they can picture the important thermodynamic and kinetic features and threshold values of the SEI formation. There is yet no clear evidence, that the properties of SEIs on HOPG in terms of Li⁺-ion conductivity and long-term stability reflect the situation in real systems.

2.2. Transition Metal Dissolution at the Cathode

While in recent cell chemistries the effect appears negligible, cathodes of future cells will be facing a major cation dissolution problem [1,21,22,25,81–83]. The cathode, containing of a transition metal oxide, decomposes, which leads to transition metal cation (M^{2+} -ions) solvation in the electrolyte. At lower voltages, the main reason is the metal disproportionation reaction of Mn according to the following equation, which is respectively also applicable also to Co and Ni [25]:



The cathode dissolution can be enhanced by an autocatalytic H_2O reaction chain, which forms HF particularly at elevated temperatures and corrodes the cathode active material. While it could be avoided by using dry high purity materials, it can still be a major issue at elevated temperatures [25,84,85]. Furthermore, a third reason for cathode metal dissolution was identified when pushing the cathode to high potentials ($>4.5 \text{ V vs. Li/Li}^+$), where a hybridization of the electron orbitals of oxygen and the metals is hypothesized to take place, leading again to a reduction of the oxidation state of the metals and a respective cation dissolution into the electrolyte [25]. While on one hand the loss of active material directly leads to capacity loss on the cathode side, the dissolved cations in the electrolyte are on the other hand a technically unwanted impurity. Several groups found transition metals on the anode by different experimental techniques. Figure 10 presents SEM images and one corresponding energy dispersive x-ray spectrum (EDX) of anodes, which were cycled against $\text{Li}_x\text{Ni}_{1/3}\text{Mn}_{1/3}\text{Co}_{1/3}\text{O}_2$ cathodes (NMC111). The full cell voltage was pushed to denoted values during cycling. The anode surface is increasingly covered by big foreign material clusters, which when analyzed by EDX show a strong presence of transition metals. Dissolved transition metal cations appear to migrate through the separator in order to be deposited on the anode, which as mentioned is enhanced by a higher upper cutoff voltage.

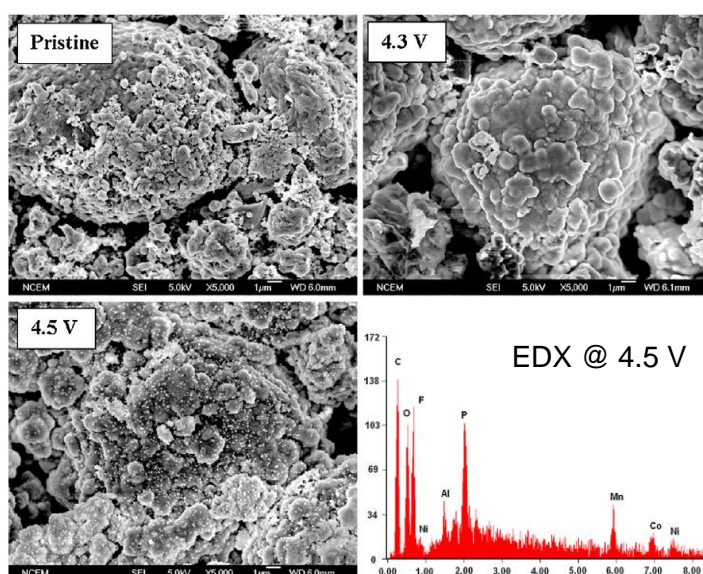


Figure 10: SEM images of the fresh and harvested MCMB anodes cycled against NMC111 cathodes with different upper charge voltage limits. The EDX spectrum corresponds to the 4.5 V anode (reproduced from [86] with permission from Elsevier).

A good illustration of the transition metal dissolution problem can be found in Figure 11. It shows the amounts of Mn, Co and Ni of harvested graphite anodes, which were cycled up to 300 cycles at the aforementioned indicated temperature in full cell setup. The indicated voltage is the upper cutoff voltage during cycling. The transition metal amounts were determined using Prompt-Gamma-Activation-Analysis (PGAA) and normalized to the active material mass. The results indicate, that not only the deposited amounts but also the core dissolution mechanism strongly depend on the cycling conditions. While the ratio of the single elements at ambient temperature and low cutoff voltage is nearly even, Mn is predominantly found in different ratios when going to more extreme cycling conditions (e.g. high cutoff voltages). The fact that Mn is predominantly found on anodes resulted into research groups focusing on the effects of Mn deposition [87–89]. However, it is noteworthy that Ni rich NMCs are expected to suffer mainly from Ni dissolution.

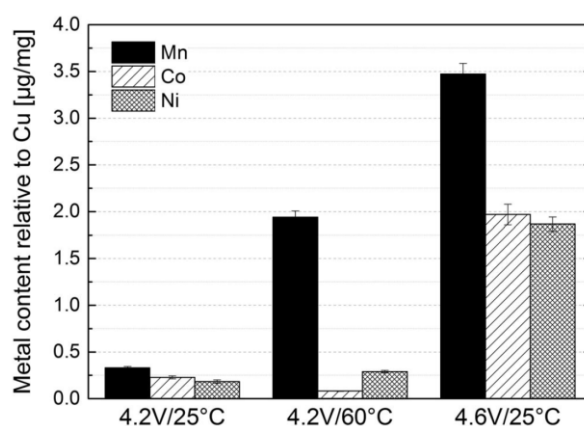


Figure 11: Concentration of Ni, Mn and Co deposited on harvested aged graphite electrodes determined by PGAA after cycling graphite/NMC111 cells up to 300 cycles at indicated temperatures and upper cutoff potentials (reproduced from [25] with permission from The Electrochemical Society).

2.3. Transition Metal Deposition at the Anode

At this point it is unclear, whether the deposition of transition metals on the anode is harmful or not. This question is particularly difficult to examine, since the deposition of metals on the cathode is a secondary process, which is overshadowed by the actually primary process, the cathode aging by means of cation dissolution. Furthermore, it is unclear what the exact mechanism and the location is where the cations are being deposited and in what chemical state they are after their deposition. Also it is unclear, if and in what way the physical and chemical properties of the SEI are affected. A brief overview of the work published on the deposition of the transition metal cations and comment the work from the application point of view is given. Since the oxidation state of the transition metals is unclear, it is only pointed out when evident.

Due to the complexity of the SEI itself, the analysis of the deposition location of transition of metal cations on the anode with conventional techniques (e.g. electrochemistry, electron microscopy, surface spectroscopy etc.) is challenging. However, their chemical state can give an indication how and where

the cations are deposited. Shkrob *et al.*, who focused on the investigation of deposited Mn (see Figure 11) found contradicting information regarding the oxidation state, which is why contradicting hypotheses on the deposition mechanism were expressed. Using X-ray photoemission spectroscopy (XPS), Boulet-Roblin *et al.* identified both Mn and Co to bound as M^{2+} species [90]. In addition, Zhan *et al.* confirmed the 2+ oxidation state by both XPS and X-ray absorption near edge spectroscopy (XANES) on delithiated electrodes. Consequently, they proposed a chemical exchange mechanism, in which Mn^{2+} -ions are exchanged with bound Li^+ -ions in organic SEI species, which would not affect the Mn^{2+} -ion oxidation state [87]. An illustration of the proposed ion exchange mechanism is presented in Figure 12. While the deposition of Mn would actually release Li^+ -ion charge carriers and retain lost capacity, the newly formed organic Mn-containing species might catalyze further electrolyte reduction or SEI transformation, so that bottom line Li^+ -ions are consumed and the Li^+ -ion conductivity of the SEI reduced [36,91]. Since the ion exchange is a charge-neutral reaction, the deposition of cations would not lead to an electron flow, while only secondary SEI transformation or reformation reactions would demand a detectable external electron flow at the anode half-cell.

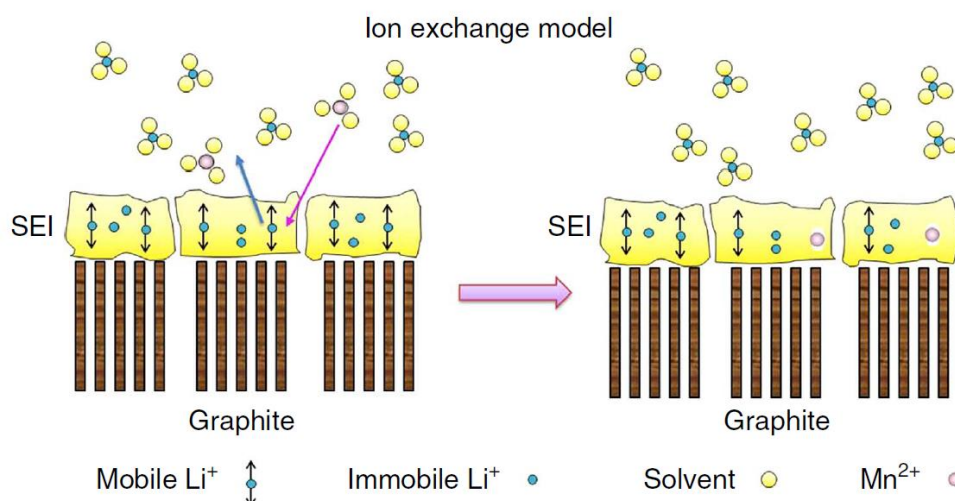


Figure 12: Proposed ion-exchange model for the deposition of Mn^{2+} -ions on the graphite anode in the graphite/LMO cells. Bound Li^+ -ions are released from organic SEI species, while Mn^{2+} -ions take the former Li^+ -ion positions (reproduced from [87] with permission from Springer Nature).

On the other hand, just like proposed by other groups [33,35,92–94], Gowda *et al.* found Mn^0 on the surface of lithiated electrodes using XANES, which is why they suggested an electrochemical reduction of Mn^{2+} -ions [89]. In detail, they proposed two possible reduction mechanisms: The first consists of a reduction of Mn^{2+} -ions at the electrode surface due to SEI defect sites (e.g. cracks). The second option consists of an electronic transport through the passivated SEI resulting in a reduction of Mn^{2+} -ions somewhere in the SEI or even on its surface. The second option was also illustrated by Danzer *et al.* in Figure 11 (failure mechanism nr. 10). The electrochemical reduction appears to be plausible from the potential point of view, since the redox potentials of the transition metals are significantly higher than the anode operation potentials [31].

First doubts concerning the simplicity of the deposition mechanism of the cation can be extracted from the work by Ochida *et al.* [35]. They compared two edge plane HOPG samples which were cycled under equal conditions: after SEI formation and a few intercalation/deintercalation cycles were performed and the electrolyte was exchanged with a Mn^{2+} -ion contaminated one. The cells were then run a few more cycles before their disassembly in fully delithiated state (high potential). While the one cell was disassembled immediately, the second was left at open circuit conditions for 24 h before disassembly. An XPS analysis revealed a similar amount of deposited Mn, though the XPS peaks were shifted by several eV. Ochida *et al.* suggest, that during the 24 h at open circuit conditions electrochemically deposited Mn was oxidized, leading to the respective shift of the XPS peaks.

A recent publication by Shkrob *et al.* refuted both earlier mentioned deposition hypotheses [88]. They were able to reproduce the contradicting XANES data, though clearly assigned Mn^0 to lithiated and Mn^{2+} to fully delithiated anodes, meaning that deposited Mn changes its oxidation state with the anode lithiation degree. In addition to the reproduction of the XANES results, using electron paramagnetic resonance spectroscopy (EPR) they revealed, that the identified reduced Mn on lithiated anodes is not in metallic $\alpha\text{-Mn}^0$ state. Furthermore, they propose the deposition to take place at the inner compact SEI layer, as the neighborhood probably consist of Li_2CO_3 . These findings are consistent with the earlier mentioned second hypothesis by Gowda *et al.*, which suggests an electron transport through the passivated SEI [89]. At this point it remains unclear, how the electrons can be transported through the insulating SEI. An illustration of the mechanism is given in Figure 13, which assumes the deposition to primarily form metallic clusters on the compact layer surface, which are later reoxidized at higher potentials.

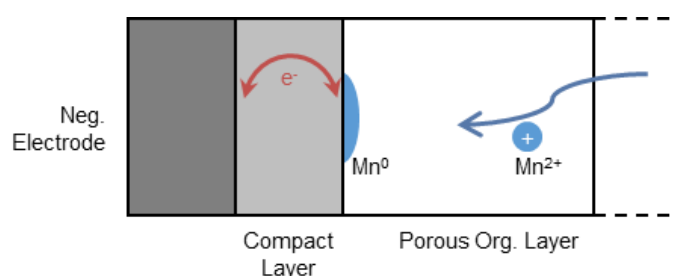


Figure 13: Combination of the hypotheses by Gowda *et al.* and Shkrob *et al.* [89,88], which assumes the electrons to be transported across the compact layer leading to a deposition of transition metals (here Mn) on the compact mineral SEI surface.

It has to be mentioned, that the ion exchange mechanism by Zhan *et al.* (Figure 12) is probably actually thermodynamically favored due to the reduction of entropy. Shkrob *et al.* stated a reasonable hypothesis on how the exchange mechanism could nevertheless be prevented [88]. The hypothesis consists of chelating anions (e.g. ethylene dicarbonate), which are originally dissolved SEI components, forming a neutral complex of Mn(II) at the positive electrode during cation dissolution. The complex would not migrate but only diffuse to the negative electrode. The strongly bound ligands could only be replaced

by similarly chelating surfaces (e.g. carbonate), which are only found in the compact SEI layer. Therefore, the organic outer porous SEI is unaffected by dissolved cations. The model is illustrated in Figure 14. a) shows the standard solvation of cations by electrolyte solvent carbonates and the strong affection to the anode due to the electric field, b) illustrates the neutralization of cations by dissolved SEI species. The neutralization of transition metal cations in such complexes might not be necessary to avoid the ion exchange, but more likely the activation energy is too high. If performed, respective electrolyte studies did not reveal any considerable cation concentration, indicating that the cations are not neutralized and simply diffuse but actually migrate to the negative electrode and are deposited quickly [21,83,88,95,96].

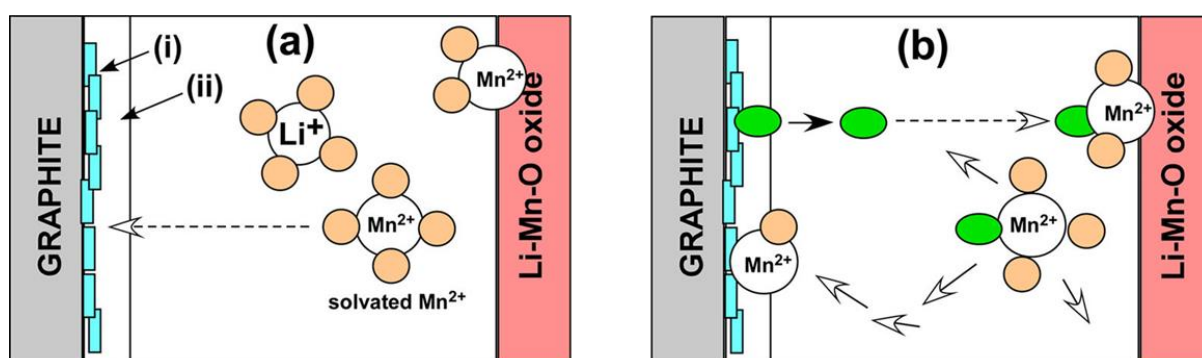


Figure 14: Two models of transport and deposition of Mn²⁺-ions in Li-ion batteries. a) Mn²⁺-ions are solvated by carbonate molecules and drift along the field lines penetrating through the outer (organic) SEI (ii) and become deposited into the inner compact SEI layer (i). b) SEI species form charge-neutral Mn(II)-complexes that diffusively migrate to the graphite surface, bypassing the outer SEI (reproduced from [88] with permission from American Chemical Society).

2.4. Open Questions & Motivation

In literature, a good overview of several SEI-related effects is provided, though they are obviously not fully understood and suffer from several almost untouched white spots. In order to better control the plurality of side reactions in state-of-the-art cells and handle upcoming problems of future materials, a deeper understanding is necessary, so that cell performance can be improved. Particularly the following questions are still unclear and serve as a motivation to perform the studies of this work:

- How does the SEI chemical and physical properties depend on the formation potential?
- How do those properties affect the SEI passivation ability (capacity fade) and Li⁺-ion conductivity (power fade)?
- Is it only a matter of chemical composition or are there further important parameters?
- How can one benefit from the knowledge of the dependency of the SEI properties on the formation potential?
- What is the deposition mechanism of transition metal cations on the anode? Where are the cations deposited and what species do they form?
- What is the influence of water during SEI formation?

- What effects do deposited transition metals have on the lifetime and power capability of a Li-ion cell?
- If disadvantageous, how can one avoid the deposition of transition metals on the anode?

3. Methodology & Design of Experiments

3.1. Automotive Framework Requirements

Since the results of this work should be applicable to the automotive and other industries, a set of framework requirements were considered. They ensure, that the results describe a realistic system, so that findings are reliable and transferrable to automotive cells.

a. SEI Formation

The SEI formation potential is highly important for the chemical and physical properties of the SEI as well as its long term stability [46,49,97,98], therefore this work considers a potentiostatic or potentiodynamic formation in the model electrode experiments. Potential controlled SEI formation allows understanding the qualitative and quantitative properties of different SEIs as well as the mechanisms induced by contaminations. However, it has to be mentioned that, in series production, the formation typically concludes of galvanostatic cycling at different rates and SOC's for technical and economic reasons, leading to a free-moving formation potential during the cycling procedure [4]. For that reason, formation procedures for commercial-like composite carbon electrodes are designed using galvanostatic steps as a base.

Since SEI formation is usually performed by the cell manufacturer soon after production at room temperature (again for economic reasons), all formation experiments in this work were performed at a fixed room-like temperature in atmosphere free environment (sealed cells).

b. Electrolyte Composition

The electrolyte is one of the major parameters affecting the composition of the SEI and therefore its properties [8,99]. Nevertheless, most of the cell manufacturers utilize similar electrolytes, meaning that mainly relative amounts of carbonate solvents or additives vary. Typical electrolytes consist of similar gravimetric ratios of cyclic alkylene carbonates like ethylene carbonate (EC) and linear carbonates like dimethyl carbonate (DMC) or ethyl methyl carbonate (EMC) as well as small mass percentages (around 2%) of additives like vinylene carbonate (VC) or fluoroethylene carbonate (FEC). The typically used salt is LiPF_6 in concentration around 1 mol L^{-1} , sometimes anion derivatives like lithium bis(oxalato)borate (LiBOB) can act as SEI-forming additives as well [4]. Instead of varying the electrolyte composition, this work focuses on one single commercially available and utilized electrolyte with the above-mentioned properties, assuming that minor electrolyte deviations would

not significantly affect the trends in the results. For that, the expected trends and conclusions are predicted to be valid also for similar electrolytes.

c. Cation Combination & Concentration

The utilized contamination cation species Mn and Ni are based on state-of-the-art automotive cathodes or are considered because of cathodes being promising candidates for future automotive applications (e.g. NMC622 or NMC811) [1,100,101]. The considered concentrations are derived from representative pre-experiment cells, which respected/considered series cell parameters (electrode, electrolyte, separator compositions and amounts). These pre-experiment cells were contaminated with a defined amount of water, cycled, stored and then analyzed with regard to transition metals.

d. Cation Deposition

One of the major aging mechanisms in Li-ion cells is the slowly ongoing cation dissolution from the cathode, whose origin can have several reasons [25,26]. Apart from diffusion forces, the dissolved cations are attracted by the low potential of the anode. Although passivated towards electrolyte reduction, the anode serves as deposition target for the cathode cations. Independently of the actual deposition mechanism, the potential of the (either lithiated or delithiated) anode is always significantly smaller than the redox potential of the considered transition metals (~ 2 V vs. Li/Li⁺). To simulate this but avoid interference with possible additional SEI formation, in this work cations are deposited at a potential by far low enough for the cations to be electrochemically reduced, but high enough to suppress further possible electrolyte decomposition. This way, results of contaminated anodes can be compared to the baseline experiments and literature.

e. Composite Carbon Electrode Composition

In order to meet the requirements of the automotive industry the partially used composite electrodes were produced based on a recipe respecting automotive standards. The major features are a high active material concentration ($\sim 96\%$), the usage of water as electrode slurry solvent, respective water based binders and a considerably high electrode mass loading of ~ 7 mg cm⁻². Those three are pointed out, as they are not necessarily a standard particularly in academia or consumer electronics.

3.2. Experimental Simplifications

To successfully achieve the goals of this work, the experimental idea is first put down by three major experimental simplifications. The first one consists of the usage of a model carbon surface, which neither facilitates any lithium intercalation nor contains any binder and/or conductive agent. In this way the physical and chemical properties of the SEI can be studied independently with both fundamental electrochemical methods and surface spectroscopy tools. In particular, the SEI is highly dependent on potentials and currents during formation, wherefore a reduction of overlap signals is necessary. The second simplification is the use of an electrochemical three-electrode setup to control and measure the potential

at the anode half-cell independently. Using a two-electrode full cell setup would not allow controlling the anodic potential and therefore would lead to misleading electrochemical results. The third simplification consists of the simulation of primary effects of a water-contaminated electrolyte and the following transition metal dissolution at the cathode by using clean electrolytes, which can be specifically contaminated with water and/or selected transition metal cations. Contaminated electrolytes can be introduced into the cell at discretionary point in time, so that the automotive framework conditions are respected and well simulated: E.g. First the SEI is formed and passivated in neat electrolyte, then the cations are introduced in the right amount and deposited in the presence of a passivated SEI on the anode.

By applying those experimental simplifications an extensive amount of overlaps can be avoided. Therefore, it enables addressing the obtained trends and results to specific effects, so that the mechanisms are developed with reasonable certainty. Hereafter an explication of the mentioned simplifications and their experimental advantages are given in detail.

3.2.1. Model Electrode Surfaces

On real electrodes, during the first polarization an overlap of intercalation and SEI formation currents (as well as currents originating from other irreversible side reaction on current collectors and electrode slurry additives) are measured at certain potentials. These individual currents can usually not be separated. Therefore, during the polarization it is unclear, how many charges are actually consumed by the SEI formation itself, which is why real composite electrodes are hardly helpful for SEI investigations. To avoid such an overlap, model surfaces can be used as a measure. They provide a broad variety of advantages in the field of Li-ion battery research. In particular, to effectively investigate SEI formation and stability, the utilization of these advantages is essential.

This work considers several 111-single-crystals like Au and Pt, model carbon structures like graphene | Pt and particularly highly oriented pyrolytic graphite (HOPG) as model surfaces. Experimental attempts with glassy carbon (GC), which is supposed to be inert against Li intercalation [59], failed in the experiments of this thesis due to an obvious reversible reaction. These attempts and some advanced experiments focused on the origin of the reversible reaction are discussed separately in chapter 3.4.

Since the SEI strongly depends on the carbon surface, results obtained on model electrode surfaces cannot necessarily be transferred into commercial systems. Though, one of the goals of this work is to verify the models originated from the model surfaces like HOPG on composite carbon electrodes, so that the model applicability is ensured. The transferability is discussed in several chapters of this work. Since HOPG is one of the major surfaces investigated in this thesis, it is described in the following in more detail.

As depicted in Figure 15b, HOPG consists of stacked graphene layers. Depending on the application it can be considered a single crystal with no roughness and only one defectless basal plane on top [102,47].

Since basal carbon layers do not facilitate any lithium intercalation, which only enters the graphite crystal on edge sites [49], it would be denoted as inactive in terms of Li intercalation. However, during the cleaning procedure one cannot assume a perfect basal plane on the crystal surface, but rather expect severe amounts of catalytically active step edges and defects, offering Li^+ -ions and solvent a spot to be reduced and/or intercalated (Figure 15a). The influence of the defect density on basal plane HOPG on the formation of the SEI is discussed in detail in chapter 6.2, where basal plane HOPG is compared to edge plane HOPG and defect-less graphene.

On the other hand, solid phase Li diffusion coefficients in graphite are known to be several orders of magnitude smaller than in liquid organic electrolytes. Furthermore, Li diffusion coefficients in HOPG itself are another few more orders of magnitude smaller than in natural graphite [103–106]. Therefore, the relatively small amount of edge sites (compared to series active material) does not lead to a significant lithium intercalation at higher crystal depths. If not suppressed, the lithium intercalation is assumed to be negligible. The correctness of this assumption is discussed in detail in chapter 4.1. HOPG can easily be cleaned by stripping off a few graphene layers using commercially available adhesive tape as a stripping tool [48,107,108]. That way, surface contamination (e.g. SEI) as well as possibly intercalated lithium residuals can be removed.

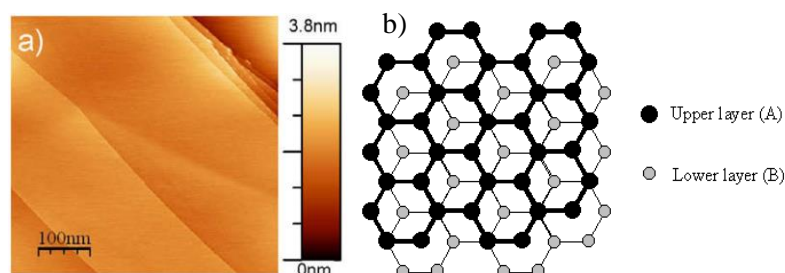


Figure 15: a) AFM Tapping on HOPG (reproduced from [107] with permission from Elsevier); b) Positional relationship between two identical graphene planes A and B (reproduced from [109] with permission from ISB Ltd.).

3.2.2. Three-Electrode Setup

For separated investigations of electrochemical processes on a single interface it is indispensable to use a so called three-electrode setup. This electrochemical setup consists of three actively participating electrodes with different tasks. Figure 16 shows schematically the electric circuit.

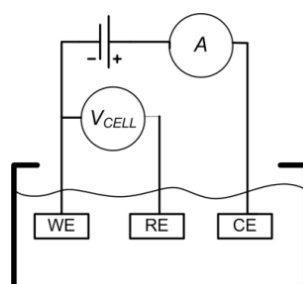


Figure 16: Schematic illustration of the electrochemical three-electrode setup (reproduced from [110] with permission from IntechOpen).

The use of a two-electrode setup would lead to a potential shift at both electrodes during current flow, so that the single half-cell potential would be unknown. Again, a three-electrode setup provides the possibility to control the sampling electrode (depicted as WE) potential during a current flow, so that only the half-cell reactions are visible and not overlaid by processes of a second electrode. For that, the investigated electrode, at which the processes of interest occur, is called the working electrode (WE). The potential of the WE is measured or set vs. a reference electrode (RE). The RE has to have a well-defined and well known interfacial potential drop, which in the ideal case is time invariant and independent from any current flows, ion movements and concentration gradients. The third electrode is called the counter electrode (CE) and provides the current counterpart to the WE. The CE potential is not of an interest, since its task is to provide currents in oxidative as well as reductive direction and –in this case- keep the concentration of solvated species stable. [71].

This work considers T-shaped three-electrode cells. Materials or samples, on which an SEI is formed, are connected as WE. The RE consists of a quasi-secondary reference electrode, which is in direct contact with the electrolyte. Possible electrochemical as well as chemical reactions, which could cause a WE potential shift, can be assumed to be negligible due to the small surface area compared to the WE and CE (several orders of magnitude) [111,112], However, as described earlier the CE needs to balance concentration variations of solvated species in order to ensure a stable potential of the quasi-secondary RE. The laterally positioned RE avoids potential shifts due to electric fields between the opposing WE and CE. All cells were either air tight or ran in a small and inert environment, so that fugitive solvent vaporization and atmospheric contamination can be avoided.

3.2.3. Water Contamination

While it is widely accepted that water impurities in Li-ion cells can be disadvantageous for the cell performance, the reaction pathway of water particularly in real cells is hardly investigated and understood. Since in real cell production it is common to heat the cell before and after electrolyte filling (to ensure lower viscosity and thus faster wetting), most of the water coordinated to any of the cell components will be decomposed to HF [6,85]. Thus, one can assume that water itself cannot act as a reactant in SEI formation, instead the role of HF needs to be investigated. For investigations of SEI formation under the influence of water, new method to actually determine the HF concentration of carbonate based electrolytes was developed. By that, several electrolytes were mixed allowing the concentration-dependent investigation of HF influences. Having in mind that the concentration of the electrochemically active species is a major factor in fundamental electrochemistry, concentration dependent experiments allowed again for the application of fundamental electrochemical techniques as well as the coupling of DFT simulation.

3.2.4. Cation Deposition Simulation

Electrolytes can be contaminated directly with transition metal cations by solving appropriate salts in the electrolyte. If these salts include an inactive anion, the cations can be utilized as active reaction

educts excluding further anion side reactions. [31,33,34,59]. Though, introducing a contaminated electrolyte before the SEI formation would not simulate adequately the processes in series cells. Therefore, the experiments described and discussed in the respective chapter considered a custom-built three-electrode setup, which facilitates an *in-situ* injection option. That way, transition metal cations can be introduced to the cell at any time, thus as well after finishing the SEI formation. The cell itself is presented in the later part of this document, a first impression of the cell with a syringe connected is given in Figure 17. The specific introduction of transition metal cations only after SEI formation is the only reliable way to electrochemically investigate the deposition mechanism and effects. This procedure replaces the first two original reaction chain steps (i. contamination attacks and corrodes cathode; ii. transition metal cations are dissolved), which are almost impossible to control experimentally [15,27,28,84,85].

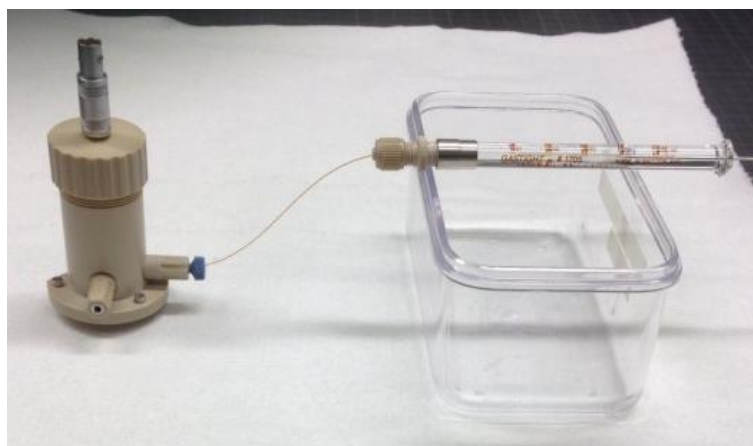


Figure 17: Assembled three-electrode T-cell for Fc/Fc⁺ and cation injection experiments: Syringe and the vertical screw plug connected via glass capillary for electrolyte injection during experiments.

3.3. Experimental Approach

In contrast to the used model electrode surfaces, which inhibit Li⁺-ion intercalation, the composite carbon electrodes are commercial-like and therefore facilitate a high Li⁺-ion capacity. Therefore, the main reaction on composite carbon electrodes is the lithiation/delithiation, while further reactions (e.g. SEI formation) are only minor side reactions and can therefore not be adequately separated (opposite to model electrode surfaces, where the only significant reaction is the SEI formation, which passivates independently of the formation potential). Therefore, the electrochemical techniques applied to the different electrodes vary significantly and lead to several pieces of information about the SEIs and the subjacent electrodes. A short overview is given in the following.

3.3.1. Methods on Model Electrode Surfaces

SEI Formation: In order to compare SEIs on model electrode surfaces, it has to be assured that the charges the SEI consumed during formation are similar independently of their formation potential. Even if passivating, small leakage or tunneling currents still penetrate the SEIs and lead to continuous growth.

Since, apart electrolyte reduction, no other significant reaction takes place at the electrodes in neat electrolyte, SEIs can be formed comparably by setting the integrated charge as cutoff criterion. In that way, SEIs are formed by the same amount of charge and can therefore be compared.

Chemical Composition: After forming the SEIs, the chemical composition can be analyzed using surface spectroscopy techniques. In this work X-ray photoelectron spectroscopy (XPS) was performed, which is a common SEI analysis technique widely used by the research society [61,73–75,113–115]. XPS can reveal chemical elemental concentrations and bonding types at the surface. Using ion sputtering, it is possible to penetrate into deeper layers and create a depth profile or qualify the SEI thickness.

Electrochemical Characterization: Since no reversible reactant couple is present at the passivated model electrode surface, no electrochemical experiments can be performed. The sealed cell used consisted of the three electrode connections and a further plug, which allowed the connection of a syringe in order to inject further electrolyte. In that way, it was possible to inject electrolyte enriched with ferrocene/ferrocenium (Fc/Fc^+) as a probe couple without disassembling the cell. The benefits of this procedure are that the SEIs are formed in neat electrolyte and are not altered during cell disassembly. The introduction of a foreign electrochemical couple allows the utilization of fundamental electrochemical techniques like cyclic voltammetry (CV) and electrochemical impedance spectroscopy (EIS). Since oxidized and reduced species are both solved in the electrolyte, all the information extracted from fundamental electrochemical experiments describes the surface properties of the electrode. The comparison of the electrochemical information of the pristine electrode and the electrodes covered with different SEIs gives information about penetrable porous and impenetrable insulating surface layers. The thickness of insulating surface layers can e.g. be deduced from the outer sphere Fc/Fc^+ reaction rate, which is further reduced when reaction electrons have to tunnel through thin insulating films [57]. By investigating baseline layers, it is also possible to characterize surfaces covered by multiple layers [116].

Using the mentioned cell syringe connector, it is also possible to inject electrolyte enriched with an appropriate transition metal salt. By applying a potential small enough, the solved cations are able to migrate to the working electrode, where they are electrochemically deposited with a surface film dependent reaction rate. However, the cell consist also of Li^0 foil as RE and CE, where cations can be deposited chemically in parallel to the actually wanted plating reaction. The deposition rate on the RE and CE can be assumed to be constant and particularly independent of possible surface layers on the working electrode. Therefore, the amount of cations deposited on the working electrode, which can be calculated by integrating the respective reduction current, is a qualitative measure for the deposition reaction rate of cations on the SEI covered working electrode.

3.3.2. Methods on Composite Carbon Electrodes

Formation Procedure: For several reasons the formation cycles of commercial cells consist of galvanostatic cycling, which is why the investigated novel formation protocols in this work are based on

galvanostatic phases. When investigating composite carbon electrodes in terms of alternative formation protocols, several quantifiable values are of interest. The first key values are included in the formation procedure itself and are particularly of interest from the battery manufacturer point of view: Apart from an SEI with good and stable electrochemical properties, a manufacturer is interested in the reduction of the manufacturing cost (represented in parts by necessary infrastructure quantity or quality). For that reason, the duration of the formation procedure, the charge losses and the necessity using advanced hardware are discussed in this work.

Electrochemical Characterization: The electrode properties after formation cycle are the critical values which have to be compared in particular in order to qualify different formation protocols. As aforementioned, the SEI has to provide two features in order to be described as successful: The one is a low resistivity (e.g. due to high ion conductivity), leading to low overpotentials and therefore to high power capability and energy efficiency. The second is a long term stability, meaning that the SEI does not grow, therefore neither Li^+ -ions are consumed leading to further reduction of cell capacity nor the SEI resistivity increases [5]. The SEI resistivity is investigated using a rate discharge test, which consists of several electrode delithiation cycles with different current rates. The comparison of the potential profiles after different formation protocols amongst themselves and with certain OCP values allow the quantification of SEI resistivity improvements. The SEI stability is investigated using simple galvanostatic aging cycle tests. The electrode is cycled constantly with a high rate for a high amount of cycles, while the discharge capacity and coulombic efficiency are obtained, which ideally should be stable and close to 100%, respectively. The reproducibility of the potential profiles during the aging cycle test gives a further indication whether the SEI is generally stable.

3.4. Suitability of Glassy Carbon as Model Electrode in Li-Ion Research

Glassy carbon is used as a model electrode surface for SEI formation experiments. While literature suggest glassy carbon do be inert against Li^+ -ions and thus suitable fundamental SEI formation investigations, we found both “single-crystal”-like samples and composite glassy carbon electrodes (made out of spherical glassy carbon powder) to show a reversible capacity in standard Li^+ -ion electrolyte. CV experiments indicate, that the capacity is provided by both an intercalation-like process (similar to graphite) and an adsorption-like process (similar to soft carbon). During the first cycle the material is changed in a way, so that a further capacity providing mechanism is facilitated in the later cycles. The spherical powder shows a long-lasting specific capacity of $\sim 110 \text{ mAh g}$ under $1\text{C}/1\text{C}$ constant current experiments. While this value is too low for application as anode active material, being a good conductor glassy carbon may be optimized to become a conductive agent for anode purposes. With this being a side topic out of focus it is considered a failed experimental attempt. It nonetheless is presented in the following due to its informative character.

Tang *et al.* performed numerous SEI formation experiments in a similar setup using glassy carbon (GC) as a model electrode surface [59,60,98]. They suggest, that “(...) lithium intercalation into glassy carbon is thought to be minimal, meaning that the electrode is effectively inert”. Truly, they obtained CV data in electrolyte similar to the one used in this work, which obviously proves that no reversible reaction takes place. The respective original data is presented in Figure 18. It shows the first and second cycle of a flat GC electrode in LiPF_6 containing electrolyte at 5 mV s^{-1} . While the reductive current is significant in the first and little lesser in the second cycle, both do not include any oxidative current in the region $< 2 \text{ V vs. Li/Li}^+$, where possibly adsorbed or intercalated lithium should be released by oxidation reactions [5]. The minor oxidation current $\sim 4 \text{ V vs. Li/Li}^+$ indicates “the oxidative stripping of SEI products” [98]. Therefore, the statement by Tang *et al.*, “that intercalation is negligible, at least at potentials greater than 0.1 V for this particular source of glassy carbon” [98], can be fully supported.

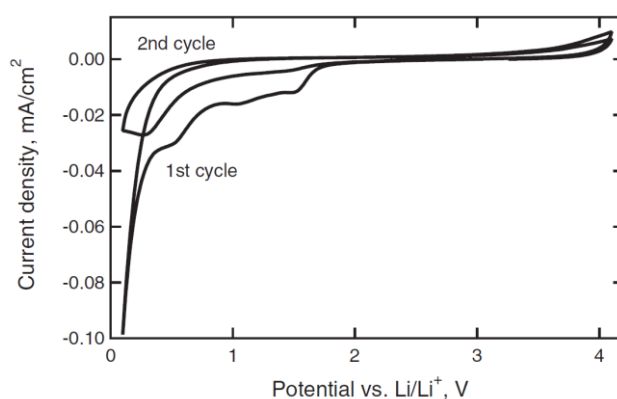


Figure 18: CV formation cycles at 5 mV s^{-1} on a glassy carbon electrode. Reduction peaks decrease on the second cycle, demonstrating passivation. No deintercalation peaks can be seen, suggesting that reversible lithium intercalation is negligible. Anodic current above 3.5 V corresponds to oxidative removal of SEI films. Figure reproduced from [98] with permission from The Electrochemical Society.

Using the work from Tang *et al.* as a base, we also obtained flat GC samples from the same supplier. While Tang *et al.* used a pre-assembled rotating disc electrode including the GC samples, we obtained spare samples. Thus, there was no certainty about the equality of the samples. CV data obtained at $400 \mu\text{A s}^{-1}$ in our setup is presented in Figure 19. The upwards scans do not only have significant oxidative currents (left plot), but both the cumulative (integrated) oxidation and reduction charges during a full scan (right plot) keep increasing with time. The coulombic efficiency is obviously very low, particularly in the first cycle due to SEI formation. On the other hand, solvent-only electrochemistry (red) shows no reversible reduction and oxidation charges. Obviously, the existence of a reversible capacity is counterintuitive when considering the earlier results by Tang *et al.* This indicates that the glassy carbon properties can vary in principle.

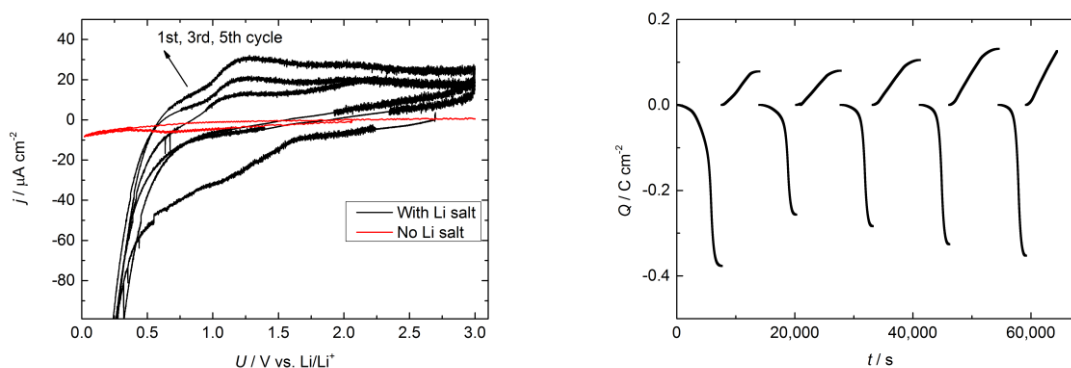


Figure 19: CV formation experiment on a flat glassy carbon electrode in the setup used in this work (red shows the first sweep only). The integrated charge Q shows a distinct reversible capacity, which increases with ongoing cycles.

Trying to understand a little more about the reversible reaction of glassy carbon, we obtained spherical glassy carbon powder (diameter $\sim 8 \mu\text{m}$) and coated commercial-like electrodes. The experimental details are similar to the ones described in ref. [5] (chapter 5) and therefore are not described here. We performed cyclic voltammetry experiments in a three-electrode setup at $50 \mu\text{V s}^{-1}$, which are presented in Figure 20. The electrode was cycled twice down to 20, in the third and fourth cycle down to 200 and 400 mV vs. Li/Li^+ , respectively. The deeper discussion of the data is out of the scope of this work, though we would like to briefly mention the electrochemical properties of the reversible reaction of spherical glassy carbon. A first eye-catcher is that the later cycles include a significant reversible reductive current plateau in the region 1.0-0.7 V vs. Li/Li^+ which cannot be found in the first cycle. It appears that the electrode active material first has to be polarized to low potentials in order to facilitate the high potential reduction reaction. Such transformation mechanism could be either of mechanical or of chemical nature. This would be compatible with a slowly increasing amount of reaction in the flat GC samples with cycling in Figure 19, which are not fully transformed in the first cycles due to the electrode thickness (1 mm). On the other hand, the CVs in Figure 20 also indicate, that the current is provided by surface reaction (e.g. adsorption/desorption) at high potentials, while a bulk-involving reaction takes place at potentials $< 200 \text{ mV vs. Li/Li}^+$.

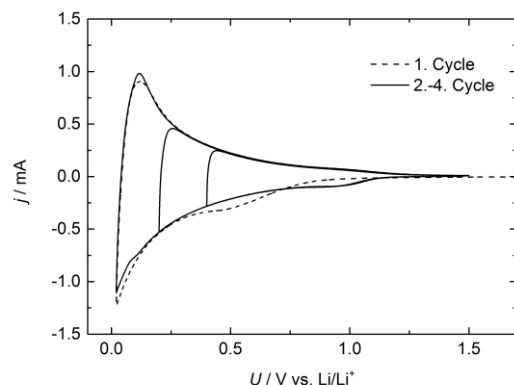


Figure 20: CV formation experiments on glassy carbon powder composite electrodes at $50 \mu\text{V s}^{-1}$. The lower vertex potential is increased in the 3rd and 4th cycle.

The conclusion of this chapter is that, even if obtained at the same supplier, complex materials like glassy carbon do not necessarily provide reproducible electrochemical properties. In this specific case, glassy carbon is not necessarily suitable for fundamental electrochemical experiments in Li^+ containing electrolyte. We could rather show that glassy carbon, which on the one hand was successfully proven to be inert against lithium intercalation by Tang *et al.*, on the other hand can also provide a significant reversible capacity. The implied electrochemical properties of spherical glassy carbon were investigated in more detail also using galvanostatic cycling ($\sim 110 \text{ mAh g}^{-1}$) and XPS. The respective results, which provide new insights into glassy carbon and its similarity to soft carbon, are out of the scope of this work and will not be further discussed.

4. Results and Discussion Section 1 – Model Electrode Surfaces

4.1. Formation of the Solid Electrolyte Interphase at Constant Potentials: a Model Study on Highly Oriented Pyrolytic Graphite

Status	Published online, 20 June 2018
Journal	Batteries & Supercaps, 2018, Volume 1, 110-121
Publisher	Wiley-VCH
DOI	10.1002/batt.201800029
Authors	Antonopoulos, Byron K.; Maglia, Filippo; Schmidt-Stein, Felix; Schmidt, Jan P.; Hoster, Harry E.

Issue Cover Profile: doi 10.1002/batt.201800064

Issue Cover Picture: doi 10.1002/batt.201800065

Contributions: B.K.A., F.M. and H.E.H. conceived and designed the experiments. B.K.A. and F.S.-S. performed the experiments. B.K.A. and J.P.S. performed the calculations. B.K.A., F.M. and H.E.H. discussed the results and wrote the paper.

Content

The solid electrolyte interphase (SEI) on graphite anodes is a key enabler for rechargeable lithium ion batteries (LIBs). It ensures that only Li^+ -ions and no damaging electrolyte components enter the anode and hinders electrolyte decomposition. Its growth should be confined to the initial SEI formation process and stop once the battery is in operation to avoid capacity/power loss. In technical LIB cells, the SEI is formed at constant current, with the potential of the graphite anode slowly drifting from higher to lower voltages. SEI formation rate, composition, and structure depend on the potential and on the chemical properties of the anode surface.

HOPG is used to study SEI formation at potentiostatic conditions, which are achievable without strong cell polarization due to the low surface area of this sample. Furthermore, the basal plane of HOPG is chemically inert, and Li^+ -ion intercalation is negligible. We study SEIs formed at four different potentials (600, 450, 300, 100 mV), analyzing their chemical composition by ex-situ XPS and their electrochemical (transport) properties through the interaction with Fc/Fc^+ as a probe species. SEI formation is found self-terminating, hence self-passivating at all potentials investigated, which implies the formation of an electronically insulating layer, which is also impermeable for SEI-forming electrolyte components

(thus: compact layer). XPS revealed Li_2CO_3 formation only for the two lower formation potentials (300 and 100 mV), i.e. the high-potential compact SEI is essentially organic. This also shows that, contrary to prevalent opinion, carbonate formation is not necessary for electrode passivation. The SEI formation process in commercial cells makes use of galvanostatic conditions, which leads to a slow potential sweep from higher to lower potentials. Given that our results indicate a suppression of direct electrochemical electrolyte decomposition already by the high-potential SEI, we conclude that the typical carbonate layers found after such galvanostatic SEI formation result from further electrochemical decomposition of the pre-formed high-potential organic compact SEI.

The presence of a compact SEI after formation is also confirmed by Fc/Fc^+ cyclic voltammetry and corresponding EIS experiments and Distribution of Relaxation Times (DRT) analysis. For all four potentials, those measurements revealed significant inhibition of charge transfer kinetics through the SEIs as compared to pristine HOPG. In agreement with the XPS observation of carbonate only for the low-potential (300 and 100 mV) SEIs, we also find that the latter exhibit much more sluggish electron transfer kinetics than the high-potential (600 and 450 mV) SEIs. Based on a simple electron tunneling model, these observations allowed us to calculate the factors by which the effective tunneling distances change, which we tentatively associate with the thicknesses of the compact SEIs.

As a side result, the CV and EIS data also reveal some information about the ionic movement (migration and diffusion) through the outer part of the SEI, the porous layer: effective permeability is found to decrease with decreasing formation potential, which we tentatively assign to a shortening of the organic polymer chains formed from ring-opening reactions of ethylene and vinylene carbonate.

In summary, the previously described two-step process of SEI formation would start at ~ 700 mV with the formation of an organic compact layer (covered by a porous one), which is then itself reduced to a much thicker compact, yet inorganic (carbonate containing) layer once potentials drop (either in a CV or due to galvanostatic control) to below ~ 400 mV. Knowing that, we conclude that by controlling the chemical and physical properties of the high-potential SEI, one can significantly influence the respective properties of the final low-potential SEI and thus influence the lifetime and conductivity properties of SEIs in commercial cells.

VIP Very Important Paper



Formation of the Solid Electrolyte Interphase at Constant Potentials: A Model Study on Highly Oriented Pyrolytic Graphite

Byron K. Antonopoulos,^[a] Filippo Maglia,^[a] Felix Schmidt-Stein,^[a] Jan P. Schmidt,^[a] and Harry E. Hoster^{*[b]}

The solid electrolyte interphase (SEI) on graphite anodes is a key enabler for rechargeable lithium-ion batteries (LIBs). It ensures that only Li⁺ ions and no damaging electrolyte components enter the anode and hinders electrolyte decomposition. Its growth should be confined to the initial SEI formation process and stop once the battery is in operation to avoid capacity/power loss. In technical LIB cells, the SEI is formed at constant current, with the potential of the graphite anode slowly drifting from higher to lower voltages. SEI formation rate, composition, and structure depend on the potential and on the chemical properties of the anode surface. Here, we characterize SEIs formed at constant potentials on the chemically inactive basal

plane of highly oriented pyrolytic graphite (HOPG). X-ray photoemission spectroscopy (XPS) detects carbonate species only at lower formation potentials. Cyclic voltammetry (CV) and Electrochemical Impedance Spectroscopy (EIS) with Fc/Fc⁺ as an electrochemical probe demonstrate how the formation potential influences ion transport and electrochemical kinetics to and at the anode surface, respectively. Breaking the EIS data down to a Distribution of Relaxation Times (DRT) reveals distinct kinetics and transport related peaks with varying Arrhenius-type temperature dependencies. We discuss our findings in the context of previous electrochemical studies and existing SEI models and of SEI formation protocols suitable for industry.

1. Introduction

Li-ion batteries (LIB) have become a technologic and commercial success through the combination of graphitic carbon and a transition metal oxide as negative and positive electrode, respectively. Li intercalated in graphite is thermodynamically slightly more stable than in metallic form: Li-ions reversibly (de-)intercalate into/out of graphite at ~100 mV vs. Li/Li⁺. This helps to avoid Li dendrites. An ideal LIB electrolyte would combine high ionic conductivity, diffusivity, broad temperature stability, and stability against electrochemical decomposition at anode or cathode. Commercially available electrolytes have been engineered to come close to those ideals, but do not quite reach all of them simultaneously.^[1–5] In particular, electro-

chemical decomposition at the negative electrode is thermodynamically possible; hence only kinetic hindrances of those side reactions make the thousands of charge/discharge cycles possible that can be achieved, e.g., with electrolytes consisting of alkyl carbonates as solvents and LiPF₆ as conducting salt.^[6,7] Kinetic suppression of ongoing electrolyte decomposition is achieved through the initial “formation” step applied to all commercial LIBs. In that first negative polarization of the graphite anode, the electrolyte is decomposed in a controlled way into a passivation layer that, once sufficient thickness is reached, will kinetically suppress ongoing electrolyte decomposition.^[8,9] Another key property gave this passivation layer the name “solid electrolyte interphase” (SEI): It acts as solid electrolyte for Li⁺ transport between the liquid electrolyte and the graphite electrode. Furthermore, it acts as a filter, preventing co-intercalation of other electrolyte components (e.g. solvent), which would otherwise quickly destroy the graphite electrode structure. In real systems, further electrolyte decomposition is not completely suppressed and continues, yet at a small rate, which grows the SEI over time. The two most prominent negative effects of this ongoing process are (i) increasingly sluggish Li⁺ transport kinetics through the SEI and (ii) irreversible incorporation of Li⁺ into the SEI, thus lowering the cell capacity. Formation and further development of the SEI depend on electrolyte and electrode composition and preparation, formation parameters and contaminations including those produced during the cell life.^[8,10–21]

From an interfacial electrochemistry perspective, the SEI can be handled as a nearly homogeneous adlayer with conducting channels. Perpendicular to the electrode, one can imagine a sequence electrode | SEI(compact layer) | SEI(porous part) | elec-

[a] B. K. Antonopoulos, Dr. F. Maglia, Dr. F. Schmidt-Stein, Dr. J. P. Schmidt
BMW Group
Petuelring 130, 80788 München, Germany

[b] Prof. Dr. H. E. Hoster
Dep. of Chemistry
Lancaster University
Lancaster, LA1 4YB, UK
and
ALISTORE European Research Institute CNRS FR 3104
Hub de l'Énergie
Rue Baudelocque, 80039 Amiens, France
and
The Faraday Institution
Quad One, Harwell Science and Innovation Campus
Didcot, UK
+44 7842 831633
E-mail: h.hoster@lancaster.ac.uk

Supporting Information and the ORCID identification number(s) for the author(s) of this article can be found under:
<https://doi.org/10.1002/batt.201800029>

trolyte.^[22] The compact layer was found to partially consist of inorganic (Li-containing) species, which were hypothesized to be formed only once lower potentials are reached during the formation process, then consuming Li^+ and parts of the organic SEI components formed at higher potentials ("two-step mechanism"^[19,23,24]). It is now well accepted that the safe and reliable operation of rechargeable LIBs demands understanding and control of side reactions, many of which are influenced by the electrode potential and the local surface chemistry and structure. Hence, in analogy to fundamental research in the electrocatalysis community,^[25,26] deeper insights require studies at well-defined model surfaces under potentiostatic conditions, and involving both electrochemical techniques as well as high resolution surface microscopy and spectroscopy.^[20,21,27–35] Particularly the SEI on Glassy Carbon (GC) was studied extensively by Tang et al.^[23,36,37] and others.^[38,39] For commercial electrolyte, Fc/Fc^+ as an electrochemical probe for the effect of the SEI on ion transport and electrochemical kinetics revealed that SEI formation can be broken down to two key steps at ~ 700 and ~ 400 mV vs. Li/Li^+ .^[35] More recently, we and others studied the formation of LiF , a frequently observed SEI component, on smooth carbon and metal single crystal surfaces and demonstrated the importance of surface electrocatalysis.^[40–42]

For the present study, we have chosen the basal plane of highly oriented pyrolytic graphite (HOPG) as a model electrode, and using a cell setup that resembles the pressure conditions of LIB electrodes. Since this surface exposes few chemically reactive sites (i.e., step edges and defects), it is electrocatalytically virtually inert. Hence, surface reactions will be dominated by the availability of reactants and the electrochemical potential. In analogy to studies on glassy carbon,^[38,39] the low surface area of HOPG^[35] allows applying potential steps followed by constant-potential periods, which on technical high-surface area electrodes would cause high current peaks, long relaxation times, and inhomogeneous potential distribution. In the electrochemical part of our experiments, we followed the protocols that Tang et al. used in their model studies at glassy carbon: SEI formation at four different potentials and probing the resulting SEI properties using cyclic voltammetry (CV) and electrochemical impedance spectroscopy (EIS) of dissolved Fc/Fc^+ . Beyond that, we analyzed the potential-dependent composition of the SEI by ex-situ X-ray photoelectron spectroscopy (XPS), and we broke down the EIS data into a Distribution of Relaxation Times (DRT). We discuss the findings of our multi-method study in the context of previous electrochemical model studies and existing SEI models^[22,23,35–39] and suggest how our findings may inform more efficient SEI formation protocols in industry.

Experimental

Basal plane HOPG (mosaic spread $0.8^\circ \pm 0.2^\circ$, Plano GmbH, Germany) was cleaned with adhesive tape before being used as a model electrode surface. It was fully covered by PET tape (T 851, 3 M, USA) leaving exposed a well-defined basal circular area with 4 mm diameter to the electrolyte. The sample was finally mounted on the sample holder and then dried at 60°C for 12 h at a pressure

$\sim 10^{-2}$ mbar in a vacuum oven (Glass Oven B-585 Drying, BÜCHI Labortechnik AG, Switzerland) before being transferred without atmosphere contact into an Argon filled glove box. The other cell components were cleaned with 2-propanol and demineralized water in an ultrasonic bath and then dried at 60°C before being transferred into the glove box for cell assembly. The glove box contained < 0.1 ppm water and < 3 ppm oxygen.

All experiments were performed several times in order to ensure reproducibility. Conspicuously deviating results were not considered. This was particularly important as some of the manually affected experimental side parameters (e.g. injection speed and position, sample preparation and washing, position of single cell features etc.) can vary. Accuracy of quantitative values (number of digits) given in this work is based on typical variances.

Electrochemistry

We used a closed 3-electrode T-cell with the option to connect a further feature (designed and manufactured by rhd instruments GmbH & Co. KG, Germany; see also their recently released "TSC battery standard"). Li foil (ca. 500 μm , Alfa Aesar, UK) served as counter and reference electrode. The sample was separated by a Whatman GF/A glass fiber separator (Sigma Aldrich, Germany) soaked in 75 μl BASF LP572 (EC:EMC 3:7, 1 M LiPF_6 , 2% wt VC, BASF, Germany). The CE and sample were pressed against each other by a spring. The sample holder included a Pt100 temperature sensor for sample temperature control. The second vertical connector ("syringe connector") was used to connect a Hamilton Gastight syringe (VWR, Germany) via a glass capillary. The syringe contained around 30 μl electrolyte enriched with 10 mMol ferrocene and ferrocenium hexafluorophosphate (Fc and Fc^+ , respectively, both from Sigma Aldrich, Germany), of which 25 μl were injected into the cell, yielding a Fc/Fc^+ concentration of 2.5 mMol L^{-1} . For SEI-free experiments, no syringe was connected and the syringe connector was sealed with an appropriate plug. 100 μl of electrolyte with $2.5 \text{ mMol Fc}/\text{Fc}^+$ concentration was used.

The assembled cell was mounted on a Microcell HC cell holder connected to a Eurotherm temperature controller (both rhd instruments GmbH & Co. KG, Germany). Unless otherwise mentioned, all electrochemical experiments were performed at 20°C . The electrochemical instrumentation was an Autolab M101 Potentiostat with FRA32M impedance spectroscopy module controlled by the manufacturer software Nova (Deutsche METROHM GmbH & Co. KG, Germany). CV experiments consisted of 5 cycles, but only the fifth was processed. EIS experiments were obtained around OCP with an amplitude of 10 mV using 50 logarithmically distributed frequencies in the range 500 kHz–0.1 Hz.

HOPG basal plane is a surface with large flat terraces, though the above described preparation method cannot avoid inducing edge defect sites facilitating Li^+ intercalation. To make sure that possibly intercalated residuals from previous experiments were stripped off by the adhesive tape, we checked the open circuit potential (OCP) after cell assembly. The cell was discarded if OCP was below 3 V vs. Li/Li^+ . All electrochemical potentials in this paper describe the potential of the working electrode in the three-electrode setup and refer to the Li metal reference electrode, thus are given vs. Li/Li^+ . Due to the high electronic conductivity of HOPG through-plane potential gradients lie in the sub- μV region and are therefore neglected.

X-Ray Photoelectron Spectroscopy

The sample holder covered by double-sided XPS compatible adhesive tape was dried similar to the HOPG. After electrochemical

treatment the cells were disassembled in the glove box for further spectroscopic analysis of the electrodes. Samples were rinsed with 1 ml dimethyl carbonate (DMC, Sigma Aldrich, Germany) using a pipette and then fixed on the sample holder. To transfer the sample from the glove box to the spectrometer it was introduced into a transfer vessel (Model 04-110A, Physical Electronics GmbH, Germany) and sealed, which itself was further vacuum sealed into an aluminum based pouch bag. The sample could be verifiably transferred into the analysis chamber without any atmosphere contact. Spectra were recorded with a PHI 5000 spectrometer (Physical Electronics GmbH, Germany) using Al K α radiation ($h\nu = 1486.6$ eV) under ultrahigh vacuum conditions. Sputtering was performed using an Ar $^+$ gun with 0.5 kV and a 4×4 mm 2 spot size, using a current that correlates to 0.25 nm min $^{-1}$ as calibrated on Si/SiO $_2$. Spectra were shifted based on the C 1s graphite binding energy at 284.8 eV on pristine HOPG. Atomic concentrations were determined via the analysis software Phi MultiPak.

2. Results and Discussion

2.1. Potentiostatic SEI Formation

To allow direct comparison with the results previously reported for GC electrodes,^[23] we formed SEIs at 600, 450, 300 and 100 mV. Lower formation potentials were not considered, as no distinct reactions take place at potentials < 100 mV, whilst potentials > 600 mV do not form a passivating SEI on HOPG.^[28,29,35] In order to achieve a comparable set of SEIs we defined three equipollent cutoff parameters terminating the potentiostatic polarization step, namely the current density, charge density and formation time at $4 \mu\text{A cm}^{-2}$, 10mC cm^{-2} and 600 s, respectively.

An exemplary reduction current density transient j after applying 100 mV is presented in Figure 1a. The profiles looked very similar for the other formation potentials. For better visibility, Figure 1b and c display two characteristic current density regimes. After the potential is applied we obtained a high reductive current, which drops to less than 5% within the first 500 ms. The drop includes a shoulder at 50 ms (indicated by the arrow), though passivates after around 100 s. No systematic relation could be found between the final passivation current j_{pass} indicated in Figure 1c and the applied potential, though the value was always below $10 \mu\text{A cm}^{-2}$. Figure 1b includes an exponential fit (dashed line) with time constant 133 ms (corresponds to 7.5s^{-1}).

In contrast to composite carbon electrodes, which suffer from electrolyte decomposition even in later cycles due to particle breathing,^[22] the non-intercalating HOPG electrode should be irreversibly passivated during this first polarization. Apart from electrochemical electrolyte reduction, the current response to the potentiostatic step may result from three further contributions: (i) charging of the double layer capacitance, (ii) Li $^+$ intercalation into the HOPG at step edges and (iii) other irreversible side reactions (e.g. production of dissolved species). Although the setup is optimized in order to avoid those current overlaps, we experimentally tested for their possible presence and significance. As shown in more details in the Supplementary Information (SI), their contributions are

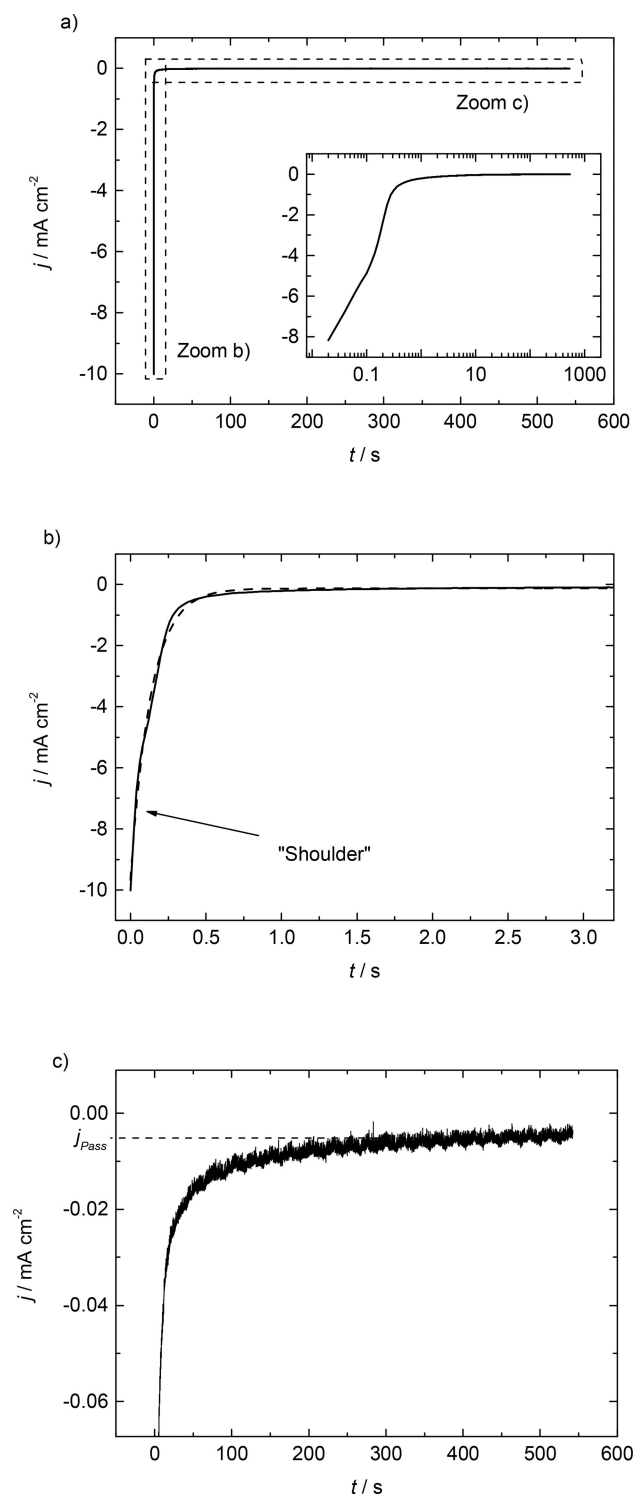


Figure 1. Current density j during a potentiostatic formation procedure on HOPG at 100 mV in neat electrolyte, inset with logarithmic abscissa. b) and c) are detailed zooms of a). The dashed line in b) indicates the exponential fit with an exponential coefficient 7.5s^{-1} .

negligible. For instance, the characteristic time constants of double layer charging currents calculated in the SI would be in the order of magnitude of 10^{-6} s, which is significantly smaller than the 133 ms resulting from the fit in Figure 1b. Hence, the 100s-scale relaxation in Figure 1c must reflect the increase of a

(quasi-)resistance, namely the expected and desired self-passivating nature of the electrochemical SEI formation.

2.2. XPS

Ex-situ X-ray photoelectron spectroscopy (XPS) was used to analyze the chemical compositions of SEIs formed at 600, 450, 300 and 100 mV. Figure 2 shows spectra of the C1s, O1s and F1s regions. Li1s spectra of all SEIs and F1s spectrum of 600 mV SEI were recorded but did not show any features beyond noise and are therefore not shown. All plotted spectra belong to samples "as transferred", without any layers removed by Ar⁺ sputtering. Even three minutes of sputtering made the O1s signal disappear completely, which is not surprising given that SEIs on basal planes are known to be significantly thinner than on edge planes.^[21,27] The peak positions in Figure 2 are in good agreement with features in previous XPS analyses of SEI layers.^[43–57]

Looking at the C1s region, both lower potential (300 and 100 mV) SEIs show a stronger response in the C=O region as compared to the high-potential SEIs (600 and 450 mV). Li₂CO₃ related features are only distinctive for the 100 mV SEI. The 600 mV SEI appears to have a higher amount of C–O bonds. Alkyl carbonates, which are typical solvent decomposition products,^[22,58–61] are not significant in the C1s region. The O1s region shows a strong response at binding energies > 534 eV at all SEIs, thus indicating the presence of alkylic species. O1s regions show no presence of Li₂O, though indicate the presence of Li₂CO₃ in both lower potential SEIs. The higher potential SEIs show no signs of Li₂CO₃. The F1s region indicates the presence of LiF and residual LiPF₆ in all SEIs, while the 450 mV SEI exhibits higher fluorophosphate content. Figure 2 also shows the elemental percentages of oxygen and fluorine normalized with the carbon concentration for the different

formation potentials. The oxygen content suggests two distinct regimes: "low-potential" (<400 mV) and "high-potential" (> 400 mV) SEIs, where the high-potential SEIs contain about twice as much oxygen as the low-potential ones, whereas only the latter exhibit carbonate features. Though, no trend is present in the fluorine content with formation potential. Nevertheless, the absolute values < 10% indicate all fluorine containing species to be present only in small amounts. Apart from residual LiPF₆, we tentatively attribute these fluorine concentrations to thin, non-passivating LiF films formed via HF reduction. We recently demonstrated, that such films form at potentials > 1 V_i^[40] and that their formation requires electrocatalytically active sites, of which HOPG has few. Hence our formation potential should have little influence on them, so that no trend was to be expected in the first place.

In summary, the XPS measurements confirm an influence of the formation potential on the SEI chemistry. Most obvious is the apparent segregation into a high (600 and 450 mV) and a low (300 and 100 mV) potential regime resulting in absence/presence of Li₂CO₃ and high/low oxygen concentrations, respectively. Hence, on HOPG, the frequently assumed direct decomposition of EC to Li₂CO₃ and ethylene – if at all – only takes place at <400 mV (in agreement with Aurbach et al.^[62]).

2.3. Electrochemical Investigations

2.3.1. Cyclic Voltammetry

We used cyclic voltammetry to investigate the electron and species transport properties of the different SEIs. Fc/Fc⁺ served as a stable probe species in the absence of intercalating Li on HOPG.^[63] The use of Li⁰ reference and counter electrode is appropriate, since Fc/Fc⁺ shows good chemical stability at low potentials.^[64,65] We injected Fc/Fc⁺ enriched electrolyte after SEI

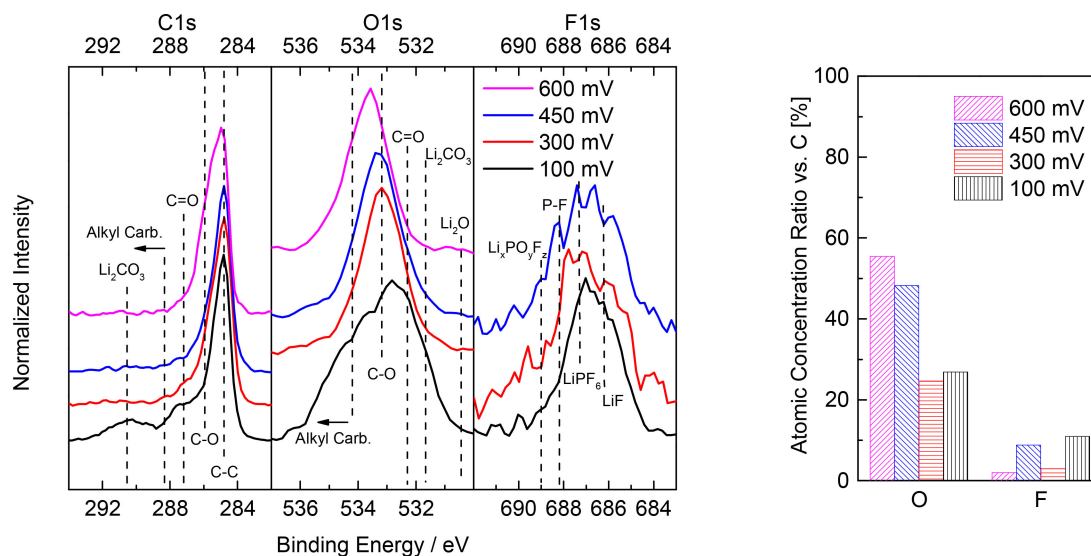


Figure 2. XPS C1s, O1s and F1s spectra (left) and elemental concentrations (right) for SEIs formed at indicated potentials. Dashed lines mark standard SEI species bindings at respective binding energies. The 600 mV SEI did not show any significant counts in the F1s region. The concentrations are given as a ratio vs. carbon.

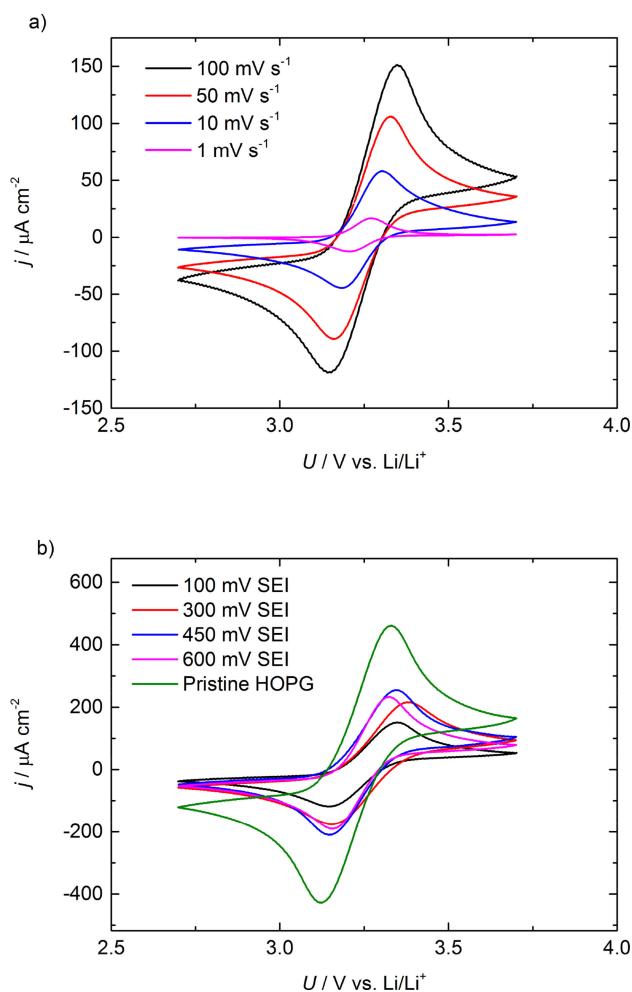


Figure 3. CVs of HOPG covered by SEIs Fc/Fc^+ environment. For every scan rate 5 cycles were obtained, only the fifth is shown. a) CVs with different scan rates of an SEI formed at 100 mV. b) CVs at 100 mV s^{-1} on pristine HOPG and different SEIs.

formation. To ensure sufficient equilibration we obtained 5 cycles per scan rate and only used the respective 5th cycle for further analysis and comparison. Figure 3a exemplarily shows the data of a 100 mV SEI (trends of CVs on different SEI are similar). Figure 3b presents the CVs on different SEIs as well as pristine HOPG obtained at 100 mV s^{-1} . The shapes generally indicate a fully reversible reaction. The peak current densities are up to two orders of magnitude higher than the current densities in neat electrolyte (see SI) and 1.5 orders of magnitude higher than the passivation currents at the end of the formation procedure (Figure 1c), confirming that any background currents can be neglected in the presence of the Fc/Fc^+ couple. The current densities are consistent with previous findings for other solvent/electrode systems.^[63,66–68]

With decreasing scan rate, the peaks get smaller (Figure 3a), as expected. However, the peak positions are not constant for the different scan rates. This indicates that the underlying processes are more complex than a Nernstian uninhibited behavior.

Comparing the CVs obtained after different formation potentials (Figure 3b), the CVs qualitatively retain the same characteristic shape, but become smaller in amplitude in the presence of an SEI. The suppression is strongest for the 100 mV SEI, whereas SEIs formed at any of the three other formation potentials yield rather similar CV amplitudes. Another obvious feature is the shift of the peak potentials, which does not seem to follow any specific trend. These latter shifts highlight that the SEI does more than just block parts of the electrochemically active surface area (ECSA) and obstruct the diffusion transport of Fc/Fc^+ . This is discussed in more detail in the SI, where we demonstrate that CV simulations only resemble the experimental trends if we not only allow for a variation of the ECSA and the effective diffusion coefficients, but also of the kinetic rate constant for the redox reaction.

In the following, we will derive the (apparent) diffusion coefficients and heterogeneous rate constants from the trends in CV peak amplitudes and positions, respectively.

Diffusion coefficients from peak amplitudes. For a given SEI, information about how diffusion transport of Fc/Fc^+ is hindered by the SEI can be determined from the scan-rate dependent peak amplitude.^[69] The anodic peak current densities j_{Peak} of different SEIs as well as pristine HOPG plotted against the square root of the scan rate ν are shown in Figure 4a. One can observe a linear dependency of the peak current densities with $\nu^{1/2}$, confirming the quasi-reversibility of the Fc/Fc^+ reaction even in the presence of an SEI.^[69–71] For quasi-reversible reactions, the oxidative peak current density j_{Peak} depends on the scan rate and is described at 20°C by the adjusted Randles-Sevcik equation [Eq. (1)].^[69]

$$j_{\text{Peak}} = 3.04 \cdot 10^5 n^{3/2} \alpha^{1/2} c_{\text{Red}}^0 (\xi D_{\text{red}} \nu)^{1/2} \text{ in } \text{A cm}^{-2} \quad (1)$$

D_{red} = effective diffusion coefficient (reduced species) = to be determined, n = transfer number = 1, α = charge transfer coefficient = 0.3,^[72] c_{Red}^0 = concentration (reduced species) = 2.5 mMol, respectively. The correction factor ξ is equal 1 for solutions where the oxidized species concentration c_{ox}^0 respects the boundary conditions $c_{\text{ox}}^0(t=0) = c_{\text{ox}}^0(x \rightarrow \infty) = 0$. Since in our experiments we started with a non-zero concentration of the oxidized species, ξ must be derived from another method. By comparison with EIS measurements (see SI), we find $\xi = 3.97$. Data is fitted using linear fits with y-intercepts equal zero. The slope is significantly higher on pristine HOPG and decreases with lowered formation potential, indicating a reduced effective diffusion coefficient. The slopes of the 100 mV SEI is distinctly smaller, whilst the other three SEIs seem to have similar diffusion properties. The analysis of the reductive peak currents leads to similar slopes, therefore they are not discussed separately (see also Dinh-Nguyen et al.^[39]). Though, they allow the conclusion that the oxidized and reduced species effective diffusion coefficients D_{ox} and D_{red} are similar too. The corresponding fit slopes as well as the resulting effective diffusion coefficients $D_{\text{eff}} = D_{\text{red}} \approx D_{\text{ox}}$, calculated using [Eq. (1)], are presented in Table 1.

The strong drop of diffusion coefficient between 300 and 100 mV resembles well the glassy carbon rotating disk

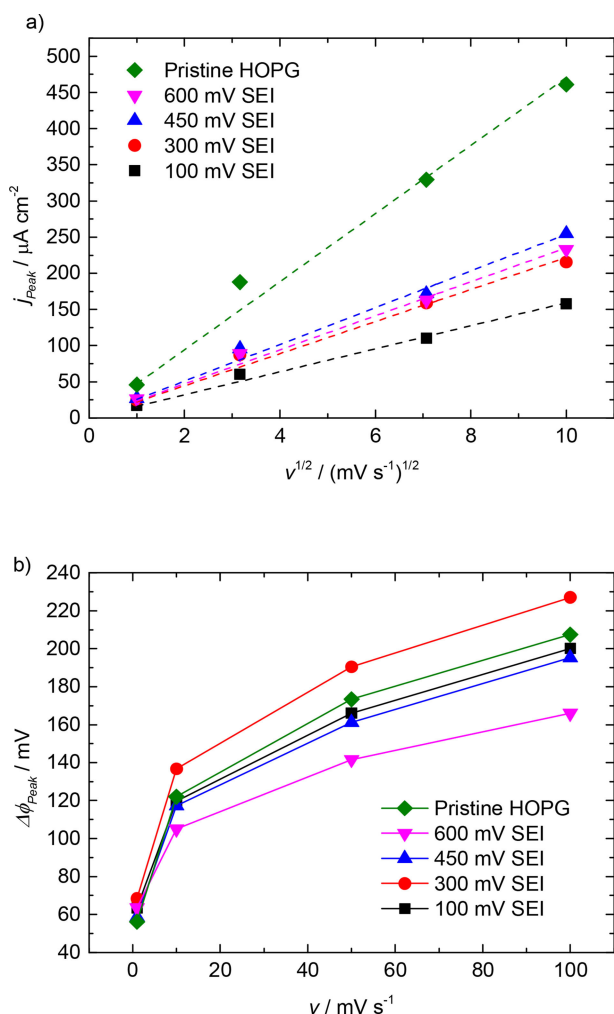


Figure 4. a) CV anodic peak current densities j_{Peak} obtained on pristine HOPG and different SEIs in Fc/Fc^+ environment plotted vs. $v^{1/2}$ and respective linear fits (dashed lines) for diffusion coefficient calculations. b) Peak potential differences $\Delta\psi_{Peak}$ of CVs obtained on pristine HOPG and different SEIs in Fc/Fc^+ environment.

electrode (GC-RDE) limiting current results by Tang et al.^[23] Interestingly, that paper has another set of data which – when analyzed appropriately – is also in good agreement with our diffusion coefficients. Figure 5a reproduces a figure of ref.^[23], which shows the OCP transient of SEI covered GC-RDE during Fc/Fc^+ injection. SEIs were formed at indicated potentials in a similar way to our study. We reprocessed that data by shifting the moment of injection (arrows in Figure 5a) to $t = 0.1$ s and present the reprocessed data in Figure 5b. Since the OCP is

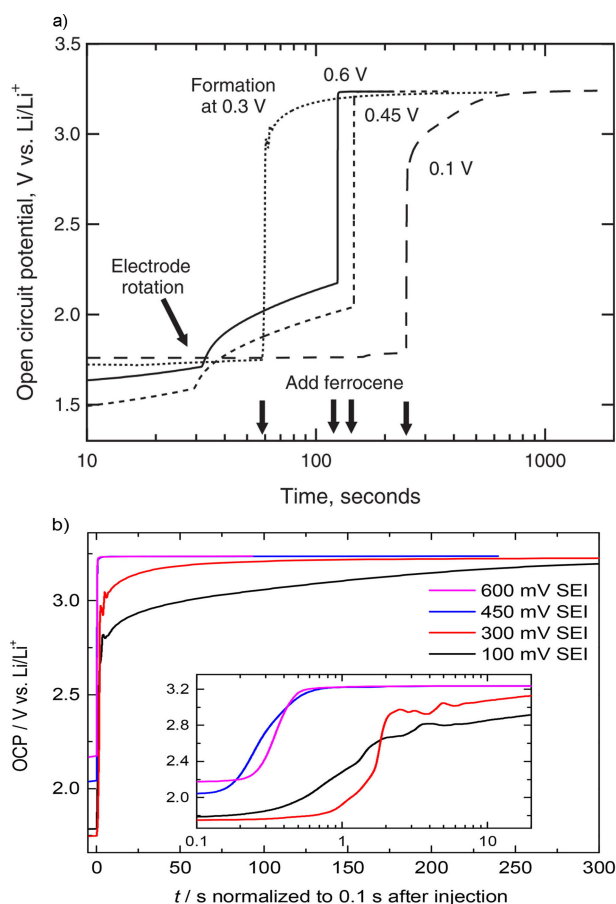


Figure 5. a) OCP transients after injection of Fc/Fc^+ in different SEIs on Glassy Carbon in a RDE system (reproduced from ref.^[23]; Journal of the Electrochemical Society by Electrochemical Society. Reproduced with permission of Electrochemical Society in the format. Republish in a journal/magazine via Copyright Clearance Center). b) Same data reprocessed by shifting the moment of injection to $t = 0.1$ s. Inset presents data with logarithmic time axis for better visibility of the initial phases.

directly correlated to the Fc/Fc^+ concentration at the electrode, the OCP slope and thus the time to reach a selected potential are qualitative measures for the Fc/Fc^+ diffusion speed. The durations for the OCP to reach 3.1 V are 0.46, 0.49, 14 and 142 s for the 600, 450, 300 and 100 mV SEI, respectively. That trend is fully compatible with the diffusion coefficients in Table 1.

Heterogeneous rate constants from peak potentials. The peak potential differences in Figure 4b generally decrease with lowered scan rate and approach the theoretical value of 57 mV for a fully reversible system.^[71] Though, without an appropriate discussion of the electrochemical background, the dependency

	Slope j_{Peak} vs. $v^{1/2}$ $10^{-4} A cm^{-2} (Vs^{-1})^{-1/2}$	D_{eff} $10^{-6} cm^2 s^{-1}$	A_{50}	$k_{0,50}$ $10^{-4} cm s^{-1}$	A_{10}	$k_{0,10}$ $10^{-4} cm s^{-1}$
Pristine HOPG	15	3.2	0.32	8.1	0.61	6.9
600 mV SEI	7.4	0.80	0.44	5.6	0.89	5.0
450 mV SEI	8.0	0.93	0.36	4.9	0.68	4.1
300 mV SEI	7.0	0.72	0.26	3.1	0.48	2.6
100 mV SEI	5.0	0.37	0.35	3.0	0.64	2.4

trend of the peak potential difference on the SEI formation potential appears to be rather random. As it was described by Matsuda and Ayabe, the heterogeneous rate constant k_0 of a quasi-reversible reaction can be determined from the peak potential difference as well as the effective diffusion coefficient [Eq. (2)].^[69]

$$k_{0,\nu} = A_\nu(\Delta\varphi_{Peak}) \cdot \left(D_{eff} \frac{nF}{RT} \nu \right)^{1/2} \quad (2)$$

where F is the Faraday constant and R the universal gas constant. $A_\nu(\Delta\varphi_{Peak})$ is a numerical function of which a set of values is tabulated in the literature.^[71] In theory, k_0 is independent of ν , though values based on experimental data can vary with scan rate, therefore the index ν is used to indicate the respective scan rate. The $k_{0,\nu}$ values listed in Table 1 are calculated with [Eq. (2)] by using A_ν values interpolated from the tabulated data in order to derive rate constants for 50 and 10 mVs^{-1} . The peak potential differences of 100 and 1 mVs^{-1} are outside the tabulated A_ν interval and can therefore not be considered. Although diffusion coefficients determined in ref.^[72] on glassy carbon vary significantly, rate constants of pristine HOPG are consistent with values derived in the corresponding glassy carbon experiments. The calculated rate constants in Table 1 slightly depend on the respective ν . Consistent with our XPS results, a much more pronounced difference can be

observed between the high (600 and 450 mV) and the low (300 and 100 mV) formation potentials regimes. Although the peak potential differences did not reveal any trend with formation potential at first, a clear trend emerges for the heterogeneous rate constants of the Fc/Fc^+ outer sphere reaction whose calculations using [Eq. (2)] include the effective diffusion coefficients. Hence the formation potential not only changes the SEI's transport properties for the probe species to reach the electrochemically active interface, but also the kinetics of the electrochemical reaction itself.

2.3.2. Electrochemical Impedance Spectroscopy

In order to widen the understanding of the individual electrochemical features and their activation energies and to obtain ionic movement coefficients, low and high-potential SEIs were investigated using EIS. As representatives, we considered 450 and 300 mV as lowest/highest potential of the high/low formation potential regime, respectively. The characteristics of SEIs formed at those two potentials differ significantly, yet the two potentials are very close to each other. This underlines the "step" characteristics of the changes between the two regimes. Figure 6 shows the Nyquist plots and the Distribution of Relaxation Times (DRT) $g(f)$, the latter calculated following the scheme from refs.^[73] and^[74] $g(f)$ is presented only in the regions

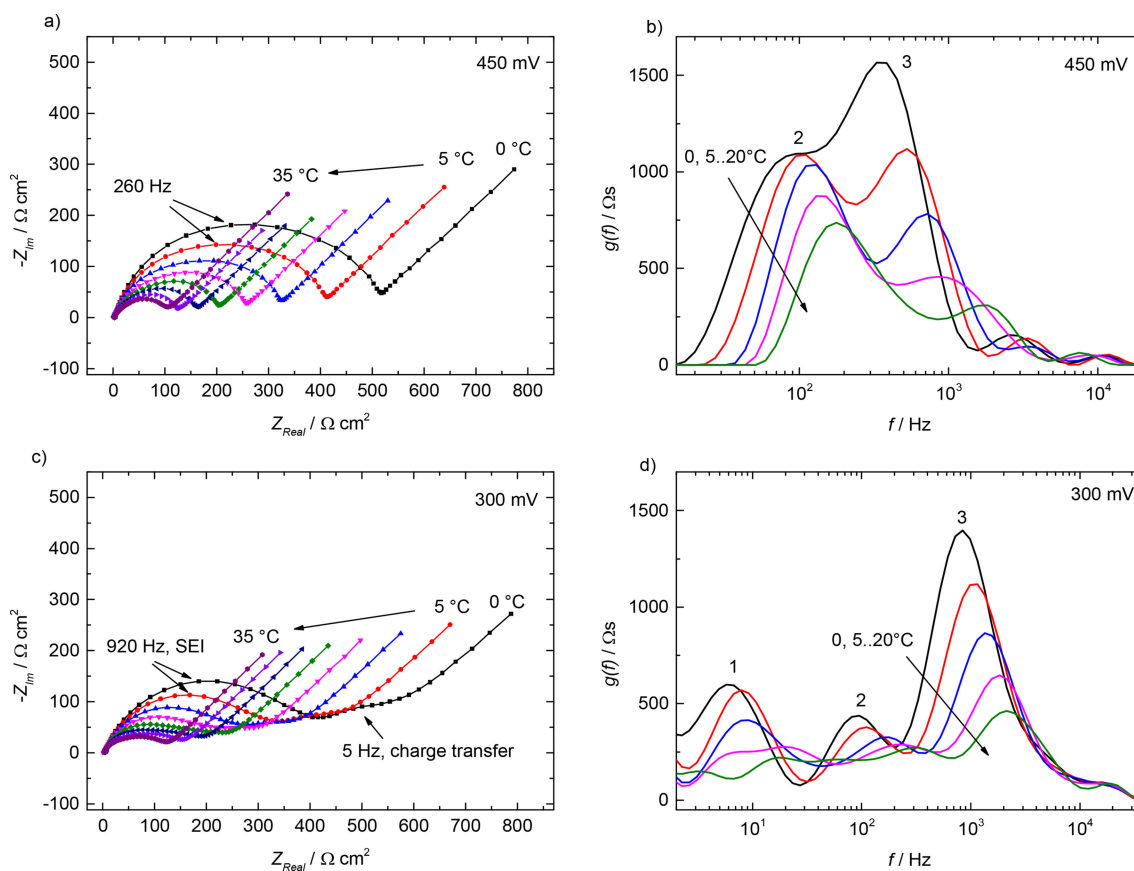


Figure 6. a) and b) Temperature dependent impedance spectra of a high-potential SEI (450 mV) in Fc/Fc^+ environment presented as Nyquist and DRT plots. c) and d) Respective impedance spectra of a low-potential SEI (300 mV) presented as Nyquist and DRT plots.

where both real and imaginary residuals are reasonably small. The DRT plots of all temperatures, DRT residuals and Bode phase plots can be found in the SI. The spectra were recorded around OCP at 5 K steps starting from 0 °C up to 35 °C as indicated by the arrows, though for better illustration DRT slopes above 20 °C are not shown. The OCP remained constant in the entire temperature interval at ~3.23 V. The high frequency intercepts decrease with rising temperature from 5 Ω cm² down to 2.5 Ω cm², which can be assigned to the variation of the electrolyte bulk conductivity.^[75]

The high-potential SEI in Figure 6a and b exhibits the following features: The Nyquist plots consist of a single distorted semicircle in the whole temperature interval. DRT plots in the shown frequency region show two broad overlapping peaks assigned as numbers 2 and 3. The frequency at the Nyquist semicircle maximum is at 260 Hz (indicated by the arrow), which lies in between the two DRT peak maxima. As discussed in detail the SI, DRT peak 3 shifts faster with rising temperature. The distortion of the Nyquist plot and the width of the DRT peaks both indicate the existence of two scattered features with different activation energies. This implies that SEIs cannot be sufficiently modeled with simple RC-containing equivalent circuits. Respective attempts usually lead to good simulation fits, though lack of physical meaning (e.g. Levi et al. used several RC-elements^[76]).

For the low-potential SEI, temperature dependent Nyquist and DRT plots (Figure 6c and d) show more features than for the high-potential SEI. Nyquist plots consist of a large distorted semicircle at high frequencies, followed by a small distorted semicircle in the low frequency region. The smaller semicircle disappears with rising temperature. It is common to assign low frequency semicircles to the Li/Li⁺ charge transfer process, whilst high frequency semicircles are related to the ion migration through the SEI.^[18,58,77,78] Although the charge transfer in the system was Fc/Fc⁺ instead of Li/Li⁺, the two distorted semicircles will be referred to as SEI and charge transfer semicircle, respectively. The low frequency charge transfer semicircle shows a corresponding peak in the DRT plot at ~5 Hz assigned as peak 1. The Nyquist maximum at around 920 Hz corresponds nicely with DRT peak 3. DRT peak 2 frequencies resemble almost the values from the DRT analysis of the high-potential SEI in Figure 6b. Both charge transfer and SEI impedances in the Nyquist plot decrease with increasing temperature, as obvious from the shrinking semicircles, particularly the disappearing charge transfer semicircle in Figure 6c as well as the DRT peak shift towards higher regions in Figure 6d. We attribute this movement characteristics to mechanism-specific activation energies, which we discuss in more detail in the SI.

For both SEIs, the DRT peaks are rather broad. On porous electrodes, such peak broadening is caused by through-plane distributions,^[73] whereas on a flat electrode like HOPG we tentatively assign it laterally inhomogeneous surface layer properties.

Both kinds of SEIs share the high frequency SEI Nyquist semicircle as a common feature with a similar total ohmic resistance. In the DRT picture, this is reflected in similar peaks 2

and 3, while the low-potential SEI includes another charge transfer feature (DRT peak 1). In both Nyquist and DRT plots the charge-transfer related features can only be separated from migration (high frequency) and diffusion (low frequency) when the charge transfer itself becomes slower, i.e., kinetically more hindered. That is only the case for the low-potential SEI (Figure 6c and d) and only at lower temperatures. The fact that it becomes distinguishable at all, however, is an important indicator that the formation potential does not only influence the porosity and tortuosity (influence on ion migration and diffusion) but also hinders the reaction kinetics (consistent with CV rate constants in Table 1). Therefore, the slightly broader high frequency response of the 450 mV SEI in both Nyquist and DRT plots (Figure 6a and b) is not to be confused with the actual Fc/Fc⁺ migration impedance as it probably includes the respective charge transfer contribution (DRT peak 1).

EIS allowed the distinct separation of two mechanisms, the ionic movement and the charge transfer. In the SI we analyze the temperature dependency of the two kinds of SEIs and calculate activation energies of charge transfer and ionic movement. The activation energies for diffusion and migration of Fc/Fc⁺ are significantly smaller than the value for charge transfer, indicating that electrons have to overcome significant energy barriers, with notable effects in particular at low temperatures. Furthermore, EIS showed that ionic movement is similar in the different SEIs, while the charge transfer is significantly more hindered in the presence of low-potential SEIs as compared to high-potential SEIs. Although EIS addresses completely different physical parameters, results qualitatively replicate the findings from CV experiments.

2.4. Discussion

We discuss our findings in the framework of the simplified two-layer model of the SEI, best represented by this sequence electrode|SEI (compact layer)|SEI (porous layer)|electrolyte. This neglects lateral inhomogeneities and reduces the SEI to a thin compact layer at the electrode surface and a significantly thicker porous layer on the electrolyte side (see Figure 7). The compact layer is quasi solid and Li⁺ conductive, while the porous layer is soaked with electrolyte. The desolvation of Li⁺

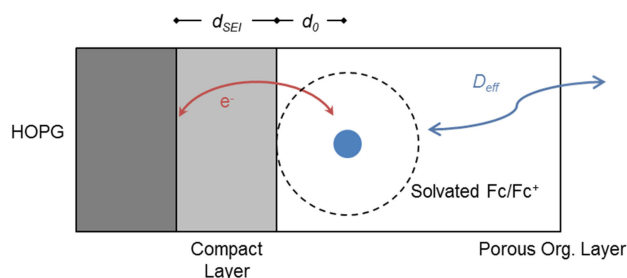


Figure 7. Proposed reaction mechanism of Fc/Fc⁺ at HOPG covered by an SEI. The electrons must tunnel through the insulating and impermeable compact layer leading to an additional exponential term in the rate constant of the outer sphere reaction. The diffusion/migration limitation is determined by the outer porous layer mainly consisting of organic compounds.

takes place at the interface between compact and porous layer.^[36,37,55–57,79–83] Inorganic species like Li_2CO_3 are believed to arise close to the electrode surface, while porous organic species are usually accumulated at the electrolyte side.^[22,55,56,84,85] We suggest that SEI formation on HOPG splits into the following steps, which will be justified in this chapter.

- > 700 mV Only negligible electrolyte reduction without an insulating surface coverage. The formed species are soluble and stripped off when re-increasing the potential.
- First Step: ~700 mV Formation of a porous long-chained organic interphase affecting ionic movement properties. **Thin electronically insulating organic compact layer** on the surface passivates further electrolyte reduction.
- Second Step: ~400 mV **Reduction of pre-formed organic compact SEI forms thicker inorganic compact SEI** at electrode surface. Shortening of organic chains leads to further reduces effective diffusion coefficient in porous layer.

Starting with the compact layer: it is the substantial passivation factor, since it is supposed to be impermeable and electronically insulating. While all investigated SEIs in this work are passivating towards further electrolyte reduction, XPS results point out differences by means of elemental concentrations, in particular Li_2CO_3 existence. Therefore, although passivating, the high-potential compact layer must consist of organic species. On the other hand, XPS showed significant amounts of inorganic species in low-potential SEIs, which consequently must be formed via reduction of the pre-formed organic compact layer. This is in agreement with the findings of both Matsouka et al. and Tang et al., who found CV reduction peaks at high potentials only in the first cycle, while the subsequent cycles included only the second (low-potential) reduction peak.^[29,35]

Effective tunneling thickness of the compact layer. Obviously, the presence and kind of a passivated SEI affects the kinetics though does not fully inhibit the Fc/Fc^+ reaction. The trend in reaction rate constant $k_{0,v}$ shown in Table 1 invites for a quantitative discussion of the Fc/Fc^+ reaction kinetics. The kinetics are strongly correlated to the formation potential, which allows us excluding two hypotheses: Neither is the SEI re-oxidized or becomes conductive at ~3.2 V (where the Fc/Fc^+ experiments were performed), nor is Fc/Fc^+ able to migrate or diffuse to the electrode surface. Otherwise we would have expected formation potential independent kinetics. Thus, independent of their chemical properties, the compact layer microphases proposed by Peled et al.^[85] must be attached tightly so that the compact layer cannot be penetrated by the Fc/Fc^+ species. We support the hypothesis that electrons tunnel through the passivated SEI to react with Fc/Fc^+ .^[30,86] Since the porous layer is soaked with electrolyte, the tunneling

takes place through the compact layer. The proposed total reaction mechanism is schematically shown in Figure 7.

Fc/Fc^+ is known to have an outer-sphere reaction, at which the electrons have to tunnel through a shell surrounding the electrochemical active center.^[87,88] If the shell radius being the minimum tunneling distance is described as d_0 , in accordance with the Marcus theory the reaction rate constant k_0 on pristine HOPG is directly proportional to $\exp(-\gamma d_0)$. $\gamma > 0$ describes the tunneling probability and depends among others on the tunneling energy barrier.

Assuming that the compact SEI layer does nothing more than adding a further tunneling barrier with a thickness d_{SEI} and a tunneling probability $\beta > 0$, we get Equation (3) for the rate constant proportionality on SEI covered HOPG:

$$k_0 \propto \exp(-\gamma d_0 - \beta d_{\text{SEI}}) \quad (3)$$

The rate constant calculated for pristine HOPG, k_0^{pristine} , corresponds to the special case where $d_{\text{SEI}} = 0$. It actually provides the proportionality constant between the rate constant of an SEI covered sample and the compact layer thickness [Eq. (4) and (5)]:

$$k_0 = k_0^{\text{pristine}} \exp(-\beta d_{\text{SEI}}) \quad (4)$$

$$\Rightarrow d_{\text{SEI}} = -\frac{1}{\beta} \ln\left(\frac{k_0}{k_0^{\text{pristine}}}\right) \text{ with } k_0 \leq k_0^{\text{pristine}} \quad (5)$$

The factor β could not be determined in this study. Table 2 shows the resulting $\beta d_{\text{SEI},v}$ calculated from $k_{0,v}$ values from Table 1. β should mainly depend on the energy levels of the

Table 2. SEI thicknesses calculated using [Eq. (5)] resulting from CVs at 50 and 10 mVs^{-1} . The factor β could not be determined experimentally, though can be assumed to be invariant.

	600 mV	450 mV	300 mV	100 mV
$\beta \cdot d_{\text{SEI},50}$	0.38	0.50	0.96	1.0
$\beta \cdot d_{\text{SEI},10}$	0.32	0.51	0.99	1.0

tunneling barrier neighborhood, therefore we assume β invariant. Thus, the presented “thicknesses” can be directly compared. Although the SEI thicknesses of the 600 and 450 mV SEIs differ slightly, the switchover to the low-potentials doubles the calculated compact layer thickness. The 450 mV, although being an edge potential before the second formation step, might thermodynamically already enable second step reactions in small rates.^[35] This would be consistent with a slightly thicker compact layer of the 450 mV SEI as compared to the 600 mV SEI. We would also like to mention that a possibly incorrectly defined Randles-Sevcik correction factor ξ in [Eq. (1)] would have no effect on these thickness values as ξ becomes obsolete in [Eq. (5)].

Evolution of Transport Properties. Particular attention also needs to be paid on the Fc/Fc^+ transport properties, which are defined by the outer porous layer that mainly consist of organic compounds. The diffusion coefficient (Table 1) is reduced significantly during the first formation step (at ~700 mV). The

further reduction between the 300 and 100 mV SEI could be caused by a reaction at ~ 400 mV, which though is sluggish and demands a high overpotential to be activated (not sufficiently given at 300 mV). One may speculate, that the reaction step could consist of a shortening of the long chained organic molecules in the porous layer. The resulting changes affect the SEI adsorption properties, which lead to the change in diffusion activation energies (presented in SI),^[89] The intrinsic diffusion coefficient is assumed to not be affected by the presence of surface layers. In agreement with Tang et al., we suggest, that the shorter polymer chains form a tighter and less porous layer with higher tortuosity and a reduced effective diffusion coefficient.^[37] This hypothesis was also studied in more detail and will be in the focus of a future publication.^[90]

Transferability to commercial electrode material. It is important to mention that both the obtained trends in kinetics and transport properties of Fc/Fc⁺ are not necessarily transferable to Li⁺.^[91] E.g. the trend in effective diffusion coefficient is not expected to be relevant, since the actual transport limitations are given by the Li⁺ migration through compact inorganic layer (which we consider impermeable for Fc/Fc⁺). On the other hand, Li⁺ intercalation rate constant is not determined by surface layers, but by other properties like the Li⁺ desolvation and the ratio of graphite surface orientation.^[31,78] Though, the ability of Fc/Fc⁺ to react via a tunneling is believed to be also possible for other transition metal cations like Mn²⁺ (particularly under those high driving forces: overpotentials > 1 V), which is important for longer-term cell degradation by side reactions like ongoing SEI growth.

In our study we could show that, on HOPG, the low-potential compact SEI is a product of high-potential SEI decomposition. Thus, having in mind commercial composite electrodes, the “optimal” reaction conditions of the two reaction steps might differ significantly. We believe that particularly the second step, which is located in the potential operation region of anodes, is crucial for the stability as well as physicochemical properties of the final SEI. On the other hand, since the second step reactions depend on the quantity and quality of the high-potential SEI, formation protocols should be optimized also in terms of improving the high-potential SEI properties. A first study validating this assumption was recently published by our group.^[92]

3. Conclusions

HOPG was used to study SEI formation at potentiostatic conditions, which are achievable without strong cell polarization due to the low surface area of this sample. Furthermore, the basal plane of HOPG is chemically inert, and Li⁺ intercalation is negligible. We studied SEIs formed at four different potentials (600, 450, 300, 100 mV), analyzing their chemical composition by ex-situ XPS and their electrochemical (transport) properties through the interaction with Fc/Fc⁺ as a probe species.

SEI formation is found self-terminating, hence self-passivating at all potentials investigated, which implies the formation

of an electronically insulating layer, which is also impermeable for SEI-forming electrolyte components (thus: compact layer). XPS revealed Li₂CO₃ formation only for the two lower formation potentials (300 and 100 mV), i.e. the high-potential compact SEI is essentially organic. This also shows that, contrary to prevalent opinion, carbonate formation is not necessary for electrode passivation. The SEI formation process in commercial cells makes use of galvanostatic conditions, which leads to a slow potential sweep from higher to lower potentials. Given that our results indicate a suppression of direct electrochemical electrolyte decomposition already by the high-potential SEI, we conclude that the typical carbonate layers found after such galvanostatic SEI formation, which is performed at least down to Li⁺ intercalation potentials (< 220 mV vs. Li/Li⁺), result from further electrochemical decomposition of the pre-formed high-potential organic compact SEI.

The presence of a compact SEI after formation is also confirmed by Fc/Fc⁺ cyclic voltammetry and corresponding EIS experiments. For all four potentials, those measurements revealed significant inhibition of charge transfer kinetics through the SEIs as compared to pristine HOPG. In agreement with the XPS observation of carbonate only for the low-potential (300 and 100 mV) SEIs, we also find that the latter exhibit much more sluggish electron transfer kinetics than the high-potential (600 and 450 mV) SEIs. Based on a simple electron tunneling model, these observations allowed us to calculate the factors by which the effective tunneling distances change, which we tentatively associate with the thicknesses of the compact SEIs.

As a side result, the CV and EIS data also reveal some information about the ionic movement (migration and diffusion) through the outer part of the SEI, the porous layer: effective permeability is found to decrease with decreasing formation potential, which we tentatively assign to a shortening of the organic polymer chains formed from ring-opening reactions of ethylene and vinylene carbonate.

In summary, the previously described two-step process of SEI formation would start at ~ 700 mV with the formation of an organic compact layer (covered by a porous one), which is then itself reduced to a much thicker compact, yet inorganic (carbonate containing) layer once potentials drop (either in a CV or due to galvanostatic control) to below ~ 400 mV. Knowing that, we conclude that by controlling the chemical and physical properties of the high-potential SEI, one can significantly influence the respective properties of the final low-potential SEI and thus influence the lifetime and conductivity properties of SEIs in commercial cells.

Acknowledgements

We gratefully acknowledge the fruitful discussions with Stefan Klink and Giorgia Zampardi (formerly RU Bochum) on the stability of ferrocene complexes, with Sebastian Keller (BMW Group) on the Laplace transformation and with Kevin Leung (Sandia National Lab) on the theoretical perspectives. This work was carried out

with funding from the Faraday Institution (faraday.ac.uk; EP/S003053/1), grant number FIRG003.

Conflict of Interest

The authors declare no conflict of interest.

Keywords: electrochemistry · highly oriented pyrolytic graphite · model electrode surface · materials science · outer sphere reaction

- [1] M. Winter, W. K. Appel, B. Evers, T. Hodal, K.-C. Möller, I. Schneider, M. Wachtler, M. R. Wagner, G. H. Wrodnigg, J. O. Besenhard, *Monatsh. Chem.* **2001**, *132*, 473–486
- [2] J. Vetter, P. Novak, Wagner, C. Veit, K.-C. Möller, J. O. Besenhard, M. Winter, M. Wohlfahrt-Mehrens, C. Vogler, A. Hammouche, *J. Power Sources* **2005**, *147*, 269–281
- [3] D. P. Abraham, J. L. Knuth, D. W. Dees, I. Bloom, J. P. Christophersen, *J. Power Sources* **2007**, *170*, 465–475
- [4] Y. Ein-Eli, B. Markovsky, D. Aurbach, Y. Carmeli, H. Yamin, S. Luski, *Electrochim. Acta* **1994**, *39*, 2559–2569
- [5] D. Andre, S.-J. Kim, P. Lamp, S. F. Lux, F. Maglia, O. Paschos, B. Stiaszny, *J. Mater. Chem. A* **2015**, *3*, 6709–6732
- [6] Y. Li, M. Bettge, B. Polzin, Y. Zhu, M. Balasubramanian, D. P. Abraham, *J. Electrochem. Soc.* **2013**, *160*, A3006–A3019
- [7] D. Aurbach, E. Zinigrad, Y. Cohen, H. Teller, *Solid State Ionics* **2002**, *148*, 405–416
- [8] P. Verma, P. Maire, P. Novak, *Electrochim. Acta* **2010**, *55*, 6332–6341
- [9] M. B. Pinson, M. Z. Bazant, *J. Electrochem. Soc.* **2013**, *160*, A243–A250
- [10] J.-Y. Eom, I.-H. Jung, J.-H. Lee, *J. Power Sources* **2011**, *196*, 9810–9814
- [11] H. Ota, Y. Sakata, A. Inoue, S. Yamaguchi, *J. Electrochem. Soc.* **2004**, *151*, A1659–A1669
- [12] B. Stiaszny, J. C. Ziegler, E. E. Krauß, J. P. Schmidt, E. Ivers-Tiffée, *J. Power Sources* **2014**, *251*, 439–450
- [13] M. Zhou, L. Zhao, S. Okada, J.-i. Yamaki, *J. Electrochem. Soc.* **2011**, *159*, A44–A48
- [14] D. Aurbach, A. Zaban, Y. Ein-Eli, I. Weissman, O. Chusid, B. Markovsky, M. Levi, E. Levi, A. Schechter, E. Granot, *J. Power Sources* **1997**, *68*, 91–98
- [15] E. Peled, D. Golodnitsky, C. Menachem, D. Bar-Tow, *J. Electrochem. Soc.* **1998**, *145*, 3482–3486
- [16] A. Schechter, D. Aurbach, H. Cohen, *Langmuir* **1999**, *15*, 3334–3342
- [17] S. S. Zhang, K. Xu, T. R. Jow, *Electrochim. Acta* **2004**, *49*, 1057–1061
- [18] D. Aurbach, K. Gamolsky, B. Markovsky, Y. Gofer, M. Schmidt, U. Heider, *Electrochim. Acta* **2002**, *47*, 1423–1439
- [19] W. Märkle, C.-Y. Lu, P. Novak, *J. Electrochem. Soc.* **2011**, *158*, A1478–A1482
- [20] E. Peled, D. Bar Tow, A. Merson, A. Gladkikh, L. Burstein, D. Golodnitsky, *J. Power Sources* **2001**, *97*, 52–57
- [21] E. Peled, D. Golodnitsky, A. Ulus, V. Yufit, *Electrochim. Acta* **2004**, *50*, 391–395
- [22] D. Aurbach, *J. Power Sources* **2000**, *89*, 206–218
- [23] M. Tang, S. Lu, J. Newman, *J. Electrochem. Soc.* **2012**, *159*, A1775–A1785
- [24] S. Zhang, M. S. Ding, K. Xu, J. Allen, T. R. Jow, *Electrochem. Solid-State Lett.* **2001**, *4*, A206–A208
- [25] M. P. Mercer, H. E. Hoster, *Nano Energy* **2016**, *29*, 394–413
- [26] N. M. Markovic, *Surf. Sci. Rep.* **2002**, *45*, 117–229
- [27] D. Bar-Tow, E. Peled, L. Burstein, *J. Electrochem. Soc.* **1999**, *146*, 824–832
- [28] J. Ma, L. Seidl, W. Ju, E. Mostafa, L. Asen, S. Martens, U. Stimming, O. Schneider, *ECS Trans.* **2014**, *64*, 407–423
- [29] M. Tang, K. Miyazaki, T. Abe, J. Newman, *J. Electrochem. Soc.* **2012**, *159*, A634–A641
- [30] M. Tang, J. Newman, *J. Electrochem. Soc.* **2012**, *159*, A1922–A1927
- [31] Y. Yamada, Y. Iriyama, T. Abe, Z. Ogumi, *Langmuir* **2009**, *25*, 12766–12770
- [32] Y. Domi, M. Ochida, S. Tsubouchi, H. Nakagawa, T. Yamanaka, T. Doi, T. Abe, Z. Ogumi, *J. Phys. Chem. C* **2011**, *115*, 25484–25489
- [33] G. Zampardi, F. La Mantia, W. Schuhmann, *RSC Adv.* **2015**, *5*, 31166–31171
- [34] P. Lu, C. Li, E. W. Schneider, S. J. Harris, *J. Phys. Chem. C* **2014**, *118*, 896–903
- [35] O. Matsuoka, A. Hiwara, T. Omi, M. Toriida, T. Hayashi, C. Tanaka, Y. Saito, T. Ishida, H. Tan, S. S. Ono, S. Yamamoto, *J. Power Sources* **2002**, *108*, 128–138
- [36] M. Tang, J. Newman, *J. Electrochem. Soc.* **2011**, *158*, A530–A536
- [37] M. Tang, J. Newman, *J. Electrochem. Soc.* **2012**, *159*, A281–A289
- [38] R. R. Jaini, B. P. Setzler, A. G. Star, T. F. Fuller, *J. Electrochem. Soc.* **2016**, *163*, A2185–A2196
- [39] M. T. Dinh-Nguyen, C. Delacourt, *J. Electrochem. Soc.* **2016**, *163*, A706–A713
- [40] D. Strmcnik, I. E. Castelli, J. G. Connell, D. Haering, M. Zorko, P. Martins, P. P. Lopes, B. Genorio, T. Østergaard, H. A. Gasteiger, F. Maglia, B. K. Antonopoulos, V. R. Stamenkovic, J. Rossmeisl, N. M. Markovic, *Nat. Catal.* **2018**, *1*, 255–262
- [41] H. E. Hoster, *Nat. Catal.* **2018**, *1*, 236–237
- [42] C. Ashworth, *Nat. Rev. Mater.* **2018**, *3*
- [43] D. Lu, M. Xu, L. Zhou, A. Garsuch, B. L. Lucht, *J. Electrochem. Soc.* **2013**, *160*, A3138–A3143
- [44] M. Xu, L. Zhou, Y. Dong, Y. Chen, A. Garsuch, B. L. Lucht, *J. Electrochem. Soc.* **2013**, *160*, A2005–A2013
- [45] Y.-C. Lu, A. N. Mansour, N. Yabuuchi, Y. Shao-Horn, *Chem. Mater.* **2009**, *21*, 4408–4424
- [46] Y. Park, S. H. Shin, H. Hwang, S. M. Lee, S. P. Kim, H. C. Choi, Y. M. Jung, *J. Mol. Struct.* **2014**, *1069*, 157–163
- [47] M.-J. Kim, J.-T. Yeon, K. Hong, S.-I. Lee, N.-S. Choi, S.-S. Kim, *Bull. Korean Chem. Soc.* **2013**, *34*, 2029–2035
- [48] H. Bryngelsson, M. Stjernedal, T. Gustafsson, K. Edström, *J. Power Sources* **2007**, *174*, 970–975
- [49] R. Dedryvere, H. Martinez, S. Leroy, D. Lemordant, F. Bonhomme, P. Biensan, D. Gonbeau, *J. Power Sources* **2007**, *174*, 462–468
- [50] V. Eshkenazi, E. Peled, L. Burstein, D. Golodnitsky, *Solid State Ionics* **2004**, *170*, 83–91
- [51] M. Xu, D. Lu, A. Garsuch, B. L. Lucht, *J. Electrochem. Soc.* **2012**, *159*, A2130–A2134
- [52] M. Nie, B. L. Lucht, *J. Electrochem. Soc.* **2014**, *161*, A1001–A1006
- [53] L. Yang, B. Ravdel, B. L. Lucht, *Electrochem. Solid-State Lett.* **2010**, *13*, A95–A97
- [54] M. Herstedt, D. P. Abraham, J. B. Kerr, K. Edström, *Electrochim. Acta* **2004**, *49*, 5097–5110
- [55] K. Edström, M. Herstedt, D. P. Abraham, *J. Power Sources* **2006**, *153*, 380–384
- [56] A. M. Andersson, A. Henningson, H. Siegbahn, U. Jansson, K. Edström, *J. Power Sources* **2003**, *119*, 522–527
- [57] A. v. Cresce, S. M. Russell, D. R. Baker, K. J. Gaskell, K. Xu, *Nano Lett.* **2014**, *14*, 1405–1412
- [58] H. Ota, K. Shima, M. Ue, J.-i. Yamaki, *Electrochim. Acta* **2004**, *49*, 565–572
- [59] K. Xu, *Chem. Rev.* **2004**, *104*, 4303–4418
- [60] D. Aurbach, B. Markovsky, I. Weissman, E. Levi, Y. Ein-Eli, *Electrochim. Acta* **1999**, *45*, 67–86
- [61] K. Tasaki, A. Goldberg, J.-J. Lian, M. Walker, A. Timmons, S. J. Harris, *J. Electrochem. Soc.* **2009**, *156*, A1019–A1027
- [62] D. Aurbach, M. D. Levi, E. Levi, A. Schechter, *J. Phys. Chem. B* **1997**, *101*, 2195–2206
- [63] N. G. Tsierkezos, *J. Solution Chem.* **2007**, *36*, 289–302
- [64] G. Zampardi, E. Ventosa, F. La Mantia, W. Schuhmann, *Chem. Commun.* **2013**, *49*, 9347–9349
- [65] K. M. Abraham, D. M. Pasquariello, E. B. Willstaedt, *J. Electrochem. Soc.* **1990**, *137*, 1856–1857
- [66] N. Tsierkezos, U. Ritter, *J. Appl. Electrochem.* **2010**, *40*, 409–417
- [67] C. Cannes, F. Kanoufi, A. J. Bard, *J. Electroanal. Chem.* **2003**, *547*, 83–91
- [68] M. Nádherná, J. Reiter, *Electrochim. Acta* **2010**, *55*, 5911–5916
- [69] H. Matsuda, Y. Ayabe, *Zeitschrift für Elektrochemie, Ber. Bunsenges. Phys. Chem.* **1955**, *59*, 494–503
- [70] A. J. Bard, L. R. Faulkner, *Electrochemical methods. Fundamentals and applications*, 2nd ed., Wiley, New York, **2001**.
- [71] C. H. Hamann, A. Hammnett, W. Vielstich, *Electrochemistry*, 2nd ed., Wiley-VCH Verlag GmbH & Co. KGaA, **2007**.
- [72] C. O. Laoire, E. Plichta, M. Hendrickson, S. Mukerjee, K. M. Abraham, *Electrochim. Acta* **2009**, *54*, 6560–6564
- [73] J. P. Schmidt, P. Berg, M. Schönleber, A. Weber, E. Ivers-Tiffée, *J. Power Sources* **2013**, *221*, 70–77
- [74] J. P. Schmidt, T. Chrobak, M. Ender, J. Illig, D. Klotz, E. Ivers-Tiffée, *J. Power Sources* **2011**, *196*, 5342–5348

- [75] D. Moosbauer, S. Zugmann, M. Amereller, H. J. Gores, *J. Chem. Eng. Data* **2010**, *55*, 1794–1798
- [76] M. D. Levi, G. Salitra, B. Markovsky, H. Teller, D. Aurbach, U. Heider, L. Heider, *J. Electrochem. Soc.* **1999**, *146*, 1279–1289
- [77] D. Aurbach, M. D. Levi, E. Levi, H. Teller, B. Markovsky, G. Salitra, U. Heider, L. Heider, *J. Electrochem. Soc.* **1998**, *145*, 3024–3034
- [78] Y. Yamada, K. Miyazaki, T. Abe, *Langmuir* **2010**, *26*, 14990–14994
- [79] M. Winter, J. O. Besenhard, M. E. Spahr, P. Novák, *Adv. Mater.* **1998**, *10*, 725–763
- [80] P. Niehoff, S. Passerini, M. Winter, *Langmuir* **2013**, *29*, 5806–5816
- [81] G. Zampardi, F. La Mantia, W. Schuhmann, *Electrochem. Commun.* **2015**, *58*, 1–5
- [82] A. Wang, S. Kadam, H. Li, S. Shi, Y. Qi, *npj Comput. Mater.* **2018**, *4*, 15–40
- [83] S. Shi, P. Lu, Z. Liu, Y. Qi, L. G. Hector, H. Li, S. J. Harris, *J. Am. Chem. Soc.* **2012**, *134*, 15476–15487
- [84] A. Zaban, D. Aurbach, *J. Power Sources* **1995**, *54*, 289–295
- [85] E. Peled, D. Golodnitsky, G. Ardel, *J. Electrochem. Soc.* **1997**, *144*, L208–L210
- [86] D. Li, D. Danilov, Z. Zhang, H. Chen, Y. Yang, Notten, P. H. L., *J. Electrochem. Soc.* **2015**, *162*, A858–A869
- [87] A. P. Abbott, C. L. Miaw, J. F. Rusling, *J. Electroanal. Chem.* **1992**, *327*, 31–46
- [88] A. D. Clegg, N. V. Rees, O. V. Klymenko, B. A. Coles, R. G. Compton, *J. Electroanal. Chem.* **2005**, *580*, 78–86
- [89] B. Sakintuna, O. Çuhadar, Y. Yürüm, *Energy Fuels* **2006**, *20*, 1269–1274
- [90] B. K. Antonopoulos, A.-C. Gentschev, F. Maglia, H. E. Hoster, *Manuscript in preparation*.
- [91] H. J. Ploehn, P. Ramadass, R. E. White, *J. Electrochem. Soc.* **2004**, *151*, A456–A462
- [92] B. K. Antonopoulos, C. Stock, F. Maglia, H. E. Hoster, *Electrochim. Acta* **2018**, *269*, 331–339

Manuscript received: May 7, 2018
 Accepted Article published: June 20, 2018
 Version of record online: July 22, 2018

Supporting Information

© Copyright Wiley-VCH Verlag GmbH & Co. KGaA, 69451 Weinheim, 2018

Formation of the Solid Electrolyte Interphase at Constant Potentials: a Model Study on Highly Oriented Pyrolytic Graphite

Byron K. Antonopoulos, Filippo Maglia, Felix Schmidt-Stein, Jan P. Schmidt, and Harry E. Hoster*EAB Special Issue

Author Contributions

H.H. Writing – review & editing:Lead

In some parts this SI refers to the equations, table and figures from the main manuscript, which will be referred to as MM-eq., mm-Table and MM-Figure, respectively.

1. Details Potentiostatic SEI Formation

1.1. Li⁺ Intercalation and Formation of Dissolved/Dilute Species

To estimate the degree of possible Li⁺ intercalation during the formation, the OCP was recorded after the polarization to check the Nernst potential. Since a lower formation potential would lead to more intercalation [1,2], only the lowest applied value of 100 mV is discussed in this section and presented in Figure 1a. OCP increases towards the final relaxation potential, which is similar to the potential before the SEI formation (indicated as $\phi_{Pristine}$). Whilst typical relaxation time constants (63.2% of exponential potential increase) of Li-ion cells are $\gg 60$ s, the OCP in Figure 1a is not of exponential shape and has a respective time constant of < 10 s [3,4]. The fast OCP rise as well as the final value indicate, that the amount of intercalated Li⁺ is negligible, since a considerable amount of intercalated Li⁺ would lead to a slowly rising mixed OCP driven by solid state diffusion and chemical Li⁺ deintercalation.

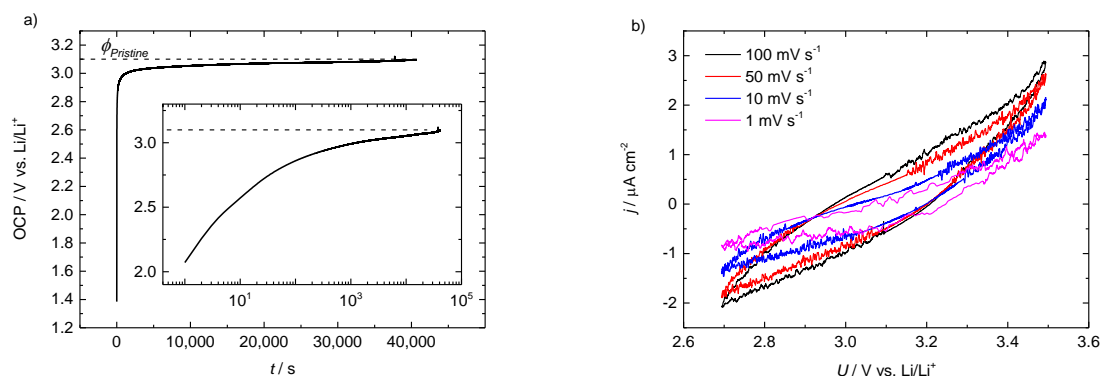


Figure 1: a) OCP immediately after the potentiostatic SEI formation in neat electrolyte at 100 mV. The inset is a duplicate with logarithmic abscissa. b) CVs with different scan rates around the equilibrated OCP after the SEI formation at 100 mV in neat electrolyte. Shapes indicate a serial R-C equivalent circuit.

Ref. [5] proposed the OCP after the formation in non-VC containing electrolyte to be determined by the concentration of a dilute species. They found the final OCP value to be around 1.7 V and dependent on the formation time and charge, which was not the case in this study. Far from it, we obtained a return of OCP back to the initial value > 3 V independent of the formation potential, time and charge. Thus, the potentiostatic formation did not accumulate any new electrochemically active species neither in the electrolyte nor near the electrode. This is confirmed by cyclic voltammograms (Figure 1b), which reveal essentially featureless profiles. It is thus safe to assume that both Li⁺ intercalation as well as irreversible reactions other than SEI formation are negligible. Likewise, the

small residual passivation current j_{pass} (MM-Figure 1c), which we observed for all formation potentials, must thus reflect a slow, ongoing SEI formation via electron tunneling.

We hypothesize that in this study the species determining the OCP is one solvent component, which is selectively reduced during the formation. A selectively reduced component would suffer from a concentration profile during the formation. The homogenization of concentration by diffusion after the formation leads to the obtained OCP slope in Figure 1a. This process is theoretically described by the Sand equation. Since the electrolyte contained 2% wt VC, which is reduced preferably [6], the OCP behavior is probably determined by the VC concentration at the electrode surface. Though, a selective reduction of solvent could also be correlated to the different enthalpy differences for desolvation of Li^+ ions of cyclic and linear carbonates [7].

1.2. Double Layer Capacitance

To understand whether the charging of the electrochemical double layer overlaps the formation current and must be considered in the discussion of the formation data, the current response of the equivalent circuit $R_0(R_{CT}|C_{DL})$ after a potential step has to be estimated. R_0 includes all the serial ohmic resistances, R_{CT} and C_{DL} are the electrolyte reduction charge transfer resistance and the double layer capacitance, respectively. The total impedance $Z_{tot}(t)$ of the circuit is described by:

$$Z_{tot}(t) = R_{CT}/(1 + j\omega R_{CT}C_{DL}) + R_0 \quad (1)$$

ω is the angular frequency, j the imaginary number. When suddenly a fixed formation potential φ_{form} is applied to the electrode, the electrode undergoes a jump in overpotential $\eta = |\varphi_{form} - OCP|$. An analogous jump in the overpotential for the equivalent circuit is described by a voltage step function $U(t) = U_0 \theta(t)$ from $U(t = 0) = 0 \text{ V}$ to $U(t > 0) = U_0$, where $\theta(t)$ is the Heaviside step function. The current response $I(t)$ is described by

$$I(t) = U(t) Z_{tot}(t)^{-1} \quad (2)$$

$$I(t) = U_0 \theta(t)(1 + j\omega\tau_{DL})(R_{tot} + j\omega R_0\tau_{DL})^{-1} \quad (3)$$

after substitution of $\tau_{DL} = R_{CT}C_{DL}$ and $R_{tot} = R_0 + R_{CT}$. By applying a Laplace transformation $f(t) \rightarrow F(s)$ the equation is transformed to

$$I(s) = \frac{U_0}{s} \cdot (1 + s\tau_{DL})(R_{tot} + sR_0\tau_{DL})^{-1} \quad (4)$$

$$I(s) = U_0 \left(\frac{1}{R_{tot}} \frac{R_{tot}(R_0\tau_{DL})^{-1}}{s[s + R_{tot}(R_0\tau_{DL})^{-1}]} + \frac{1}{R_0} \frac{1}{s + R_{tot}(R_0\tau_{DL})^{-1}} \right) \quad (5)$$

Inverting the Laplace transformation, one gets:

$$I(t) = U_0 [R_{tot}^{-1} + (R_0^{-1} - R_{tot}^{-1}) \exp(-R_{tot}(R_0\tau_{DL})^{-1} \cdot t)] \quad (6)$$

Eq. (6) is of the typical RC-circuit charging/discharging nature $\hat{A} + \hat{B} \exp(-\alpha t)$, from which one can extract the characteristic time constant $\tilde{\tau} = \alpha^{-1}$. After $t = 5 \tilde{\tau}$ the capacitance is assumed to be fully charged. Extracting $\tilde{\tau}$ from eq. (6) and reinserting the substituted values, the time constant of the investigated circuit is

$$\tilde{\tau} = R_0 R_{CT} C_{DL} (R_0 + R_{CT})^{-1} \quad (7)$$

In this work the investigated surface was basal plane HOPG with a free surface area of 0.13 cm². Typical values of the specific double layer capacitance of pristine basal plane HOPG are in the order of magnitude of a few $\mu\text{F cm}^{-2}$ [8,9]. Therefore, it is reasonable to assume that C_{DL} is around 0.5 μF . As it will be discussed later in this work, R_0 was constantly around 20 Ω . R_{CT} is the charge transfer resistance of the electrolyte reduction at a specific potential. Since the experimental setup does not allow to determine R_{CT} , it remains as a variable in the approximation of the time constant $\tilde{\tau}$:

$$\tilde{\tau} \approx 10^{-5} R_{CT} (10 \Omega + R_{CT})^{-1} \text{ s} \quad (8)$$

Although the charge transfer resistance remains unknown, the equation shape itself already allows an approximation of the time constant $\tilde{\tau}$, since $\lim_{R_{CT} \rightarrow \infty} (\tilde{\tau}) \approx 10 \mu\text{s}$ and $\lim_{R_{CT} \rightarrow 0} (\tilde{\tau}) = 0 \mu\text{s}$:

$$\Rightarrow 0 \mu\text{s} < \tilde{\tau} < 10 \mu\text{s} \quad (9)$$

2. Relation between Free Surface Area and Diffusion Coefficient

In this section we discuss in detail the obtained CV data using an alternative interpretation model. Tang et al. hypothesized, that the reduced electrolyte forms a porous layer, which is fully soaked with electrolyte. While the charge transfer of the Fc/Fc⁺ reaction is not affected by the SEI (reaction rate constant is equal to the value at a pristine electrode), the porous medium reduces both the effective diffusion coefficient (directly proportional) and the free surface area of the electrode [5]. On average

the effective surface area A_{eff} scales with the porosity $p(\varphi)$, which is a function of formation potential φ , directly proportional as well: $A_{eff}(\varphi) = p(\varphi) \cdot A_0$.

The obtained current in CVs must therefore be normalized to the effective free surface area, so that the Randles-Sevcik equation (MM-eq. 1) must be adjusted appropriately:

$$\frac{I}{A_{eff}(\varphi)} \propto (D_{eff}(\varphi) \cdot \nu)^{1/2} \quad (10)$$

$$\frac{I}{A_0} \propto p(\varphi)^{3/2} \cdot (D_{eff,pristine} \cdot \nu)^{1/2} \text{ with } p_{pristine} = 1 \quad (11)$$

The equation can be restructured, so that the porosity can easily be calculated by

$$p(\varphi) = \left(\frac{\text{Slope } j_{Peak} \text{ vs. } \nu^{1/2}, \langle \text{Pristine} \rangle}{\text{Slope } j_{Peak} \text{ vs. } \nu^{1/2}, \langle \varphi \text{-SEI} \rangle} \right)^{2/3} \quad (12)$$

When processing the original CV data using this approach instead of MM-eq. (1) one gets the results listed in Table 1. Since the theoretical background is completely different, values slightly differ from the ones listed in MM-Table 1. k_0 is set by definition to the rate constant of the pristine sample ($k_{0,50}$).

Table 1: Electrochemical results assuming a direct proportionality between porosity and effective surface area.

	Slope j_{Peak} vs. $\nu^{1/2}$	Porosity p	A_{eff}	D_{eff}	k_0
	$10^{-4} \text{ A cm}^{-2} (\text{V s}^{-1})^{-1/2}$	%	10^{-2} cm^2	$10^{-6} \text{ cm}^2 \text{ s}^{-1}$	$10^{-4} \text{ cm s}^{-1}$
Pristine	15	100	12.6	3.22	8.1
600mV	7.4	62.9	7.91	2.03	8.1
450mV	8.0	66.2	8.33	2.14	8.1
300mV	7.0	60.6	7.61	1.96	8.1
100mV	5.0	48.5	6.10	1.57	8.1

While it is impossible to judge from the data itself which of the two hypotheses is more reasonable, one can simulate CVs using the calculated results from the two tables. If one a hypothesis is correct, the simulation should allow the way back, so that simulated results reproduce the measured data. Therefore, we simulated CVs with the software EC-Lab from BioLogic considering the physical values either from MM-Table 1 or Table 1 and by using the boundary conditions from the experiments. That way a direct comparison of simulation and experimental data is possible. The simulations results based on the two hypotheses can be found in Figure 2. a) shows the data based on our hypotheses (stable surface area, varying rate constant), while b) shows the results based on Tang

hypothesis (stable rate constant, varying surface area). The pristine data served as a calculation fundament in both hypotheses, therefore the resulting simulated data is equal, respectively. The data in b) differ in a major characteristic from the measured data, since the movement of peak potential difference $\Delta\varphi_{Peak}$ cannot be resembled. On the other hand, the peak potential differences of the measured data are perfectly resembled by the slopes in MM-Figure 3a. When moving the 300 mV SEI slope by 20 mV (e.g. due to a shifted reference potential in the experiment), the simulated data almost appears to be a copy of the measured data.

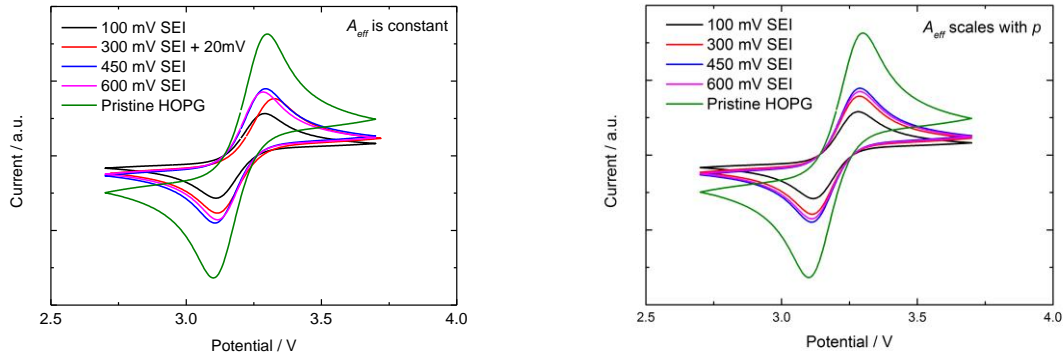


Figure 2: Simulated cycling voltammetry experiments based on the two indicated hypotheses. Boundary conditions can be found in MM-Table 1 and Table 1.

Therefore, we conclude that the process responsible for the decrease of the effective diffusion coefficient does not have a significant impact on the free surface area, while on the other hand the charge transfer is affected by the presence of an SEI. We agree on the idea, that a porous sponge like the outer SEI might reduce the free surface area, though in this study it's either not blocking the surface in terms of Fc/Fc^+ reaction or the effective diffusion coefficient is predominantly reduced by a change in tortuosity instead of porosity. For this reason the data in this study was analyzed with the assumption of a constant surface area.

3. In-depth EIS Analysis: Activation Energies & Diffusion Coefficients

3.1. Temperature Dependent DRT Peak Shifts

The temperature dependent position of DRT peaks 2 and 3 (MM-Figure 6) contains information about the migration properties of Fc/Fc^+ . Figure 3 shows the reciprocal peak frequencies f_{Peak} plotted vs. $1/T$ derived from the three visible contributions indicated by the DRT peak numbers. Assuming an Arrhenius dependency, the slopes of the linear fits in Figure 3 allow a calculation of the exponential term of the respective mechanisms:

$$\begin{aligned}
 f_{Peak} &\propto \exp(-E_A/RT) \\
 \Rightarrow \ln f_{Peak} &\propto -E_A/RT
 \end{aligned}
 \tag{13}$$

with E_A being the (apparent) activation energy. The activation energies of DRT peaks 2 and 3 are independent of the SEI formation potential at ~ 0.28 and ~ 0.41 eV, respectively. The apparent activation energy of the charge transfer peak 1 is significantly higher: ~ 0.58 eV. This higher temperature sensitivity made it possible to detect the additional features in the Nyquist and DRT plots in Figure 7 at lower temperatures. In turn, one may speculate that the charge-transfer kinetics at the high-voltage SEI is associated with an apparent activation energy closer to those of migration so that the related features remain indistinguishable even at lower temperatures.

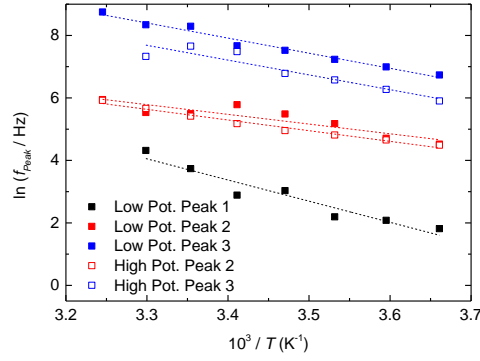


Figure 3: Arrhenius plot of characteristic frequencies f_{peak} (dots) derived from EIS DRT plots and respective linear fits (dashed lines).

3.2. Warburg-based Diffusion Coefficients

In the context of MM-eq. (1) we discussed the introduced Randles-Sevcik correction factor ζ . Apart from CVs also EIS experiments allow the calculation of effective diffusion coefficients, which can in turn be used to determine the correction factor ζ . Diffusion coefficients can be calculated from EIS by inverting the following equation [10]:

$$\sigma = \frac{RT}{2^{1/2}n^2F^2} \left(\frac{1}{c_{ox}^b D_{ox}^{1/2}} + \frac{1}{c_{red}^b D_{red}^{1/2}} \right) \quad (14)$$

where σ in $\Omega \text{ cm}^2 \text{ s}^{-1/2}$ is the Warburg diffusion coefficient and c_i^b are the bulk concentrations of the respective species. In all experiments the bulk concentrations were equal and controlled experimentally. Furthermore, CVs revealed the similarity of the oxidized and reduced effective diffusion coefficients ($D_{ox} \approx D_{red}$). Therefore, eq. (14) can be simplified to

$$D_{eff} = 2 \left(\frac{RT}{n^2 F^2 c^b \sigma} \right)^2 \quad (15)$$

The Warburg coefficient under assumed semi-infinite boundary conditions (all Nyquist plots show a perfect 45° slope) is the proportionality factor of the impedance Z and $f^{1/2}$ in the lower frequency region (Warburg region) [10]:

$$Z(f) = (2\pi)^{-1/2} \sigma (f^{-1/2} - if^{-1/2}) \quad (16)$$

which reflects diffusion controlled equilibration of the near-electrode concentration gradients of Fc and Fc⁺. Plots of Z_{Real} vs $f^{-1/2}$ (f = modulation frequency) will yield the Warburg diffusion σ and the related effective Fc/Fc⁺ diffusion coefficient D_{eff} , which can be compared to the CV-based values in MM-Table 1. Z_{Real} at 20 °C of both high and low-potential SEIs are plotted vs. $f^{1/2}$ in Figure 4a. The linear fit slopes σ considering only the Warburg region are 68.7 and 61.9 $\Omega \text{ cm}^2 \text{ s}^{1/2}$ for the low and high-potential SEI, respectively. Using eq. (15) we can calculate the two effective diffusion coefficients as 4.65 and $5.73 \cdot 10^{-6} \text{ cm}^2 \text{ s}^{-1}$ for the two SEIs, respectively. In order to adjust the coefficients calculated using MM-eq. 1 and eq. (15), correction factors of 4.09 and 3.85 for the low and high-potential SEIs would be appropriate. This small deviation indicates, that the calibration method is reasonable. We defined the correction factor ζ as 3.97, which we used for calculation of D_{eff} in MM-Table 1.

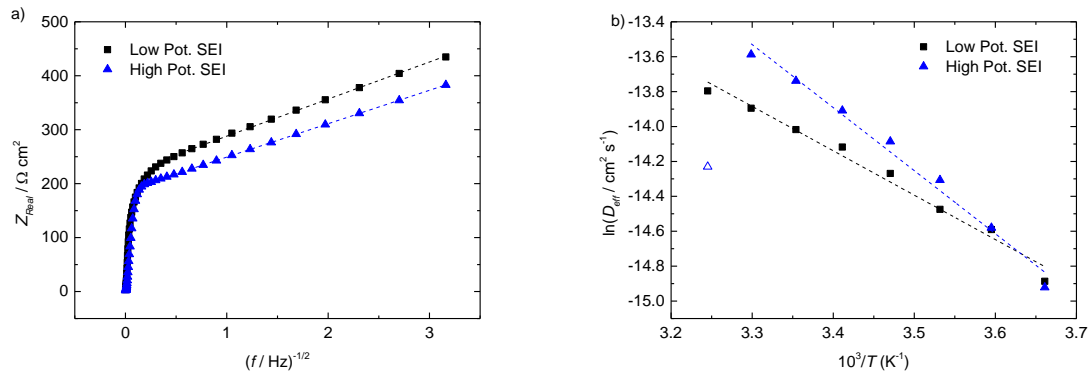


Figure 4: a) Z_{Real} plotted vs. $f^{1/2}$ for low and high-potential SEIs at 20 °C. Linear plots consider frequencies < 5 Hz. b) Arrhenius plot of diffusion coefficients D_{eff} of a low and high-potential SEI extracted from EIS experiments in Fc/Fc⁺ environment and respective linear fits. The high-potential SEI fit neglects the diverging value at 35 °C.

3.3. Temperature Dependent Warburg-based Diffusion Coefficients

Based on the Warburg impedances, the temperature dependent EIS data allows calculating and comparing temperature dependent effective diffusion coefficients for the low and high-potential SEI. The results extracted from spectra shown in MM-Figure 6 are presented in an Arrhenius plot in Figure 4b. Again, assuming an Arrhenius dependency of the effective diffusion coefficient, the slopes of the linear fits (dotted lines) reflect apparent activation energies. They correspond to 21 and 30 kJ mol^{-1} for the low and high-potential SEI, respectively. We refrain from a microscopic interpretation of those

values since that would require information about the microscopic structure of the SEI and its interaction with the diffusing species, which again is not available.

4. Supplementary EIS Data

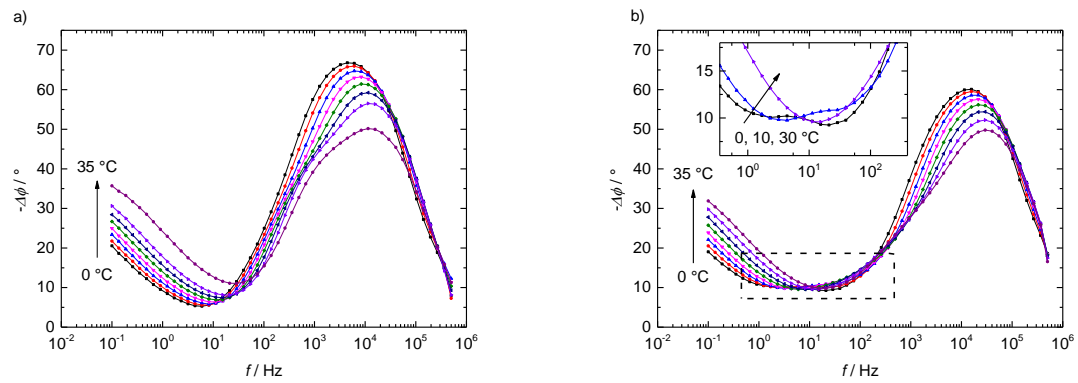


Figure 5: Temperature dependent impedance spectra of a) high and b) low-potential SEIs in Fc/Fc^+ environment presented as Bode phase plots. The inset in b) is a zoom of the boxed area, respectively.

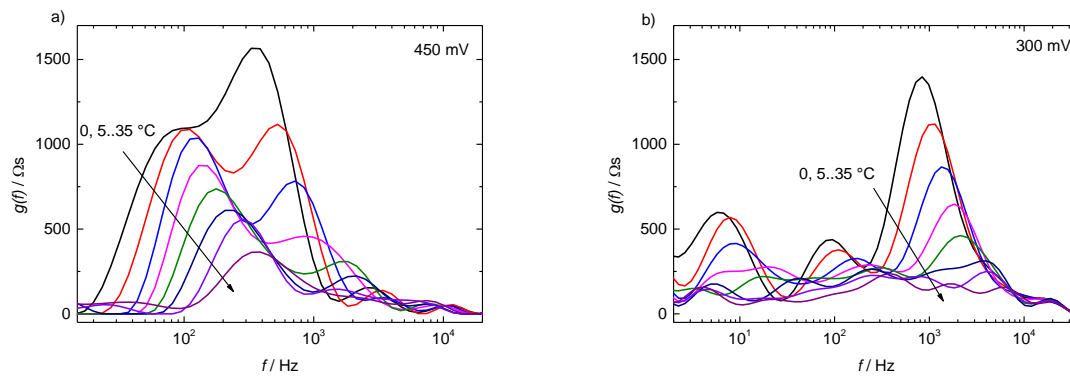


Figure 6: Temperature dependent impedance spectra of a) high and b) low-potential SEIs in Fc/Fc^+ environment presented as DRT plots.

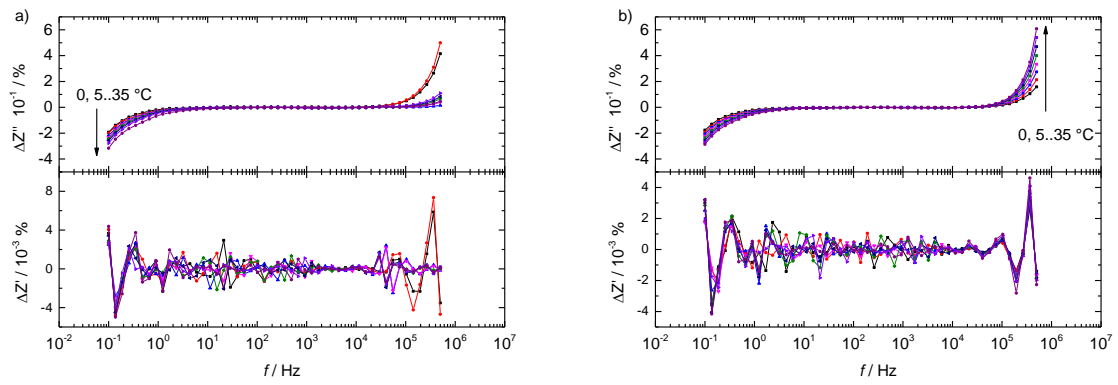


Figure 7: Real and imaginary DRT residuals of temperature dependent impedance spectra of a) high and b) low-potential SEIs.

5. SI-References

- [1] S. Zhang, M. S. Ding, K. Xu, J. Allen, T. R. Jow, *Electrochem. Solid-State Lett.* **2001**, *4*, A206-A208
- [2] V. A. Sethuraman, Winkle, N. Van, D. P. Abraham, A. F. Bower, P. R. Guduru, *J. Power Sources* **2012**, *206*, 334–342
- [3] M. Reichert, D. Andre, A. Rösmann, P. Janssen, H.-G. Bremes, D. U. Sauer, S. Passerini, M. Winter, *J. Power Sources* **2013**, *239*, 45–53
- [4] E. Markevich, M. D. Levi, D. Aurbach, *J. Electroanal. Chem.* **2005**, *580*, 231–237
- [5] M. Tang, J. Newman, *J. Electrochem. Soc.* **2012**, *159*, A281-A289
- [6] H. Ota, Y. Sakata, A. Inoue, S. Yamaguchi, *J. Electrochem. Soc.* **2004**, *151*, A1659-A1669
- [7] Y. Yamada, Y. Iriyama, T. Abe, Z. Ogumi, *Langmuir* **2009**, *25*, 12766–12770
- [8] P. Los, *J. Electrochem. Soc.* **1994**, *141*, 2716–2721
- [9] W. Yuan, Y. Zhou, Y. Li, C. Li, H. Peng, J. Zhang, Z. Liu, L. Dai, G. Shi, *Sci. Rep.* **2013**, *3*, 2248–2254
- [10] A. J. Bard, L. R. Faulkner, *Electrochemical methods. Fundamentals and applications*, 2nd ed., Wiley, New York, **2001**

4.2. The Dynamic Impedance Properties of Solid Electrolyte Interphase on HOPG

Status	Manuscript in preparation
Journal	-
Publisher	-
DOI	-
Authors	Antonopoulos, Byron K.; Gentschev, Ann-Christin; Maglia, Filippo; Hoster, Harry E.

Contributions: B.K.A., F.M. and H.E.H. conceived and designed the experiments. B.K.A. performed the experiments. B.K.A. and A.-C.G. performed the calculations. B.K.A., A.-C.G., F.M. and H.E.H. discussed the results and wrote the paper.

Content

The dependencies of the solid electrolyte interphase (SEI) properties of graphite electrodes on the formation parameters has been extensively studied with several approaches and techniques by the research society. The latter chapter presented a promising approach, in which the SEI is formed on highly oriented pyrolytic graphite (HOPG) in a half-cell setup, followed by electrochemical investigations in ferrocene environment. In this chapter, we dig deeper into the properties of SEIs on HOPG and investigate an eye-catching structural stability difference of SEIs formed on HOPG at high or low potentials. The results show that SEIs formed at potentials > 400 mV vs. Li/Li⁺, although being passivating and chemically stable, show a structural though reversible transformation. Depending on the frequency of the applied electric field, migration of ions becomes faster or slower. Similar behavior cannot be observed on HOPG covered by a low-potential SEI (formed at < 400 mV vs. Li/Li⁺).

This interesting phenomenon underlines the different nature of high- and low-potential SEIs. The insensitivity of the low-potential SEI towards external polarization implies the finalized status of the low-potential SEI. On the other hand, the structural instability of the high-potential SEI, particularly of the outer porous layer, give rise to a completely novel approach in SEI formation procedures on the field of high-potential SEI engineering, which is presented in chapter 5.

The Dynamic Impedance Properties of the Solid Electrolyte Interphase on HOPG

Byron Konstantinos Antonopoulos^a, Dr. Ann-Christin Gentshev^{a,1}, Dr. Filippo Maglia^a, Prof. Dr. Harry Ernst Hoster^{b,c}

^a BMW Group, Petuelring 130, 80788 München, Germany

^b Energy Lancaster, Dep. of Chemistry, Lancaster University, Lancaster, LA1 4YB, United Kingdom

^c ALISTORE European Research Institute, CNRS FR 3104, Hub de l'Energie, Rue Baudelocque, 80039 Amiens, France

Corresponding author: h.hoster@lancaster.ac.uk; +44 7842 831633

Co-Author Addresses:

- Konstantinos.Antonopoulos@bmw.de
- Ann-Christin.Gentshev@bmw.de
- Filippo.Maglia@bmw.de

Abstract:

The dependencies of the solid electrolyte interphase (SEI) properties of graphite electrodes on the formation parameters has been extensively studied with several approaches and techniques by the research society. A promising approach is the SEI formation on highly oriented pyrolytic graphite (HOPG) in a half-cell setup, followed by electrochemical investigations in ferrocene environment. In this article, we shortly present an eye-catching structural stability difference of SEIs formed on HOPG at high or low potentials. The results show that SEIs formed at potentials > 400 mV vs. Li/Li⁺, although being passivating and chemically stable, show a structural though reversible transformation. Depending on the frequency of the applied electric field, migration of ions becomes faster or slower. Similar behavior cannot be observed on HOPG covered by a low-potential SEI (formed at < 400 mV vs. Li/Li⁺). The mechanism responsible for the different behavior is elucidated here. Moreover, novel approaches in formation procedures of composite electrodes including high-potential SEI engineering, are discussed.

Keywords: Solid electrolyte interphase (SEI), Li-ion battery, Highly oriented pyrolytic graphite (HOPG), EIS

¹ New Affiliation: BMW Group Technology Office USA, 2606 Bayshore Parkway, Mountain View, CA 94043, USA

1. Introduction

Negative electrodes of state-of-the-art Li-ion batteries consist of graphitic carbons, which operate at potentials < 300 mV vs. Li/Li⁺ in order to enable Li⁺ intercalation [1]. This potential region is below the electrochemical stability window of the carbonate solvent containing electrolytes. Therefore, during the polarization of the negative electrode, a three-dimensional layer of electrolyte decomposition products, formed through several parallel reaction pathways, evolves. This layer, known as solid electrolyte interphase (SEI), ideally prevents further electrolyte decomposition after the first cell cycling without significantly reducing Li⁺ movement properties. In reality, the SEI de- and recomposes during the cell lifetime resulting in Li⁺ consumption and reduced ionic conductivity. The formation cycle parameters (current rate, temperature etc.) have significant influence on the chemical, electrochemical and physical properties of the SEI. These factors are crucial to obtain an SEI with high stability and low impedance, thus enhancing lifetime, power capability and energy efficiency [2–5]. While fundamental research in electrocatalysis research provides a necessary groundwork, further studies towards the application are necessary to deeper understand processes in real systems [6–11].

In a recent publication we presented chemical and electrochemical properties of SEIs formed at different potentials on highly oriented pyrolytic graphite (HOPG) [12]. The flat basal HOPG surface, which inhibits Li⁺ intercalation, allows for the analysis and comparison of potentiostatically formed SEIs in terms of diffusion coefficients and kinetic properties using cyclic voltammetry (CV) and electrochemical impedance spectroscopy (EIS). By combining electrochemistry and XPS results it was possible to address the formation of inorganic SEI species like Li₂CO₃ to low formation potentials, whilst at high formation potentials only organic solvent decomposition products could be observed. Since the SEI was found to be insulating in terms of electrolyte reduction independently of the formation potential, inorganic species must be formed via decomposition of the previously formed organic SEI species. This conversion reaction most likely takes place at a potential around 400 mV vs. Li/Li⁺, where a sudden change of chemical as well as electrochemical SEI properties was determined. This threshold potential allows the classification of SEIs into two groups, namely high- and low-potential SEIs. As the low-potential SEI is formed by decomposition of the high-potential SEI, it seems likely that the properties of high-potential SEIs strongly influence the properties of subsequently developing low-potential SEIs.

In this paper we further investigate the electrochemical behavior of the two SEI classes. The two edge formation potentials of 300 and 450 mV vs. Li/Li⁺, which are slightly higher and lower than the earlier introduced threshold potential, are used to investigate a striking difference in the behavior of the two kinds of SEIs during EIS experiments in the presence of ferrocene and ferrocenium hexafluorophosphate (Fc/Fc⁺) as a surface sensitive electrochemical couple [13]. The results are discussed from the perspective of improving the stability of SEIs in commercial Li-ion batteries.

2. Experimental

Electrochemical experiments on HOPG were performed with the instrumentation, cell setup, materials and preparation procedures as fully described in reference [12]. As measurement cell, a T-shaped cell with Li foil as reference and counter electrode was used. SEIs were formed at the potentials 450 or 300 mV vs. Li/Li⁺ in 75 μ l LP572 electrolyte. After formation, 25 μ l Fc/Fc⁺ containing electrolyte (10 mMol) was injected without disassembling the cell. Numerous cyclic voltammetry scans were performed until achieving reproducible current behavior in order to ensure electrolyte homogeneity. EIS experiments were preceded by an OCP determination step, where several spectra were obtained in potentiostatic mode with 10 mV amplitude in the frequency range 500 kHz - 0.1 Hz consisting of 50 logarithmically distributed frequencies (unless otherwise stated). The measured impedances are normalized with the original HOPG free surface area (circular, 4 mm diameter). All experiments were performed at 20 °C, controlled by a Peltier element attached to the cell. The obtained trends could be fully reproduced in several experiments.

3. Results and Discussion

3.1. Electrochemical Impedance Spectroscopy

In our previous work we proposed a model, which describes the evolution of chemical and physical properties on HOPG during the two SEI formation potential steps at \sim 700 and at \sim 400 mV vs. Li/Li⁺. During the first formation step an initial organic passivation layer is formed due to electrolyte and in particular solvent reduction. It consist of a porous outer layer and a compact inner electronically insulating layer, which cannot be penetrated by electrolyte [12]. As SEIs formed at potentials above that first threshold potential are neither stable nor insulating, the investigation of potentials $>$ 700 mV vs. Li/Li⁺ is of no practical interest [14]. The second step at \sim 400 mV vs. Li/Li⁺ transfers the organic compact into an inorganic compact layer. In this study we focus on the SEI differences before and after that second step potential. For that, SEIs were formed at 450 and 300 mV vs. Li/Li⁺ (referred to as high- and low-potential SEIs, respectively) using a potentiostatic step procedure. Subsequently, using a syringe connected via a capillary, a defined amount of Fc/Fc⁺ containing electrolyte was injected into the cell without the need of disassembling it. As no Li⁺ intercalates into the substrate, Fc/Fc⁺ is the only well-defined electrochemical couple, thus allowing surface sensitive electrochemical investigations (for details see reference [12]). The presented EIS experiments were performed in equilibrium conditions, as described in the experimental section.

Figure 1 shows five consecutively obtained EIS spectra of a low-potential SEI presented as Nyquist plots. Since the potentiostat is not supposed to act as a frequency generator, but to measure the impedance with minimal perturbation, one can assume the total alternating current (AC) duration to be little. The investigated electrochemical system appears to be stable, as the difference between the

consecutive spectra is negligible. The plots consist of a distorted semicircle in the high/middle frequency range followed by a straight slope usually referred as diffusion or Warburg slope.

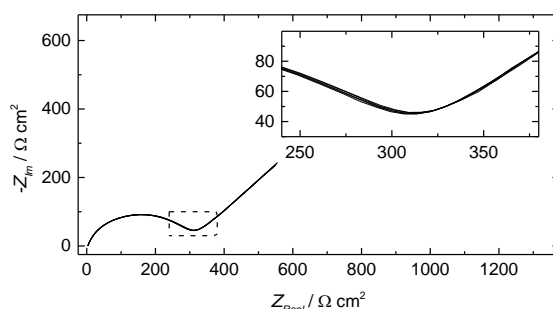


Figure 1: Impedance spectra presented as Nyquist plots of a low-potential SEI in Fc/Fc⁺ environment. Five consecutive spectra are presented. Inner plot is a zoom of the dashed area.

The same experiments were also performed for the high-potential SEI. The five consecutively obtained EIS spectra are shown in red in Figure 2. The arrow indicates the time sequence of the experiments from the 1st to the 5th measurement. Again, the spectra appear as one distorted semicircle followed by the diffusion slope. In contrast to the low-potential SEI in Figure 1, impedances are generally slightly higher and not constant, since the distorted semicircle tends to shrink with increasing experiment number. After the EIS series, an extensive CV experiment was performed consisting of scan rates in the interval 100-1 mV s⁻¹, followed by a repetition of a further EIS series with another five consecutive cycles. Respective Nyquist plots are shown in Figure 2 in blue. Again, the arrow indicates the evolution of impedance with increasing experiment number. The EIS shrinking trend remains, though the semicircle size is noticeably increased compared to the red series as a consequence of the intermediate CV experiments. In the Supplementary Information (SI) we present evidence that the shrinking trend is neither time nor temperature induced (chapter 7.1).

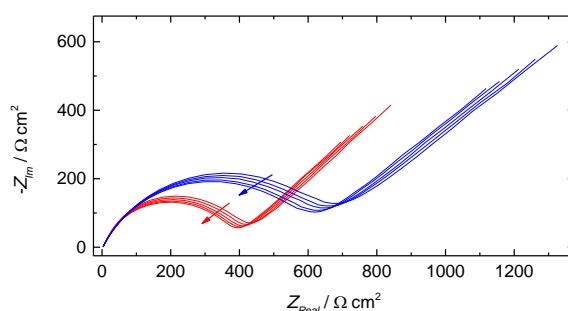


Figure 2: Impedance spectra presented as Nyquist plots of a high-potential SEI in Fc/Fc⁺ environment. Five consecutive spectra are presented, experiment directions are indicated by the arrows. Colors: See text.

Based on these observations, the most plausible hypothesis is that the semicircle shrinkage trend observed at the high-potential SEI is induced by the EIS experiment itself (Schrödinger's cat principle): By applying an AC current, we actually change the system properties. Since during the EIS experiments

a broad range of frequencies is applied, the question arises whether it is a specific frequency region that induces the impedance shrinking. Trying to shed some light on this aspect, we performed two more series of EIS experiments each one consisting again of five consecutive spectra on the high-potential SEI. The two series examine either the high (500 kHz - 100 Hz) or the low (5 Hz - 0.1 Hz) frequencies. Both regions were scanned using 20 logarithmically distributed frequencies. The respective Nyquist plots are shown in Figure 3. The EIS experiments in a) were obtained in the high- and in b) in the low-frequency region. The scaling of abscissas and ordinates is not equal for illustration reasons, though identical in a) and b). While the low-frequency series in b) is almost invariant, the high-frequency series in a) shows the previously reported shrinking trend with increasing number of experiment, as indicated by the arrow. The EIS perturbation time is slightly different during the two series, as the same amount of AC waves are applied, but the wavelength varies. Nevertheless, the little perturbation at high frequencies is still more effective. Those results indicate that there is probably some kind of resonance frequency interval.

To summarize the experimental observations: During high-frequency polarization the impedance of the high-potential SEI is reduced, while long-time polarization e.g. during CV causes an impedance rise. On the other hand, the low-potential SEI is not affected by any polarization.

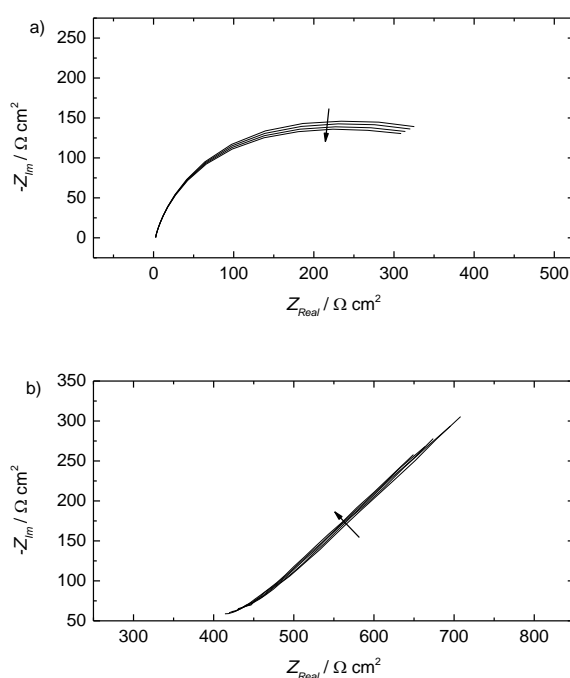


Figure 3: EIS series presented as Nyquist plots of a high-potential SEI using only high (a) and low (b) frequency region. Arrow indicates the experiment direction.

3.2. Discussion

In order to deepen the discussion and interpretation of the presented results, it is necessary to reconsider the mechanisms that can be visualized with EIS. Several research papers state that at high frequencies

one measures the impedance of the Li^+ migration through the outer porous organic SEI layer, while the middle frequency response can be attributed to the Li^+ charge transfer [15–18]. Although in our case the charge transfer is represented by the Fc/Fc^+ reaction (HOPG prevents Li^+ intercalation), we expect a contribution by all mobile ions to the migration response in the higher frequencies. It is important to keep in mind that at those frequencies ions do not move over longer distances, but only vibrate locally. Therefore, the obtained EIS response reflects the local effective ionic mobility on the microscopic level.

The above presented data (particularly Figure 3) indicates that the high-potential SEI is structurally influenced by the high-frequency stimulation during the EIS experiments. As the migration is limited by the porous layer, the respective qualitative properties should determine the high-frequency stability. We therefore believe, that, by stimulating the electrode with high frequencies, the porous layer species are disordered, which in EIS experiments reveals a higher ionic conductivity. Although similar conductivity trends were obtained for polymer electrolytes, we emphasize that the respective ion conductivity takes place in a completely different way in dry polymer electrolytes and the herein investigated solvent-soaked porous organic species [19]. Now, if the polymeric species are disordered, one can expect a pore growth on the microscopic scale. Such pore growth would increase the effective diffusion coefficient and therefore improve the migration in terms of short distance ion mobility, which is obtained in EIS at high frequencies. The counterpart is the long time polarization e.g. during CV cycling, which might order the species. A tight orientation would reduce local pore sizes and appear as a reduction of effective mobility. The presented results of the high-potential SEI indicate that the structural changes are reversible, so that chemical changes are assumed to be negligible. The respective mechanism is schematically presented in Figure 4, where we use the poly(VC) (typical high-potential reduction product of vinylene carbonate [20]) as representative for other possibly formed long-chained polymeric species. The arrows indicate the stimulation kind (long-time or high-frequency polarization), leading to a tight or coarse-meshed orientation, affecting the ion mobility positively or negatively. If randomly oriented species are not exposed to an external field, the system relaxes and tends to parallel orientation, as it is energetically favored due to minimization of the forces between the polar $\text{C}=\text{O}$ bonds. This trend is indicated by the reversed trend induced by the rest period, which is described around Figure 5 in the SI. The pore growth would locally lead to higher porosity and lower tortuosity, which is why we obtain smaller migration resistances. On the other hand, in low-potential SEIs the porous layer consists of different organic species, which cannot form local pores of significant size even when being disordered. In our previous publication we suggested that during the second SEI formation step at ~ 400 mV vs. Li/Li^+ organic chain shortening reactions could take place [12]. The longer the chains of the linear-like organic species in the porous SEI, the more likely it becomes that porosity and tortuosity depend on the molecule orientation. Therefore, a possible reorientation of organic SEI species on low-potential SEIs might be negligible and thus is not observable in the EIS experiments.

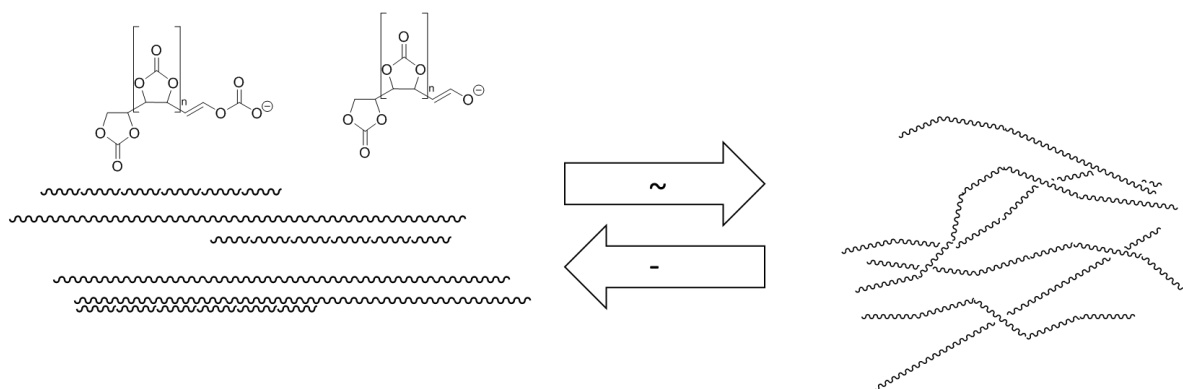


Figure 4: Schematic representation of the influence of the reversible structural changes of the outer porous SEI when formed at high potentials, represented by the poly(VC). Arrows indicate the changes of high-frequent or long-time polarization, respectively.

At this stage it is not clear, which physical driving force induces the reorientation. One would suggest the reorientation of asymmetrical polar SEI species, which are randomly arranged by an alternating, though realigned by a continuous electric field. Though, only short (porosity and tortuosity unaffected) asymmetrical species like LMC are reasonable [21]. Furthermore, typically co-occurring symmetrical polar species like LEDC should not be sensitive to an electric field unpolung at all [21]. We rather support the hypothesis that the relatively big Fc/Fc^+ and solvated Li^+ complexes force long-chained species to align in parallel while continuously migrating in one direction and to realign randomly when vibrating locally in a high-frequency field. In order to have a further indication for the plausibility of this mechanism, it is helpful to approximate the ionic vibration distance: How far do ions roughly move during the EIS experiments and how is it comparable to a typical poly(VC) length? The vibration distance approximation assumptions are presented in the SI and result into orders of magnitude from μm to sub- μm while going from middle to high EIS frequencies. On the other hand, each poly(VC) segment has a length of two C-C bonds with $\sim 150 \text{ pm}$ each. Assuming a typical unipolar polymer chain length of 10.000 repeating units [22,23], the respective polymer lengths would as well be in the μm region. In our eyes it appears reasonable that a movement of ions over distances of several polymer lengths forces the polymers to align in parallel to the movement driving force, which would be the electric field perpendicular to the electrode. Contrariwise, the ionic movement in the sub- μm length scale could push the polymers apart and provoke the coarse-meshed matrix presented in Figure 4. Although the consideration is based on several assumptions, it gives a good indication for the reasonability of the suggested model.

4. Conclusion and Outlook

In conclusion, we presented an interesting phenomenon, which underlines the different nature of high- and low-potential SEIs. The insensitivity of the low-potential SEI towards external polarization implies the finalized status of the low-potential SEI. On the other hand, the structural instability of the high-

potential SEI, particularly of the outer porous layer, give rise to a completely novel approach in SEI formation procedures. The presented model could be also applicable to Li^+ migration in the absence of Fc/Fc^+ and on composite carbon electrodes. If so, the reorientation could have a significant impact on the stability and Li^+ conductivity of the later formed final SEI. Results give rise to future investigations on the field of high-potential SEI engineering, which was already successfully published in reference [24].

5. Acknowledgements

We thank Prof. Brett Lucht (University of Rhode Island) for his comments and ideas on the reorientation driving forces.

6. References

- [1] D. Andre, S.-J. Kim, P. Lamp, S.F. Lux, F. Maglia, O. Paschos, B. Stiaszny, *J. Mater. Chem. A* 3 (2015) 6709–6732.
- [2] P. Verma, P. Maire, P. Novak, *Electrochim. Acta* 55 (2010) 6332–6341.
- [3] M.B. Pinson, M.Z. Bazant, *J. Electrochem. Soc.* 160 (2013) A243–A250.
- [4] J. Vetter, P. Novak, Wagner, C. Veit, K.-C. Möller, J.O. Besenhard, M. Winter, M. Wohlfahrt-Mehrens, C. Vogler, A. Hammouche, *J. Power Sources* 147 (2005) 269–281.
- [5] M. Winter, W.K. Appel, B. Evers, T. Hodal, K.-C. Möller, I. Schneider, M. Wachtler, M.R. Wagner, G.H. Wrodnigg, J.O. Besenhard, *Monatsh. Chem.* 132 (2001) 473–486.
- [6] M. P. Mercer, H. E. Hoster, *Nano Energy* 29 (2016) 394–413.
- [7] N.M. Markovic, *Surf. Sci. Rep.* 45 (2002) 117–229.
- [8] D. Strmcnik, I.E. Castelli, J.G. Connell, D. Haering, M. Zorko, P. Martins, P.P. Lopes, B. Genorio, T. Østergaard, H.A. Gasteiger, F. Maglia, B.K. Antonopoulos, V.R. Stamenkovic, J. Rossmeisl, N.M. Markovic, *Nat. Catal. (Nature Catalysis)* 1 (2018) 255–262.
- [9] S. Shi, P. Lu, Z. Liu, Y. Qi, L.G. Hector, H. Li, S.J. Harris, *J. Am. Chem. Soc.* 134 (2012) 15476–15487.
- [10] H.E. Hoster, *Nat Catal* 1 (2018) 236–237.
- [11] A. Wang, S. Kadam, H. Li, S. Shi, Y. Qi, *npj Comput Mater* 4 (2018) 15–40.
- [12] B.K. Antonopoulos, F. Maglia, F. Schmidt-Stein, J.P. Schmidt, H.E. Hoster, *Batteries & Supercaps* (2018) doi: 10.1002/batt.201800029.
- [13] M. Tang, J. Newman, *J. Electrochem. Soc.* 159 (2012) A1922–A1927.
- [14] J. Ma, L. Seidl, W. Ju, E. Mostafa, L. Asen, S. Martens, U. Stimming, O. Schneider, *ECS Trans.* 64 (2014) 407–423.
- [15] D. Aurbach, K. Gamolsky, B. Markovsky, Y. Gofer, M. Schmidt, U. Heider, *Electrochim. Acta* 47 (2002) 1423–1439.

- [16] H. Ota, K. Shima, M. Ue, J.-i. Yamaki, *Electrochim. Acta* 49 (2004) 565–572.
- [17] D. Aurbach, M.D. Levi, E. Levi, H. Teller, B. Markovsky, G. Salitra, U. Heider, L. Heider, J. *Electrochem. Soc.* 145 (1998) 3024–3034.
- [18] Y. Yamada, K. Miyazaki, T. Abe, *Langmuir* 26 (2010) 14990–14994.
- [19] D. Golodnitsky, E. Strauss, E. Peled, S. Greenbaum, J. *Electrochem. Soc.* 162 (2015) A2551-A2566.
- [20] B. Zhang, M. Metzger, S. Solchenbach, M. Payne, S. Meini, H.A. Gasteiger, A. Garsuch, B.L. Lucht, *J. Phys. Chem. C* 119 (2015) 11337–11348.
- [21] M. Nie, D. Chalasani, D.P. Abraham, Y. Chen, A. Bose, B.L. Lucht, *J. Phys. Chem. C* 117 (2013) 1257–1267.
- [22] P. Smith, P.J. Lemstra, J.P.L. Pijpers, A.M. Kiel, *Colloid Polymer Sci* 259 (1981) 1070–1080.
- [23] M.G.M. Knaus, M.M. Giuman, A. Pöthig, B. Rieger, *Journal of the American Chemical Society* 138 (2016) 7776–7781.
- [24] B.K. Antonopoulos, C. Stock, F. Maglia, H.E. Hoster, *Electrochim. Acta* 269 (2018) 331–339.
- [25] O. Borodin, G.D. Smith, *The journal of physical chemistry. B* 113 (2009) 1763–1776.

7. Supplementary Information

7.1. Temperature & Time Dependency

In order to understand whether the semicircle shrinking observed during consecutive measurements simply depends on time, a new measurement sequence was performed in which the blue series presented in Figure 2 was followed by two more consecutive EIS series, as shown in Figure 5. For better comparison, the blue series from Figure 2 is also re-plotted in this diagram. Again, the arrow indicates the total experiment direction. Contrary to the blue and green series, spectra of the pink series were obtained with an intermediate waiting time of 1 h. After that, we obtained the green series consisting again of directly consecutive spectra. The trend of shrinking semicircles remains and does not depend on rest periods between the single EIS experiments. On the contrary, a slight increase can be observed as an effect of the rest period, indicating a possible relaxation of the mechanism responsible for the semicircle shrinkage. The sample temperature was set to 20 °C constantly with the respective temperature sensor countersteering any temperature deviations close to the sample. Therefore, we assume the temperature has remained constant within the little margin of error of the sensor throughout the whole experiment series. This proves, that the shrinking trend is neither time nor temperature driven.

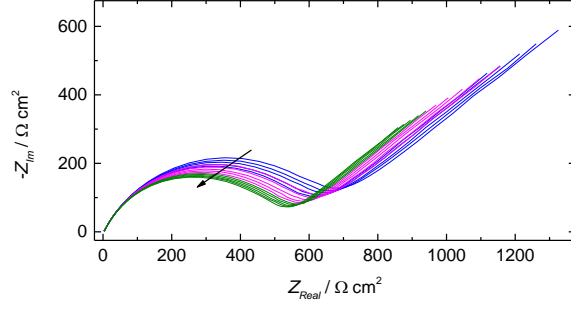


Figure 5: Impedance spectra presented as Nyquist plots of a high-potential SEI in Fc/Fc⁺ environment. Five consecutive spectra are presented for each series, experiment direction is indicated by the arrow. Colors: See text.

7.2. Approximation of Vibration Distance

The ion movement distance can be calculated using the frequency dependent current density $j(f)$. The total charge flux during one AC half-wave Q is

$$Q = \frac{j(f) A}{2 f} = F n$$

where A is the flux area surface, F is the Faraday constant and n the moved amount of substance. During EIS both solvated anions and cations are moved in the opposite direction, therefore all ions contribute to the current density. Although the total ion concentration c would have to be summed as 2 molar (1 mol Li⁺ and PF₆⁻ each, Fc/Fc⁺ negligible), we assume the salt to be dissociated only to a degree of 50% in the applied solvent mixture [25]. With $n = c V$ the movement distance s can be calculated using

$$s(f) = \frac{U_{eff}}{2 f Z_{Real}(f) F c}$$

with the effective voltage $U_{eff} = 10 \text{ mV}/\sqrt{2}$.

4.3. The Role of Interface in Stabilizing Reaction Intermediates for Hydrogen Evolution and SEI Formation in Aprotic Electrolyte

Status	Manuscript in preparation
Journal	-
Publisher	-
DOI	-
Authors	Castelli, Ivano E.; Strmcnik, Dusan; Zorko, Milena; Østergaard, Thomas M.; Martins, Pedro; Lopes, Pietro P.; Antonopoulos, Byron K.; Maglia, Filippo; Markovic, Nenad M.; Rossmeisl, Jan

Contributions: I.E.C. and J.R. designed and performed the calculations. D.S. P.P.L. and B.K.A. designed the experiments. D.S., M.Z., P.M. and P.P.L. performed the experiments. I.E.C., D.S., T.Ø., B.K.A., F.M., N.M. and J.R. discussed the results and wrote the paper.

Content

We investigate the SEI layer formation and related reduction reactions on the single crystal (111) facets of Au, Pt, Ir and Cu in an organic aprotic electrolyte, LP57, with LiPF₆ salt, by combining idealized experiments with realistic quantum mechanical simulations of the interface. Based on previous work it is known that the SEI layer formation under these conditions involves LiF formation accompanied with H₂ evolution. We find that the trends in measured overpotential correlates with the work function of the electrode surfaces and that the work function determines the potential for Li adsorption. The reaction path is investigated further by electrochemically open simulations suggesting that the overpotential of the reaction is related to stabilizing the active structure of the interface having Li adsorbed. The Li is needed to facilitate the dissociation of HF which is the source of hydrogen. Further experiments on the other proton sources, water and acid, show that if the hydrogen evolution involves negatively charged intermediates, F⁻ or HO⁻, a cation is needed at the interface to stabilize it. When the proton source is an acid there is no negatively charged intermediate and thus the hydrogen evolution can proceed at much lower overpotentials. This reveals a situation where the overpotential for electrocatalysis is related to stabilizing the active structure of the interface facilitating the reaction. This has implications for the SEI layer formation in Li-ion batteries and for reduction reactions in alkaline environment where there also in aqueous electrolyte can be negatively charged intermediates.

The role of interface in stabilizing reaction intermediates for hydrogen evolution and SEI formation in aprotic electrolyte.

Ivano E. Castelli,^{1,2} Dusan Strmcnik,³ Milena Zorko,³ Thomas Østergaard,¹ Pedro Martins,³ Pietro P. Lopes,³ Byron K. Antonopoulos,⁴ Filippo Maglia,⁴ Nenad Markovic,³ and Jan Rossmeisl^{1,*}

¹Nano-Science Center, Department of Chemistry, University of Copenhagen, DK-2100, Copenhagen Ø, Denmark

²Department of Energy Conversion and Storage, Technical University of Denmark, DK-2800, Kgs. Lyngby, Denmark

³Materials Science Division, Argonne National Laboratory, Argonne, IL, USA

⁴Battery Cell Technology, BMW Group, München, Germany

* e-mail: jan.rossmeisl@chem.ku.dk

Abstract:

We investigate the SEI layer formation and related reduction reactions on the single crystal (111) facets of Au, Pt, Ir and Cu in an organic aprotic electrolyte, 1M LiPF₆ in EC/EMC, by combining idealized experiments with realistic quantum mechanical simulations of the interface. In our previous work, we have established that the SEI layer formation on these systems involves LiF formation accompanied with H₂ evolution. In the present paper, we find that the measured overpotential correlates with the work function of the electrode surfaces and that the work function determines the potential for Li⁺ adsorption. The reaction path is investigated further by electrochemical simulations suggesting that the overpotential of the reaction is related to stabilizing the active structure of the interface having Li⁺ adsorbed. The Li⁺ is needed to facilitate the dissociation of HF which is the source of proton. Further experiments on the other proton sources, water and methanesulfonic acid, show that if the hydrogen evolution involves negatively charged intermediates, F⁻ or HO⁻, a cation at the interface can stabilize them and facilitate the reaction kinetics. When the proton source is an acid there is no negatively charged intermediate and thus the hydrogen evolution can proceed at much lower overpotentials. This reveals a situation where the overpotential for electrocatalysis is related to stabilizing the active structure of the interface facilitating the reaction rather than providing the reaction energy. This has implications for the SEI layer formation in Li-ion batteries and for reduction reactions in alkaline environment as well as for design principles for better electrodes.

Introduction

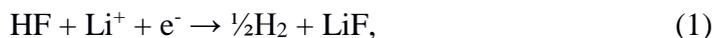
Electrocatalytic reactions are important for technologies such as batteries, fuel cells and electrolyzers. These reactions take place at the interface between an electrode and an electrolyte. Despite its importance, only little is understood regarding the relationship between reactions and interfaces at the atomic scale. This is to a large extent because the electrochemical interface is a very complex system both to characterize experimentally and to model computationally.¹⁻⁶ The reactions taking place at the interface can be influenced by the atomic and electronic structure of the electrode surface, by the electrolyte structure and electrostatic properties. It is known that the presence of covalently or non-covalently bonded species at the interface can in some cases influence the electrochemical properties.^{2,7-9} An understanding of these effects can help in designing more active and more stable materials for energy storage and conversion devices.

One of the devices that could benefit from the in-depth understanding of the electrochemical interface is the Li-ion battery (LIB). Even though the performance and safety of LIB is linked with the formation of the solid electrolyte interphase (SEI) layer on the graphite anode, a complete understanding of the nature of the SEI at the atomic scale is still missing and thus the development of electrolytes and electrodes is a matter of chemical intuition and trial and error.¹⁰⁻¹⁵ The largest challenge for more fundamental studies seems to be the high complexity of the real systems, where we encounter many undefined components of the electrochemical interface, including defects on the electrode material, impurities in the electrolyte, as well as purposefully added components that ensure proper electrical and mechanical properties of the device. In the simulations, on the other hand, it is a challenge just to include the most essential parts of the interface. Thus, there is a huge gap between the 'ideal' conditions modeled in simulations and the 'real' conditions in experiments. We aim to reduce this gap by combining experiments under idealized conditions with density function theory (DFT) simulations under conditions as realistic as possible to understand interface reactions at the atomic level.

In the present work, we investigate the hydrogen evolution reaction (HER) from different proton donors on single crystal metal surfaces in an aprotic electrolyte commonly used in LIB, consisting of a binary solvent mixture of ethylene carbonate (EC) and ethyl methyl carbonate (EMC) with lithium hexafluorophosphate (LiPF₆) salt.

We employ state of the art density function theory (DFT) simulations, to gain insight into the reduction reaction mechanisms. We use a recently developed methodology (called Generalized computational electrode) combined with ab-initio molecular dynamics (AIMD) to simulate the interface as an open system, in equilibrium with the electrochemical environment and at constant potentials relative to a computational reversible lithium electrode. The output of these simulations are phase-diagrams for the stable structure of the interface as function of the potential, the structure of the electrode surface and the composition of the electrolyte.^{16,17} The stable structures are then used to investigate trends in the reduction reactions.¹

Firstly, we investigate trends in catalytic activity for different surfaces for hydrogen evolution with HF as a proton source in an aprotic solvent. Recently, we have described the role of H₂O and HF impurities in the formation of LiF, which is one of the main SEI components,¹⁸⁻²⁰ and hydrogen evolution at the interface for different surfaces, from model (111) single crystals (Cu, Au, Pt, and Ir) to more realistic carbon systems (graphite and graphene). We have shown that the formation of LiF is caused by the electro-reduction of impurity HF, according to the reaction:



which is an exergonic reaction with an energy gain larger than 4 eV at U=0 versus Li/Li⁺.¹⁴ Based on the simulations we find that the trends in the measured overpotentials are related to stabilizing the active structure of the interface. This suggests that the ions of the electrolyte play a direct role for splitting the HF molecule.

Finally, we study the trends as the proton source is changed from HF to a weak (H₂O) or to strong (methanesulfonic, MSA) acid on Pt and Au. The experiments and simulations conclude that if the proton source leaves a negatively charged intermediate (F⁻ for HF and OH⁻ for water), the presence

¹ All calculations are carried out using the GPAW code^{32,33} for the quantum mechanics calculations and the Atomic Simulation Environment (ASE)³⁴ to handle the structures. All the computational data presented here are collected in an open source database available at the address: <https://nano.ku.dk/english/research/theoretical-electrocatalysis/katladb/>. The computational and experimental details are reported in the Supplemental Information (SI).

of Li^+ at the interface is needed to facilitate the dissociation of HF or water. If free protons are available, hydrogen is evolved at much lower overpotentials.

Results and Discussion

Figure 1a shows the cyclic voltammetry (CV) experiments of different single crystal FCC(111) surfaces, namely Cu, Au, Ir, and Pt.¹⁴ Two additional surfaces, namely the (100) and (110) terminations for Au, are added in Supplementary figure S1. Note that the shape of the CVs, which display an initial exponential current increase, followed by a sharp decrease towards 0, indicate a passivation process, consistent with our previous findings, that the impurity HF in the electrolyte is reduced to passive LiF film and hydrogen according to reaction (1). The activity for this reaction decreases in the order $\text{Ir}(111) > \text{Pt}(111) \gg \text{Au}(111) > \text{Cu}(111)$.

Descriptors for the electrochemical response

To get a hint of the reaction mechanism we correlate the potential for the measured activity with different quantities which are easily calculated. The aim is to identify possible descriptors for the measured electrochemical response, which may suggest parts of the reaction path. We define the measured electrochemical response as the potential of maximum current, see Figure 1a. We consider the species that are involved in the reaction (1), namely H^* , Li^* , F^* , and HF^* and the work function of the electrode surface. The adsorption energies are calculated for the surface in vacuum and relative to neutral reference molecule or solids. E.g. for Li it is the energy of:



Where * represents the surface. The correlation between the possible descriptors (y-axis) and the measurements (x-axis) are shown in Figure 1c.

The adsorption energies of the species involved in the HF dissociation and the LiF formation are very different in nature. H_{vac}^* adsorbs as a neutral species and forms a covalent bond with the metal slab while F_{vac}^* and Li_{vac}^* adsorb as F^- and Li^+ , respectively, and form ionic bonds. The trends for the adsorption are thus also different. The adsorption energy of H_{vac}^* shows no-correlation with the experimental overpotential. This may be counter intuitive as it is known that the H adsorption energy is a good descriptor for HER at acidic conditions.^{21,22} In Figure 1c it is found that both the adsorption energy of Li_{vac}^* (Figure 1c.1) and the work function (Figure 1c.2) are good descriptors for the reactions, suggesting that there is a strong correlation between the two. The work function seems to determine the adsorption energies of the ions F_{vac}^* and Li_{vac}^* . For the positive charged Li_{vac}^* ion, the larger the work function, the stronger the adsorption. The opposite trend holds for adsorption of the negative F_{vac}^* ions, as shown in Figure S2. This reflects that Li_{vac}^* and F_{vac}^* adsorb as ions, whereas H_{vac}^* adsorbs as a neutral and polarizable intermediate having only little interaction with the field. The potential for the electrochemical response measured in experiments is one-to-one correlated with the adsorption energy of Li_{vac}^* and thereby to the work function of the metal and anti-correlated with the adsorption energy of F_{vac}^* . This suggest that Li_{vac}^* is important for the hydrogen evolution reaction. We would like to note that the adsorption of Li_{vac}^* is different from underpotential deposition of Li (Li UPD). At low coverages, Li is adsorbed as a positive ion, and thus the adsorption energy correlates with the work function. Once that the coverage is increased, Li will adsorb as metal, the correlation is broken, and the adsorption is now independent on the electric field. The situation is different for the adsorption of H which adsorbs as a neutral atom at a low coverage and only a higher coverage is adsorbed as a proton. We will come back to this point in the next section.

Electrolyte simulations

The electrolyte plays a crucial role for the nature of the adsorbed $\text{Li}_{\text{interface}}^*$, which is partly solvated at the surface (for simplicity, we will omit the subscript interface and indicate $\text{Li}_{\text{interface}}^*$ as Li^*). We therefore include the electrolyte explicitly in the calculations, in the way described in the Computational Methods section and in Ref ¹⁴ and ¹⁷ (for the case of water). The phase diagram of Li^* in LP57 obtained using the generalized computational electrode (GCE) combined with AIMD is shown in Figure 1b. Li^* is not present at the interface at large potential, but the coverage increases going towards lower potentials, where Li^* is found non-specifically adsorbed in the double layer. The presence of Li^* atoms is necessary to screen a change in the potential in combination with a reorientation of the dipoles of the electrolyte molecules. The situation in EC:EMC is somewhat different from liquid water as the water molecules are more mobile and have larger dipoles.²³ On the other hand, the situation is also different from solid oxide electrolytes, where the potential is screened only by vacancies and oxygen ions.²⁴

The adsorption potential of Li^* is the potential of the phase transition between 0 and 1 Li^* at the interface, as shown with an arrow in Figure 1b. This is the potential where



is in equilibrium. The adsorption of Li^* is mostly electrostatic, therefore it depends on the potential set up by the slab at the interface. As for the case of adsorption of Li in vacuum, Li here is present as a Li^+ ion. It has been reported that Li UPD on Au(111) is seen only at a potential of around 0.9 V vs Li/Li^+ , which is at a lower potential than the estimated adsorption potential of Li^* .^{25,26} The adsorption potential for Li^* differs from the adsorption energy in vacuum calculations as the electrolyte, potential and electrochemical environment is included in the former, but not in the latter. However, due to a similar interaction with the electrodes, these two quantities are closely related and therefore it is expected that the adsorption potential for Li^* also should correlate with the experiments.

The diagonal in Figure 1c.3 corresponds to the perfect agreement between the measured potential and the calculated potential for Li^+ -adsorption. There is a slight constant offset of $\sim 0.2\text{V}$ for Ir, Au and Cu. Pt is the only material above the diagonal. The offset is related to where we read off the experimental potential on the polarization curve (we have chosen the potential of maximum current), so a perfect quantitative agreement cannot in general be expected, however, in this case the agreement is remarkable. We will later return to Pt, which in this context is slightly out of the trend. However, the good correlation strongly indicates that the presence of Li^* at the interface is required to run the electrochemical charge transfer reactions measured in the experiments. To qualify how Li^* can participate in the reaction, the possible reaction mechanisms have to be addressed and to compare reaction paths the potential should be kept constant. In practice in the simulations, this is done by choosing different structures of the electrolyte compensating the change in the species adsorbed and their position. The rigorous way to deal with this is to use GCE and run AIMD simulations for the different adsorbate fragments in the proposed reaction paths and make a Boltzmann weighted average of structures of the electrolyte. Due to the heavy computational load of this method, a lighter version has been chosen here, for which the reaction paths have been calculated for a set of different initial structures of the electrolyte at the adsorption potential of Li keeping the work function close to constant.

Figure 1d shows the calculated energetics of possible reaction paths for the formation of LiF and H_2 molecule. To the left the reference state $\text{Li}(\text{s})$, $\text{HF}(\text{sol})$ and the clean slab, $*$, is shown. This state corresponds to potential 0V versus Li/Li^+ . The next state is $\text{Li}^+ + \text{e}^- + \text{HF}(\text{sol}) + *$ at the adsorption potential of Li^* for the different surfaces. Here, we assume that $\text{HF}(\text{sol})$ is in equilibrium with HF^* and, as we are at the adsorption potential of Li, that Li^+ is in equilibrium with Li^* . This is the initial

state of the reaction. For the two first states, the potential vs. Li/Li^+ can be read off at the y-axis to the right.

When Li and HF are adsorbed, $\text{Li}^* + \text{HF}^*$, two different paths can be followed: In one case, HF dissociates alone (indicated with a dashed line as $\text{Li}^* + \text{H}^* + \text{F}^*$) and this is always up-hill in energy compared to the previous step in the reaction path. In the other case, HF^* first adsorbs together with Li^* , forming a LiHF complex (solid line, LiHF^*) at the surface and HF dissociates later. For all surfaces Li^* speeds up the HF dissociation reaction, as the solid lines are below the dashed lines (Figure 1d). After HF dissociation there is a LiF^* molecule at the interface and H^* adsorbed on the surface. The last step of the reaction corresponds to the formation of $\text{H}_2(\text{g})$ and $\text{LiF}(\text{s})$ in the rock salt structure.

Although the descriptors in Figure 1c, namely the adsorption energy of Li^* (Figure 1c.1), the work function of the clean slab (Figure 1c.2), and the Li adsorption potential (Figure 1c.3) are quantities that describe the LiF formation process, they do not reproduce the full picture. The activity of the surface towards the Hydrogen Evolution Reaction (HER), is not taken into account. To do this, we consider that

the energy of the initial state, $\text{Li}^+ + \text{e}^- + \text{HF}(\text{sol})$, must be high enough to overcome all the steps for LiF formations and HER (as shown in Figure 2a.1). By increasing(decreasing) the overpotential, the energy of the initial state moves up(down) towards smaller potentials versus Li/Li^+ . For all of the surface the LiHF^* complex forms spontaneously at the potential for Li adsorption suggesting that, in the presence of HF close to the surface, Li^+ is adsorbed at smaller overpotentials. This potential is probably closer to the experiments. For all the surfaces except Pt, the overpotential is determined by the presence of LiHF^* at the interface. However, for Pt, the overpotential has to be increased slightly beyond the Li^+ adsorption potential to overcome the energy of the dissociated state. This is due to relatively weak hydrogen adsorption and strong Li^+ adsorption (Figure S2). This to some extent explains why Pt is off trends when using the simple descriptors such as the work function. Comparing the calculated HER potential with experiments shows a very clear correlation, see Figure 1c.4, as said before the absolute agreements between experiments and simulations could not be expected, but we note that the trends are captured perfectly in the simulations and that Pt shows that if the hydrogen binding is weak and the work function is large the adsorption of H^* rather than the formation of the LiHF^* intermediate become potential determining. A brief discussion on this point and how can be used to identify the potential determining steps in future anode materials is included in the SI and in Figure S4. With respect to the other quantities in Figure 1c, the computational HER potential (Figure 1c.4) is not a good descriptor since it can be obtained only through full simulations of the reaction intermediates. Although, this gives the most precise picture of the process, it is complicated and tedious to calculate and it cannot be used to screen anode materials and interfaces.

In conclusion, setting up the active interface is therefore a necessity to allow for the reaction to run. This means that the electrochemical response that measures the production of H_2 molecules happens at a potential corresponding to the adsorption potential of Li^* in the presence of HF, at lower overpotentials the barrier for HF splitting leaving a F^- at the interface is too high. The reaction runs much faster if Li^* is present at the interface stabilizing the F^- ion by forming the LiHF^* intermediate.

To investigate if this effect is a prerogative of Li^+ , we have conducted experiments where the LiPF_6 salt has been substituted with NaPF_6 salt on $\text{Au}(111)$ and $\text{Pt}(111)$. The experiments show only a small constant decrease in terms of overpotential for Na compared to Li, and thus Na^* plays a similar role as Li^* for the SEI layer and H_2 formation, as reported in Figure S5. The small decrease in overpotential is consistent with the slightly lower overpotential needed for the adsorption of Na^* compared to Li^* , as indicated by the simulations This is probably related to the different solvation shell of Li^+ compared to Na^+ ²⁷ and thus that Na^* can keep more of the solvation at the interface than Li^* can.

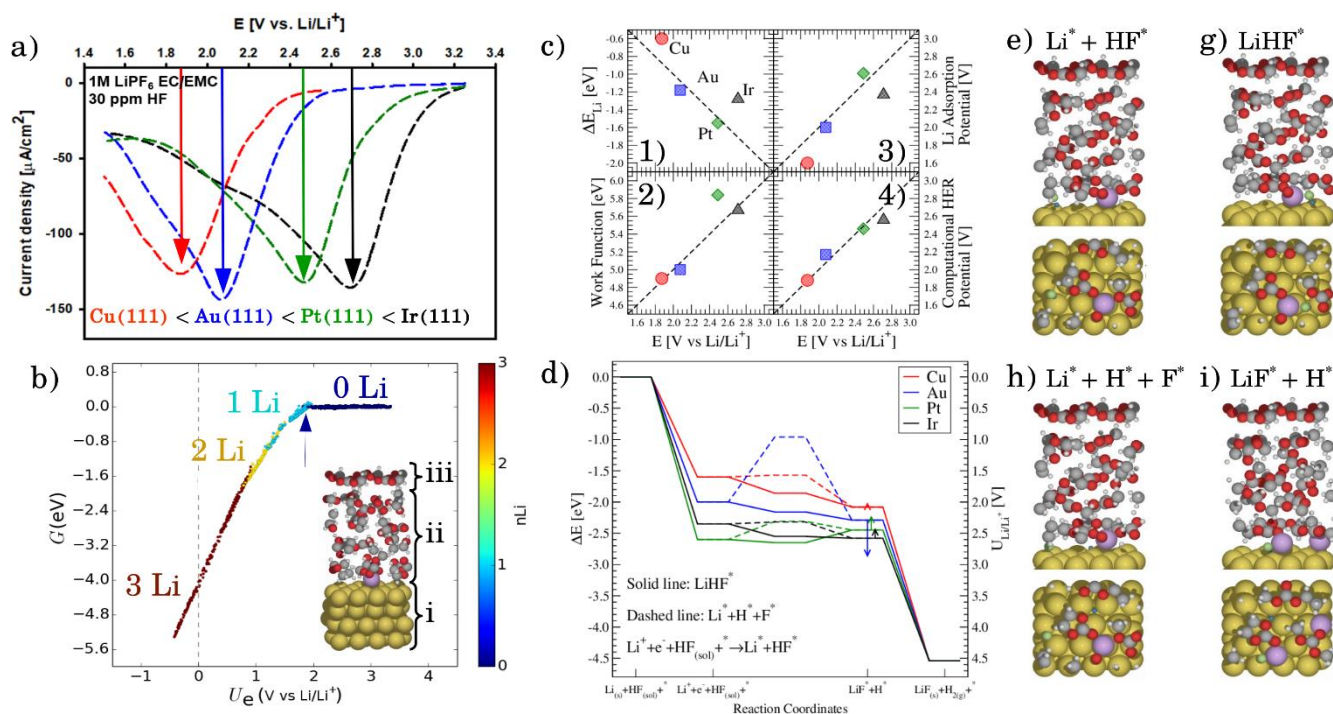
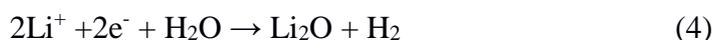


Figure 1: a) measured first electrochemical response b) phase diagram of Li in LP57 on Au111. The coverage of Li atoms is obtained by dividing n_{Li} by 16, which is the number of surface atoms. The adsorption potential of Li is indicated with an arrow. inset) structure of the simulations: H atoms are represented in white, C in gray, O in red, Au in gold, and Li in purple. Different configurations of Li (at the interface as shown here and dissolved in the electrolyte) have been considered. The arrow indicated Li adsorption potential. c) correlations between the first electrochemical response (arrows in Figure 1a) and the calculated adsorption energy of Li (Figure 1c.1, ΔE_{Li} , calculated versus slab+electrolyte and Li bulk), the work function of the clean metal slabs (Figure 1c.2), the adsorption potential of Li, i.e. the potential where Li starts to be non-specific adsorbed (Figure 1c.3, arrows from Figure 1b), and the computational HER potential (Figure 1c.4). d) reaction paths for the splitting of HF and the formation of LiF. The structures of the reaction paths are shown in Figures e-i where only the bottom layer of the electrolyte has been let free to relax, while the top three layers were kept frozen (Au atoms are reproduced in gold, H in gray (except the one participating to the reaction that is shown in blue), O in red, F in green, and Li in purple).

Trends for other proton sources.

The reaction above suggests that the stabilization by Li^* of the anion close to the negatively charged electrode surface is crucial for understanding the trend. However, this also suggests that the reaction is anion specific and that the Li^* may not be needed if there are free protons available in the electrolyte.

We consider two different proton sources added to the electrolyte: water and acid. In the case of water, the general reaction that we consider is



This can run via different pathways as shown in Figure 2a.2. Similar to the case of LiF formation (reported in Figure 2a.1 for completeness) one pathway for the dissociation of water not involving the presence of Li^* , i.e. $\text{H}_2\text{O} + \text{e}^- + * \rightarrow \text{HO}^- + \text{H}^*$. This is up-hill in energy of around 1.5 eV. In the most favorable pathway, instead, water adsorbs in a bridge position between two Li atoms, after

which, one H is transferred to the surface. H₂ is formed when this process is repeated. In the cyclicvoltammetry experiment, reported in Figure 2b, the electrochemical response corresponding to the H₂ formation from water impurities happens at a higher overpotential than the H₂ formation from HF (1.8 V vs 2.6 V in the Li/Li⁺ scale on Pt(111) respectively). A single Li* is insufficient to dissociate water. Two Li*s are needed to form a Li₂H₂O complex from which the water easily can dissociate. The formation of the Li₂H₂O complex happens at a lower potential than the formation of LiHF. Therefore, just as for HF, water needs the presence of cations at the interface to dissociate. This situation is similar to alkaline hydrogen evolution, where the proton source also is water, though the electrolyte is different. The measured potential for the HER in water correlates now with the adsorption potential of Li⁺ ions together with water (Li₂H₂O) (light blue arrows in Figure 2b) for both the investigated surfaces.

The situation is again different when free protons from a strong acid are added to the electrolyte and this corresponds to acidic hydrogen evolution reaction in the LP57 (Figure 2a.3). In this, case the reaction is simply:



The evolution of H₂ does not depend on the Li* coverage and happens at a potential close to the hydrogen evolution in acid aqueous conditions. Figure 2b shows the polarizations curves obtained in experiments for Au(111) and Pt(111), where we use the potential measured for Hsol on Pt(111) as the equilibrium potential for HER. The measured difference between Au and Pt in this case corresponds to the difference in hydrogen adsorption energy, just as has been suggested for understanding trends in HER activity in acid aqueous solutions.²⁸⁻³⁰ We note that a catalyst that cannot catalyze HER in acid cannot work in alkaline either, as all reactions paths involve the H* intermediate, so the descriptor in acid is a minimal requirement for the catalysts.³¹ The two additional reactions from water and acid confirm our reaction model. In fact, when protons are already present in the electrolyte no specific structure of the interface is needed. In the case of HF and H₂O proton sources, an overpotential is needed to obtain the active structure of the interface, to dissociate the proton source. Once that HF and H₂O are dissociated the hydrogen evolution is downhill in free energy.

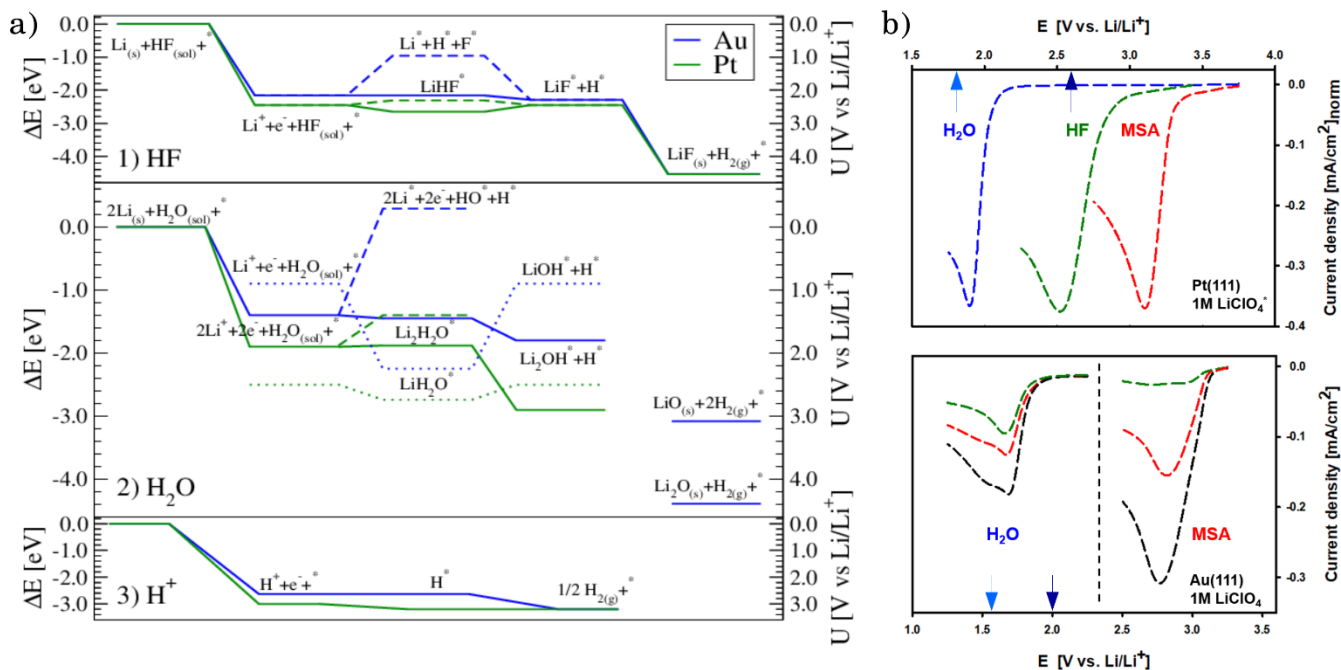


Figure 2: a) reaction paths for the three reactions considered on Au(111), in blue, and Pt(111), in green: H₂ formation from HF (1), from H₂O (2, the structures of the interface are shown in Figure S3) and from protons (3). b) Cyclic-voltammety on Pt(111) and Au(111). The two arrows in each plot indicates the adsorption potential for 1 and 2 Li (darker and lighter blue, respectively) as calculated from the AIMD simulations. It shows a good correlation between the two response peaks and these values.

Conclusion:

The SEI layer and hydrogen formation in an aprotic electrolyte, LP57, is found to be related to the formation of the active structure of the interface. The anions which are reaction intermediates need to be stabilized by a nearby cations before the proton source can dissociate near the negatively charged electrode surface. The potential for adsorbing cations directly depends on the work function of the electrode surface. This makes this catalysis very different from the HER catalysis in acidic aqueous environments, where the adsorption energy plays a much more pronounced role as a descriptor. The acidic trends can be obtained by adding a stronger acid in the electrolyte, in that case the surface catalysis determine the overpotential as no anions are intermediates.

We have used experiments made as ideal as possible, with very clean electrolytes and single crystal, single facet metal surfaces. The simulations on the other hand have been made as realistic as possible including the electrolyte, ions and potential using the generalized hydrogen electrode and ab initio molecular dynamics. We show that with this combination it is possible to bridge the gap between experiments and simulations and obtain comparisons which are close not only qualitative but also quantitative. We speculate that the effect of creating the optimal structure of the interface is general for electrocatalytic reaction where charged intermediates need to be stabilized by nearby counter ions.

References:

- (1) Holze, R. Structure of Electrified Interfaces. Herausgegeben von J. Lipkowski Und P. N. Ross. VCH Verlagsgesellschaft, Weinheim/VCH Publishers, New York, 1993. 406 S., Geb. 196.00 DM/125.00 \$. — ISBN 3- 527- 28787- 6/0- 89573- 787- 6. *Angew. Chemie* **1994**, *106* (19), 2067–2068.
- (2) Stamenkovic, V. R.; Strmcnik, D.; Lopes, P. P.; Markovic, N. M. Energy and Fuels from Electrochemical Interfaces. *Nat. Mater.* **2016**, *16*, 57.
- (3) Nørskov, J. K.; Bligaard, T.; Rossmeisl, J.; Christensen, C. H. Towards the Computational Design of Solid Catalysts. *Nat. Chem.* **2009**, *1*, 37.
- (4) Schnur, S.; Groß, A. Challenges in the First-Principles Description of Reactions in Electrocatalysis. *Catal. Today* **2011**, *165* (1), 129–137.
- (5) Taylor, C. D.; Wasileski, S. A.; Filhol, J. S.; Neurock, M. First Principles Reaction Modeling of the Electrochemical Interface: Consideration and Calculation of a Tunable Surface Potential from Atomic and Electronic Structure. *Phys. Rev. B - Condens. Matter Mater. Phys.* **2006**, *73* (16), 1–16.
- (6) Antonopoulos, B. K.; Maglia, F.; Schmidt-Stein, F.; Schmidt, J. P.; Hoster, H. E. Formation of the Solid Electrolyte Interphase at Constant Potentials: A Model Study on Highly Oriented Pyrolytic Graphite. *Batter. Supercaps* **2018**, 1–13.
- (7) Strmcnik, D.; Kodama, K.; van der Vliet, D.; Greeley, J.; Stamenkovic, V. R.; Markovic, N. M. The Role of Non-Covalent Interactions in Electrocatalytic Fuel-Cell Reactions on Platinum. *Nat. Chem.* **2009**, *1* (6), 466–472.
- (8) McCrum, I. T.; Janik, M. J. PH and Alkali Cation Effects on the Pt Cyclic Voltammogram Explained Using Density Functional Theory. *J. Phys. Chem. C* **2016**, *120* (1), 457–471.
- (9) Subbaraman, R.; Tripkovic, D.; Strmcnik, D.; Chang, K. C.; Uchimura, M.; Paulikas, a P.; Stamenkovic, V.; Markovic, N. M. Enhancing Hydrogen Evolution Activity in Water Splitting by Tailoring Li⁺-Ni(OH)₂-Pt Interfaces. *Science (80-.)*. **2011**, *334* (December), 1256–1260.
- (10) An, S. J.; Li, J.; Daniel, C.; Mohanty, D.; Nagpure, S.; Wood, D. L. The State of Understanding of the Lithium-Ion-Battery Graphite Solid Electrolyte Interphase (SEI) and Its Relationship to Formation Cycling. *Carbon N. Y.* **2016**, *105*, 52–76.
- (11) Peled, E.; Menkin, S. Review—SEI: Past, Present and Future. *J. Electrochem. Soc.* **2017**, *164* (7), A1703–A1719.
- (12) Wang, A.; Kadam, S.; Li, H.; Shi, S.; Qi, Y. Review on Modeling of the Anode Solid Electrolyte Interphase (SEI) for Lithium-Ion Batteries. *npj Comput. Mater.* **2018**, *4* (1).
- (13) Blomgren, G. E. The Development and Future of Lithium Ion Batteries. *J. Electrochem. Soc.* **2017**, *164* (1), A5019–A5025.
- (14) Strmcnik, D.; Castelli, I. E.; Connell, J. G.; Haering, D.; Zorko, M.; Martins, P.; Lopes, P. P.; Genorio, B.; Østergaard, T.; Gasteiger, H. A.; et al. Electrocatalytic Transformation of HF Impurity to H₂ and LiF in Lithium-Ion Batteries. *Nat. Catal.* **2018**, *1* (4), 255–262.
- (15) Antonopoulos, B. K.; Stock, C.; Maglia, F.; Hoster, H. E. Solid Electrolyte Interphase: Can Faster Formation at Lower Potentials Yield Better Performance? *Electrochim. Acta* **2018**, *269*, 331–339.
- (16) Rossmeisl, J.; Chan, K.; Ahmed, R.; Tripković, V.; Björketun, M. E. PH in Atomic Scale Simulations of Electrochemical Interfaces. *Phys. Chem. Chem. Phys.* **2013**, *15* (25), 10321–10325.
- (17) Hansen, M. H.; Rossmeisl, J. PH in Grand Canonical Statistics of an Electrochemical Interface. *J. Phys. Chem. C* **2016**, *120* (51), 29135–29143.
- (18) Verma, P.; Maire, P.; Novák, P. A Review of the Features and Analyses of the Solid Electrolyte Interphase in Li-Ion Batteries. *Electrochim. Acta* **2010**, *55* (22), 6332–6341.
- (19) Edström, K.; Herstedt, M.; Abraham, D. P. A New Look at the Solid Electrolyte Interphase on Graphite Anodes in Li-Ion Batteries. *J. Power Sources* **2006**, *153* (2), 380–384.

- (20) Aurbach, D. Review of Selected Electrode-Solution Interactions Which Determine the Performance of Li and Li Ion Batteries. *J. Power Sources* **2000**, *89* (2), 206–218.
- (21) Nørskov, J. K.; Bligaard, T.; Logadottir, A.; Kitchin, J. R.; Chen, J. G.; Pandelov, S.; Stimming, U. Trends in the Exchange Current for Hydrogen Evolution. *J. Electrochem. Soc.* **2005**, *152* (3), J23.
- (22) Skúlason, E.; Tripkovic, V.; Björketun, M. E.; Gudmundsdóttir, S.; Karlberg, G.; Rossmeisl, J.; Bligaard, T.; Jónsson, H.; Nørskov, J. K. Modeling the Electrochemical Hydrogen Oxidation and Evolution Reactions on the Basis of Density Functional Theory Calculations. *J. Phys. Chem. C* **2010**, *114* (42), 18182–18197.
- (23) Xu, K. Nonaqueous Liquid Electrolytes for Lithium-Based Rechargeable Batteries. *Chem. Rev.* **2004**, *104* (10), 4303–4417.
- (24) Zeng, Z.; Hansen, M. H.; Greeley, P.; Rossmeisl, J. Ab Initio Thermodynamic Modeling of Electri Fi Ed Metal – Oxide Interfaces : Consistent Treatment of Electronic and Ionic Chemical Potentials. **2014**.
- (25) Saito, T.; Uosaki, K. Surface Film Formation and Lithium Underpotential Deposition on Au(111) Surfaces in Propylene Carbonate. *J. Electrochem. Soc.* **2003**, *150* (4), A532.
- (26) Paddon, C. A.; Compton, R. G. Underpotential Deposition of Lithium on Platinum Single Crystal Electrodes in Tetrahydrofuran. *J. Phys. Chem. C* **2007**, *111* (26), 9016–9018.
- (27) Cresce, A. V.; Russell, S. M.; Borodin, O.; Allen, J. A.; Schroeder, M. A.; Dai, M.; Peng, J.; Gobet, M. P.; Greenbaum, S. G.; Rogers, R. E.; et al. Solvation Behavior of Carbonate-Based Electrolytes in Sodium Ion Batteries. *Phys. Chem. Chem. Phys.* **2017**, *19* (1), 574–586.
- (28) Breiter, M. W. Electrochemical Study of Hydrogen Adsorption on Clean Platinum Metal Surfaces. *Ann. N. Y. Acad. Sci.* **2006**, *101* (3), 709–721.
- (29) Greeley, J.; Jaramillo, T. F.; Bonde, J.; Chorkendorff, I.; Nørskov, J. K. Computational High-Throughput Screening of Electrocatalytic Materials for Hydrogen Evolution. *Nat. Mater.* **2006**, *5* (11), 909–913.
- (30) Durst, J.; Simon, C.; Siebel, A.; Rheinländer, P. J.; Schuler, T.; Hanzlik, M.; Herranz, J.; Hasché, F.; Gasteiger, H. A. Hydrogen Oxidation and Evolution Reaction (HOR/HER) on Pt Electrodes in Acid vs. Alkaline Electrolytes: Mechanism, Activity and Particle Size Effects. *ECS Trans.* **2014**, *64* (3), 1069–1080.
- (31) Sheng, W.; Myint, M.; Chen, J. G.; Yan, Y. Correlating the Hydrogen Evolution Reaction Activity in Alkaline Electrolytes with the Hydrogen Binding Energy on Monometallic Surfaces. *Energy Environ. Sci.* **2013**, *6* (6), 1509–1512.
- (32) Mortensen, J. J.; Hansen, L. B.; Jacobsen, K. W. Real-Space Grid Implementation of the Projector Augmented Wave Method. *Phys. Rev. B - Condens. Matter Mater. Phys.* **2005**, *71* (3), 1–11.
- (33) Enkovaara, J.; Rostgaard, C.; Mortensen, J. J.; Chen, J.; Dułak, M.; Ferrighi, L.; Gavnholt, J.; Glinsvad, C.; Haikola, V.; Hansen, H. a; et al. Electronic Structure Calculations with GPAW: A Real-Space Implementation of the Projector Augmented-Wave Method. *J. Phys. Condens. Matter* **2010**, *22* (25), 253202.
- (34) Hjorth Larsen, A.; JØrgen Mortensen, J.; Blomqvist, J.; Castelli, I. E.; Christensen, R.; Dułak, M.; Friis, J.; Groves, M. N.; Hammer, B.; Hargus, C.; et al. The Atomic Simulation Environment - A Python Library for Working with Atoms. *J. Phys. Condens. Matter* **2017**, *29* (27).

Supplementary Information: The role of interface in stabilizing reaction intermediates for hydrogen evolution in aprotic electrolyte.

Ivano E. Castelli, Dusan Strmcnik, Milena Zorko, Thomas Østergaard, Pedro Martins, Pietro P. Lopes, Byron K. Antonopoulos, Filippo Maglia, Nenad Markovic, and Jan Rossmeisl

Computational Methods

In this work, we have used two different computational methodologies based on Density Functional Theory (DFT) depending on the purpose of the calculations: standard DFT has been used to calculate the descriptors for the electrochemical response and the reaction paths, while ab-initio molecular dynamics (AIMD) has been used to calculate the solid/liquid interface and the phase diagrams of Li in the electrolyte. In this section, we report the computational details for the two methodologies.

All calculations have been performed using the GPAW code^{1,2} combined with the ASE package for handling the crystal structures.³ These calculations are collected in a ASE database format available online in the KatlaDB repository. [<https://nano.ku.dk/english/research/theoretical-electrocatalysis/katladb/>]

At first, we have performed standard DFT to investigate the descriptors for the electrochemical response. Even if it does not give accurate results for the electrode/electrolyte interface, this method gives valuable information that can be later on verified using AIMD. The calculations for these descriptors (figure S1) are performed using a 4x4x4 unit cells with the two bottom layers kept frozen to reproduce the bulk of the slab and the two top layer let free to relax as well as the adsorbate. We include a vacuum of 16Å to separate the periodic images in the direction normal to the surface and we apply a dipole correction to separate the contribution to the electrostatic interaction between the periodic images. We use a 4 × 3 × 1 Monkhorst-Pack k-point grid, 0.2 grid spacing, and BEEF-vdW as exchange-correlation functional.⁴ The adsorption energy, ΔE , is calculated as the difference in the DFT total energy between the surface with and without the adsorbate ($E_{\text{slab+ads}}$ and E_{slab} , respectively) minus the adsorbate in its standard state (E_{ads}):

$$\Delta E = E_{\text{slab+ads}} - E_{\text{slab}} - E_{\text{ads}}$$

As standard states for the adsorbates, we use the metal bulk reference for all the species, except for hydrogen and fluorine, for which we use H₂ and F₂ molecules, respectively.

After this preliminary investigation, we have explicitly included the electrolyte in our calculations. To investigate the structure of the interface (Figure 1b and S3), we have used ab-initio molecular dynamics (AIMD) simulations in which each step of a molecular dynamic simulation, run at room temperature, is calculated at the DFT level.⁵ All the calculations are performed in the Linear Combination of Atomic Orbitals (LCAO) mode,⁶ using double zeta polarized basis set, RPBE as exchange-correlation functional,⁷ a single K-point (gamma), and we apply the dipole correction to the electrostatic potential in the direction normal to the surface. A Berendsen thermostat,⁸ with characteristic time of 2000 fs and a time step of 1 fs, has been used to control the temperature in the molecular dynamics. To obtain the phase diagrams of Li in the electrolyte, we have to consider different initial structures, namely different possible positions and coverages of Li. In each structure, we can distinguish three regions: (i) a fixed metal slab composed of 4x4x4 unit cells, (ii) the electrolyte, and (iii) a fixed top layer of the electrolyte, as shown in the inset of figure 1b. As fixed top layer, we use the ice structure of ethylene carbonate (EC),¹⁰ with total dipole along the direction normal to the surface equal zero. The top layer has the double function of confining the electrolyte at

the correct experimental density and mimicking the electrolyte bulk structure. In addition, to not affect the orientation of the molecules, the dipole in the normal direction should be zero. The LP57 is composed of ethylene carbonate (EC) and ethyl methyl carbonate (EMC) with a ratio 3:7 in weight. This corresponds, in our simulations, to 8 molecules of EMC and 4 of EC. An example of the used structure is shown in the inset of figure 1a. The energy difference between the structures is calculated using an equivalent for Li of the generalized computational hydrogen electrode for Li. The Gibbs free energy, G , is calculated as a function of the enthalpy of the system, ΔE , and of the electronic work function (the calculated work function), U_e , with respect to the Li/Li⁺ potential, Φ : $G = \Delta E - n_{Li}(\Phi - U_e)$, where n_{Li} is the number of Li atoms in the configuration. In addition to ensure every state is visited with equal probability, we perform a quantum Monte Carlo simulation at 300 K before calculating the phase diagram. A similar procedure has been applied previously to water and to the LP57.^{5,11}

Accurate calculations have been performed on top of the various solid/liquid structures at different electrostatic potential and Li coverage. In particular, for the descriptors shown in figure 1c, we start from the structure of the electrolyte at a potential corresponding to the adsorption potential of Li, indicated with an arrow in Figure 1b. The adsorption energy ΔE_{Li} is now calculated including the electrolyte, as:

$$\Delta E_{Li} = E_{\text{slab+electrolyte+ads}} - E_{\text{slab+electrolyte}} - E_{\text{ads}}$$

This calculations have been performed in the grid mode, using RPBE, and a denser k-point grid of 2x2x1. Similar approach has been used to calculate the reaction paths shown in Figure 1d and 2a. For these calculations, the energy difference between the relevant structures is calculated simply as the difference between the total energies since all structures have the same number of atoms, just in different configurations.

Experimental Methods

Extended surface electrode preparation: Pt(111), Ir(111), Au(111), Au (110), Au (100) and Cu (111) electrodes were prepared by inductive heating for 5 min at 1,050 °C for Pt, 800 °C for Au and Cu and 1,200 °C for Ir electrodes in an argon hydrogen flow (3% hydrogen). The annealed specimens were cooled slowly to room temperature under an inert atmosphere and then assembled into a rotating disk electrode (RDE). Voltammograms were recorded in argon-saturated electrolytes.

Chemicals: For non-aqueous experiments involving HF electroreduction, LP57 (1M LiPF₆ in EC:EMC (3:7 wt)) purchased from BASF, was used. The HF content measured in LP57 was 30 ppm. Argon gas used for purging was 5N5 quality and purchased from Airgas. In experiments involving H₂O and methanesulfonic acid (MSA) as proton donors, 1M LiClO₄ (Sigma Aldrich) in EC:EMC (3:7 wt) was used. H₂O and MSA (both purchased from Sigma Aldrich) were added just before the experiment.

Electrochemical measurements: A three-electrode glass cell was used in all experiments. All of the experiments executed in this cell were performed within minutes of introducing the electrolyte into the cell. Gold wire was used as a counter electrode and Ag/AgCl or Ag/Ag⁺ electrode was used as reference electrodes for aqueous and non-aqueous experiments, respectively. All potentials are given on Li/Li⁺ scale. The conversion of Ag/Ag⁺ to Li/Li⁺ scale was done by electrodepositing and stripping Li on a glassy carbon electrode in a separate experiment, establishing the position of the Li/Li⁺ reversible potential. Experiments were controlled using an Autolab PGSTAT 302N potentiostat. For the rotating disk experiments, a Pine MSR electrode rotator was used. All reported voltammograms were first cycle measurements (unless explicitly stated otherwise) to limit the effects of possible contamination from the electrolyte. All non-aqueous electrochemical experiments were performed inside the glovebox.

Cyclic Voltammetry

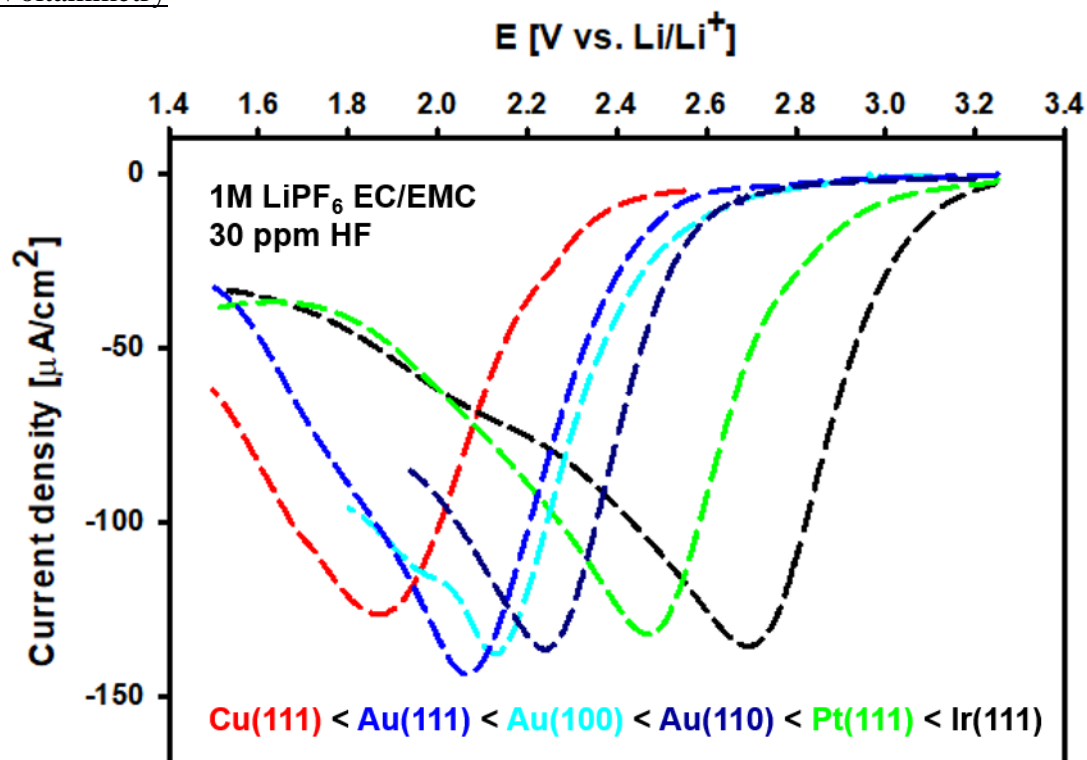


Figure S1: Measured cyclic voltammetry for LiPF₆ in Cu(111), Au(111,100, and 110), Pt(111), and Ir(111)

Descriptors for the Electrochemical Response in Vacuum

Because of the high computational cost of AIMD, the possible descriptors for the electrochemical response have been first investigated considering only the metal slab and adsorbate without electrolyte (Figure S1). The adsorption energy of H, Li, F, and HF is considered as possible descriptor for the measured first electrochemical response. Only the adsorption of Li correlates with the measured electrochemical response. This indicates that the presence of Li at the interface plays a key role in the electrochemical reactions. This correlation is valid not only for 111 terminations, but also for 100 and 110 Au surfaces. Due to the high computational cost, AIMD have not been run for these two terminations, but similar results as for 111 surfaces are expected.

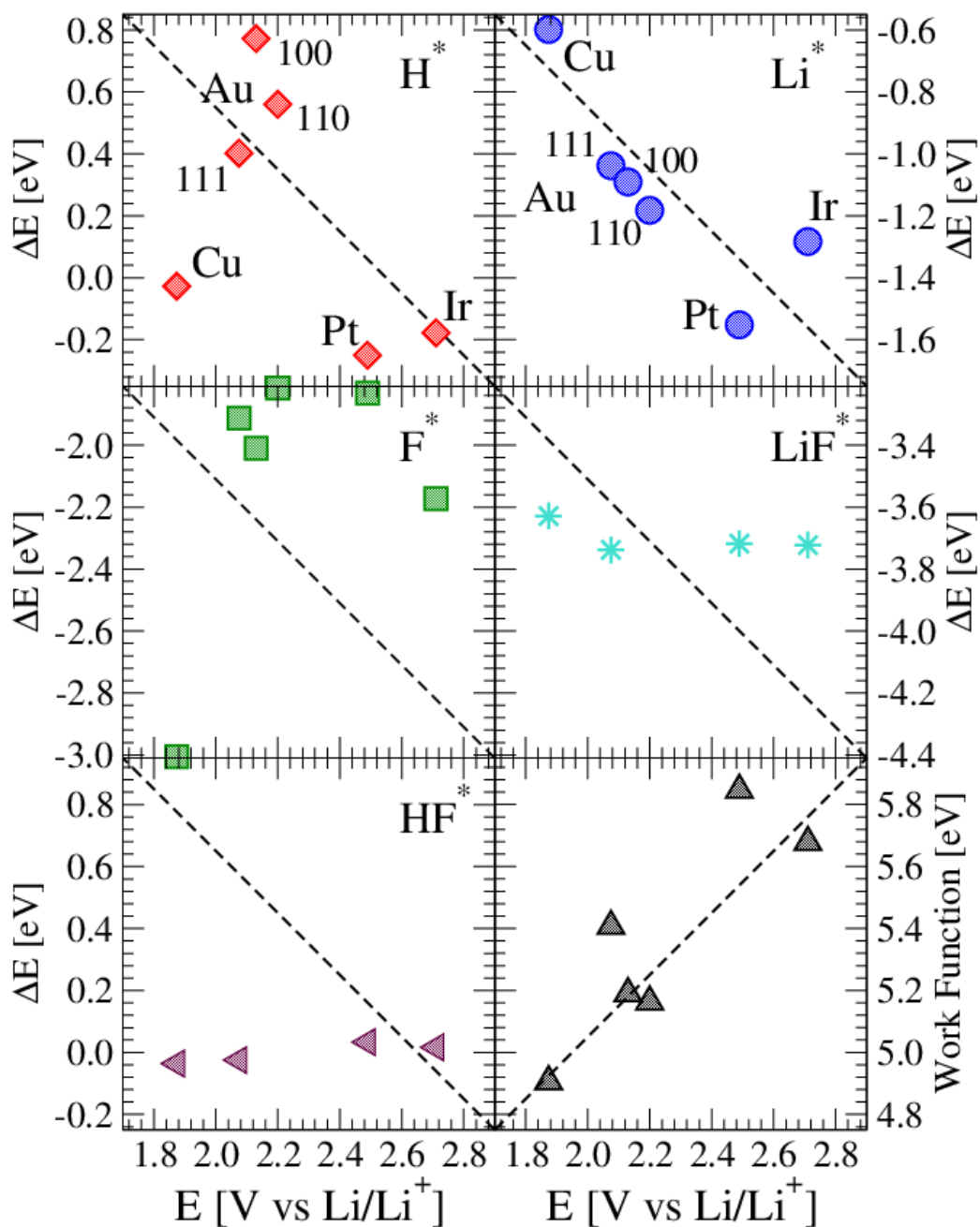


Figure S2: descriptors for the first electrochemical response in vacuum. The possible descriptors investigated here are the adsorption energy of H, Li, F, LiF, and HF as well as the work function of the clean slab.

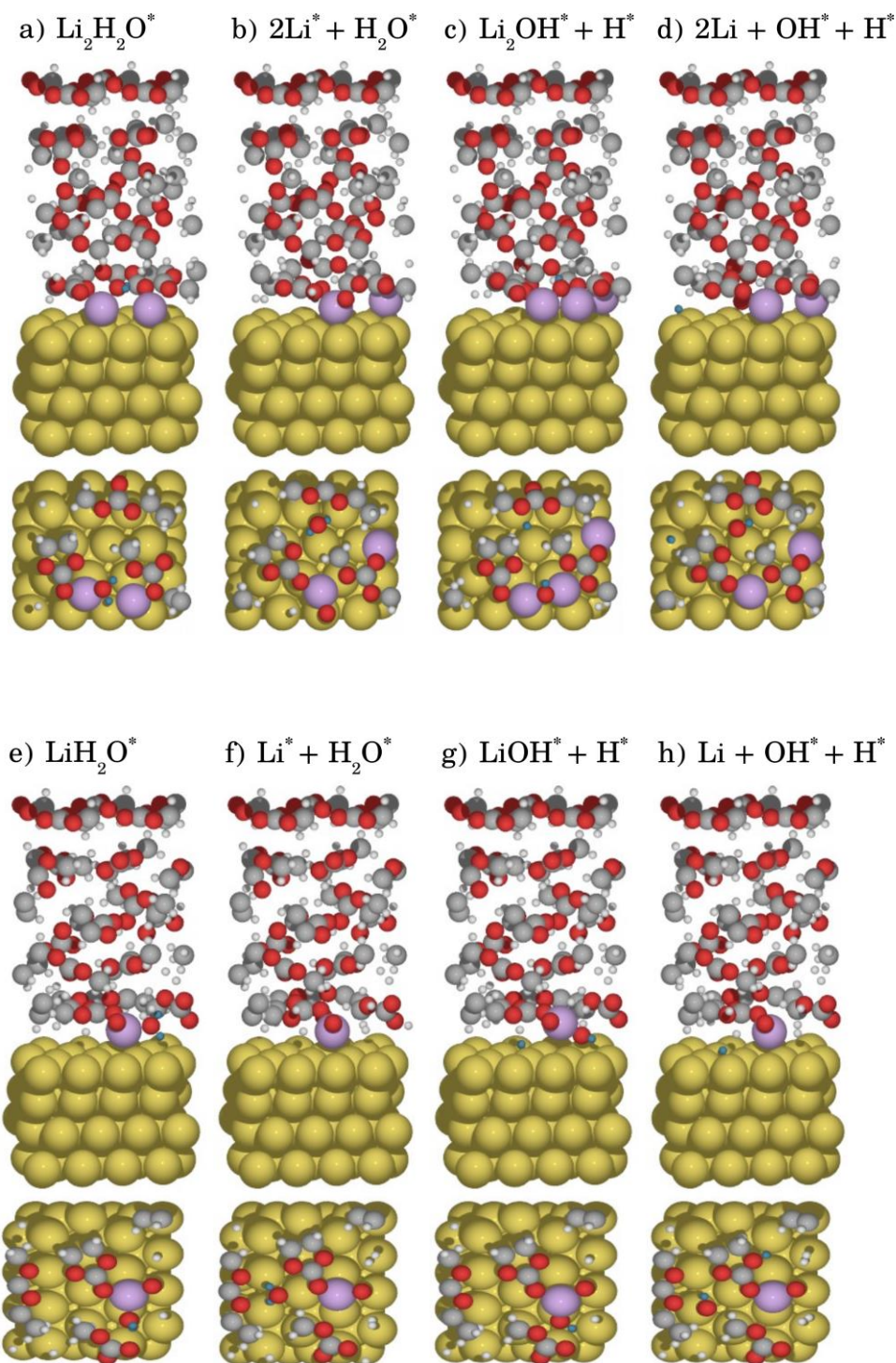


Figure S3: structures considered for the investigation of the LiO_x formation of Figure 2a,2.

Prediction of the limiting step for the LiF formation

As we have shown in Figure 2.d and explained in the “Electrolyte simulations” section, we have identified two different limiting steps for the LiF formation. On Cu, Au, and Ir, in fact, the overpotential is determined by the presence of LiHF^* at the interface, while for Pt, the adsorption of H^* is the potential determining step. To understand this, we plot the correlation between the work function and the adsorption energy of H^* (Figure S4). These two quantities are descriptors for the two relevant potential determining steps. In Figure S2, it is shown that the adsorption of LiF^* is independent from the work function and the metal surface, and thus the only relevant quantity for the $\text{LiF}^* + \text{H}^*$ level is the adsorption of H^* . For LiHF^* , instead, since it is computationally expensive to calculate the adsorption energy of LiHF^* with the correct electrolyte structure, the work function can

be used as a descriptor of the adsorption of LiHF^* . Figure S4 shows that if the energy levels of LiHF^* and $\text{LiF}^* + \text{H}^*$ are aligned (either by changing the work function or the adsorption of H^*), as indicated by the horizontal and vertical arrows, respectively, Au, Pt, and Ir lay on a line. The reason why Cu is off this line could be related with the electronic structure of the surface that make H^* weakly adsorbed. This frontier can be used to predict which potential determining step is the relevant one for the design of novel anode materials.

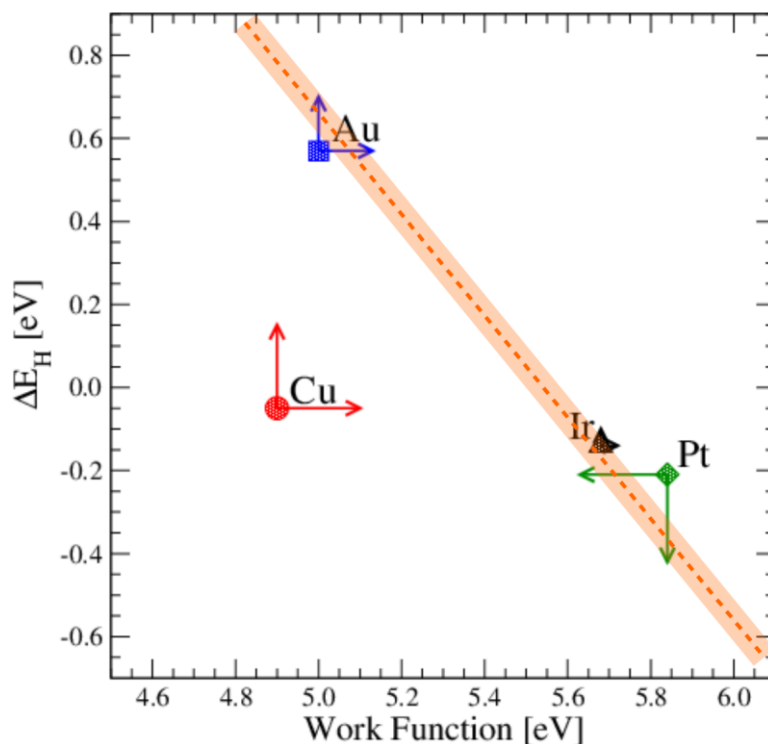


Figure S4: Correlation between the work function and the adsorption energy of H^* for the 4 surfaces considered. The arrows indicates the shift in work function or adsorption energy that is required to align the energy levels of LiHF^* and $\text{LiF}^* + \text{H}^*$ of Figure 1.d. The frontier between the two possible potential determining steps is indicated in orange.

Different cations

CV experiments and the AIMD method has been applied to the situation when NaPF_6 , instead of LiPF_6 , is used as salt. The CVs are shown in Figure S3a and the DFT phase diagrams in figure S3b. A small difference is seen between the potential of the electrochemical response corresponding to the H_2 evolution and formation of LiF and NaF , respectively, and this correlates with the simulations.

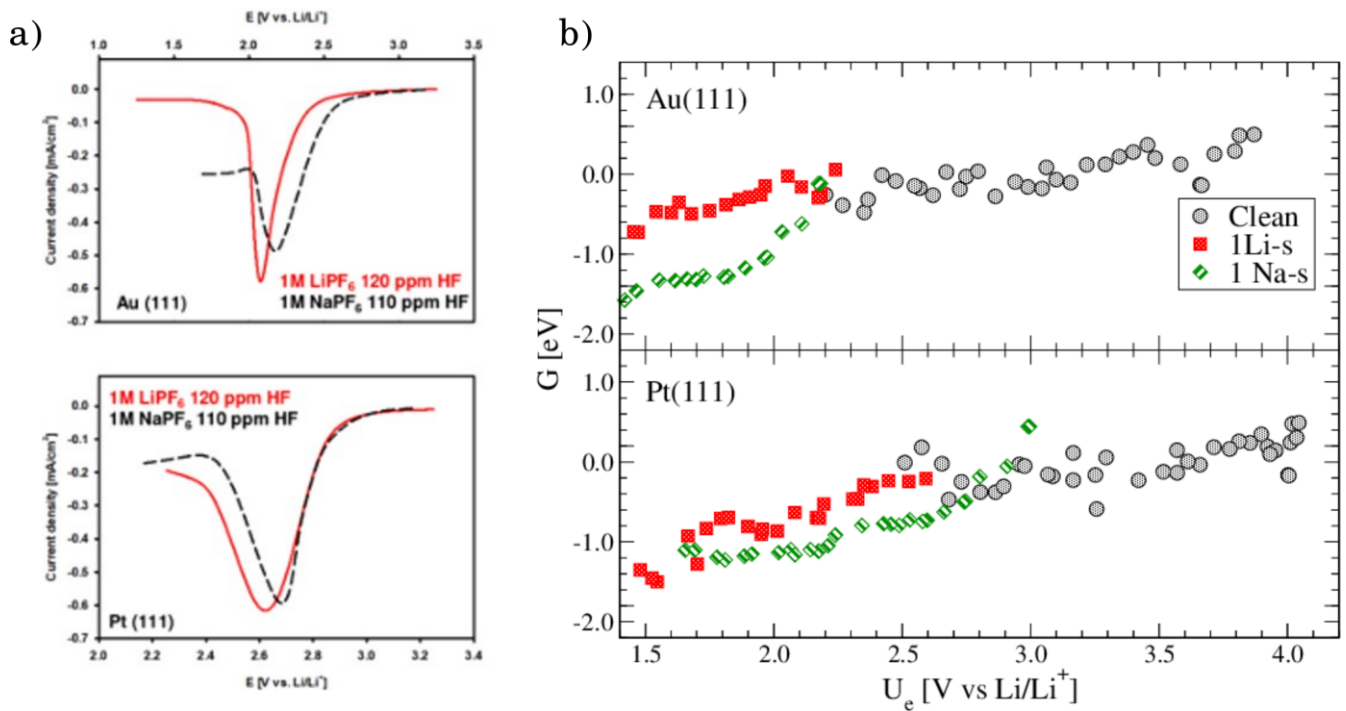


Figure S5: a) CVs of LiPF₆ and NaPF₆ on Au(111) and Pt(111), respectively. b) phase diagram of Li and Na in EC:EMC on Au(111) and Pt(111). The adsorption potential of the different cations shifts of less than 100 mV to a higher potential when Na is considered instead of Li. The potential scale for both calculations and experiments is Li/Li⁺.

- (1) Mortensen, J. J.; Hansen, L. B.; Jacobsen, K. W. Real-Space Grid Implementation of the Projector Augmented Wave Method. *Phys. Rev. B - Condens. Matter Mater. Phys.* **2005**, *71* (3), 1–11.
- (2) Enkovaara, J.; Rostgaard, C.; Mortensen, J. J.; Chen, J.; Dułak, M.; Ferrighi, L.; Gavnholt, J.; Glinsvad, C.; Haikola, V.; Hansen, H. a; et al. Electronic Structure Calculations with GPAW: A Real-Space Implementation of the Projector Augmented-Wave Method. *J. Phys. Condens. Matter* **2010**, *22* (25), 253202.
- (3) Hjorth Larsen, A.; Jørgen Mortensen, J.; Blomqvist, J.; Castelli, I. E.; Christensen, R.; Dułak, M.; Friis, J.; Groves, M. N.; Hammer, B.; Hargus, C.; et al. The Atomic Simulation Environment - A Python Library for Working with Atoms. *J. Phys. Condens. Matter* **2017**, *29* (27).
- (4) Wellendorff, J.; Lundgaard, K. T.; Møgelhøj, A.; Petzold, V.; Landis, D. D.; Nørskov, J. K.; Bligaard, T.; Jacobsen, K. W. Density Functionals for Surface Science: Exchange-Correlation Model Development with Bayesian Error Estimation. *Phys. Rev. B - Condens. Matter Mater. Phys.* **2012**, *85* (23), 32–34.
- (5) Hansen, M. H.; Rossmeisl, J. Statistical Treatment of the Aqueous Electrochemical Interface from First Principles. 1–13.
- (6) Larsen, A. H.; Vanin, M.; Mortensen, J. J.; Thygesen, K. S.; Jacobsen, K. W. Localized Atomic Basis Set in the Projector Augmented Wave Method. *Phys. Rev. B - Condens. Matter Mater. Phys.* **2009**, *80* (19), 1–10.
- (7) Hammer, B.; Hansen, L. Improved Adsorption Energetics within Density-Functional Theory Using Revised Perdew-Burke-Ernzerhof Functionals. *Phys. Rev. B* **1999**, *59* (11), 7413–7421.
- (8) Berendsen, H. J. C.; Postma, J. P. M.; Van Gunsteren, W. F.; Dinola, A.; Haak, J. R. Molecular Dynamics with Coupling to an External Bath. *J. Chem. Phys.* **1984**, *81* (8), 3684–3690.
- (9) Bunn, C. W. The Crystal Structure of Ethylene. *Trans. Faraday Soc.* **1944**, *40*, 23.

- (10) Brown, C. J. The Crystal Structure of Ethylene Carbonate. *Acta Crystallogr.* **1954**, 7 (1), 92–96.
- (11) Strmcnik, D.; Castelli, I. E.; Connell, J. G.; Haering, D.; Zorko, M.; Martins, P.; Lopes, P. P.; Genorio, B.; Østergaard, T.; Gasteiger, H. A.; et al. Electrocatalytic Transformation of HF Impurity to H₂ and LiF in Lithium-Ion Batteries. *Nat. Catal.* **2018**, 1 (4), 255–262.

5. Results and Discussion Section 2 – Transfer to Real Electrodes – Solid Electrolyte Interphase: Can faster formation at lower potentials yield better performance?

Status	Published online, 20 March 2018
Journal	Electrochimica Acta, 2018, Volume 269, 331–339
Publisher	Elsevier Ltd.
DOI	10.1016/j.electacta.2018.03.007
Authors	Antonopoulos, Byron K.; Stock, Christoph; Maglia, Filippo; Hoster, Harry E.

B.K.A., C.S., F.M. and H.E.H. conceived and designed the experiments. B.K.A. and C.S. performed the experiments. B.K.A, F.M. and H.E.H. discussed the results and wrote the paper.

Content

To make a Lithium Ion Battery (LIB) reliably rechargeable over many cycles, its graphite-based negative electrode requires the solid electrolyte interphase (SEI) as a protection layer. Core element of conventional SEI formation is a lengthy, low-current galvanostatic charging step, which due to its time consumption contributes heavily to cell manufacturing costs. Inspired by previous findings at smooth carbon model electrodes we explored new protocols to form the solid electrolyte interphase (SEI) on carbon composite electrodes in a three-electrode setup. Main motivation is to make the formation process shorter (for cost reasons) whilst maintaining or even improving the quality of the SEI.

Cyclic voltammetry showed that also for carbon composite electrodes the formation process splits into two potential regions. The electrochemical reduction reactions that contribute to SEI formation predominantly take place in the range 1.2...0.78 V vs. Li/Li⁺ (high-potential region) and 0.24...0.18 V vs. Li/Li⁺ (low-potential region). Driving the potential quickly through the high-potential region and down to the onset of the low-potential region showed much sharper Li intercalation peaks even during the first reduction sweep. We interpreted that as an indicator for better Li⁺-ion conductivity of an SEI formed predominantly at potentials < 0.24 V vs. Li/Li⁺.

Based on these insights, we tested two advanced SEI formation protocols that combine galvanostatic and potentiostatic steps and minimize “high-potential” SEI components. In subsequent galvanostatic charge/discharge cycles, the resulting electrodes showed clearly superior rate capabilities, in agreement with the expectations from the CV experiments. There was even evidence that the potential region

180...20 mV vs. Li/Li⁺ could potentially be skipped, which would save hours of time in a commercial formation process.

Based on the principles of electrochemical film growth, SEI formation at lower potentials (hence, higher overpotentials for involved electrochemical reduction steps) may occur at higher nucleation rate, thus creating more and smaller grains with more overall grain boundary regions. Such a morphology may provide more channels for Li⁺-ion transport, in analogy to the known enhanced Li⁺-ion transport along grain boundaries in the particles of positive electrode materials

A third advanced formation protocol was based on some recent empirical findings for HOPG electrodes: applying 10mV multi-frequency excitations between the high-potential and low-potential SEI formation periods, using an Electrochemical Impedance Spectroscopy instrument (“EIS formation protocol”). Similar to the other two unconventional protocols, the resulting SEI showed superior rate capability. Whilst we could only present this observation as a preliminary empirical finding, we tentatively proposed an orienting/alignment effect of the local AC field on the precursor SEI (from the high-potential region) that may eventually lead to a less entangled, more open structure to be “cured” in the subsequent low-potential region.

The presented approaches and models may inspire a new field of SEI optimization research in defined cell chemistries. Given that all three approaches seem to warrant a faster (=cheaper) formation process and/or an SEI with better Li transport properties (=more power), they should be tested at commercially produced full cells as soon as possible.



Solid electrolyte interphase: Can faster formation at lower potentials yield better performance?



Byron Konstantinos Antonopoulos^a, Christoph Stock^a, Filippo Maglia^a, Harry Ernst Hoster^{b,*}

^a BMW Group, Petuelring 130, 80788 München, Germany

^b Dept. of Chemistry, Lancaster University, Lancaster, LA1 4YB, United Kingdom

ARTICLE INFO

Article history:

Received 24 March 2017

Received in revised form

14 February 2018

Accepted 1 March 2018

Keywords:

SEI formation

Li-ion battery

Pre-charge

Composite carbon electrodes

Cyclic voltammetry

ABSTRACT

To make a Lithium Ion Battery (LIB) reliably rechargeable over many cycles, its graphite-based negative electrode requires the solid electrolyte interphase (SEI) as a protection layer. The SEI is formed through chemical and particularly electrochemical side reactions of electrolyte components in the first charging cycle(s) after manufacturing of a LIB. The SEI ideally serves two purposes: (i) act as a sieve permeable to Li ions but not to other electrolyte components and (ii) passivate the electrode against further electrolyte decomposition. Core element of conventional SEI formation is a lengthy, low-current galvanostatic charging step, which due to its time consumption contributes heavily to cell manufacturing costs. Here, we report on some non-conventional SEI formation protocols for composite carbon electrodes, inspired by recent experimental findings at smooth model electrodes. Acknowledging that the SEI forms in two main steps, taking place in a high-potential and a low-potential region, respectively, we demonstrate that less time spent in the high-potential region not only makes the process faster but even yields SEIs with superior kinetic properties. We tentatively explain this via basic rules of thin film growth and the role of grain boundaries for ion transport. We also report on the positive influence of multi-frequency potential modulations applied between high-potential and low-potential formation. Given that any new cell chemistry in principle requires its own tailor-made formation process, technologic success of future LIB cells will benefit from a systematic, well-understood toolbox of formation protocols. This paper is meant as a first step, highlighting potentially low-hanging fruits, but also flagging the demand for further systematic studies on model systems and on commercially manufactured cells.

© 2018 Elsevier Ltd. All rights reserved.

1. Introduction

The first few cycles of a Li-ion battery are referred to as the formation cycles. During these cycles, and in particular during the very first charging, a complex interplay of (electro-)chemical (side) reactions of electrolyte components creates the Solid Electrolyte Interphase (SEI) covering the surface of the negative electrode (anode). For high power/energy densities as well as a long cell lifetime, the SEI should provide good electronic insulation, fast Li⁺ conductivity and be stable under both cycling and calendar aging conditions. Core element of conventional SEI formation is a lengthy,

low-current galvanostatic charging step, which is supposed to ensure a uniform SEI structure [1–8]. On the other hand, in order to reduce manufacturing costs, formation cycles should be as simple and short as possible. From an industry perspective, these conflicting requirements make it necessary to appropriately adjust the formation protocols in order to compromise between customer expectations in terms of performance and cost [2,3,9–11]. Given that no new cell chemistry is brought to manufacturing level without fine adjustment of multiple electrolyte additives for optimized SEI formation, the formation protocols, i.e., applied currents and potentials, should deserve similar attention and possibly new approaches based on both fundamental and empirical studies.

Matsuoka et al. [12] examined the SEI formation on highly oriented pyrolytic graphite (HOPG), which served as a starting point for another recent study by our group [13,14]. This study identified a two-step formation mechanism with threshold steps occurring at

* Corresponding author.

E-mail addresses: Konstantinos.Antonopoulos@bmw.de (B.K. Antonopoulos), Christoph.Stock@bmw.de (C. Stock), Filippo.Maglia@bmw.de (F. Maglia), h.hoster@lancaster.ac.uk (H.E. Hoster).

~700 and ~400 mV vs. Li/Li⁺. The chemical nature of the SEI compact layer formed at the higher potential step (700 mV) differs significantly from that formed below 400 mV. From potentiostatic experiment current transients we concluded that both SEIs passivate the surface against ongoing SEI formation at the same potential. Hence, the low-potential (carbonate and Li containing) must SEI form through further reduction reaction of the compact high-potential SEI. Electrochemical reactions of solvent molecules only play a minor role in the second step. Under this hypothesis, the chemical and physical properties of the final SEI layer could be affected and therefore controlled by controlling the properties of the high-potential layer.

For this paper, we transferred the insights gained at low surface area carbon electrodes (glassy carbon and highly oriented pyrolytic graphite, HOPG [13,15–19]) to graphite powder based electrodes as used in commercial battery cells. Specifically, we used state-of-the-art composite electrodes in three-electrode half-cells (thus investigated only the graphite half-cell behavior) and commercially established electrolyte. We tested new protocols that make use of the separation of the formation process into a high-potential and a low-potential region, appreciating that those two regions may not be equally “valuable”. A conventional constant-current formation process does not actively manage the time spent in certain potential regions, thus possibly leaving room for improvement. Inspired by a coincidental discovery in previous Electrochemical Impedance Spectroscopy (EIS) experiments at HOPG electrodes, we also tested the influence of superimposed multi-frequency potential modulations on the SEI formation process.

The first part of this paper reports on cyclic voltammetry (CV) results that demonstrate the interplay of the high-potential and the low-potential formation regimes and their overall effect on the subsequently SEI-covered negative electrode. Based on those results, three non-conventional but still commercially applicable formation protocols are tested and benchmarked via their performance in subsequent test cycles. We observe benefits of spending less time in the high-potential regime, which we rationalize based on the principles of electrochemical film growth. Our results do not only confirm the potential technologic relevance of the previously discussed two-step SEI formation mechanism, but provide a springboard for a new formation parameter space to optimize SEI formation. This has the potential to not only speed-up the formation process in commercial cell manufacturing (where it is one of the most costly production steps [20]) but also to improve the performance of the negative electrode altogether.

2. Experimental

2.1. Setup

Investigated electrodes consisted of MAG-D20 graphite (Hitachi Chemical), 2%wt CMC/SBR binder (Dow Chemical/JSR, respectively) and 2%wt Super-C65 carbon (Timcal) as conductive agent. The demineralized water-containing slurry was coated on 10 μm thick copper foil (Schlenk) with a total loading of ~7 mg cm⁻². After pre-drying, calendaring to a porosity of 35% and punching, electrodes were finally dried at 120 °C for 12 h in a vacuum oven (~10⁻² mbar, Glass Oven B-585 Drying, Büchi Labortechnik). The electrolyte used was EC:EMC 3:7 with 2%wt VC and 1 M LiPF₆ (LP572, from BASF). Electrodes were transferred without atmosphere contact into an Argon filled glove box, where they were weighted individually for a first capacity approximation. The other cell components were cleaned with iso-propanol and demineralized water in an ultrasonic bath and then dried at 60 °C before being transferred into the glove box for cell assembly. The glove box contained <0.1 ppm water and <3 ppm oxygen. CV experiments were performed in T-

shaped ECC-Ref cells with glass fiber separator with 75 μm thickness (both from EL-Cell) soaked with 250 μl of electrolyte. The potentiostat used for CVs was a Bio-Logic VMP 3. All other experiments were performed in Swagelok type T-cells including a Celgard 2325 PP/PE separator soaked with 80 μl of electrolyte. Cells were cycled using a Maccor Series 4200 cycler. In both EL-Cells and Swagelok type cells, counter and reference electrodes were separated and made of Li foil (Alfa Aesar), thus all experiments were performed in three-electrode half-cell configuration. This ensures that any potential changes reflect changes of the graphite working electrode since they are measured against the current-free reference. Any deteriorations of the Li counter electrode, which may well occur, will demand more polarization of that electrode for any given current, but that would not affect the potential determined for the working electrode.

After cell assembly and sealing, cells rested for ~3 h before applying external currents or voltages in order to avoid poor electrode wetting.

2.2. Test protocols

If not otherwise stated, cells were formed with one of the formation protocols described in the following section. The given rates were calculated based on the electrode active mass loading and a capacity density of 360 mAh g⁻¹. After formation through one of the described protocols, the cells were stored at room temperature for another 5 days. Before being tested, cells were conditioned and the effective capacity was determined. C-rates of testing protocols and state of charge (SOC) calibration are calculated from this effective capacity. All tests were performed in a climate chamber at 25 °C. In the sections below, lithiation and delithiation of the electrode will be referred as charging and discharging, respectively.

2.2.1. Formation protocols

While the formation protocols of commercial cell production lines are kept under lock and key by the manufacturers, we have chosen a “standard formation protocol”, broadly used in laboratories and research production lines, as our benchmark [4–8]. Against that benchmark, we tested three non-conventional formation protocols (see details of all four protocols below). The latter are either inspired by our previous work [13,14] mentioned above or by CV experiments presented below. The specific fundamentals are elucidated in the respective discussion sections. Briefly, combinations of sequential high- and low-rate galvanostatic and of potentiostatic steps allow us to control the time spent in different potential regions. Furthermore, we demonstrate the effect of small potentiostatic oscillations as part of the SEI formation protocol. Unless otherwise stated, from here on all potentials are given vs. Li/Li⁺.

Fig. 1 depicts the standard benchmark and the three non-conventional formation protocols used in this study. The current rate ordinate units are shown as fractional C-rates. The dashed FC-arrows indicate that, after the profile shown in Fig. 1, further cycling (FC) is performed.

2.2.1.1. Standard formation protocol (benchmark). <i> charge at 0.1 C until potential ≤ 20 mV; <ii> maintain 20 mV until current ≤ 0.05 C; <iii> discharge at 0.1 C until potential ≥ 1.5 V. <iv> charge at 0.1C to 50% SOC (based on calculated/predicted capacity). Charging and discharging phases were separated by 20 min relaxation phases. Fig. 1 depicts only the first charging half-cycle (steps <i> and <ii>, respectively), while the FC-arrow represents the subsequent phases.

2.2.1.2. High-rate formation protocol. Similar to the standard

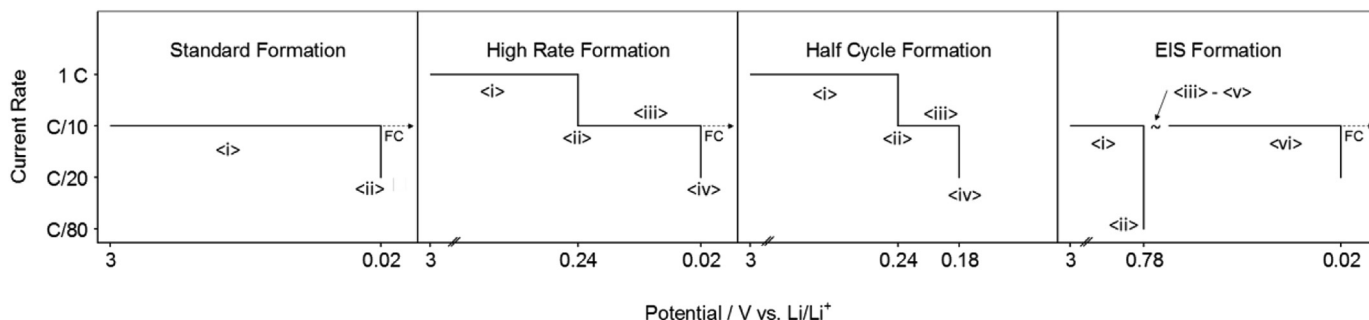


Fig. 1. Schematical representation of current profiles of the investigated formation profiles. The vertical bars are potentiostatic steps. The dashed FC-arrow indicates “further cycling” after the presented profiles. For more details see text.

formation but minimizing time spent in “high-potential” region by starting the formation with a higher charging rate: <i> charge at 1 C until potential ≤ 240 mV; <ii> maintain 240 mV until current ≤ 0.1 C; <iii> charge at 0.1 C until potential ≤ 20 mV; <iv> maintain 20 mV until current ≤ 0.05 C; <v> discharge at 0.1 C until potential ≥ 1.5 V; <vi> charge at 0.1 C to 50% SOC. Steps <iii>–<vi> are identical to the standard formation protocol.

2.2.1.3. Half-cycle formation protocol. Similar to the high-rate protocol, but terminating with a constant-voltage phase at 180 mV: <i> charge at 1 C until potential ≤ 240 mV; <ii> maintain 240 mV until current ≤ 0.1 C; <iii> charge at 0.1 C until potential ≤ 180 mV; <iv> maintain 180 mV until current ≤ 0.05 C.

2.2.1.4. EIS formation protocol. Makes use of a side-effect of potential modulations for EIS (electrochemical impedance spectroscopy, using the Bio-Logic potentiostat): <i> charge at 0.1 C until potential ≤ 780 mV; <ii> maintain 780 mV until current $\leq 32 \mu\text{A}$ ($-C/80$); <iii> open circuit potential (OCP) for 30 min; <iv> EIS cycle: potentiostatic modulation with 10 mV amplitude around OCP, using 50 logarithmically distributed frequencies in range 500 kHz ... 0.1 Hz; <v> repeat EIS cycle 50 times; <vi> transfer cell to the Maccor cyclers and apply Standard Formation Protocol.

2.2.1.5. Conditioning, SOC calculation. After applying the formation protocols and before testing the electrode performance, cells were checked for quality and the nominal capacities were re-determined. For that, the cells were charged and discharged similar to the Standard Formation Protocol for ~ 3.75 cycles: <i> charge at 0.1 C until potential ≤ 20 mV; <ii> maintain 20 mV until current ≤ 0.05 C; <iii> discharge at 0.1 C until potential ≥ 1.5 V; <iv> repeat 4 times. Charging and discharging phases were separated by 20 min relaxation phases. The last discharge capacity was used for re-determination of C-rates and calibration of the SOC scale for the testing protocols.

2.2.2. Testing protocols

2.2.2.1. Cycle aging test at 1 C. <i> charge at 1 C until potential ≤ 20 mV; <ii> maintain 20 mV until current ≤ 0.05 C; <iii> relax for 20 min; <iv> discharge at 1 C until potential ≥ 1.5 V; <v> go back to <i>.

2.2.2.2. Variable rate (0.33 ... 5 C) discharge test. <i> charge at 0.1 C until potential ≤ 20 mV; <ii> maintain 20 mV until current ≤ 0.05 C; <iii> relax for 20 min; <iv> discharge at x C until potential ≥ 1.5 V ($x = 0.33, 0.5, 1, 2, 3, 5, 0.1$); <v> relax for 20 min; <vi> repeat three times for every x, then go to next x in list.

2.2.2.3. OCP vs. SOC profiles. Charge/discharge cycles interrupted at

certain SOC values for OCP reading: <i> charge at 0.1 C until potential ≤ 20 mV, interrupted at SOC values 10, 30, 50, 70 and 90% for precise OCP reading; <ii> maintain 20 mV until current ≤ 0.05 C; <iii> relax for 20 min; <iv> discharge at 0.1 C until potential ≥ 1.5 V, interrupted at SOC values 90, 70, 50, 30 and 10% for OCP reading.

OCP reading steps: wait for stable open circuit potential ($d\text{OCP}/dt < 0.1 \text{ mV s}^{-1}$), but no longer than 60 min; then register OCP and continue with charge/discharge. The two OCP values from discharging and charging directions were averaged for each SOC.

All experiments were reproduced with three different cells to avoid conclusions based on random findings. The error bars in some of the diagrams below reflect standard deviations within those cohorts.

3. Results and discussion

3.1. Cyclic voltammetry experiments

Cyclic voltammetry (CV) is less commonly used for composite electrodes than galvanostatic methods. However, at sufficiently slow scan rates, CV scans nicely show onset and possible passivation potentials of electrochemical reactions. For an HOPG electrode, Matsuoka et al. obtained slow SEI formation CVs in a similar electrolyte as we use here (yet different solvent ratio), and identified two major reaction steps at ~ 400 and ~ 700 mV [12]. These two steps, which correspond to two different SEI formation stages, may shift by several 100 mV at other graphite materials [13,21].

To identify the position of potential steps and their relative magnitude on our electrodes, we performed formation CVs on

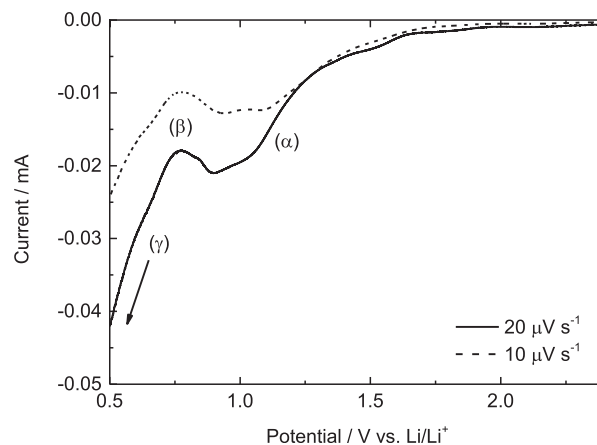


Fig. 2. High-potential region of SEI formation CVs using indicated scan rates. Full cycles are presented in the [supporting information](#). Peak assignment: see section 3.1.

freshly built cells. Starting at OCP (~ 3 V), we went down to 20 mV at a rate of 20 and 10 $\mu\text{V s}^{-1}$ and back up to 1.5 V. Fig. 2 shows the high-potential regions of the respective first negative going scans. Although not perfectly sharp, a first distinct reduction reaction is apparent in a negative peak/shoulder (α) at ~ 920 mV. The local current minimum (β) at 780 mV corresponds to the passivation potential at which the reaction is almost fully completed and further (secondary) mechanisms (γ) start taking place. This onset potential is used and discussed in the later part of this work.

Since both scan rates produced similar results, the remaining part of this section is restricted to 20 $\mu\text{V s}^{-1}$ results for the sake of brevity. In the following, the results of two related experiments will demonstrate that the time spent in the high-potential region makes a difference for the intercalation kinetics in the first scan.

Experiment 1. Fig. 3a shows the potential region <300 mV of first and third scan, in continuation of the CV plotted in Fig. 2. Table 1 lists all distinguishable peak potentials. The first and third cycle differ during the intercalation sweep (negative currents) at <210 mV: the first scan does not exhibit separable current peaks and the current keeps increasing as the scan reaches the lower potential limit. On the other hand, the third scan shows the typical graphite intercalation features, including a current drop at potentials below 50 mV due to Li^+ saturation in graphite [21–23]. The third scan exhibits three negative peaks (labelled (i), (ii), (iii)) at 179, 131 and 67 mV; the a shoulder at ~ 48 mV could be a fourth intercalation step. The small current increase at ~ 30 mV could be attributed to Li plating.

The deintercalation currents in the subsequent positive going scans split into three peaks (labelled (v), (vi), (vii)). Peak (v) is much smaller in the first cycle, but (apart from a 3 mV shift) peaks (vi) and (vii) are virtually identical for 1st and 3rd cycle (see Table 1). Those peaks reflect the known deintercalation steps of graphite [22,23]. Their presence even in the first scan demonstrates that the negative currents in the first scan must reflect Li^+ intercalation, albeit not at the potentials of peaks (i)–(iii) but shifted to more negative potentials. This causes the fourth intercalation step (shoulder in 3rd scan) to be of minor occurrence in the 1st scan, therefore the corresponding deintercalation peak (v) is small. Our chosen scan rate of 20 $\mu\text{V s}^{-1}$ is comparably low [12], hence the peak shifts are unlikely to be experimental artifacts but will rather reflect additional kinetic barriers for Li intercalation during this first negative polarization [24]. In this picture, the polarization to very low potentials (<100 mV) removes at least part of these initially inhibiting

Table 1

Potentials of CV peak maxima of the slopes presented in Fig. 3, given in mV vs. Li/Li^+ .

Exp.	Scan Rate		Intercalation Maxima				Deintercalation Maxima		
			(i)	(ii)	(iii)	(iv)	(v)	(vi)	(vii)
1	20 $\mu\text{V s}^{-1}$	1. Cycle	–	–	–	–	~ 144	207	252
		3. Cycle	179	131	67	–	141	204	250
2	5000/20 $\mu\text{V s}^{-1}$	1. Cycle	171	124	~ 55	–	149	205	250
		3. Cycle	185	135	70	36	~ 155	206	249

barriers, allowing inconspicuous Li^+ deintercalation in the subsequent reversed potential sweep and separated intercalation and deintercalation peaks in all following cycles.

Experiment 2. Given that no such first-intercalation inhibitions were reported on similar electrodes in previous works where higher formation scan rates were used [25], the long time (~ 13 h) spent in the higher potential region ($\sim 1.2 \dots 0.24$ V) is a likely reason for our observation. This is confirmed by the results of experiment 2, presented in Fig. 3b, which shows very similar data as in Fig. 3a, but without a “legacy” as produced by the 13 h spent at high potential. Here, the initial potential scan from OCP down to 240 mV was performed at 5 mV s^{-1} , which reduced the time spent in the 1.2 ... 0.24 V region to only ~ 3 min.

At such a high scan rate, the electrolyte reduction reactions are driven into diffusion limited regime, which limits the current drawn from the potentiostat and the total charge spent in the high-potential reaction. After reaching 240 mV (see steep current step in Fig. 3b: currents at 5 mV s^{-1} are out of plotted range), the scan rate is reduced to (and kept at) 20 $\mu\text{V s}^{-1}$ for the following cycles between 20 mV and 1.5 V.

In contrast to experiment 1, the shorter time spent in the high-potential regime reduced the kinetic inhibition of Li intercalation in the first negative going scan. This is apparent from the much more pronounced peaks even in the first cycle of experiment 2 (see Table 1 for peak positions), in particular peak (i) (which has the earliest onset potential). Unlike in experiment 1, all relevant features, including total charge, position of lithiation peaks (i) and (ii) (at ~ 180 and ~ 130 mV), as well as the broad lithiation peak starting at ~ 110 mV, and overall slopes of the current profiles are similar for 1st and 3rd cycle. Only differences in the first intercalation scan are negative shifts of peaks (i)–(iii) by ~ 13 mV and a not fully developed peak 4, all indicative for a minor kinetic inhibition. The

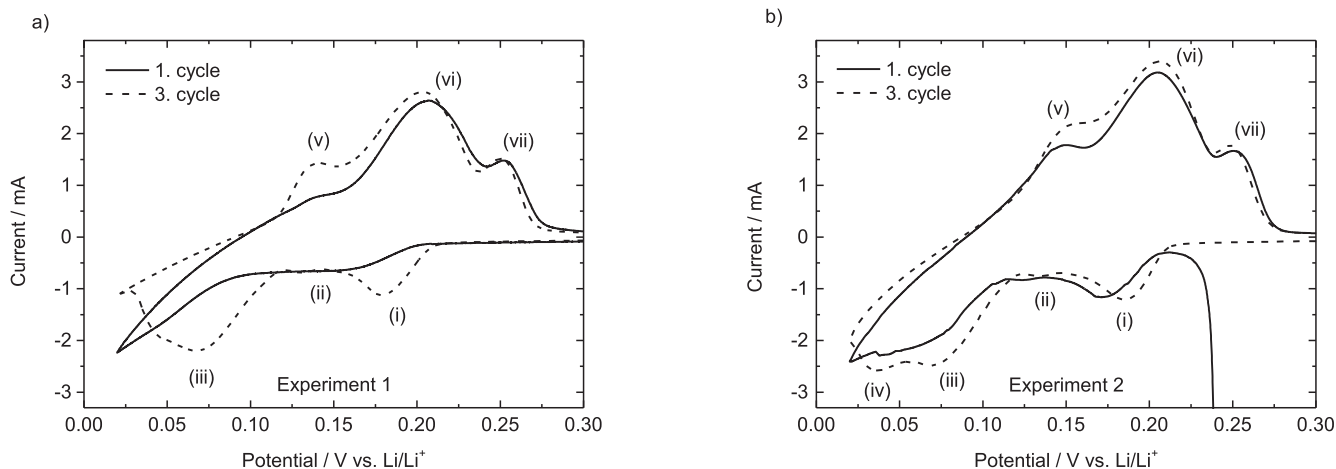


Fig. 3. Effects of spending more or less time in the high-potential region on (de-)intercalation CV features. Solid and dashed lines indicate the first and third scans, respectively, of graphite electrodes in the range 20 mV ... 1.5 V. First scan starts from OCP in negative direction (see Fig. 2) a) Scan rate 20 $\mu\text{V s}^{-1}$; b) Scan started with 5 mV s^{-1} down to 240 mV, then continued with 20 $\mu\text{V s}^{-1}$. Potential positions of numbered peaks are listed in Table 1.

deintercalation peaks (v)–(vii) are at the same positions but slightly larger in the third than in the first cycle, reflecting lower Li uptake in the first cycle but otherwise similar conditions.

Apart from those effects on the first-cycle (de-)intercalation features, the time spent in the high-potential region also influences later cycles. This is obvious when comparing the respective third cycle profiles in Fig. 3a and b. E.g., peak (iv) (at 50 mV) in Fig. 3b only appears as a “shoulder” in Fig. 3a. Since the three-electrode setup excludes contributions from other electrodes, we tentatively assign these differences to different SEIs formed depending on how much formation time is allowed in the high-potential region. The sharper and higher (de-)intercalation peaks observed in experiment 2 indicate that formation protocols with less time spent at higher potentials may produce SEIs with lower Li⁺ transport barriers. Those include ionic movement and Li⁺ desolvation.

3.2. High-rate formation protocol

Our findings in the previous section indicate advantages of spending less time in the high-potential region during SEI formation. This provides the starting point for our attempt to accelerate the formation and improve the properties of the SEI at the same time. Since formation of cells in series production is performed galvanostatically for practical reasons, we designed a specific galvanostatic protocol that causes potential profiles very similar to the dynamic CV formation of experiment 2 in the previous section (cf. Fig. 3b). This “high-rate formation protocol” differs from the standard formation protocol in one aspect: instead of a galvanostatic charge at 0.1 C all the way down to 20 mV, the cell is charged at 1 C down to 240 mV. The 10-fold higher current makes the galvanostat impose a faster negative potential sweep on the working electrode. The potential of 240 mV is kept until the current drops to 0.1 C, which is then kept galvanostatically until the potential reaches 20 mV (see Fig. 1b and related explanation for more details). Note that the potentiostatic part of this protocol is a “relaxation” step during which the current only gets smaller. In contrast to abrupt potentiostatic steps, this is technically manageable even for large capacity electrodes, whilst the time spent in the high-potential region is still short.

For the high-rate and the standard protocol, Fig. 4 shows the resulting potential profiles and the relative SOC during the respective formation processes. The relative capacities are calculated by normalizing the integrated charges to the actual electrode capacity (determined in the later conditioning step, see

experimental section), and is therefore given as SOC. As expected, due to the high current, the potential of the high-rate cell drops to the step potential of 240 mV within <3 min. In the subsequent potentiostatic step at 240 mV, the current drops to <0.1C in <5 min, indicating rather quick self-passivation of the electrolyte reduction process. Apart from those differences in the beginning, the potential profiles produced by both protocols have similar shapes. The plateaus (i), (iii) and (iv) in Fig. 4 are the galvanostatic representatives of the respectively numbered CV peaks in Fig. 3, meaning that the currents are dominated by Li intercalation, with some (capacity-wise minor) superimposed contributions from SEI formation. The three plateaus during the “high-rate formation” are higher by 10–20 mV than those of the standard formation, reflecting a lower lithiation overpotential achieved through the high-rate as compared to the standard protocol.

Fig. 5a demonstrates that also the barriers for subsequent delithiation are lower after the high-rate than after the standard formation protocol. The potential profiles from the rate discharge test show the most pronounced differences for higher C-rates: at 2 C, the charging overpotential is lower by more than 100 mV for the “high-rate” than for the “standard” SEI. Note that the OCP values from OCP/SOC show (thermodynamically) no difference for the two formation protocols, underlining that the different protocols only affect the cell kinetics combination. There is consensus that the major cause for overpotentials at the graphite negative electrode is the low Li⁺ conductivity of the SEI compact layer [26]. Since the counter electrode is irrelevant in our three-electrode half-cell setup, we conclude that the high-rate formation protocol forms an SEI with better Li⁺ conductivity and/or desolvation kinetics as compared to the standard protocol. Using 50% SOC as a comparison point, both 1 C and 2 C slopes indicate a reduction of effective SEI resistance by 27%.

To exclude the possibility that this kinetic improvement is offset by inferior long-term performance/stability, we performed cycle aging tests. Discharge capacities and coulombic efficiencies during 100 cycles are presented in Fig. 5b. The capacity is very stable at >360 mAh g⁻¹ over the whole test duration. The error bars are nearly of constant height indicating a similar aging of the three tested cells. The coulombic efficiency rises to >99.9% with negligible error bars until cycle 20, where a larger scatter in the values obtained for the cells can be observed. Overall, Fig. 5b confirms very good cycle behavior of the cells that were initiated via the high-rate formation protocol, indistinguishable from the normally formed cells (presented in SI).

3.3. Half-cycle formation protocol

As mentioned in the introduction, a key driver to try and rethink the formation process is the need to save time, i.e., saving costs in the cell supply chain. The high-rate formation protocol just demonstrated time savings via an initially high charge rate that drives the potential of the graphite electrode rapidly down to 240 mV. Apart from saving irreversible charge losses this seemed to have even improved the kinetic properties of the resulting SEI.

Appreciating that the high-rate protocol brought the formation time from >24 h down to 11 h (see Fig. 4), further time and irreversible losses could be saved by restricting the formation process to the truly relevant potential windows and by skipping the final charge/discharge cycle. Our previous experiments at HOPG surfaces confirmed previous findings that SEI formation predominantly takes place in two steps, with the second step being largely complete in the potential region >200 mV [13]. Hence, polarizing the electrode to potentials below 200 mV might not be necessary for full passivation or long-term stability. However, Fig. 4 illustrates that >9 h of the formation process are spent in that very region.

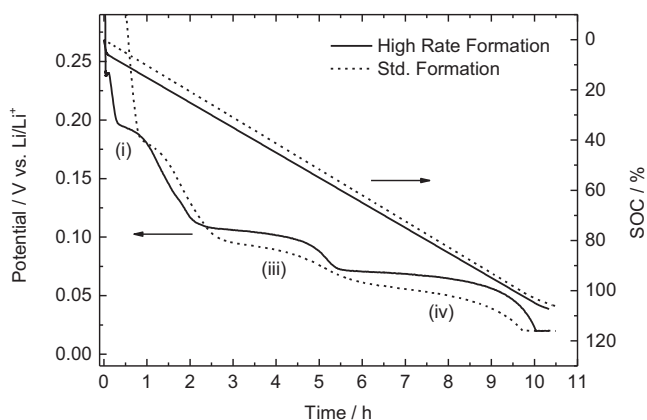


Fig. 4. Potential and normalized charge profiles during the first lithiation half-cycle of a high-rate formation protocol. For comparison, the profile during a standard formation protocol is shown. Plateaus correspond to respective lithiation peaks in Fig. 3 and Table 1.

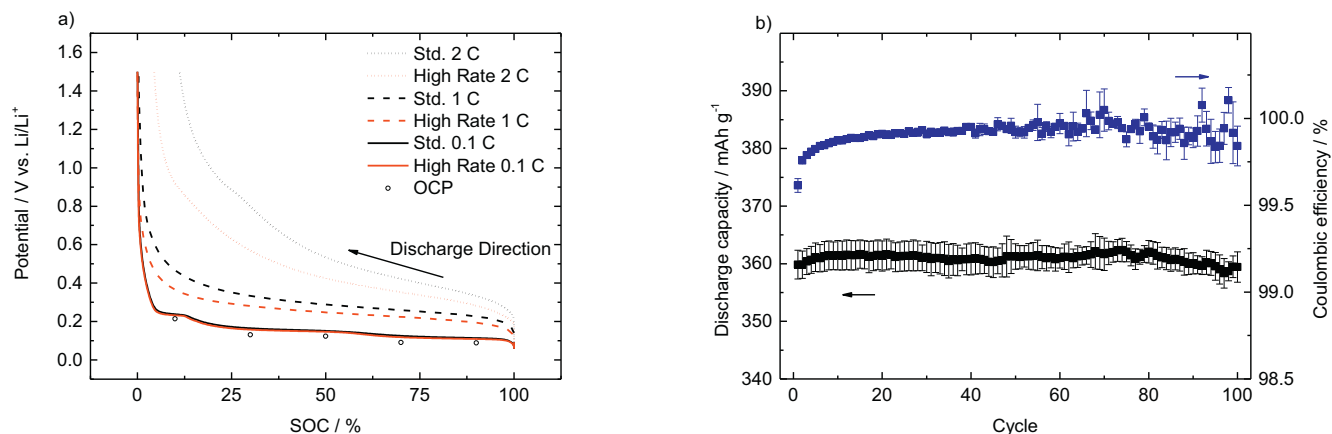


Fig. 5. a) Rate discharge potential profiles at different current rates after applying the standard or high-rate formation protocol; circles indicate the OCP at respective SOC. b) Discharge capacity and coulombic efficiency of graphite electrodes pretreated with the high-rate formation protocol during a cycle aging test.

The half-cycle formation protocol (Fig. 1c) thus stops the controlled passivation process at 180 mV instead of 20 mV. In detail: similar to the high-rate protocol, the cell is charged at 1 C until the negative electrode reaches 240 mV, where the potential is held to let the current relax down to 0.1 C. The 0.1 C current is then kept until 180 mV are reached. 180 mV are then kept until the current reaches <0.05 C.

As illustrated in Fig. 6, this process is finished after 1.2 h, including the 11 min final potentiostatic step at 180 mV until 0.05 C are reached. After that, only the OCP is recorded. The half-cycle protocol ends at the end of the first plateau (~ 190 mV), which (similar to peak (i) in the CV in Fig. 3) reflects the first stage of graphite lithiation. This is supported by the subsequent OCP value of 213 mV, which according to Fig. 5b belongs to about 10% SOC.

In the following we will test whether bringing the formation time from 27 h (standard formation plus subsequent full cycle) down to 1.2 h comes with poorer rate performance or long-term stability.

Fig. 7a (rate discharge test) shows that, for the same C-rates (0.1, 1 and 2 C), the potential profiles of the cells after half-cycle formation are very similar to those obtained for cells after high-rate formation (Fig. 5a). Accordingly, the amounts by which the discharge overpotentials are reduced are very similar, too, which

confirms the beneficial effect of spending less time in the high-potential region. The matching OCP values confirm that also this SEI formation protocol does not affect the thermodynamic electrode properties.

Cycle aging tests of the cells after the half-cycle formation protocol (Fig. 7b) show a behavior very similar to the one observed for the high-rate protocol (Fig. 5b). The capacity is initially at 360 mAh g^{-1} . The respective error bar height is constant, indicating that the cells behave similarly (note that the error bars mainly reflect systematic errors of inaccurate active masses). This is underlined by the high efficiency $>99.9\%$ and its virtually missing error bars. Discharge capacity and coulombic efficiency start dropping slightly after the 70th cycle, which leads to a loss of capacity of 3% after the 100 cycles. Here, the time saving half-cycle protocol may indeed exhibit a small weakness as compared to high-rate or standard protocol (as far as laboratory type three-electrode half-cells can tell). Comparing the coulombic efficiencies in Figs. 5a and 7a, however, it is clear that the additional hours spent in the potential region <180 mV do not visibly reduce the number of “starting” cycles required to reach $>99.9\%$.

The very time saving half-cycle protocol deserves further studies beyond laboratory three-electrode half-cells: industrially manufactured full cells may behave totally different (see also supporting information) [27,28]. Those studies will have to quantify the actual gain in performance and durability that are gained in the additional hours of the longer formation protocols.

3.4. EIS formation protocol

This third alternative formation protocol is a first step beyond the rather smooth combinations of galvanostatic and potentiostatic periods. Here, we provide preliminary evidence that a frequency stimulation (as used in electrochemical impedance spectroscopy, EIS), applied during the formation process, can also improve the kinetic properties of the SEI. Testing of this approach was inspired by a rather coincidental discovery during a model study on SEI formation on HOPG (to be published separately [14]). Previous attempts with a similar approach were published by Wang et al. [29]. In their work, a continuous charging current was supplemented by current pulses throughout the whole first charging half-cycle. However, cycling results were incoherent and strongly depended on the amplitude of the overlapping current pulses.

The EIS formation protocol (see Fig. 1d) starts and ends with the standard formation protocol. However, after reaching 780 mV (see “ β ” in Fig. 2), where in our picture the high-potential SEI is formed,

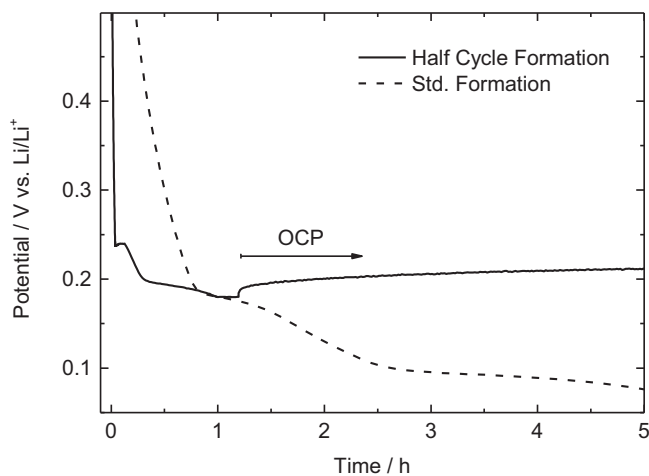


Fig. 6. Potential profile during a half-cycle formation protocol. The active operation is completed after 1.2 h, after which OCP is obtained. For comparison, the profile during a standard formation protocol is shown.

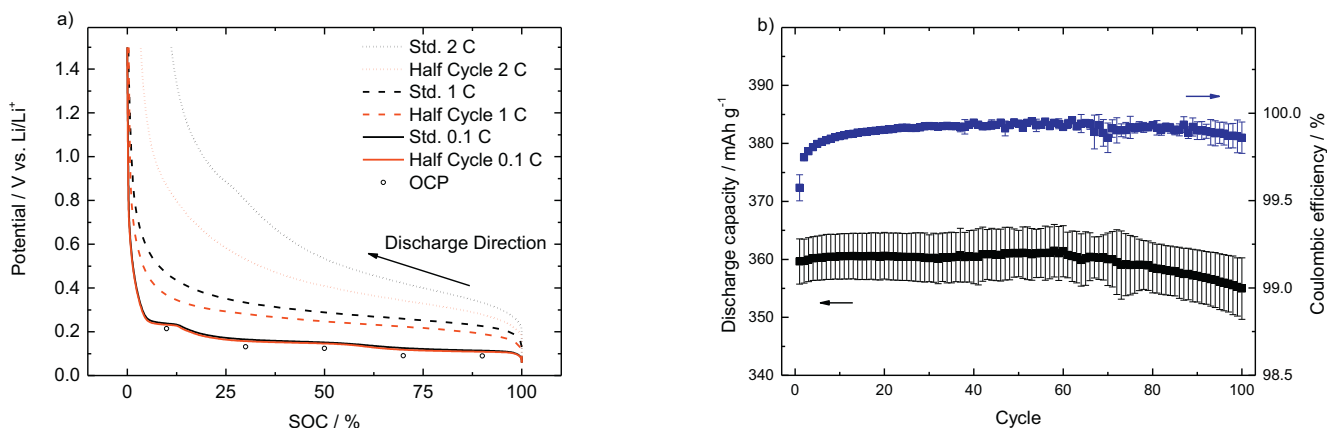


Fig. 7. a) Rate discharge potential profiles at different current rates after applying the standard or half-cycle formation protocol; circles indicate the OCP at respective SOCs. b) Discharge capacity and coulombic efficiency of graphite electrodes pretreated with the half-cycle formation protocol during a cycle aging test.

this high-potential SEI is subject to “AC treatment” (50 EIS spectra at 10 mV amplitude and 50 logarithmically distributed frequencies in range 500 kHz ... 0.1 Hz). After that, galvanostatic charging down to 20 mV is continued at 0.1 C. Prior to the EIS treatment, the potential of 780 mV is held to allow the current to relax down to C/80. (See SI for the recorded impedance spectra; note that those were not recorded at any thermodynamically well-defined potential).

Fig. 8a compares the rate performance of the resulting electrode to that achieved after the standard formation protocol at 0.1, 1 and 2 C. Again, the OCP values are not affected by the alternative treatment. The rate performance, however, shows improvements: using the overpotentials of the 1 C and 2 C profile at 50% SOC as benchmark points, the SEI resistance is reduced by 45–50%. Those improvements did not occur when the potentiostatic period at 780 mV was just followed by a long OCP phase without the additional AC excitation. Hence, the EIS treatment itself must have made the difference.

The high-potential SEI as formed at 780 mV and above is a precursor for the subsequent low-potential SEI formation, which (as discussed in the previous sections) predominantly occurs in the potential window 240 ... 180 mV. Since the AC excitation is applied around OCP, no net currents could feed any ongoing electrochemical reaction of the SEI. Given that any chemical reaction should also have happened in the control experiment without EIS, we are left with the option that the AC excitation causes physical or

structural changes to the high-potential SEI. As a working hypothesis, we suggest a re-orientation of the SEI components with respect to the graphite surface in response to the alternating near-surface electric field. If such a re-orientation includes disentangling of polymers, one could imagine a scenario where the subsequent low-potential reactions consolidate a structure that provides more/wider/better oriented/less tortuous channels for Li transport. Clearly, a better understanding and an efficient exploitation of the observed phenomena require further studies including more specific AC excitations in combination with spectroscopic analyses of the resulting SEI layers, which would be beyond the scope of this paper.

The cycle performance tests results in profiles similar to those presented above. The coulombic efficiency quickly reaches >99.9% with almost no error bars. The discharge capacity shows the possibility of extracting >360 mAh g⁻¹. The error bars are constant, indicating a similar cell behavior within the cohort. After the 60th cycle the discharge capacity starts dropping slightly while the respective error bars grow. This is coherent with the observed drop of coulombic efficiency to ~99.8%. Considering the stable discharge capacity in the cycles 20 ... 50 as a reference, the cell suffers from a capacity loss of 1.5% after 100 cycles. Here, the growth of the error bars in principle indicates a scattering of the single cell capacities, though a capacity fade is presumed as well.

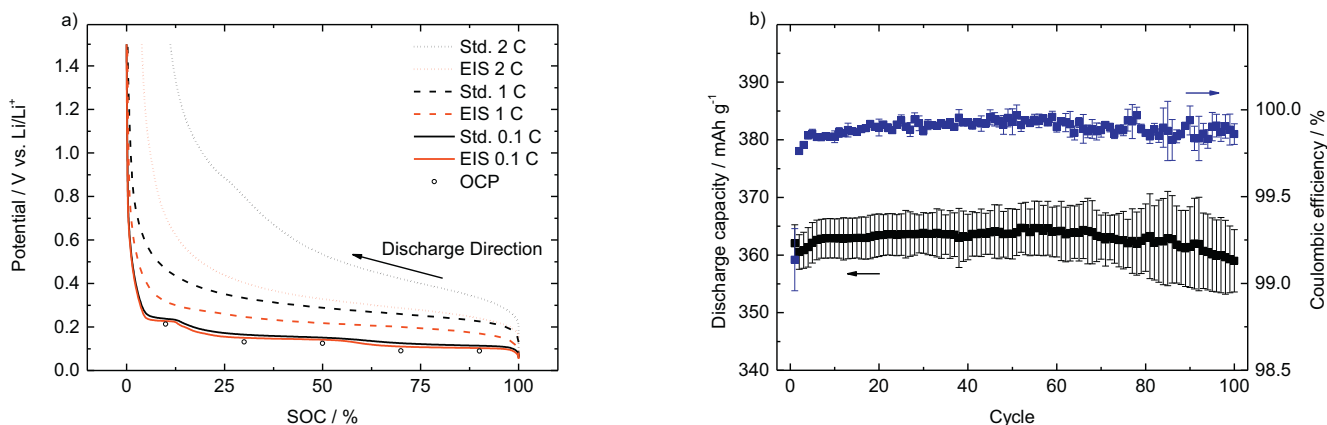


Fig. 8. a) Rate discharge potential profiles at different current rates after applying the standard or EIS formation protocol; circles indicate the OCP at respective SOCs. b) Discharge capacity and coulombic efficiency of graphite electrodes pretreated with the EIS formation protocol during a cycle aging test.

3.5. Discussion

Our results underline that the two-step SEI formation, distinguishing a high-potential and a low-potential region, is more than an academic concept and can be utilized to tune SEI properties. Cyclic voltammetry as initial SEI forming treatment showed sharper lithiation peaks if the high-potential region from OCP down to 240 mV was passed at higher rate in the very first scan. The (technically more relevant) galvanostatic high-rate and half-cycle protocols used initially high currents to make the galvanostat quickly drive the potential down to 240 mV and then continued charging the cells more slowly. Mass transport limitations allow for the “rushing” through the high-potential region without uncontrollably large currents. In comparison to the standard protocol, where a lower current keeps the electrode in the higher potential region for longer, both alternative protocols yielded to SEIs that provided the graphite electrodes with better rate capabilities.

Without direct information about structure and chemistry of the SEI after the various formation processes, we tentatively rationalize the observed behavior based on the principles of electrochemical film deposition. The electrochemical reactions contributing to SEI formation are multi-step reduction processes; hence the attempt of growing most of the SEI at less positive potentials implies growth at higher overpotentials. This comes with a higher nucleation rate and thus a higher granularity of the film [30,31]. Additionally, less positive potentials facilitate reactions with lower onset potentials, further increasing the film inhomogeneity. Grain boundaries are considered essential for ion transport at the positive electrode: For instance, Noh et al. reported that Li^+ moves faster along grain boundaries, thus leading to smaller inner-particle concentration gradients [32–34]. Going back to the negative electrodes, Li^+ has to strip off its solvation shell at the SEI compact layer in order to move through the SEI compact layer minerals at the electrode surface before intercalating [35–37]. Adapting the grain boundary concept from the positive electrode materials, grain and phase boundaries of inorganic species in the compact layer could act as ion channels, similar to the concepts discussed by Zhang et al. [38]. Li^+ moves predominantly along the phase and grain boundaries instead of through the bulk. The existence of ion channels would be compatible with the SEI microphase model, which was early proposed by Peled et al. [39] and diffusivity results by Bhattacharya et al. [40].

In this picture, the higher current and concomitantly higher SEI growth rate in the high-potential region, in combination with subsequent growth at higher overpotentials over longer periods in the low-potential region would create a more granular, open SEI with more efficient ion channels. Longer & slower growth at higher potentials, on the other hand, creates a smoother, less permeable SEI. A slow formation rate is probably only advantageous for the formation of the final compact layer, to ensure chemical passivation and long term stability.

More clarity must be provided through surface sensitive microscopy and spectroscopy on SEIs formed according to the various protocols, possibly in combination with model studies on Li^+ conductivity of different ex-situ deposited SEI layers (e.g. Li_2CO_3) with varying crystallite sizes. Ex-situ and in-situ structure analyses will also be the only way to get some understanding about the rather unexpected effects of applying 10 mV multi-frequency excitations between the high-potential and low-potential SEI formation periods, i.e., the “EIS formation protocol”.

Accepting the positive effect of the three alternative formation protocols on the Li transport kinetics of the resulting SEI, one should still highlight that all protocols yielded cells with similar cycle aging characteristics (apart from some nuances). This is in contrast to the widely accepted rule that the SEI should be formed

with slow rates to make it chemically and physically uniform [2,3]. Uniformity shall warrant a homogenous current distribution, which in turn guarantees better long-term stability.

Given the relevance of the SEI as one of the main contributors to the internal resistance of a full cell [41], we expect our findings to trigger further studies. The three-electrode half-cells allowed us to selectively study SEI formation on graphite, without overpotentials occurring at the counter electrode tampering with our working electrode potentials during formation and subsequent experiments. Experiments at such cells, however, cannot replace similar studies at technical full cells but are rather their starting point: Firstly, the cycle performances of half cells are not directly comparable to those of full cells. Capacity fading after >70 cycles could reflect degradation of the graphite working electrode but also dendrite formation at the Li counter electrode. Our cycle aging tests thus only allow us to conclude that none of the SEI formation protocols deteriorated the subsequent cycle aging in a way that would flag a principal problem of that protocol. They do not allow conclusions about formation protocols and the resulting longer-term cyclability. Secondly, we can't know what effects our alternative formation protocols would have on technical cathode materials. In summary, the work presented here motivates and informs similar experiments with commercial full cells, ideally in combination with further analytical methods including gas evolution analyses.

4. Conclusion

Inspired by previous findings at smooth carbon model electrodes we explored new protocols to form the solid electrolyte interphase (SEI) on carbon composite electrodes in a three-electrode setup, as they are used as negative electrodes in commercial lithium ion batteries. Main motivation is to make the formation process shorter (for cost reasons) whilst maintaining or even improving the quality of the SEI.

Cyclic voltammetry showed that also for carbon composite electrodes the formation process splits into two potential regions. The electrochemical reduction reactions that contribute to SEI formation predominantly take place in the range 1.2 ... 0.78 V vs. Li/Li^+ (high-potential region) and 0.24 ... 0.18 V vs. Li/Li^+ (low-potential region). Driving the potential quickly through the high-potential region and down to the onset of the low-potential region showed much sharper Li intercalation peaks even during the first reduction sweep. We interpreted that as an indicator for better Li^+ conductivity of an SEI formed predominantly at potentials <0.24 V vs. Li/Li^+ .

Based on these insights, we tested two advanced SEI formation protocols that combine galvanostatic and potentiostatic steps and minimize “high-potential” SEI components. In subsequent galvanostatic charge/discharge cycles, the resulting electrodes showed clearly superior rate capabilities, in agreement with the expectations from the CV experiments. There was even evidence that the potential region 180 ... 20 mV vs. Li/Li^+ could potentially be skipped, which would save hours of time in a commercial formation process.

Based on the principles of electrochemical film growth, SEI formation at lower potentials (hence, higher overpotentials for involved electrochemical reduction steps) may occur at higher nucleation rate, thus creating more and smaller grains with more overall grain boundary regions. Such a morphology may provide more channels for Li^+ transport, in analogy to the known enhanced Li^+ transport along grain boundaries in the particles of positive electrode materials.

A third advanced formation protocol was based on some recent empirical findings for HOPG electrodes: applying 10 mV multi-

frequency excitations between the high-potential and low-potential SEI formation periods, using an Electrochemical Impedance Spectroscopy instrument (“EIS formation protocol”). Similar to the other two unconventional protocols, the resulting SEI showed superior rate capability. Whilst we could only present this observation as a preliminary empirical finding, we tentatively proposed an orienting/alignment effect of the local AC field on the precursor SEI (from the high-potential region) that may eventually lead to a less entangled, more open structure to be “cured” in the subsequent low-potential region.

The presented approaches and models may inspire a new field of SEI optimization research in defined cell chemistries. Given that all three approaches seem to warrant a faster (=cheaper) formation process and/or an SEI with better Li transport properties (=more power), they should be tested at commercially produced full cells as soon as possible.

Acknowledgements

We acknowledge the providing of electrodes and partial cell building and testing by the technical laboratory of the BMW Group. Furthermore we would like to thank Prof. Brett Lucht (Rhode Island University) for fruitful discussions on the topic of ion channels in the SEI.

Appendix A. Supplementary data

Supplementary data related to this article can be found at <https://doi.org/10.1016/j.electacta.2018.03.007>.

References

- [1] F.M. Kindermann, P.J. Osswald, S. Klink, G. Ehlert, J. Schuster, A. Noel, S.V. Erhard, W. Schuhmann, A. Jossen, Measurements of lithium-ion concentration equilibration processes inside graphite electrodes, *J. Power Sources* 342 (2017) 638–643.
- [2] J.Q. Xu, Dynamic Formation Protocol for Lithium-ion Battery, US20150060290 (2015), (Xu, Jeff Qiang).
- [3] P.-C.J. Chiang, M.-S. Wu, J.-C. Lin, A novel Dual-current formation process for advanced lithium-ion batteries, *Electrochem. Solid-State Lett.* 8 (2005) A423.
- [4] Z. Chen, J.R. Dahn, Improving the capacity retention of LiCoO₂ cycled to 4.5 V by heat-treatment, *Electrochem. Solid State Lett.* 7 (2004) A11–A14.
- [5] M.A. McArthur, S. Trussler, J.R. Dahn, In situ investigations of SEI layer growth on electrode materials for lithium-ion batteries using spectroscopic ellipsometry, *J. Electrochem. Soc.* 159 (2012) A198–A207.
- [6] R. Jung, M. Metzger, F. Maglia, C. Stinner, H.A. Gasteiger, Oxygen release and its effect on the cycling stability of LiNi_xMn_yCo_zO₂ (NMC) cathode materials for Li-Ion batteries, *J. Electrochem. Soc.* 164 (2017) A1361–A1377.
- [7] R. Jung, M. Metzger, D. Haering, S. Solchenbach, C. Marino, N. Tsiouvaras, C. Stinner, H.A. Gasteiger, Consumption of fluoroethylene carbonate (FEC) on Si-C composite electrodes for Li-Ion batteries, *J. Electrochem. Soc.* 163 (2016) A1705–A1716.
- [8] S. Klink, W. Schuhmann, F. La Mantia, Vertical distribution of overpotentials and irreversible charge losses in lithium ion battery electrodes, *ChemSusChem* 7 (2014) 2159–2166.
- [9] P. Verma, P. Maire, P. Novak, A review of the features and analyses of the solid electrolyte interphase in Li-ion batteries, *Electrochim. Acta* 55 (2010) 6332–6341.
- [10] M. Winter, W.K. Appel, B. Evers, T. Hodal, K.-C. Möller, I. Schneider, M. Wachtler, M.R. Wagner, G.H. Wroldnig, J.O. Besenhard, Studies on the anode/electrolyte interface in lithium ion batteries, *Monatshefte fuer Chemie/Chem. Monthly* 132 (2001) 473–486.
- [11] M.B. Pinson, M.Z. Bazant, Theory of SEI formation in rechargeable batteries: capacity fade, accelerated aging and lifetime prediction, *J. Electrochem. Soc.* 160 (2013) A243–A250.
- [12] O. Matsuoka, A. Hiwara, T. Omi, M. Toriida, T. Hayashi, C. Tanaka, Y. Saito, T. Ishida, H. Tan, S.S. Ono, others, Ultra-thin passivating film induced by vinylene carbonate on highly oriented pyrolytic graphite negative electrode in lithium-ion cell, *J. Power Sources* 108 (2002) 128–138.
- [13] B.K. Antonopoulos, F. Maglia, F. Schmidt-Stein, H.E. Hoster, Chemical, Electrochemical and Physical Dependencies of the Solid Electrolyte Interphase on the Formation Potential, (in submission).
- [14] B.K. Antonopoulos, A.-C. Gentschev, F. Maglia, H.E. Hoster, The dynamic impedance properties of solid electrolyte interphase on HOPG, (in submission).
- [15] M. Tang, S. Lu, J. Newman, Experimental and theoretical investigation of solid-electrolyte-interphase formation mechanisms on glassy carbon, *J. Electrochem. Soc.* 159 (2012) A1775–A1785.
- [16] M. Tang, K. Miyazaki, T. Abe, J. Newman, Effect of graphite orientation and lithium salt on electronic passivation of highly oriented pyrolytic graphite, *J. Electrochem. Soc.* 159 (2012) A634–A641.
- [17] M. Tang, J. Newman, Electrochemical characterization of SEI-type passivating films using redox shuttles, *J. Electrochem. Soc.* 158 (2011) A530–A536.
- [18] M. Tang, J. Newman, Transient characterization of solid-electrolyte-interphase using ferrocene, *J. Electrochem. Soc.* 159 (2012) A281–A289.
- [19] M. Tang, J. Newman, Why is the solid-electrolyte-interphase Selective? Through-Film ferrocenium reduction on highly oriented pyrolytic graphite, *J. Electrochem. Soc.* 159 (2012) A1922–A1927.
- [20] P.A. Nelson, K.G. Gallagher, I. Bloom, D.W. Dees, Modeling the Performance and Cost of Lithium-ion Batteries for Electric-drive Vehicles, Argonne National Laboratory, 2012.
- [21] J. Ma, L. Seidl, W. Ju, E. Mostafa, L. Asen, S. Martens, U. Stimming, O. Schneider, Applications of ionic liquids in electrochemical energy conversion and storage, *ECS Trans.* 64 (2014) 407–423.
- [22] E. Markevich, M.D. Levi, D. Aurbach, New insight into studies of the cycling performance of Li-Graphite electrodes a combination of cyclic voltammetry, electrochemical impedance, and differential self-discharge measurements, *J. Electrochem. Soc.* 152 (2005) A778–A786.
- [23] M.D. Levi, C. Wang, D. Aurbach, Self-discharge of graphite electrodes at elevated temperatures studied by CV and electrochemical impedance spectroscopy, *J. Electrochem. Soc.* 151 (2004) A781–A790.
- [24] H. Matsuda, Y. Ayabe, Zur Theorie der Randles-Sevcikischen Kathodenstrahl-Polarographie, *Zeitschrift für Elektrochemie, Ber. Bunsen Ges. Phys. Chem.* 59 (1955) 494–503.
- [25] H. Ota, Y. Sakata, A. Inoue, S. Yamaguchi, Analysis of vinylene carbonate derived SEI layers on graphite anode, *J. Electrochem. Soc.* 151 (2004) A1659–A1669.
- [26] J.-K. Park (Ed.), Principles and Applications of Lithium Secondary Batteries, first ed., Wiley-VCH Verlag GmbH & Co. KGaA, 2012.
- [27] G. Amatucci, A. Du Pasquier, A. Blyr, T. Zheng, J.-M. Tarascon, The elevated temperature performance of the LiMn₂O₄/C system: failure and solutions, *Electrochim. Acta* 45 (1999) 255–271.
- [28] H. Ota, K. Shima, M. Ue, J.-i. Yamaki, Effect of vinylene carbonate as additive to electrolyte for lithium metal anode, *Electrochim. Acta* 49 (2004) 565–572.
- [29] F.-M. Wang, H.-Y. Wang, M.-H. Yu, Y.-J. Hsiao, Y. Tsai, Differential pulse effects of solid electrolyte interface formation for improving performance on high-power lithium ion battery, *J. Power Sources* 196 (2011) 10395–10400.
- [30] L. Guo, P.C. Seardon, On the influence of the nucleation overpotential on island growth in electrodeposition, *Electrochim. Acta* 55 (2010) 4086–4091.
- [31] A. Rinaldi, O. Wijaya, H. Hoster, Lithium-oxygen cells, *ChemElectroChem* 3 (2016) 1944–1950.
- [32] H.-J. Noh, Z. Chen, C.S. Yoon, J. Lu, K. Amine, Y.-K. Sun, Cathode material with nanorod structure—an application for advanced high-energy and safe lithium batteries, *Chem. Mater.* 25 (2013) 2109–2115.
- [33] H.-J. Noh, J.W. Ju, Y.-K. Sun, Comparison of nanorod-structured Li[Ni_{0.54}Co_{0.16}Mn_{0.30}]O₂ with conventional cathode materials for Li-ion batteries, *ChemSusChem* 7 (2014) 245–252.
- [34] D. Andre, S.-J. Kim, P. Lamp, S.F. Lux, F. Maglia, O. Paschos, B. Stiaszny, Future generations of cathode materials: an automotive industry perspective, *J. Mater. Chem. A* (2015) 6709–6732.
- [35] C. Julien, Z. Stoyanov, Materials for Lithium-ion Batteries, Springer Netherlands; Imprint; Springer, Dordrecht, 2000.
- [36] P.B. Balbuena, Y. Wang, Lithium-ion Batteries: Solid-electrolyte Interphase, Imperial College Press, London, 2004.
- [37] R.T. Jow, K. Xu, O. Borodin, M. Ue (Eds.), Electrolytes for Lithium and Lithium-ion Batteries, Springer, New York, 2014.
- [38] B. Zhang, M. Metzger, S. Solchenbach, M. Payne, S. Meini, H.A. Gasteiger, A. Garsuch, B.L. Lucht, Role of 1,3-propane sultone and vinylene carbonate in solid electrolyte interface formation and gas generation, *J. Phys. Chem. C* 119 (2015) 11337–11348.
- [39] E. Peled, D. Golodnitsky, G. Ardel, Advanced model for solid electrolyte interphase electrodes in liquid and polymer electrolytes, *J. Electrochem. Soc.* 144 (1997) L208–L210.
- [40] S. Bhattacharya, A.T. Alpas, Micromechanisms of solid electrolyte interphase formation on electrochemically cycled graphite electrodes in lithium-ion cells, *Carbon* 50 (2012) 5359–5371.
- [41] M. Park, X. Zhang, M. Chung, G.B. Less, A.M. Sastry, A review of conduction phenomena in Li-ion batteries, *J. Power Sources* 195 (2010) 7904–7929.

1. Supporting Information for Publication

1.1. Formation CVs

Figure S1 shows the full cycles of the experiment which is presented only in parts in Figure 2 of the main manuscript.

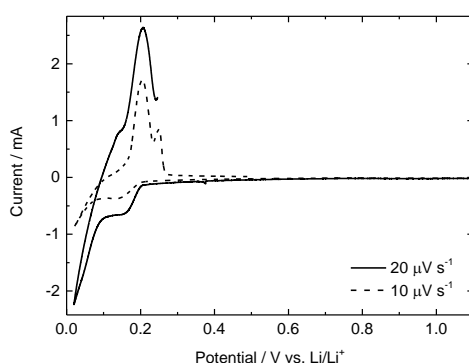


Figure S1: Slow SEI formation CVs using indicated scan rates.

1.2. Cycle Aging Test Details

For comparative reasons the cycle aging results of the electrodes used in this study after the benchmarking standard formation protocol are shown in Figure S2. Both the discharge capacity and the coulombic efficiency remain highly stable until around the 70th cycle.

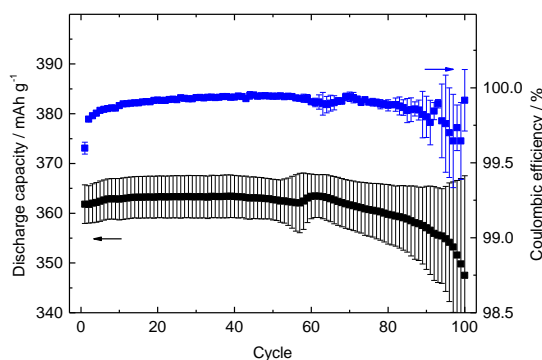


Figure S2: Discharge capacity and coulombic efficiency (cycle aging test) of graphite electrodes pretreated with the standard formation protocol as a benchmark.

The cycle aging data of the cell pretreated with the high-rate, half-cycle and EIS formation protocols (already presented in the main manuscript) are shown in Figures S3, S4 and S5, respectively. The red solid line resembles the main capacity of the cells pretreated with the benchmark formation protocol, which is also shown in Figure S2. Capacities are similar within the error bars.

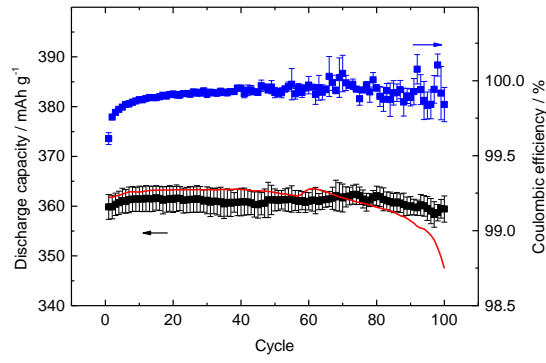


Figure S3: Discharge capacity and coulombic efficiency (cycle aging test) of graphite electrodes pretreated with the high-rate formation protocol. The solid red line resembles the mean capacity of Figure S2.

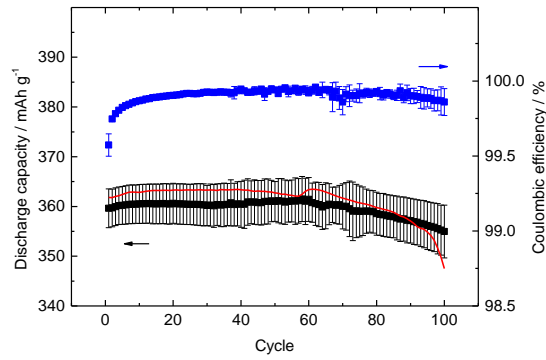


Figure S4: Discharge capacity and coulombic efficiency (cycle aging test) of graphite electrodes pretreated with the half-cycle formation protocol. The solid red line resembles the mean capacity of Figure S2.

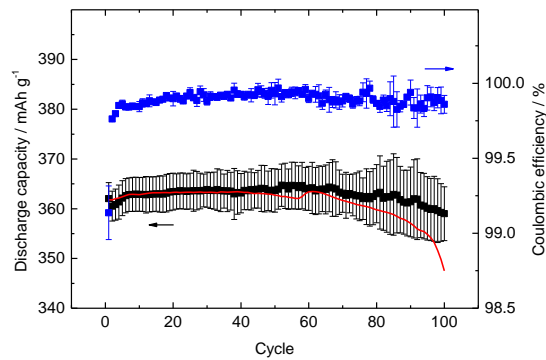


Figure S5: Discharge capacity and coulombic efficiency (cycle aging test) of graphite electrodes pretreated with the EIS formation protocol. The solid red line resembles the mean capacity of Figure S2.

1.3. Data of EIS Perturbation Experiments

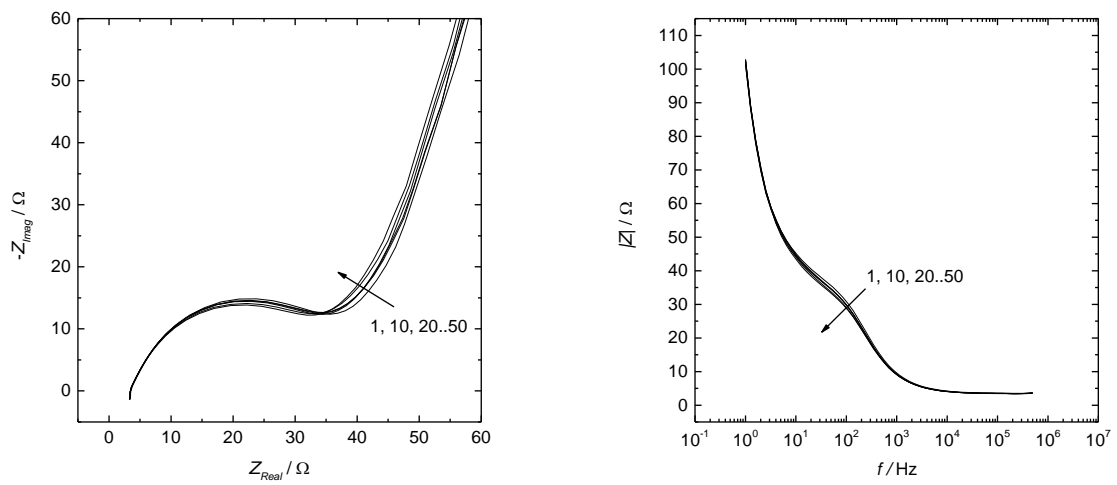


Figure S6: Exemplary Nyquist and Bode plots of data collected during the perturbation of electrodes using the EIS function of the potentiostat in the EIS formation protocol. 50 loops were obtained, only every tenth is shown (indicated by the arrows).

6. Results and Discussion Section 3 – Influence of Electrolyte Contaminations

6.1. The Deposition Mechanism of Transition Metal Cations on the Negative Electrodes of Li-Ion Batteries

Status	Manuscript in preparation
Journal	-
Publisher	-
DOI	-
Authors	Antonopoulos, Byron K.; Kirdar, Cansu; Maglia, Filippo; Hoster, Harry E.

Contributions: B.K.A., C.K. and F.M. conceived and designed the experiments. B.K.A. and C.K. performed the experiments. B.K.A., F.M. and H.E.H. discussed the results and wrote the paper.

Content

We investigate the deposition mechanism of transition metal cations on HOPG as model negative electrode in Li-Ion Batteries. For that, different SEIs with known properties are formed and electrolytes contaminated with Mn or Ni salts injected. By observing the current after injection and electrochemically approximating the evolution of the insulating surface layer thickness in ferrocene environment, we are able to formulate a deposition mechanism. Cations migrate through the organic porous layer and approach the surface of the compact layer, which cannot be penetrated. As usually the compact layer is thin enough, at low electrode potentials (e.g. in lithiated state) electrons can tunnel through the compact layer in order to reduce the cations. When the electrode is pushed to higher potentials (e.g. in delithiated state), the transition metals are reoxidized and form electronically insulating sectors or even a fully covering layer. The metals are reversibly reduced again at low potentials, though based on literature findings probably not to metallic but to $M(0)$ complexes. All transition metal species are expected to be bad Li^+ -ion conductors, so that reactive surface area of electrode particles in commercial cells would be blocked leading to a power fade and at high rates to a respective capacity fade. The ionic selectivity of the compact layer suggests that coating of positive electrode materials with respective species (e.g. Li_2CO_3) could avoid cation dissolution.

New Insights on the Deposition Mechanism and Location of Transition Metal Cations on the Negative Electrodes of Li-Ion Batteries

Byron Konstantinos Antonopoulos^a, Cansu Kirdar^a, Filippo Maglia^a, Harry E. Hoster^b

^a BMW Group, Petuelring 130, 80788 München, Germany

^b Energy Lancaster, Dep. of Chemistry, Lancaster University, Lancaster, LA1 4YB, United Kingdom

Corresponding author: Konstantinos.Antonopoulos@bmw.de; Tel: +49 89 382 65969

Co-Author Addresses: Cansu.Kirdar@bmw.de, Filippo.Maglia@bmw.de, H.Hoster@lancaster.ac.uk

Abstract:

We investigate the deposition mechanism of transition metal cations on HOPG as model negative electrode in Li-Ion Batteries. For that, different SEIs with known properties are formed and electrolytes contaminated with Mn or Ni salts injected. By observing the current after injection and electrochemically approximating the evolution of the insulating surface layer thickness in ferrocene environment, we are able to formulate a deposition mechanism. Cations migrate through the organic porous layer and approach the surface of the compact layer, which cannot be penetrated. As usually the compact layer is thin enough, at low electrode potentials (e.g. in lithiated state) electrons can tunnel through the compact layer in order to reduce the cations. When the electrode is pushed to higher potentials (e.g. in delithiated state), the transition metals are reoxidized and form electronically insulating sectors or even a fully covering layer. The metals are reversibly reduced again at low potentials, though based on literature findings probably not to metallic but to $M(0)$ complexes. All transition metal species are expected to be bad Li^+ -ion conductors, so that reactive surface area of electrode particles in commercial cells would be blocked leading to a power fade and at high rates to a respective capacity fade. The ionic selectivity of the compact layer suggests that coating of positive electrode materials with respective species (e.g. Li_2CO_3) could avoid cation dissolution.

1. Introduction

The energy density of positive electrode materials of state-of-the-art Li-ion batteries is one of the major limits for increasing the energy and power densities of the full cell. An optimization of the positive electrode is attempted with several approaches. Those approaches include the general trend of increasing the upper cutoff potential and the application of Ni-rich oxides (e.g. $\text{Li}_x\text{Ni}_{0.8}\text{Mn}_{0.1}\text{Co}_{0.1}\text{O}_2$) as electrode active material [1]. Both approaches lead to an increased transition metal dissolution, which is amplified by the presence of electrolyte impurities, particularly of HF [1–6]. The dissolved cations are attracted by the low potential of the negative electrode, thus they are deposited. Respective electrolyte studies did not reveal any considerable cation concentration, indicating that both the cation migration to the negative electrode and the subsequent deposition reaction are fast [2,4,5,7,8]. The deposited transition metals are believed to cause a power fade at the negative electrode. A respective capacity fade due to the deposition is assigned differently by different research teams [6,9–16]. Generally, in order to avoid a respective cell ageing, several actions repressing dissolution are taken in state-of-the-art cells [1]. Though, the increased cation dissolution from next generation positive electrodes demands a better understanding of the cation deposition mechanism on the negative electrode.

The negative electrode surface is fully covered by the multi-component solid electrolyte interphase (SEI), which consists of inorganic species at the electrode surface and organic species at electrolyte side. It is formed by reduction of electrolyte components particularly during the first charging cycle, which leads to Li^+ and therefore to capacity consumption. The SEI of state-of-the-art negative electrodes is optimized to be a good electronic insulator and therefore passivator, whilst allowing Li^+ to migrate and diffuse through it. This enables a long cell lifetime with little capacity and power fade [17–21]. The SEI presence and properties allow coming up with numerous possible mechanism on how and where transition metal cations are deposited on the negative electrode and how they affect the cell properties (e.g. capacity and power). Recent publications found contradicting information on the oxidation state of deposited Mn on the electrode, which is why they respectively hypothesized contradicting deposition mechanisms. On one hand, Zhan et al. found Mn^{2+} using X-ray absorption near edge spectroscopy (XANES) on delithiated electrodes. Consequently, they proposed a chemical exchange mechanism, in which Mn^{2+} is exchanged with bound Li^+ in organic SEI species, which would not affect the Mn^{2+} oxidation state [22]. A higher oxidation state on delithiated electrodes was also confirmed by Boulet-Roblin et al. using XPS [23]. On the other hand and in accordance with other groups [13,15,24–26], Gowda et al. found Mn^0 on the surface of lithiated electrodes using XANES, which is why they suggested an electrochemical reduction of Mn^{2+} [27]. In detail, they proposed two possible reduction mechanisms: The first consists of a reduction of Mn^{2+} at the electrode surface due to SEI defect sites (e.g. cracks). The second option consists of an electronic transport through the passivated SEI resulting in a reduction of Mn^{2+} somewhere in the SEI or even on its surface. Again, Shkrob et al. refuted both theories. In addition to the reproduction of both contradicting XANES results, using electron paramagnetic spectroscopy (EPR) they revealed, that the oxidation state of deposited Mn strongly depends on the lithiation state of the *post-mortem* investigated electrodes and that, if any, reduced Mn is not in metallic $\alpha\text{-Mn}^0$ state. Furthermore, they propose the deposition to take place at the inner compact SEI layer, as the neighborhood consist of Li_2CO_3 [8].

The objective of this work is to provide more evidence for the applicability of published incoherent hypotheses on the transition metal deposition on the negative electrode. Based on our recent results on the SEI two-step formation mechanism on highly oriented pyrolytic graphite (HOPG) we investigate the deposition rate and subsequent SEI thickness evolution [17]. For that, we enrich neat electrolyte with Mn^{2+} and Ni^{2+} containing salts and different concentrations and deposit the cations on different

SEIs on HOPG. Using cyclic voltammetry (CV) in ferrocene environment, we approximate the SEI thicknesses and correlate them to the electrochemically deposited charge. Findings allow supporting and consolidating the expressed hypotheses, whose impact to commercial cells is discussed.

2. Experimental

Since sample preparation and cell assembly was described in detail in ref. [17], only differences and additional information are given. The tape used for covering the HOPG sample was an optimized PET tape (SB 8901, 3M, USA), leaving exposed a circular basal HOPG area with a diameter of 4 mm. The cell described in ref. [17] was optimized by means of electrode contacts and positions for an easier handling. It meanwhile became commercially available (TSC battery standard, rhd instruments, Marburg, Germany). SEI formation was performed in neat electrolyte (LP572, EC:EMC 3:7, 1 M LiPF₆, 2% VC, BASF, Ludwigshafen, Germany), while different enriched electrolyte derivatives were injected afterwards for cation deposition and CV experiments. The salts used for enrichment were Manganese(II) bis(trifluoromethanesulfonate) (Mn-Tf), Nickel(II) acetylacetonate (Ni(AcAc)₂) both with purities >95%, ferrocene and ferrocenium hexafluorophosphate (Fc and Fc⁺, respectively) with 98% and 97% purity, respectively. All salts were obtained from Sigma Aldrich, Germany. For deposition experiments, one electrolyte flask was enriched with 1000 ppm Mn-Tf and one with 500 ppm Ni(AcAc)₂. The enriched electrolyte used for CVs included 10mMol Fc and Fc⁺.

Cells were assembled using 75 μ l neat electrolyte. The syringe connected to the cell contained \sim 15 μ l Mn-Tf or Ni(AcAc)₂ enriched electrolyte for injection after SEI formation. The injected volumes of Mn-Tf electrolyte were 4 or 8 μ l and for of Ni(AcAc)₂ electrolyte 6 or 12 μ l. The lower and higher volume correspond to final cation concentrations of 0.2 mMol and 0.4 mMol in the cell, respectively. That way, the areal contamination becomes comparable. After injection and deposition of transition metals on the HOPG, cells were reinserted into the glovebox to avoid atmosphere contact during the following procedure. The syringe connected to the cell was detached and a fresh syringe was connected. It contained around 35 μ l Fc/Fc⁺ enriched electrolyte. The total electrolyte volume being already in the cell varied depending on the injected cation salt and its concentration. Therefore, the amount of injected Fc/Fc⁺ electrolyte was predetermined appropriately (\sim 29 μ l), so that a final Fc/Fc⁺ concentration of 2.5 mMol was achieved. The cells were then sealed without a syringe attached and brought back to the potentiostat for CV experiments.

Unless otherwise stated, all working electrode potentials in this work are given vs. Li/Li⁺.

3. Results and Discussion

3.1. Experiment and Evaluation Methodology

The experiments consisted of four steps. The potential profile is shown schematically in Figure 1 with numbers indicating the single experimental steps. During step <1> the SEI is formed potentiostatically. In accordance with [17], we applied potentials of either 100 or 600 mV in order to form high and low potential SEIs. Three equipollent cutoff criteria during the first step (SEI formation) were defined, namely the current density, charge density and formation time at 4 μ A cm⁻², 10 mC cm⁻² and 600 s, respectively. The current profiles look alike the ones presented in ref. [17], therefore they are not shown or discussed. After step <1> was terminated by one of the cutoff criteria, the potential was set to 1.2 V in the cation deposition step <2>. This potential is greater than the first significant electrolyte reduction threshold potential (\sim 800 mV), so that possible continuation of electrolyte reduction is thermodynamically suppressed [28]. In order to avoid cation deposition on the

counter or reference electrode as much as possible, the working electrode potential needs to be as low as possible. The standard potentials of $\text{Mn}^0/\text{Mn}^{2+}$ and $\text{Ni}^0/\text{Ni}^{2+}$ are significantly higher than the applied 1.2 V [28,29], thus we tentatively assume the deposition on the reference and counter electrodes to be negligible.

After ~10 min at 1.2 V the cation electrolyte was injected and the potential held for 2 h total time. Step <3> consisted of a relaxation phase, during which OCP was recorded for ~20 h, during which Fc/Fc^+ containing electrolyte was injected into the cells. In step <4> CVs with four scan rates (100, 50, 10, 1 mV s^{-1}) were obtained. To ensure equilibrated conditions, 5 scans were obtained per scan rate, though only the fifth is further processed and evaluated. Pristine HOPG was investigated without steps <1> and <2>, whilst reference SEI experiments in neat electrolyte excluded step <2>.

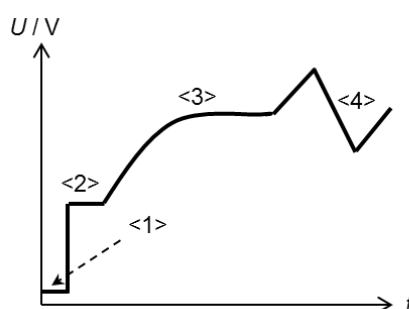


Figure 1: Potential profile of the four experimental steps plotted schematically vs. time. 1. Step: SEI Formation; 2. Step: Cation Deposition; 3. Step: Relaxation; 4. Step: CVs in Fc/Fc^+ environment

The evaluated steps, which lead to the results discussed and compared in the later part of this work, are steps <2> and <4> (cation deposition & CVs in Fc/Fc^+ environment, respectively). A typical current density transient of injection step <2> is presented in Figure 2. The slopes in all experiments look alike, therefore Figure 2 exemplifies the features. During the first moments of the potentiostatic step an oxidative current is obtained, which can be attributed to double layer discharge. The current quickly levels off at a background value $\sim 26 \mu\text{A cm}^{-2}$ before the $\text{Ni}(\text{AcAc})_2$ enriched electrolyte is injected, as indicated by the arrow. The origin of background current is unknown; one may speculate it is connected to the reduction of vinylene carbonate (VC) [28][30]. At the moment of injection (indicated by the arrow in Figure 2) the reduction current is abruptly increased, but relaxes back to the background value after ~30 min. The speed of the return to the background current density varied depending on the cation concentration and element, though all values were passivated at the end of this potentiostatic deposition step. In order to estimate the amount of deposited cations, we integrated the charge between the dashed baseline and the actual current density slope.

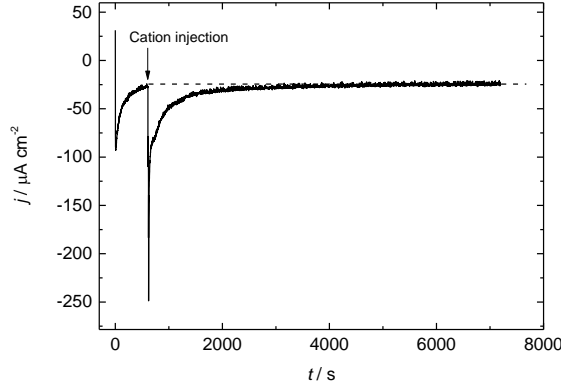


Figure 2: Current density during step <2> (cation deposition step) at 1.2 V vs. Li/Li⁺. The SEI was formed at 600 mV vs. Li/Li⁺. 0.4 mMol Ni(AcAc)₂ enriched electrolyte is injected at the moment indicated by the arrow. To calculate the actually reduced cations, the charge between the actual slope and the dashed baseline is integrated.

Since the Fc/Fc⁺ reaction is surface sensitive only, respective information like diffusion and rate constants give rise to interpretation in terms of possible surface layers and their properties. In ref. [17] we introduced the CV interpretation scheme by discussing in detail whether the Fc/Fc⁺ reaction is a quasi-reversible outer-sphere reaction. As both shapes and current densities of all CVs look like the ones presented in ref. [17], they are not shown separately in this paper. Though, we will introduce the scheme briefly for clarification. In a first step the oxidative peak current densities j_{peak} of the CVs are plotted against the scan rate ν in order to extract diffusion coefficients. This can be done by the adjusted Randles-Sevcik equation for 20 °C:

$$j_{Peak} = 3.04 \cdot 10^5 n^{3/2} \alpha^{1/2} c_{Red}^0 (\xi D_{red} \nu)^{1/2} \text{ in A cm}^{-2} \quad (1)$$

n , α , D_{red} and c_{Red}^0 are the transfer number, charge transfer coefficient, reduced species effective diffusion coefficient and concentration, respectively. α is assumed to be 0.3 [31], n and c_{Red}^0 are 1 and 2.5 mMol, respectively. $\xi = 0.73$ is a correction factor introduced due to the deviant boundary condition, as the original Randles-Sevcik equation is based on $c_{ox}^0(t=0) = c_{ox}^0(x \rightarrow \infty) = 0$. In this experiment, the oxidized species concentration c_{ox}^0 does not fulfil this boundary condition. The reasonability and plausibility and exact value of such a correction was argued in ref. [17]. In all experiments CVs revealed the diffusion coefficients of reduced and oxidized species to be similar, therefore we define the effective diffusion coefficient $D_{eff} := D_{red} \approx D_{ox}$.

Matsuda and Ayabe introduced a numerical function $\Lambda_\nu(\Delta\varphi_{Peak})$ for quasi-reversible reactions, of which a set of values can be found in the literature [32,33]. Λ_ν brings the CV peak potential difference $\Delta\varphi_{Peak}$ and the heterogeneous reaction rate constant k_0 in relation. The index ν indicates the scan rate used for extraction of $\Delta\varphi_{Peak}$, as it varies with ν in quasi-reversible reactions.

$$k_{0,\nu} = \Lambda_\nu(\Delta\varphi_{Peak}) \cdot \left(D_{eff} \frac{nF}{RT} \nu \right)^{1/2} \quad (2)$$

F is the faraday constant and R the universal gas constant. For our analysis, we interpolated the tabulated values of Λ_ν . The peak potential differences at 100 and 1 mV s⁻¹ are outside the tabulated region in all experiments, wherefore they cannot be considered for processing with Eq. (2). As the processing of results extracted from CVs at 50 and 10 mV s⁻¹ give the same results [17], we only use

the 10 mV s^{-1} . Furthermore, we assume the Fc/Fc^+ electron transfer to take place via electron tunneling through both molecular shell and insulating surface layers on the electrode surface. These can consist of either electrolyte reduction products or of other transition metal containing compounds. The rate constant of the pristine HOPG k_0^{Pristine} calculated using Eq. (2) serves as a calibration, since it depends only on the electron transfer through the Fc^{z+} shell. Therefore, we can approximate the total insulating surface layer thickness d_{SL} on the electrode surface, through which electrons have to tunnel in order to reduce or oxidize Fc^{z+} species [17,34]:

$$\Rightarrow d_{SL} = -\frac{1}{\beta} \ln \left(\frac{k_0}{k_0^{\text{Pristine}}} \right) \text{ with } k_0 \leq k_0^{\text{Pristine}} \quad (3)$$

The factor β describes the tunneling probability and cannot be determined with this experimental setup. As it should depend mainly on the electron energy levels before and after the tunneling barrier, we assume β to be constant, so that thickness results can be compared qualitatively. Due to the rate constant division in Eq. (3) a possibly incorrectly chosen correction factor ζ would not influence the d_{SL} values.

3.2. Comparison of Reference, Mn-Tf and Ni(AcAc)₂ Experiments

The SEIs investigated were formed at 600 and 100 mV vs. Li/Li^+ . We could show in our previous publication, that these two SEIs consist of a significantly different compact layer in terms of both thickness and chemical composition [17]. Since the experiments in this work were performed in a second generation of cells, the respective reference experiments in neat electrolyte were repeated and resulting SEIs characterized electrochemically. Apart from that, the two SEIs were exposed to Mn-Tf or $\text{Ni}(\text{AcAc})_2$ enriched electrolytes, both with two different concentrations. All experiments including the reference experiments in neat electrolyte and on pristine HOPG are presented in Table 1. The single experiments are given numbers for a more easy discussion in the text. Amongst others, Table 1 lists, if applicable, the ratio of deposited to originally injected charge ($Q_{\text{cat,dep}}$) during the cation deposition step <2>. After injection, cations can be deposited electrochemically on the working electrode or chemically on the counter and reference electrodes both consisting of Li^0 . Though, the chemical deposition rate on Li^0 is independent of the SEI covering the HOPG, thus can be assumed constant in all experiments. Therefore, the different cation single $Q_{\text{cat,dep}}$ values qualitatively reflect the electrochemical deposition rate of the respective cations on the working electrode. Table 1 also presents the SEI-specific rate constants $k_{0,10}$ of the Fc/Fc^+ charge transfer. Using eq. (3) we calculated the relative surface layer thicknesses d_{SL} , which are listed in the table too.

Starting with the pristine and reference experiments (1, 2, 3), they appear to have slightly higher rate constants than determined in ref. [17]. Though, the resulting layer thicknesses of the reference exp. 2 & 3 have the same ratio. We believe, that the deviation of the values presented in Table 1 to the ones in ref. [17] are caused by the design adjustments between the two cell generations. Nevertheless, the ratio between the surface layer thicknesses indicates, that the experiments generated reliable results for qualitative analysis.

It is an eye-catching phenomenon that $Q_{\text{cat,dep}}$ strongly depends on the SEI formation potential (see exp. 5/6 or 8/9). The high-potential SEI, which has a thinner insulating compact layer [17], facilitates more cation deposition. We therefore conclude that, by analogy to the Fc/Fc^+ charge transfer, the cation deposition rate is significantly smaller in the presence of a thick low-potential compact SEI layer. In addition, when increasing the electrolyte contamination amount, the deposition ratio decreases (see exp. 4/5 or 7/8). We tentatively assign that trend to a passivating character of the deposited cation complexes.

If we now have a look at the surface layer thicknesses d_{SL} extracted from CVs in ferrocene environment, they concur with the trends of respective deposited charge ratios. Due to the smaller amount of deposited cations on the low potential SEIs (exp. 6 & 9), the increase of thickness with respect to the reference exp. 2 is small. On the other hand, the increase of d_{SL} at the high potential SEI experiments (e.g. exp. 5 & 8) is significant. We conclude, that as expected the higher the amount of deposited cations is, the thicker the respective resulting surface layers are. Furthermore, the deposition of Ni^{2+} generally leads to distinctly thicker surface layers compared to the similar Mn^{2+} experiments, which is independently of the SEI covering the surface (c.f. exp. 5/8 or 6/9).

Table 1: Deposited cation charge ratio $Q_{cat,dep}$, Fc/Fc^+ rate constant $k_{0,10}$ and insulating surface layer thicknesses d_{SL} of the single experiments. Values and trends are discussed in the text.

Nr.	SEI Formation Potential	Cat. Conc.	$Q_{cat,dep}$	$k_{0,10}$	βd_{SL}
1	Pristine HOPG	-	-	2.1	-
2	Reference SEI	600	-	1.8	0.15
3	Reference SEI	100	-	1.1	0.56
4	Mn-Tf	600	0.2	98	1.0
5	Mn-Tf	600	0.4	62	0.76
6	Mn-Tf	100	0.4	37	0.85
7	$\text{Ni}(\text{AcAc})_2$	600	0.2	89	2.0
8	$\text{Ni}(\text{AcAc})_2$	600	0.4	84	2.8
9	$\text{Ni}(\text{AcAc})_2$	100	0.4	22	1.2

3.3. Discussion of the Deposition Mechanism

Just like in our earlier publication [17] we discuss the tabled results based on a simplified two-layer SEI model, which consists of an insulating compact layer on the electrode surface and an organic porous layer on the electrolyte side. Since practically no Li^+ intercalation takes place in HOPG, the electrode does not suffer from intercalation/deintercalation volume changes (“breathing”) [17,35]. Therefore, we assume the SEI not to suffer from cracking due to limited elasticity. However, the exemplary Figure 2 presents a distinct reductive current directly associated with the injection of transition metal cations. Thus, on HOPG, it appears unlikely that the cations are reduced in cracks [27]. Furthermore, diffusion/migration of the transition metal cations through the compact SEI to the electrode surface is unlikely to take place already due to the differing oxidation state [22], which is supported by the trends of $Q_{cat,dep}$ and d_{SL} values in the experiment pairs 4/5 and 7/8. On the other hand, an $\text{Li}^+/\text{M}^{2+}$ ion exchange in present SEI species should not lead to the current transient presented in Figure 2 and the d_{SL} evolution in the experiment pair 4/7, particularly if cations would be exchanged in the porous organic layer (as proposed by Zhan et al. [22]). It is unclear, but as well not of importance for this study, whether the ion exchange is prevented by a neutralizing cation shell [8] or simply a high activation energy necessary to remove two Li^+ and exchange it with one M^{2+} .

Although passivated, no SEI is insulating in terms of the Fc/Fc^+ charge transfer taking place via tunnel electrons [17,36]. Similar conductivity was observed for 2,5-di-*tert*-butyl-1,4-dimethoxybenzene (DBDMB) as redox mediator [37]. We tentatively suggest that the investigated transition metal cations can too be reduced by tunneling electrons. The mechanism is schematically presented in Figure 3a for

Mn deposition. d_{SEI} describes the thickness of the SEI compact layer. In this model solved cations or respective complexes can move through the porous to the “surface” of the compact SEI, where the cations are reduced. Domains or even a fully covering layer of Mn^0 (or Ni^0) are formed. The current peak after the cation injection in Figure 2 corresponds to the reduction of the cations to respective species. This hypothesis is in line with both our experimental findings and a proposed but not proven mechanism. Apart from that, we actually underline the hypothesis by Shkrob et al. [8] as well, which claim that the deposition of transition metal cations does not take place on top of the SEI or the electrode surface, but on the inner mineral compact layer surface.

The model presented in Figure 3a varies in a small yet important component from the original in reference [17]. If cations would be reduced to elementary metals, they would form conducting sectors or particles. Thus, electrons e.g. would have to tunnel through the insulating compact SEI from/to a conductive metal domain or layer. Accordingly, the Fc/Fc^+ charge transfer could happen at the transition metal surface, thus not depend on the thickness metal domains. Though, Table 1 clearly shows the dependency of the Fc/Fc^+ charge transfer kinetics on the amounts of deposited metals (experiments 4/5 and 7/8). It therefore appears reasonable, that actually an insulating layer is formed due to the cation deposition, slowing down both the further cation deposition and the the Fc/Fc^+ reaction (see evolution of $Q_{cat,dep}$ and d_{SL} in Table 1). This would again contradict the reduction of cations to elementary domains proposed earlier by ourselves.

An explanation to this controversy would be the (electro-) chemical reoxidation of the elementary transition metals. Both Mn^0 and Ni^0 are known to be very reactive, thus we expect them to chemically react with electrolyte or SEI components “immediately”. $Mn(II)$ or $Ni(II)$ containing compounds like fluorides, carbonates or alkyl carbonates would be formed and the respective species would be embedded in present SEI minerals [8,13,15]. Respective oxidized metal compounds were found on graphite electrodes by numerous groups [8,22,27,38–40]. Even more, XPS [24] and -ray absorption spectroscopy (XAS) data [8] revealed a change of oxidation state of the deposited transition metals with time. In our experiments, a sufficient amount of time passed in the OCP step <3> before the CV experiments in Fc/Fc^+ environment were started, and the potential went to >3 V as well. It appears quite congruent with existing literature that deposited M^0 domains were reoxidized during step <3>. It is important to mention that the rate of the metal reoxidation probably depends on numerous factors such as electrode potential, SEI and electrolyte composition and particularly impurities.

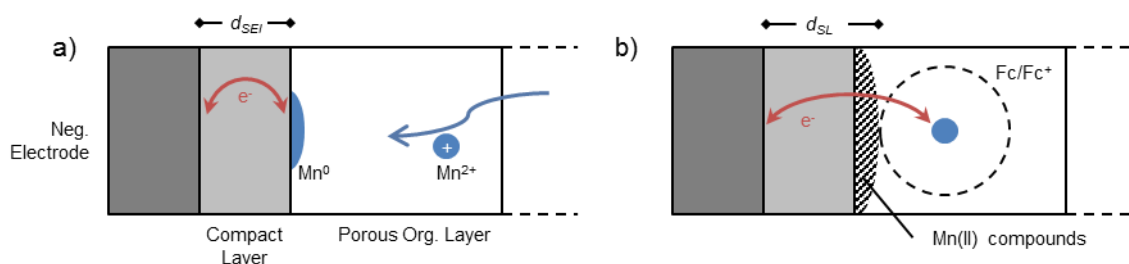


Figure 3: a) Proposed deposition mechanism of transition metal cations on the SEI compact layer surface via tunneling electrons, shown representatively for Mn. b) Fc/Fc^+ reaction scheme after the deposition of transition metals shown representatively for deposited Mn.

The thickness sum d_{SL} of all insulating layers on the HOPG surface (SEI compact layer, transition metal insulation layer etc.) determine the Fc/Fc^+ reaction rate in the performed CV experiments. The respective Fc/Fc^+ reaction mechanism is schematically shown in Figure 3b. One assumption made in eq. (3) is, that the surface layer has a homogeneous electronic state density, thus represents a single tunneling barrier. The insulating properties of the metal compounds can vary significantly from those

of the compact layer itself. Therefore, it is necessary to mathematically separate electron tunneling through the two layers using

$$\beta_M d_M = \beta d_{SL} - \beta_{SEI} d_{SEI} \quad (4)$$

with $\beta_{SEI} d_{SEI}$ and $\beta_M d_M$ describing the compact SEI and transition metal compounds, respectively. The reference experiments (Exp. 2/3 in Table 1) provide the necessary $\beta_{SEI} d_{SEI}$ -baselines. The $\beta_M d_M$ values for all relevant experiments (4-9) are presented in Figure 4 vs. the absolute amount of deposited cations. The trend is linear, the slopes reflect the thickness differences between Mn and Ni in Table 1. We tentatively assign this difference to a greater Fc/Fc⁺ charge transfer tunneling barrier β_M of Ni compounds but to a real difference in the d_M values. We emphasize, that this does not contradict the similar deposition rates of the cations (reflected by $Q_{cat,dep}$), since they depend solely on the SEI compact layer tunneling barriers β_{SEI} .

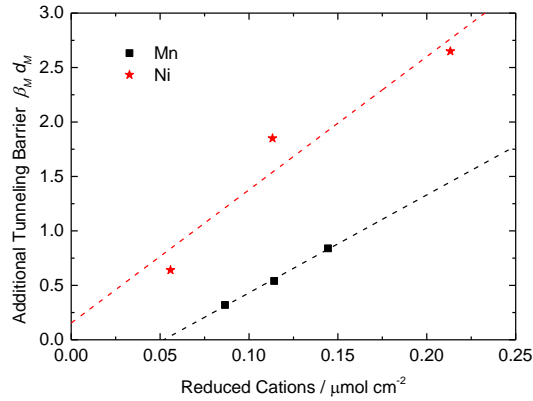


Figure 4: Additional Fc/Fc⁺ charge transfer tunneling barrier induced by the deposition of indicated transition metal cations, presented vs. the absolute amounts of deposited cations.

If we now transfer this model to commercial Li-ion cells with thick and porous composite electrodes, whose cathodes continuously suffer from cation dissolution, cations would be preferably deposited on outer anode particles [11,40]. Once reoxidized, the cations form an additional insulating surface layer, so that future cations are rather reduced on other uncovered particles in the deeper electrode section leading to a full anode surface coverage in the long run. As a result, the electrode will suffer in whole from power fade. A thicker SEI might slow down the deposition; since (opposite to our study) there is no sacrificial electrode in real cells, deposition cannot be avoided. Apart from the power fade, the deposited compounds might have an advantageous effect on the anode capacity retention by avoiding SEI cracking, so that in total actually less Li⁺ is consumed during the cell lifetime. Since we expect this to be strongly dependent on a variety of parameters, it could explain the inconsistent trend in capacity loss published by different groups (mentioned in the introduction).

Our hypothesis includes two uncertainties which remain unanswered. The first one is: At what point are the non-metallic but probably reduced Mn(0) complexes formed (described in [8])? It remains unclear, whether tunneling electrons form Mn⁰, which is subsequently or after a full cycle transformed to Mn(0), or electrons form respective species immediately. The slow passivation of the cation deposition itself suggests, that electronically conducting α -Mn⁰ is slowly transformed to Mn(0). The second uncertainty is the following: What kind of Mn(0) complexes are formed on the lithiated electrodes? Both from the OCP as well as the cyclability point of view the reversible lithiation of Li_xMn₃O₄ or other equivalent transition metal oxides are consistent with the experimental data [41,42].

On the other hand, the consistency of delithiated Mn_3O_4 with the Mn^0 -like XAS behavior and the Li_2CO_3 neighborhood found with EPR is questionable. Also the formation of alloys can be doubted [43].

From our study we also conclude that coating the cathode active material with a thin layer of Li^+ conducting minerals (e.g. Li_2CO_3) could avoid the dissolution, as we have proven its cation selection abilities (Li^+ vs. M^{2+}). Such a coating would suppress the movement of dissolved transition metal cations and thus generally hinder the dissolution, whilst Li^+ movement would not be affected significantly.

4. Conclusion

We investigated the deposition mechanism of transition metal cations on HOPG. For that, we formed different SEIs with known properties and injected electrolytes contaminated with Mn or Ni salts without disassembling the cells. By observing the current transients after injection and electrochemically approximating the evolution of the insulating surface layer thicknesses in Fc/Fc^+ environment, we were able to formulate a cation deposition mechanism. Cations move through the organic porous layer and approach the surface of the compact layer, which cannot be penetrated. With the compact layer being sufficiently thin, electrons can tunnel through the compact layer in order to reduce the cations to metallic clusters or even layers. We could prove that, although probably energetically favored, an ion exchange at the porous organic layer (proposed by other groups) does not take place due to neutralizing ion shells or high activation energy barriers. When the electrode is pushed to higher potentials (e.g. in delithiated state), the transition metals are reoxidized and form electronically insulating sectors or even a fully covering layer. All transition metal species are expected to be bad Li^+ conductors, so that the reactive surface areas of electrode particles in commercial cells would be blocked leading to a power fade and, at high rates, to a respective capacity fade. A catalysis of electrolyte reduction leading to more classical SEI species cannot be supported neither excluded by this study. On the contrary, transition metal containing species may lead to less SEI cracks by electrode breathing and therefore actually reduce respective Li^+ consumption by SEI reformation. The ionic selectivity of the compact layer suggests, that coating of positive electrode materials with respective species (e.g. Li_2CO_3) could avoid cation dissolution effectively without significantly limiting the Li^+ movement.

5. References

- [1] D. Andre, S.-J. Kim, P. Lamp, S.F. Lux, F. Maglia, O. Paschos, B. Stiaszny, *J. Mater. Chem. A* 3 (2015) 6709–6732.
- [2] B. Stiaszny, J.C. Ziegler, E.E. Krauß, J.P. Schmidt, E. Ivers-Tiffée, *J. Power Sources* 251 (2014) 439–450.
- [3] D. Lu, M. Xu, L. Zhou, A. Garsuch, B.L. Lucht, *J. Electrochem. Soc.* 160 (2013) A3138-A3143.
- [4] Y. Li, M. Bettge, B. Polzin, Y. Zhu, M. Balasubramanian, D.P. Abraham, *J. Electrochem. Soc.* 160 (2013) A3006-A3019.
- [5] K. Amine, J. Liu, S. Kang, I. Belharouak, Y. Hyung, D. Vissers, G. Henriksen, Selected papers presented at the conference High Energy Density Electrochemical Power Sources 129 (2004) 14–19.
- [6] I. Buchberger, S. Seidlmayer, A. Pokharel, M. Piana, J. Hattendorff, P. Kudejova, R. Gilles, H.A. Gasteiger, *J. Electrochem. Soc.* 162 (2015) A2737-A2746.
- [7] A. Blyr, C. Sigala, G. Amatucci, D. Guyomard, Y. Chabre, J.-M. Tarascon, *J. Electrochem. Soc.* 145 (1998) 194–209.

- [8] I.A. Shkrob, A.J. Kropf, T.W. Marin, Y. Li, O.G. Poluektov, J. Niklas, D.P. Abraham, *J. Phys. Chem. C* 118 (2014) 24335–24348.
- [9] J.L. Esbenschade, A.A. Gewirth, *J. Electrochem. Soc.* 161 (2014) A513–A518.
- [10] I.H. Cho, S.-S. Kim, S.C. Shin, N.-S. Choi, *Electrochem. Solid-State Lett.* 13 (2010) A168–A172.
- [11] L. Yang, M. Takahashi, B. Wang, *Electrochimica Acta* 51 (2006) 3228–3234.
- [12] H. Tsunekawa, Tanimoto, a, Satoshi, R. Marubayashi, M. Fujita, K. Kifune, M. Sano, *J. Electrochem. Soc.* 149 (2002) A1326–A1331.
- [13] C. Delacourt, A. Kwong, X. Liu, R. Qiao, W.L. Yang, P. Lu, S.J. Harris, V. Srinivasan, *J. Electrochem. Soc.* 160 (2013) A1099–A1107.
- [14] T. Tsujikawa, K. Yabuta, T. Matsushita, M. Arakawa, K. Hayashi, *J. Electrochem. Soc.* 158 (2011) A322–A325.
- [15] X. Xiao, Z. Liu, L. Baggetto, G.M. Veith, K.L. More, R.R. Unocic, *Physical chemistry chemical physics PCCP* 16 (2014) 10398–10402.
- [16] M. Bettge, Y. Li, B. Sankaran, N.D. Rago, T. Spila, R.T. Haasch, I. Petrov, D.P. Abraham, *Journal of Power Sources* 233 (2013) 346–357.
- [17] B.K. Antonopoulos, F. Maglia, F. Schmidt-Stein, J.P. Schmidt, H.E. Hoster, *Batteries & Supercaps* (2018) doi: 10.1002/batt.201800029.
- [18] P. Verma, P. Maire, P. Novak, *Electrochim. Acta* 55 (2010) 6332–6341.
- [19] D. Aurbach, E. Zinigrad, Y. Cohen, H. Teller, *Solid State Ionics* 148 (2002) 405–416.
- [20] M. Winter, W.K. Appel, B. Evers, T. Hodal, K.-C. Möller, I. Schneider, M. Wachtler, M.R. Wagner, G.H. Wrodnigg, J.O. Besenhard, *Monatsh. Chem.* 132 (2001) 473–486.
- [21] M.B. Pinson, M.Z. Bazant, *J. Electrochem. Soc.* 160 (2013) A243–A250.
- [22] C. Zhan, J. Lu, A. Jeremy Kropf, T. Wu, A.N. Jansen, Y.-K. Sun, X. Qiu, K. Amine, *Nat Comms* 4 (2013) 2473.
- [23] L. Boulet-Roblin, M.E. Kazzi, P. Novak, C. Villevieille, *J. Electrochem. Soc.* 162 (2015) A1297–A1300.
- [24] M. Ochida, Y. Domi, T. Doi, S. Tsubouchi, H. Nakagawa, T. Yamanaka, T. Abe, Z. Ogumi, *J. Electrochem. Soc.* 159 (2012) A961–A966.
- [25] K. Amine, Z. Chen, Z. Zhang, J. Liu, W. Lu, Y. Qin, J. Lu, L. Curtis, Y.-K. Sun, *J. Mater. Chem.* 21 (2011) 17754.
- [26] T. Joshi, K. Eom, G. Yushin, T.F. Fuller, *J. Electrochem. Soc.* 161 (2014) A1915–A1921.
- [27] S.R. Gowda, K.G. Gallagher, J.R. Croy, M. Bettge, M.M. Thackeray, M. Balasubramanian, *Phys. Chem. Chem. Phys.* 16 (2014) 6898.
- [28] O. Matsuoka, A. Hiwara, T. Omi, M. Toriida, T. Hayashi, C. Tanaka, Y. Saito, T. Ishida, H. Tan, S.S. Ono, S. Yamamoto, *J. Power Sources* 108 (2002) 128–138.
- [29] S. Komaba, N. Kumagai, Y. Kataoka, *Electrochimica Acta* 47 (2002) 1229–1239.
- [30] J. Ma, L. Seidl, W. Ju, E. Mostafa, L. Asen, S. Martens, U. Stimming, O. Schneider, *ECS Trans.* 64 (2014) 407–423.
- [31] C.O. Laoire, E. Plichta, M. Hendrickson, S. Mukerjee, K.M. Abraham, *Electrochim. Acta* 54 (2009) 6560–6564.
- [32] H. Matsuda, Y. Ayabe, *Zeitschrift für Elektrochemie, Berichte der Bunsengesellschaft für physikalische Chemie* 59 (1955) 494–503.
- [33] C.H. Hamann, A. Hammnett, W. Vielstich, *Electrochemistry*, 2nd ed., Wiley-VCH Verlag GmbH & Co. KGaA, 2007.
- [34] A.D. Clegg, N.V. Rees, O.V. Klymenko, B.A. Coles, R.G. Compton, *J. Electroanal. Chem.* 580 (2005) 78–86.
- [35] V.A. Sethuraman, Winkle, N. Van, D.P. Abraham, A.F. Bower, P.R. Guduru, *J. Power Sources* 206 (2012) 334–342.

- [36] M. Tang, J. Newman, *J. Electrochem. Soc.* 159 (2012) A1922-A1927.
- [37] H. Bülter, F. Peters, J. Schwenzel, G. Wittstock, *J. Electrochem. Soc.* 162 (2015) A7024-A7036.
- [38] A. Jarry, S. Gottis, Y.-S. Yu, J. Roque-Rosell, C. Kim, J. Cabana, J. Kerr, R. Kostecki, *J. Am. Chem. Soc.* 137 (2015) 3533–3539.
- [39] J.S. Park, X. Meng, J.W. Elam, S. Hao, C. Wolverton, C. Kim, J. Cabana, *Chem. Mater.* 26 (2014) 3128–3134.
- [40] J. Wandt, A. Freiberg, R. Thomas, Y. Gorlin, A. Siebel, R. Jung, H.A. Gasteiger, M. Tromp, *J. Mater. Chem. A* 4 (2016) 18300–18305.
- [41] C.M. Julien, M. Massot, *Materials Science and Engineering: B* 97 (2003) 217–230.
- [42] J. Gao, M.A. Lowe, H.D. Abruña, *Chem. Mater.* 23 (2011) 3223–3227.
- [43] P. Poizot, S. Laruelle, S. Grugeon, L. Dupont, J.-M. Tarascon, *Nature* 407 (2000) 496–499.

6.2. Electrocatalytic Transformation of HF Impurity to H₂ and LiF in Lithium-Ion Batteries

Status	Published online, 09 April 2018
Journal	Nature Catalysis, 2018, Volume 1, 255–262
Publisher	Macmillan Publishers Ltd.
DOI	10.1038/s41929-018-0047-z
Authors	Strmcnik, Dusan; Castelli, Ivano E.; Connell, Justin G.; Haering, Dominik; Zorko, Milena; Martins, Pedro; Lopes, Pietro P.; Genorio, Bostjan; Østergaard, Thomas M.; Gasteiger, Hubert A.; Maglia, Filippo; Antonopoulos, Byron K.; Stamenkovic, Vojislav R.; Rossmeisl, Jan; Markovic, Nenad M.

Contributions: D.S., J.G.C., B.K.A, H.A.G. and N.M.M. conceived and designed the experiments. D.S., J.G.C., D.H., M.Z., P.M., P.P.L. and B.G. performed the experiments. I.E.C., T.Ø. and J.R. performed the calculations. D.S., J.G.C., I.E.C., F.M., B.K.A., J.R., H.A.G., V.R.S. and N.M.M. discussed the results and wrote the paper.

Content

The formation of solid electrolyte interphase on graphite anodes plays a key role in the efficiency of Lithium-ion batteries. However, to date, fundamental understanding of the formation of LiF as one of the main solid electrolyte interphase components in hexafluorophosphate-based electrolytes remains elusive. Here, we present experimental and theoretical evidence that LiF formation is an electrocatalytic process that is controlled by the electrochemical transformation of HF impurity to LiF and H₂. The experimental results indicate that the simultaneous formation of LiF(s) and H₂ in 1 M LiPF₆ on anode electrodes is much simpler than was considered thus far. Through systematic investigation, it was possible to gain fundamental understanding of how the synergy between the structure and nature of surface atoms, covalent and non-covalent forces, and ppm levels of electrolyte (H₂O and HF), as well as electrode material defects, control the electrocatalytic dissociation of HF and the concomitant adsorption of H_{ad} (HER), the interaction of F⁻ and Li⁺, and the precipitation of LiF - a key part of the SEI. Although this work does not directly address the role of LiF in battery performance, it creates a platform for such understanding. We conclude that our finding is of general importance and we believe it will lead to new opportunities for the improvement of existing systems and the design of new LIB technologies.

Electrocatalytic transformation of HF impurity to H₂ and LiF in lithium-ion batteries

Dusan Strmcnik^{1*}, Ivano E. Castelli², Justin G. Connell¹, Dominik Haering³, Milena Zorko¹, Pedro Martins¹, Pietro P. Lopes¹, Bostjan Genorio¹, Thomas Østergaard², Hubert A. Gasteiger³, Filippo Maglia⁴, Byron K. Antonopoulos⁴, Vojislav R. Stamenkovic¹, Jan Rossmeisl^{2*} and Nenad M. Markovic¹

The formation of solid electrolyte interphase on graphite anodes plays a key role in the efficiency of Li-ion batteries. However, to date, fundamental understanding of the formation of LiF as one of the main solid electrolyte interphase components in hexafluorophosphate-based electrolytes remains elusive. Here, we present experimental and theoretical evidence that LiF formation is an electrocatalytic process that is controlled by the electrochemical transformation of HF impurity to LiF and H₂. Although the kinetics of HF dissociation and the concomitant production of LiF and H₂ is dependent on the structure and nature of surface atoms, the underlying electrochemistry is the same. The morphology, and thus the role, of the LiF formed is strongly dependent on the nature of the substrate and HF inventory, leading to either complete or partial passivation of the interface. Our finding is of general importance and may lead to new opportunities for the improvement of existing, and design of new, Li-ion technologies.

Advancing and deploying renewable energy technologies requires the application of experimental and computational methods capable of characterizing solid–aqueous and solid–organic electrochemical interfaces at atomic and molecular levels. Whereas fundamental understanding of the forces that control the efficiency of solid–aqueous interfaces is rather advanced^{1–5}, the picture of solid–organic interfaces is still quite hazy due to the lack of complementary information about structure–function relationships in organic solvents. For example, despite decades of research into Li-ion batteries (LIBs), whose performance largely depends on the formation of the so-called solid electrolyte interphase (SEI) on the graphite anode, detailed mechanistic understanding of the nature of SEI formation and its resulting structure remains elusive^{6–11}. As a result, the development of electrolytes for LIB remains a somewhat empirical process, with the most common electrolytes consisting of a combination of lithium hexafluorophosphate (LiPF₆) salt with a binary solvent mixture of cyclic and linear alkyl carbonates such as ethylene carbonate (EC) and ethyl methyl carbonate (EMC). The selection of these electrolytes is based on their high salt solubility, high ionic conductivity and the formation of a stable SEI that simultaneously minimizes electrolyte decomposition while still providing high Li⁺ diffusivity¹².

The morphological and compositional picture of the SEI formed in such environments is complex, involving numerous proposed reaction products, with solid LiF (LiF_(s)) consistently found as one of the main SEI components^{8,13–15}. It is generally accepted that the formation of LiF_(s) can occur through both chemical reactions of LiPF₆ with water or HF with organic or inorganic carbonates, as well as through the electrochemical reduction of PF₃O and/or PF₆[–] (refs 16–19). Although plausible, it has never been confirmed experimentally that these reactions do indeed lead to the formation of LiF_(s). However, one report provided some evidence that the formation

of LiF_(s) could also be controlled by the electroreduction of HF²⁰, with HF being a highly detrimental product formed in the reaction between trace levels of H₂O and LiPF₆ (refs 21–27). Impurity levels of HF present in organic electrolytes can affect all components of the battery, impacting the formation of the SEI as well as inducing dissolution (corrosion) of the oxide cathode materials and inactive components of the cell^{28–31}. All of these processes can significantly affect battery performance and, as a result, understanding the role of HF electrochemistry in EC:EMC LiPF₆ electrolytes at atomic and molecular levels would contribute immensely to the current understanding of the fundamental electrochemistry of LIB electrolytes.

The study reported herein identifies the electrocatalytic transformation of HF to LiF_(s) and H₂ in EC:EMC LiPF₆ electrolytes by using a surface science-based strategy that has been successfully used in the past to unravel the complexities controlling the efficiency of energy conversion and storage processes at solid–aqueous electrochemical interfaces^{32–35}. The formation of LiF_(s) and H₂ was first explored on well-characterized single crystals of Ir(111), Pt(111), Au(111) and Cu(111) and graphene-modified Pt(111). Then, the knowledge gained from model systems was translated to carbon-based materials ranging from basal plane and edge-exposed highly ordered pyrolytic graphite (HOPG) to real graphite anodes. From experimental and computational trends established on single crystals, we found that HF dissociation and concomitant LiF_(s) and H₂ formation are governed by a synergy between the nature of surface atoms and potential-driven covalent and non-covalent interactions in the double layer. Beyond mechanistic understanding, these results provide insights into the previously overlooked importance of electrocatalysis in the formation of LiF_(s) and H₂ on metals, graphene, basal plane and edge-exposed HOPG, and more realistic graphite powder surfaces in organic electrolytes. Furthermore, our approach reveals intriguing relationships between the substrate-controlled

¹Materials Science Division, Argonne National Laboratory, Argonne, IL, USA. ²Nano-Science Center, Department of Chemistry, University of Copenhagen, Copenhagen, Denmark. ³Chair of Technical Electrochemistry, Department of Chemistry and Catalysis Research Center, Technische Universität München, Garching, Germany. ⁴Battery Cell Technology, BMW Group, München, Germany. *e-mail: strmcnik@anl.gov; jan.rossmeisl@chem.ku.dk

morphology of and passivation by $\text{LiF}_{(s)}$, as well as between the density of surface defects and the kinetics of electrolyte decomposition. Taken together, the results reveal that $\text{LiF}_{(s)}$ precipitation and H_2 evolution during SEI formation in LIBs is in fact controlled by an interplay between the electrochemical and chemical reactivity of two impurities— H_2O and HF.

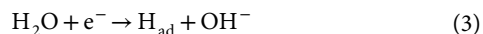
Results

Electrochemistry of H_2O and HF on metal single crystals. We began by evaluating the concentration of various organic and inorganic impurities present in commercially available 1 M LiPF_6 in EC:EMC (3:7 wt%) electrolytes (commercially known as LP57 and hereafter referred to simply as 1 M LiPF_6), with particular interest in determining the concentration of the two most significant impurities— H_2O and HF^{21,25–27}. While the amount of water in the electrolytes was determined using a standard Karl Fischer titration, a novel method was implemented for the determination of HF. Some 100 μl of sample electrolyte was injected into 10 ml of total ion strength adjustment buffer (TISAB) and the concentration of fluoride ion was determined with a fluoride ion-selective electrode (ISE) using a calibration curve generated using previously prepared standards. Perhaps counterintuitively, the dilution of the non-aqueous sample of LiPF_6 in TISAB essentially quenches any further hydrolysis of LiPF_6 , which makes such analysis possible (for more details, see the Supplementary Methods, Supplementary Fig. 1 and Supplementary Table 1). The concentrations of HF and H_2O in the as-received, commercial 1 M LiPF_6 were found to be in the ranges 30–60 ppm and 1–5 ppm, respectively, with the markedly lower H_2O concentration resulting from the slow but quantitative conversion of H_2O to HF. To measure the rate of this conversion, a fixed quantity of water was added to homemade 1 M LiPF_6 and the concentrations of H_2O and F^- were measured as a function of time. As shown in Fig. 1, for the initial value of HF present in the as-prepared electrolytes (~20 ppm), the addition of 50, 100 and 150 ppm of water resulted in the formation of 120, 220 and 300 ppm of HF, as expected based on the following equations.



One mole of H_2O leads to the formation of two moles of HF (see Methods for details). The ability to control and quantitatively measure the transformation of H_2O into HF in 1 M LiPF_6 served as an important method to explore how different concentrations of HF may affect the electrochemistry, as discussed below.

To demonstrate a strong link between the chemistry of HF in LiPF_6 electrolytes and the electrocatalytic dissociation of water in aqueous electrolytes, we first summarize trends in the hydrogen evolution reaction (HER) on Cu(111), Au(111), Ir(111) and Pt(111) in 0.1 M KOH (Fig. 2a). The HER in alkaline solutions is usually assumed to proceed by the following reaction steps³⁶.



where H_{ad} is the adsorbed reactive intermediate. The rate of this reaction was strongly dependent on the nature of the electrode material and increased in the order $\text{Cu}(111) < \text{Au}(111) \ll \text{Pt}(111) < \text{Ir}(111)$. This arose due to differences in the water dissociation step ($\text{Cu} > \text{Ir} > \text{Pt} > \text{Au}$)^{37,38} and metal– H_{ad} binding energies ($\text{Ir} \sim \text{Pt} \gg \text{Au} \sim \text{Cu}$)^{39,40}. An optimal balance between these two descriptors resulted in activity that decreased in the order $\text{Ir}(111) > \text{Pt}(111)$

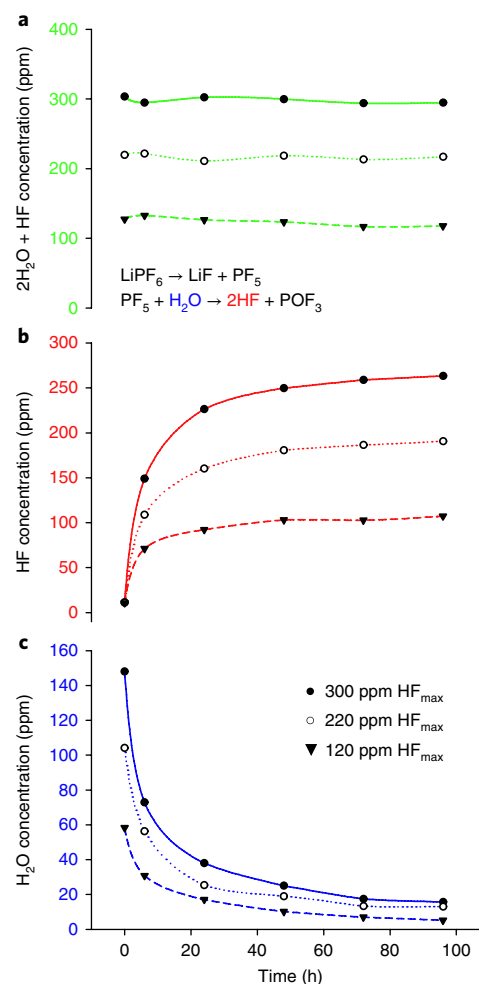


Fig. 1 | Chemical transformation of H_2O to HF in 1 M LiPF_6 . Concentrations of water (blue) and HF (red) as a function of time after the addition of different concentrations of water (50, 100 and 150 ppm) to 1 M LiPF_6 in EC:EMC (3:7 wt%). The HF concentration was measured using a fluoride ISE and the H_2O concentration was measured via Karl Fischer titration. The total H concentration (green), presented as the sum of $2\text{H}_2\text{O} + \text{HF}$, is constant and confirms the quantitative transformation of H_2O to HF in a 1:2 ratio. Note that: (1) the starting values for HF were 20 ppm for the as-prepared electrolyte, which affected the final HF concentration after the addition of water; and (2) the final values of HF were not reached after 96 h. After 14 days, the water concentrations were 4.9, 2.5 and 2.1 ppm, respectively, and the HF concentrations were close to the maximum values depicted in green; that is, 300, 220 and 120 ppm, respectively. The HF concentrations were divided by 1.1 to compare stoichiometry, based on the molar masses 20 and 18 g mol^{-1} for HF and H_2O , respectively.

$\gg \text{Au}(111) > \text{Cu}(111)$. The same trend was observed for polarization curves recorded on these single crystal surfaces in 1 M LiPF_6 (Fig. 2b), suggesting that the reaction steps in this organic electrolyte may be conceptually similar to those involved in H_2 production from H_2O ⁴¹. A noticeable difference is that for all surfaces depicted in Fig. 2b, an initial exponential increase in current was followed by a rather fast deactivation and very little activity during subsequent sweeps (for Au(111), see Supplementary Fig. 2), indicating passivation from surface product(s) formed during the course of the reaction (in line with LiO_2 electrochemistry in organic environments⁴²).

The morphology and chemical nature of the deposit were explored by combing ex situ atomic force microscopy (AFM) and

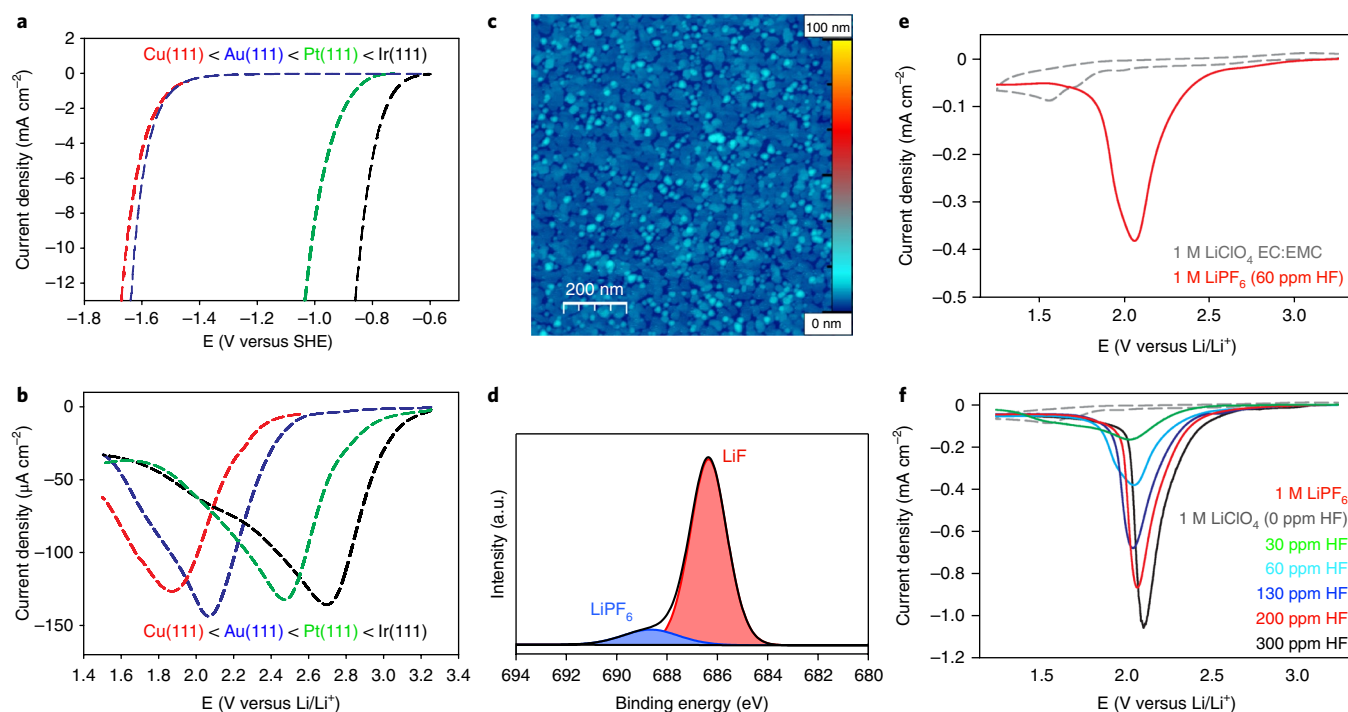


Fig. 2 | Electrochemical transformation of HF to LiF and H₂ on well-defined metal surfaces. **a**, HER trend on four metal single crystal surfaces in 0.1 M KOH. **b**, HER trend on the same surfaces in 1 M LiPF₆ containing 30 ppm HF. **c**, AFM image of a LiF film on an Au(111) surface after 2 potential sweeps from 3.3 to 1.25 V versus Li/Li⁺. **d**, F 1s XPS spectrum of Au(111) after 2 potential sweeps from 3.3 to 1.25 V versus Li/Li⁺. The formation of LiF_(s) was further confirmed using a combination of inductively coupled plasma mass spectrometry and fluoride ISE to quantify the ratio between Li⁺ and F⁻ produced after dissolution of the SEI film in water (see also Supplementary Methods and Supplementary Table 1). Li and F were found to be in a 1:1 stoichiometric ratio, with the amount corresponding to a ~2.5-nm-thick film (when compact). **e**, Electrochemical response of Au(111) in 1 M LiPF₆ containing 60 ppm HF and in HF-free EC:EMC (3:7 wt%) with 1 M LiClO₄. **f**, Dependence of the main electroreduction peak on Au(111) on the concentration of HF. Different concentrations of HF were obtained by adding the appropriate amounts of water to homemade 1 M LiPF₆. The measurement in 1 M LiClO₄ was taken as 0 ppm HF. HF concentrations were measured before and after the electrochemical experiment. All curves were measured with a sweep rate of 50 mV s⁻¹.

X-ray photoelectron spectroscopy (XPS). For clarity, we summarize only the results for Au(111) as a representative of the single crystals considered in this work (Fig. 2c,d). A close inspection of AFM images revealed the presence of a compact, crack free film with large (around 50–100 nm) two-dimensional grain size domains (Fig. 2c), while chemical analysis of this film via XPS (Fig. 2d) indicated that it consists predominately of LiF_(s) and a small amount of either LiP_xO_yF_{z(s)} formed from side reactions or—even more likely—LiPF₆ due to residual salt not removed during sample rinsing (for more details, see Supplementary Figs. 7–9 and Supplementary Table 2). We note that the SEI peak positions are shifted to slightly higher binding energies than expected due to differential charging of the highly insulating LiF layer relative to the conductive substrate⁴³. This phenomenon is quite common when analysing SEI layers on LIB electrodes, but is seldom discussed, leading to a large spread in binding energy values for SEI components reported in the literature⁸. Based on these results and a complementary experiment in which the composition of the dissolved film was probed by inductively coupled plasma mass spectrometry and fluoride ISE measurements (for details, see Supplementary Table 1), we concluded that a compact layer of LiF_(s) was formed on Au(111), as well as other single crystal metal surfaces, during the first cathodic sweep. To develop mechanistic insights into the process(es) that may lead to LiF_(s) formation, we made use of the rotating disk electrode (RDE) method to explore how the current-voltage traces shown in Fig. 2b were affected by both the rotation rate of the electrode and the concentration of HF (Fig. 2f). As displayed in Supplementary Fig. 3 for Au(111), the current increased with increasing rotation rate for the same concentration of HF, indicating that the reaction is mediated

by the transport of at least one of the reactants to the electrode surface, and that the reactant is present in a small concentration (that is, its supply is limited). Notice also that although diffusion-limited currents are never established because of potential-dependent surface passivation by LiF_(s) (that is, currents do not follow a Levich-type behaviour), the peak current and corresponding charge still increase with the rotation rate. Furthermore, systematic variation of the concentration of HF in 1 M LiPF₆ between 30 and 300 ppm (Fig. 2f) yielded a linear increase in the kinetic current density with increasing HF concentration, strongly suggesting that the reduction process is controlled by HF electrochemistry. Additional confirmation is provided by the fact that no reaction takes place between 2.0–2.5 V in 1 M LiClO₄ (Fig. 2e).

Based on the above experimental evidence, it is plausible to conclude that the reduction process(es) observed during the very first potential sweep from 3.5 to 1.5 V is governed by the surface electrochemistry of HF reduction; for example, the dissociation of HF and subsequent H₂ production according to equations (5) and (6):



A schematic representation of the proposed processes that control H₂ and HF production is given in Fig. 3 and supported by

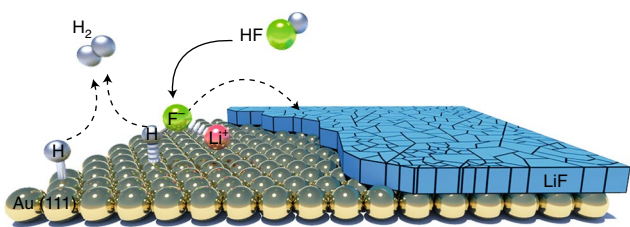


Fig. 3 | Schematic of the proposed reaction mechanism for the electrocatalytic conversion of HF to H₂ and LiF. The thickness of the LiF film, as well as its morphology, is affected by the kinetics of the electrochemical reaction (equation (5)), transport of the reactant HF and the kinetics of the LiF crystallization process (equation (7)). DFT calculations have pointed out that there is a correlation between the first electrochemical response and the non-specific adsorption potential of Li⁺ for the different investigated metals (Supplementary Fig. 15b). This also suggests that the non-specific adsorption of Li⁺ plays a critical role in the splitting of HF, as shown in the schematics and reaction path in Supplementary Fig. 15a. It seems, in fact, that the presence of Li⁺ in the double layer reduces the barrier for the dissociation of the HF molecule (see Supplementary Methods for more details).

density functional theory (DFT) calculations that are described in detail in the Supplementary Methods. As summarized by equations (5)–(7), the potential-controlled dissociative adsorption of HF leads to the formation of H_{ad} and F⁻, which—in an electrochemical-chemical reaction scheme—are very quickly transformed to H₂ and LiF_(s). In line with the HER in aqueous environments, it is likely that the kinetics of the HER in 1 M LiPF₆ is directed by an optimal balance between the energy required for the dissociation of HF and the metal–H_{ad} binding energy, supporting the proposition that there are inherently close ties between interfacial phenomena in aqueous and organic environments—a very important subject that has rarely been discussed².

Besides the obvious similarities between aqueous and organic environments, there are also important differences between the HER in alkaline and EC:EMC LiPF₆ electrolytes. By comparing Fig. 2a,b it is obvious that, in contrast with OH⁻ in alkaline solution, the generated F⁻ ions in equation (7) readily react with Li⁺ ions present in the double layer of the metal–1 M LiPF₆ interface. This, in turn, results in the formation of spectator LiF_(s), which blocks the metal active centres required for the HER to take place. In addition to this surface poisoning effect, deactivation of the HER is also caused by the diffusion-limited transport of HF to the electrode surface. Taken together, the shape of the current-voltage curves in Fig. 2b is controlled by a delicate balance between the transport of HF to the surface, the kinetics of the electrochemical reduction of HF to H₂ on metal surfaces (equations (5) and (6)), and the kinetics of LiF_(s) formation in the double layer and its passivation of the metal surfaces (equation 7). We note that our mechanistic insight differs significantly from a previous hypothesis that the first reduction peak centred at around 2.5 V is the result of the so-called underpotential deposition of hydrogen (H_{upd})²⁰ during HF reduction on polycrystalline Pt. In particular, our results for Cu(111) and Au(111), which do not form H_{upd} but show the same behaviour as Pt(111) and Ir(111) (Fig. 2b), clearly demonstrate that the sharp peak is caused by the HER rather than the formation of H_{upd}. Note also that purely kinetic current for the HER from HF is observed only in the early stages of the electroreduction process between 2.50 and 2.25 V. In this potential range, the current is linearly dependent on the concentration of HF. However, the total charge under individual curves approaches a constant value with increasing HF concentration (Supplementary Fig. 4), consistent with precipitation of LiF_(s) at or near the electrode that lags behind the electrochemical HER step but ultimately leads

to passivation of the active surface. As we discuss further below, the kinetics of these processes, as well as the thickness and morphology of LiF_(s), is critically dependent on the nature of the substrate.

Electrochemistry of HF on carbon systems. To bridge the gap between the model systems discussed above and real graphitic anode materials, HF electrochemistry in 1 M LiPF₆ was examined on multilayer graphene (MLG) synthesized on Pt(111) single crystals via chemical vapour deposition (see Methods for details). The Pt(111)–MLG offers the closest possible approximation to a defect-free, well-ordered graphite surface, as shown by a combination of crystal truncation rod and scanning tunnelling microscopy measurements that indicate the presence of around five layers of graphene on Pt(111) (Supplementary Figs. 10 and 11) and show that the topmost layer of graphene is nearly defect free (Supplementary Fig. 10). A representative electrochemical response on such a surface (Fig. 4a) revealed that the main voltammetric feature on the negative sweep direction from 3.25 V is a sharp peak at ~0.25 V, which is ~2 V more negative than that observed on the rather inactive Au(111) surface. This sharp peak, which was enlarged by increasing both the rotation rate and the concentration of HF (Fig. 4b), is associated with the HF-controlled production of H₂ and LiF_(s) by analogy with related processes on single crystals (see equations (5)–(7)). Under our experimental conditions, XPS analysis (Supplementary Figs. 8 and 9) confirmed that the main surface product formed below 1.0 V is LiF_(s). The difference in reactivity between metal surfaces and graphene is in good agreement with the intrinsically high energy barrier required for splitting HF (attenuating the dissociation kinetics), accompanied by lower availability of non-specifically adsorbed Li⁺ (due to the lower work function; Supplementary Fig. 16) and a weak graphene–H_{ad} interaction (reducing the surface coverage by H_{ad}). Note that no organic or inorganic carbonates were found in the SEI on MLG (Fig. 4d), indicating unique properties of this carbon surface compared with other carbon samples found in the literature.

In contrast with single crystal surfaces (Fig. 2), subsequent cycles on Pt(111)–MLG (Supplementary Fig. 5) did not exhibit strong deactivation due to surface passivation, indicating that film morphology may vary between metal and graphitic substrates. Indeed, AFM images of LiF_(s) on graphene (Fig. 4c) revealed a highly porous, granular film (grain size: 10–30 nm), with a root mean square roughness 5 times higher relative to films formed on single crystal metals (Fig. 2c and Supplementary Table 3). Cracks and grain boundaries in the film were also observed on both small and larger scales (20 μm × 20 μm; Supplementary Fig. 12), in contrast with films formed on metal surfaces. As such, it is plausible to expect the film to be permeable to species from the electrolyte, which may explain, at least qualitatively, why LiF_(s) does not passivate graphene surfaces for further HF reaction in subsequent cycles.

Additional insight into the morphological role of the substrate on the SEI layer can be gleaned by comparing HF electrochemistry on more defected HOPG surfaces, which are even closer in structure to real graphite anode materials. Electrochemical results are summarized in Fig. 4e,f for basal-plane and edge-exposed HOPG, respectively. In agreement with previous findings⁴⁴, the very first polarization curve recorded on the basal plane shows two sharp reduction peaks at 0.7 and 0.25 V. During the second potential excursion, the more positive peak completely vanishes, whereas the peak at 0.25 V remains unchanged even after several consecutive cycles, resembling the behaviour of this feature observed for graphene. In agreement with graphene electrochemistry, the current density for the reduction process at 0.25 V is enhanced as the rotation rate (Supplementary Fig. 6) and concentration of HF are increased, suggesting that this process is also controlled by HF dissociation and the formation of LiF_(s) and H₂. In contrast, the reduction peak at 0.7 V was only observed in the first scan and was highly dependent on the cleavage of the HOPG substrate, which indicates

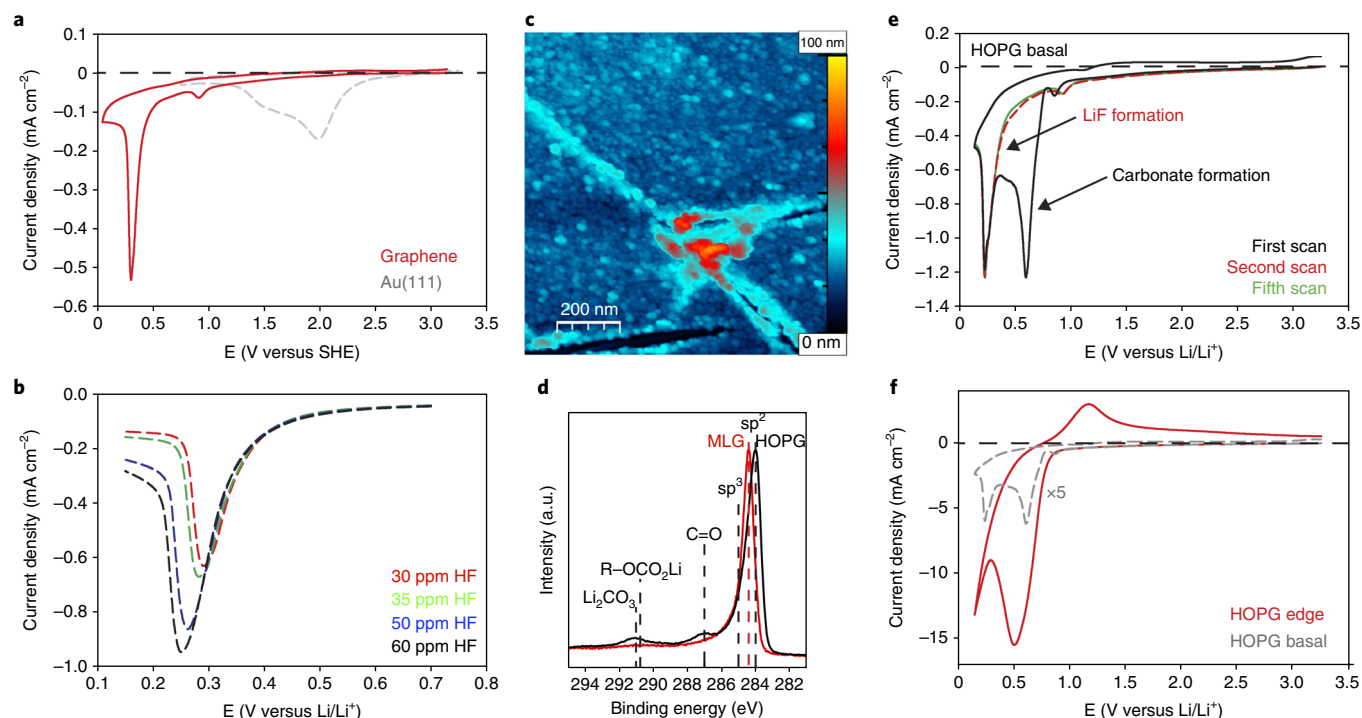


Fig. 4 | Electrochemical transformation of HF to LiF and H₂ on well-defined carbon surfaces. **a**, Electrochemical response of Pt(111)-MLG in 1M LiPF₆ containing 30 ppm HF compared with Au(111) in the same electrolyte. **b**, Dependence of the main cathodic peak of Pt(111)-MLG in 1M LiPF₆ on the concentration of HF. **c**, AFM image of the LiF film on graphene after 1 potential scan from 3.5–0.1V versus Li/Li⁺. **d**, XPS C1s spectra of Pt(111)-MLG and basal-plane HOPG after a potential excursion to 0.25V versus Li/Li⁺, respectively. **e**, Electrochemical response of basal-plane HOPG in 1M LiPF₆ containing 60 ppm HF. **f**, Electrochemical response of edge-exposed HOPG in 1M LiPF₆ containing 60 ppm HF. All measurements were performed at 50 mV s⁻¹.

that the density of defects such as step edges and other defects on HOPG may control the kinetics of this process. XPS analysis of the C1s of HOPG surfaces revealed the presence of C=O (287.0 eV), R-OCO₂Li (~291 eV) and CO₃ (~291 eV) species^{3,18,44} that were not observed on Pt(111)-MLG surfaces (Fig. 4d). At this point, we do not have any direct evidence to explain the absence of solvent decomposition and carbonate formation on graphene; however, the appearance of the additional feature at 0.7V on HOPG surfaces along with the additional features in the C1s strongly indicate that this electrochemical feature is related to solvent decomposition on HOPG. The role of defects was further probed on edge-exposed HOPG (Fig. 4f), where a tremendous increase in the reduction current below 0.8V was observed, completely obscuring the formation of LiF_(s) and H₂ by simultaneous electrolyte decomposition and/or Li intercalation processes^{45–49}. In our opinion, these observations, along with the strong dependence of the electrochemical response on the HOPG cleavage, warrants the explanation that surface defects on graphite, which were to a large extent absent on our graphene sample, are most likely to be the active sites for solvent decomposition. Note also that almost no LiF was found on HOPG surfaces when the potential window was closed to 0.5V versus Li/Li⁺. As shown in Supplementary Fig. 7, significant LiF formation on HOPG or graphene does not take place until electrodes are cycled through the electrochemical process at 0.25V. This directly opposes the proposed mechanism of LiF formation that is often found in the literature, which suggests that surface carbonates react with HF and produce LiF_(s)^{16,17,23,29}.

Electrochemistry of HF in real systems. To close the loop, we directly monitored H₂ production on real, high-surface-area graphitic anode materials to understand the influence of HF content

on the HER in 1M LiPF₆ under battery-operating conditions. Both RDE and online electrochemical mass spectrometry (OEMS) were used to explore HF electrochemistry on SLP30 graphite in 1M LiPF₆ electrolytes containing 60 or 260 ppm HF. Figure 5a shows the first reductive voltammetric scan obtained either on an SLP30 graphite-coated RDE (0.3 mg SLP30 cm⁻² disk at 50 mV s⁻¹) or in an SLP30/lithium-iron-phosphate cell (4.7 mg SLP30 cm⁻² disk at 0.2 mV s⁻¹) connected to the OEMS. In the first potential cycle from 3.5V, the first current onset in RDE curves recorded at 50 mV s⁻¹ (Fig. 5a) was observed at ~2V, followed by a sharp increase in activity at around 0.5V. Not surprisingly, due to the very slow sweep rate for polarization curves recorded in the OEMS setup (0.2 mV s⁻¹), it was very difficult to obtain clear-cut evidence for the potential at which the first reaction might start. As in the past, however, OEMS provides quantitative information about the potential-dependent production of gases that can be formed in the course of the reaction, as summarized in electrolytes containing 60 (Fig. 5b) and 260 ppm HF (Fig. 5c). Several observations are noteworthy. First, a fourfold increase in HF concentration produces roughly a fourfold increase in hydrogen production (indicated by the accumulated amount of H₂ in the OEMS cell at the end of the reductive voltammetric scan; that is, at 0V), which confirms the correlation between HF concentration and the amount of evolved hydrogen. Second, the HER onset is observed at ~2V, suggesting that the currents observed in the RDE experiment were most likely due to H₂ production. Third, it is plausible that the small, yet clearly discernible, currents starting at ~2V on model carbon systems under the same experimental conditions (Fig. 4 and Supplementary Figs. 5 and 6) can also be linked to HF reduction to H₂. That H₂ formation is clearly observable in OEMS experiments is due to the 20-times-higher active surface area of SLP30 graphite than graphene or HOPG samples, which leads

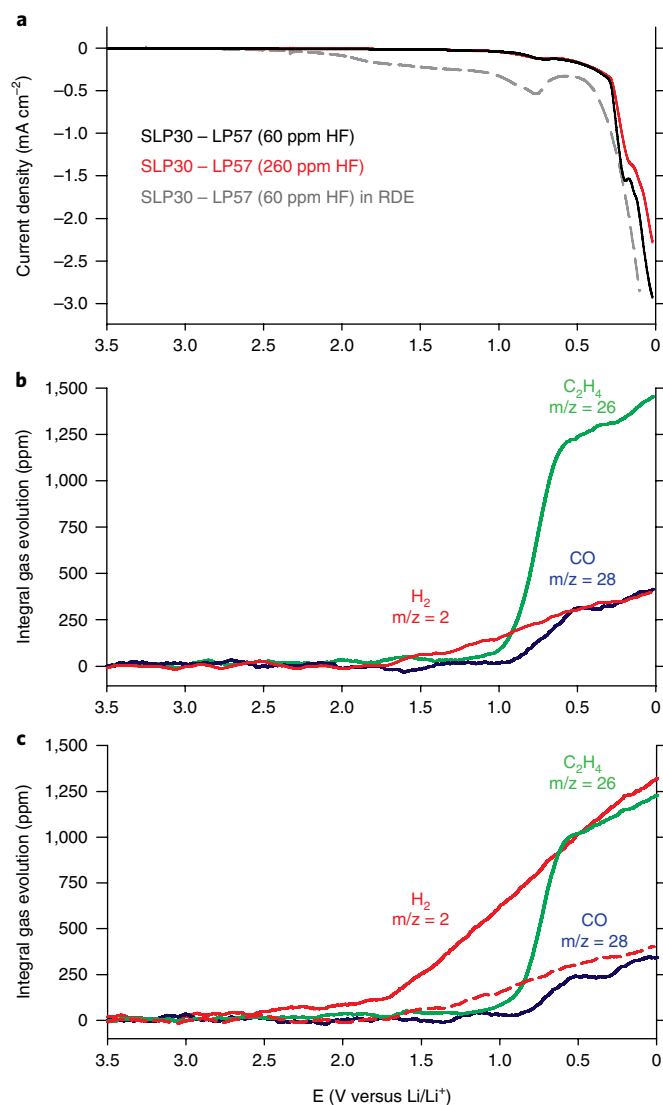


Fig. 5 | Electrochemical transformation of HF to LiF and H₂ on a real graphite sample. **a**, Electrochemical response of SLP30 graphite in 1 M LiPF₆ in a real graphite/lithium-iron-phosphate cell (black and red curves), measured at 0.2 mV s⁻¹ and in the RDE configuration of our 3-electrode electrochemical cell (grey curve), measured at 50 mV s⁻¹. **b,c**, OEMS measurements of gas evolution from SLP30 graphite electrodes during the potential scan 3.5–0 V versus Li/Li⁺ in 1 M LiPF₆ containing 60 ppm HF (**b**) and 260 ppm HF (**c**). The dashed red line in **c** is the H₂ trace from **b**, shown for comparison.

to a significant increase in the number of active surface sites, possibly surface defects, and thus higher currents. Finally, the evolution of C₂H₄ (a well-known product of the reduction of EC) and CO (a minor reduction product) initiates just below 1.0 V versus Li/Li⁺, which is identical to the previously reported onset potential and C₂H₄/CO ratio⁵⁰ and clearly indicates that the LiF formed from the reduction of HF does not result in a sufficiently passivating surface to prevent EC reduction.

As expected, there are differences and similarities between model experiments in an RDE configuration and real battery cells. Although the chemistry does not really change from the model to real system, the relative abundance of SEI components, as well as the onset of their production, does. We argue that this is mainly caused by the significantly larger ratio of electrode surface area to electrolyte volume (~10⁶ times) for the graphite electrode in the OEMS cell

compared with well-defined surfaces in the three-electrode electrochemical cell. This difference probably introduces a significant number of surface defects, as well as imposing a restriction on the maximum possible LiF surface coverage³¹ on graphite that can be achieved upon complete reduction of all residual HF in the OEMS cell. In a typical battery cell, this will result in the formation of only one or two monolayers of LiF, compared with several nanometres in a typical RDE configuration.

Nevertheless, the above experimental results indicate that the simultaneous formation of LiF_(s) and H₂ in 1 M LiPF₆ on anode electrodes is much simpler than was considered thus far. Through systematic investigation, it was possible to gain fundamental understanding of how the synergy between the structure and nature of surface atoms, covalent and non-covalent forces, and ppm levels of electrolyte (H₂O and HF), as well as electrode material defects, control the electrocatalytic dissociation of HF and the concomitant adsorption of H_{ad} (HER), the interaction of F⁻ and Li⁺, and the precipitation of LiF—a key part of the SEI. Although this work does not directly address the role of LiF in battery performance, it creates a platform for such understanding. We conclude that our finding is of general importance and we believe it will lead to new opportunities for the improvement of existing systems and the design of new LIB technologies.

Methods

Extended surface electrode preparation. Pt(111), Ir(111), Au(111), Pt-poly and Ir-poly electrodes were prepared by inductive heating for 5 min at 1,050 °C for Pt, 800 °C for Au and Cu, and 1,200 °C for Ir electrodes in an argon hydrogen flow (3% hydrogen). The annealed specimens were cooled slowly to room temperature under an inert atmosphere and then assembled into an RDE. Voltammograms were recorded in argon-saturated electrolytes.

Preparation of carbon samples. Multilayer graphene was grown on Pt(111) heated to 1,050 °C in methane flow. The HOPG ZYA-type crystal with basal exposed plane (Princeton Scientific) was assembled into the RDE and freshly cleaved with adhesive tape inside the glove box before each experiment. The HOPG ZYA-type crystal with an edge-exposed plane (Princeton Scientific) was cut parallel to the edge surface with a stainless steel blade to expose fresh surface and subsequently washed with EMC, dried and inserted into the RDE. SLP30 graphite powder (TIMREX by Imerys Graphite & Carbon; Brunauer–Emmett–Teller (BET) surface area: ~7 m² g⁻¹) was dry-casted from an EMC suspension onto a glassy carbon electrode assembled into the RDE with a loading of 0.3 mg cm⁻². For the OEMS experiments, SLP30 graphite was prepared as an ink with polyvinylidene fluoride and N-methyl-2-pyrrolidone and then blade-coated onto a porous Celgard separator (see Supplementary Information for details). In both cases, the electrode with SLP30 was dried overnight in a vacuum oven at 95 °C.

Chemicals. For the aqueous experiments, 0.1 M KOH was prepared from highest-purity Sigma–Aldrich KOH and Millipore Milli-Q water. For the non-aqueous experiments, LP57 (1 M LiPF₆ in EC:EMC (3:7 wt)) purchased from BASF, or homemade 1 M LiPF₆ prepared from EC, EMC and LiPF₆ (all from BASF) were used. Argon gas used for purging was 5N5 quality and purchased from Airgas. 1 M LiPF₆ electrolytes containing various concentrations of HF were prepared by adding the appropriate volumes of water to homemade 1 M LiPF₆ and waiting for 2 weeks for the H₂O concentration to fall below 5 ppm (see main text and Supplementary Information). Note that according to equations (1) and (2), LiF is also formed in this process. However, this LiF stays as a precipitate in the electrolyte container and does not make it into the electrochemical cell.

Water and HF determination. Water content in electrolytes was measured using Karl Fischer titration (Mettler Toledo) placed inside an Ar-filled glove box with a H₂O level below 0.5 ppm. HF content was measured using fluoride ISE (Mettler Toledo perfectION combination fluoride electrode) in our newly developed method for fluoride determination in LiPF₆ electrolytes. Low-level TISAB of the following composition was used for all fluoride measurements: 57 ml glacial acetic acid, and 58 g sodium chloride dissolved in water in a 1 l volumetric flask and with the pH adjusted to 5.0–5.5 using 1 M NaOH (all chemicals were purchased from Sigma–Aldrich).

Electrochemical measurements. With the exception of the OEMS experiments (see Supplementary Methods), a three-electrode glass cell was used in all experiments. All of the experiments executed in this cell were performed within minutes of introducing the electrolyte into the cell, thus preventing significant reaction of HF with the glass. Furthermore, fluoride ISE measurements before and

after electrochemistry revealed no significant changes in the HF concentration, further indicating that there was no significant reaction of HF with the glass. Finally, XPS measurements of the electrode surfaces revealed no evidence of Si, indicating that there was no participation of dissolved SiO_x in the reactions studied. Gold wire was used as a counter electrode and Ag/AgCl or Ag/Ag⁺ electrodes were used as reference electrodes for the aqueous and non-aqueous experiments, respectively. All potentials are given either on an RHE scale or an Li/Li⁺ scale. Conversion of the Ag/Ag⁺ scale to an Li/Li⁺ scale was done by electrodeposition and stripping Li on a glassy carbon electrode in a separate experiment, establishing the position of the Li/Li⁺ reversible potential. Experiments were controlled using an Autolab PGSTAT302N potentiostat. For the rotating disk experiments, a Pine Modulated Speed Rotator system was used. All reported polarization curves and voltammograms were first-cycle measurements (unless explicitly stated otherwise) to limit the effects of possible contamination from the electrolyte. All non-aqueous electrochemical experiments were performed inside the glove box.

XPS measurements. XPS measurements were performed using a SPECS PHOIBOS 150 Hemispherical Energy Analyzer with a monochromated Al K α X-ray source. The load-lock of the analytical ultra-high vacuum system was connected directly to an Ar-filled glove box, enabling the loading of samples without any exposure to ambient atmosphere. Survey spectra were measured using a pass energy of 40 eV at a resolution of 0.2 eV step⁻¹ and a total integration time of 0.2 s point⁻¹. Core-level spectra were measured using a pass energy of 20 eV at a resolution of 0.05 eV step⁻¹ and a total integration time of 0.5 s point⁻¹. A charge-neutralizing electron flood gun was used for some samples to attempt to address differential charging between highly insulating LiF and conductive substrates. Deconvolution was performed using CasaXPS software (<http://www.casaxps.com/>) with a Shirley-type background and 70–30 Gaussian–Lorentzian peak shapes. In general, spectra were charge referenced using the position of the Au 4f_{7/2} at 84.0 eV, Pt 4f_{7/2} at 71.2 eV and C1s at 284.0 eV for the Au, Pt–MLG and HOPG samples, respectively. See the Supplementary Methods for a detailed discussion of charge referencing, differential charging and charge compensation on these samples.

AFM measurements. After the electrochemical measurements, the samples were taken out of the glove box and transferred to a Bruker Dimension Icon Atomic Force Microscope in a vibration isolation enclosure for imaging. An Si TESP-V2 tapping tip was used to obtain the images.

DFT calculations. The calculations were performed using the GPAW code^{51,52}, and the structures as well as the molecular dynamics were run using the ASE package⁵³. The calculations were performed using RPBE as an exchange–correlation functional⁵⁴ and a single k-point (Gamma), and we applied the dipole correction to correctly handle the electrostatic potential in the z-direction at the periodic boundary condition. The characteristic time for the Berendsen thermostat was set to 2,000 fs and the time step was set to 1 fs. This procedure has been previously applied to water⁵⁵ (see Supplementary Methods for details).

Data availability. All data that support the findings of this study are available from the corresponding author upon reasonable request.

Received: 30 August 2017; Accepted: 23 February 2018;

Published online: 9 April 2018

References

- Ross, P. N. & Lipkowsky, J. *Structure of Electrified Interfaces* (VCH, New York, 1993).
- Stamenkovic, V. R., Strmcnik, D., Lopes, P. P. & Markovic, N. M. Energy and fuels from electrochemical interfaces. *Nat. Mater.* **16**, 57–69 (2017).
- Wieckowski, A. *Interfacial Electrochemistry* (Marcel Dekker, New York, 1999).
- Marković, N. & Ross, P. N. Surface science studies of model fuel cell electrocatalysts. *Surf. Sci. Rep.* **45**, 117–229 (2002).
- Nørskov, J. K., Bligaard, T., Rossmeisl, J. & Christensen, C. H. Towards the computational design of solid catalysts. *Nat. Chem.* **1**, 37–46 (2009).
- An, S. J. et al. The state of understanding of the lithium-ion-battery graphite solid electrolyte interphase (SEI) and its relationship to formation cycling. *Carbon NY* **105**, 52–76 (2016).
- Peled, E. & Menkin, S. Review—SEI: past, present and future. *J. Electrochem. Soc.* **164**, A1703–A1719 (2017).
- Verma, P., Maire, P. & Novák, P. A review of the features and analyses of the solid electrolyte interphase in Li-ion batteries. *Electrochim. Acta* **55**, 6332–6341 (2010).
- Nie, M., Abraham, D. P., Chen, Y., Bose, A. & Lucht, B. L. Silicon solid electrolyte interphase (SEI) of lithium ion battery characterized by microscopy and spectroscopy. *J. Phys. Chem. C* **117**, 13403–13412 (2013).
- Owejan, J. E., Owejan, J. P., Decaluwe, S. C. & Dura, J. A. Solid electrolyte interphase in Li-ion batteries: evolving structures measured in situ by neutron reflectometry. *Chem. Mater.* **24**, 2133–2140 (2012).
- Soto, F. A., Ma, Y., Martinez De La Hoz, J. M., Seminario, J. M. & Balbuena, P. B. Formation and growth mechanisms of solid–electrolyte interphase layers in rechargeable batteries. *Chem. Mater.* **27**, 7990–8000 (2015).
- Xu, K. Nonaqueous liquid electrolytes for lithium-based rechargeable batteries. *Chem. Rev.* **104**, 4303–4417 (2004).
- Aurbach, D. Review of selected electrode–solution interactions which determine the performance of Li and Li ion batteries. *J. Power Sources* **89**, 206–218 (2000).
- Edström, K., Herstedt, M. & Abraham, D. P. A new look at the solid electrolyte interphase on graphite anodes in Li-ion batteries. *J. Power Sources* **153**, 380–384 (2006).
- Zhang, B. et al. Role of 1,3-propane sultone and vinylene carbonate in solid electrolyte interface formation and gas generation. *J. Phys. Chem. C* **119**, 11337–11348 (2015).
- Leroy, S., Martinez, H., Dedryvère, R., Lemordant, D. & Gonbeau, D. Influence of the lithium salt nature over the surface film formation on a graphite electrode in Li-ion batteries: an XPS study. *Appl. Surf. Sci.* **253**, 4895–4905 (2007).
- Leroy, S. et al. Surface film formation on a graphite electrode in Li-ion batteries: AFM and XPS study. *Surf. Interface Anal.* **37**, 773–781 (2005).
- Aurbach, D., Zinigrad, E., Cohen, Y. & Teller, H. A short review of failure mechanisms of lithium metal and lithiated graphite anodes in liquid electrolyte solutions. *Solid State Ion.* **148**, 405–416 (2002).
- Aurbach, D., Markovsky, B., Shechter, A., Ein-Eli, Y. & Cohen, H. A comparative study of synthetic graphite and Li electrodes in electrolyte solutions based on ethylene carbonate–dimethyl carbonate mixtures. *J. Electrochem. Soc.* **143**, 3809–3820 (1996).
- Lee, H., Cho, J.-J., Kim, J. & Kim, H.-J. Comparison of voltammetric responses over the cathodic region in LiPF₆ and LiBETI with and without HF. *J. Electrochem. Soc.* **152**, A1193–A1198 (2005).
- Terborg, L. et al. Investigation of thermal aging and hydrolysis mechanisms in commercial lithium ion battery electrolyte. *J. Power Sources* **242**, 832–837 (2013).
- Kawamura, T., Okada, S. & Yamaki, J. Decomposition reaction of LiPF₆-based electrolytes for lithium ion cells. *J. Power Sources* **156**, 547–554 (2006).
- Aurbach, D. et al. Recent studies on the correlation between surface chemistry, morphology, three-dimensional structures and performance of Li and Li-C intercalation anodes in several important electrolyte systems. *J. Power Sources* **68**, 91–98 (1997).
- Plakhotnyk, A. V., Ernst, L. & Schmutzler, R. Hydrolysis in the system LiPF₆–propylene carbonate–dimethyl carbonate–H₂O. *J. Fluor. Chem.* **126**, 27–31 (2005).
- Nakajima, T. & Groult, H. *Fluorinated Materials for Energy Conversion* (Elsevier, Oxford, 2005).
- Lux, S. F. et al. The mechanism of HF formation in LiPF₆ based organic carbonate electrolytes. *Electrochem. Commun.* **14**, 47–50 (2012).
- Aurbach, D. Electrode–solution interactions in Li-ion batteries: a short summary and new insights. *J. Power Sources* **119–121**, 497–503 (2003).
- Zhang, Z. & Zhang, S. S. *Rechargeable Batteries: Materials, Technologies and New Trends* (Springer, New York, 2015).
- Wang, R., Li, X., Wang, Z. & Guo, H. Manganese dissolution from LiMn₂O₄ cathodes at elevated temperature: methylene methanedisulfonate as electrolyte additive. *J. Solid State Electrochem.* **20**, 19–28 (2016).
- Pieczonka, N. P. W. et al. Understanding transition-metal dissolution behavior in LiNi_{0.5}Mn_{1.5}O₄ high-voltage spinel for lithium ion batteries. *J. Phys. Chem. C* **117**, 15947–15957 (2013).
- Kang, S. J., Yu, S., Lee, C., Yang, D. & Lee, H. Effects of electrolyte-volume-to-electrode-area ratio on redox behaviors of graphite anodes for lithium-ion batteries. *Electrochim. Acta* **141**, 367–373 (2014).
- Strmcnik, D. et al. When small is big: the role of impurities in electrocatalysis. *Top. Catal.* **58**, 1174–1180 (2015).
- Marković, N., Gasteiger, H., Grgur, B. & Ross, P. Oxygen reduction reaction on Pt(111): effects of bromide. *J. Electroanal. Chem.* **467**, 157–163 (1999).
- Strmcnik, D. S. et al. Unique activity of platinum adislands in the CO electrooxidation reaction. *J. Am. Chem. Soc.* **130**, 15332–15339 (2008).
- Subbaraman, R. et al. Origin of anomalous activities for electrocatalysts in alkaline electrolytes. *J. Phys. Chem. C* **116**, 22231–22237 (2012).
- Vetter, K. J. *Electrochemical Kinetics: Theoretical and Experimental Aspects* (Academic, New York, 1967).
- Thiel, P. A., Madey, T. E. & Sloan, A. P. The interaction of water with solid surfaces: fundamental aspects. *Surf. Sci. Rep.* **7**, 211–385 (1987).
- Henderson, M. A. The interaction of water with solid surfaces: fundamental aspects revisited. *Surf. Sci. Rep.* **46**, 1–308 (2002).
- Trasatti, S. Work function, electronegativity, and electrochemical behaviour of metals: III. Electrolytic hydrogen evolution in acid solutions. *Electroanal. Chem. Interfac. Electrochem.* **39**, 163–184 (1972).
- Greeley, J., Jaramillo, T. F., Bonde, J., Chorkendorff, I. & Nørskov, J. K. Computational high-throughput screening of electrocatalytic materials for hydrogen evolution. *Nat. Mater.* **5**, 909–913 (2006).

41. Strmcnik, D., Lopes, P. P., Genorio, B., Stamenkovic, V. R. & Markovic, N. M. Design principles for hydrogen evolution reaction catalyst materials. *Nano Energy* **29**, 29–36 (2016).
42. Staszak-Jirkovský, J. et al. Water as a promoter and catalyst for dioxygen electrochemistry in aqueous and organic media. *ACS Catal.* **5**, 6600–6607 (2015).
43. Maibach, J., Lindgren, F., Eriksson, H., Edström, K. & Hahlin, M. Electric potential gradient at the buried interface between lithium-ion battery electrodes and the SEI observed using photoelectron spectroscopy. *J. Phys. Chem. Lett.* **7**, 1775–1780 (2016).
44. Matsuoka, O. et al. Ultra-thin passivating film induced by vinylene carbonate on highly oriented pyrolytic graphite negative electrode in lithium-ion cell. *J. Power Sources* **108**, 128–138 (2002).
45. Alliaia, D., Kötz, R., Novák, P. & Siegenthaler, H. Electrochemical SPM investigation of the solid electrolyte interphase film formed on HOPG electrodes. *Electrochem. Commun.* **2**, 436–440 (2000).
46. Jeong, S.-K., Inaba, M., Abe, T. & Ogumi, Z. Surface film formation on graphite negative electrode in lithium-ion batteries: AFM study in an ethylene carbonate-based solution. *J. Electrochem. Soc.* **148**, A989–A993 (2001).
47. Domi, Y. et al. Electrochemical AFM observation of the HOPG edge plane in ethylene carbonate-based electrolytes containing film-forming additives. *J. Electrochem. Soc.* **159**, A1292–A1297 (2012).
48. Domi, Y. et al. In situ AFM study of surface film formation on the edge plane of HOPG for lithium-ion batteries. *J. Phys. Chem. C* **115**, 25484–25489 (2011).
49. Peled, E. et al. Composition, depth profiles and lateral distribution of materials in the SEI built on HOPG-TOF SIMS and XPS studies. *J. Power Sources* **97–98**, 52–57 (2001).
50. Metzger, M., Strehle, B., Solchenbach, S. & Gasteiger, H. A. Origin of H₂ evolution in LIBs: H₂O reduction vs. electrolyte oxidation. *J. Electrochem. Soc.* **163**, A798–A809 (2016).
51. Mortensen, J. J., Hansen, L. B. & Jacobsen, K. W. Real-space grid implementation of the projector augmented wave method. *Phys. Rev. B Condens. Matter Mater. Phys.* **71**, 1–11 (2005).
52. Enkovaara, J. et al. Electronic structure calculations with GPAW: a real-space implementation of the projector augmented-wave method. *J. Phys. Condens. Matter* **22**, 253202 (2010).
53. Hjorth Larsen, A. et al. The atomic simulation environment—a Python library for working with atoms. *J. Phys. Condens. Matter* **29**, 273002 (2017).
54. Hammer, B., Hansen, L. & Nørskov, J. Improved adsorption energetics within density-functional theory using revised Perdew–Burke–Ernzerhof functionals. *Phys. Rev. B* **59**, 7413–7421 (1999).
55. Hansen, M. H. & Rossmeisl, J. pH in grand canonical statistics of an electrochemical interface. *J. Phys. Chem. C* **120**, 29135–29143 (2016).

Acknowledgements

This research was sponsored by BMW Technology Corporation. The research was conducted at Argonne National Laboratory—a US Department of Energy Office of Science laboratory operated by UChicago Argonne under contract number DE-AC02-06CH11357 and in part at the Technische Universität München. We acknowledge support from the Office of Science, Office of Basic Energy Sciences and Materials Sciences and Engineering Division. We also thank C. Thompson and H. You for help with the AFM and crystal truncation rod measurements.

Author contributions

D.S., J.G.C., H.A.G. and N.M.M. conceived and designed the experiments. D.S., J.G.C., D.H., M.Z., P.M., P.P.L. and B.G. performed the experiments. I.E.C., T.Ø. and J.R. performed the calculations. D.S., J.G.C., I.E.C., F.M., B.K.A., J.R., H.A.G., V.R.S. and N.M.M. discussed the results and wrote the paper.

Competing interests

The authors declare no competing interests.

Additional information

Supplementary information is available for this paper at <https://doi.org/10.1038/s41929-018-0047-z>.

Reprints and permissions information is available at www.nature.com/reprints.

Correspondence and requests for materials should be addressed to D.S. or J.R.

Publisher's note: Springer Nature remains neutral with regard to jurisdictional claims in published maps and institutional affiliations.

In the format provided by the authors and unedited.

Electrocatalytic transformation of HF impurity to H₂ and LiF in lithium-ion batteries

Dusan Strmcnik^{1*}, Ivano E. Castelli², Justin G. Connell¹, Dominik Haering³, Milena Zorko¹, Pedro Martins¹, Pietro P. Lopes¹, Bostjan Genorio¹, Thomas Østergaard², Hubert A. Gasteiger³, Filippo Maglia⁴, Byron K. Antonopoulos⁴, Vojislav R. Stamenkovic¹, Jan Rossmeisl^{2*} and Nenad M. Markovic¹

¹Materials Science Division, Argonne National Laboratory, Argonne, IL, USA. ²Nano-Science Center, Department of Chemistry, University of Copenhagen, Copenhagen, Denmark. ³Chair of Technical Electrochemistry, Department of Chemistry and Catalysis Research Center, Technische Universität München, Garching, Germany. ⁴Battery Cell Technology, BMW Group, München, Germany. *e-mail: strmcnik@anl.gov; jan.rossmeisl@chem.ku.dk

Electrocatalytic transformation of HF impurity to H₂ and LiF in lithium ion batteries

Supplementary information

Supplementary methods

Development of a new method for fluoride determination in LP57:

Our new method targets the specific problem of fluoride determination in Li-ion battery electrolytes. As a sensor, we chose the fluoride ion selective electrode (ISE) because it offers i) wide concentration range for analysis, ii) high throughput, iii) low cost and iv) straightforward operation. The problem with fluoride ISE, however, is that it does not work well in non-aqueous solvents. It usually requires a significant addition (approx. 10% of water) to the organic electrolyte in order for it to work. In the case of EC/EMC/LiPF₆ electrolyte, such an addition is not possible as water doesn't mix with this electrolyte in a roughly 0.05-0.95 volume ratio, and water also reacts with LiPF₆ in the electrolyte to form HF and POF₃, thus compromising the sample. We overcame these obstacles by developing a simple, yet effective protocol for analyzing battery electrolyte samples:

1. Generate a calibration curve with a fluoride standard in 1:1 H₂O:TiSAB (total ion strength adjustment buffer) aqueous solution
2. Prepare 10 ml 1:1 H₂O:TiSAB mixture with a magnetic stirrer, stirring at medium speed
3. Prepare the fluoride electrode for measurement, (wash fluoride electrode with H₂O, dry the fluoride electrode)
4. Transfer 100 µl of electrolyte sample out of the glove box (the sample is not shaken or stirred during sampling)
5. Inject 100 µl of the sample into 10 ml H₂O:TiSAB mixture (dilution of 1:100) while stirring – in this counterintuitive step we dilute the non-aqueous sample in a 100 times excess of H₂O/TISAB. We found that EC/EMC/LiPF₆ mixes well with water in this ratio but more importantly, this step inhibits reaction (1), essentially freezing the fluoride concentration in the sample to its original value. This has been confirmed by measuring known amounts of fluoride standard in organic electrolyte (Supplementary Figure 1). Moreover, we demonstrated that the addition of 1% EC/EMC to TiSAB does not change the response of the fluoride ISE as well as that the measured fluoride value does not change significantly within 24 hours of measurement.
6. Place fluoride electrode in H₂O:TiSAB mixture with the sample while stirring
7. Measure the potential of the fluoride electrode (with internal reference electrode) or the potential of the fluoride electrode versus a reference electrode immersed in the H₂O:TiSAB mixture
8. Use the calibration curve to calculate the fluoride content of the organic sample, also taking into account the dilution of the sample

Analysis of LP57 commercial electrolyte, SEI composition:

Supplementary Table 1 summarizes the analysis results of 2 samples: As-received commercial LP57 and the water dissolved SEI from Au(111).

The LP57 electrolyte (1M LiPF₆ in EC:EMC (3:7 wt%)) was obtained from BASF and was tested for organic and inorganic impurities using Agilent Technologies 7000C GS-MS Triple Quad, Perkin Elmer NexION 300D ICP-MS, Mettler-Toledo C20 Karl-Fischer Titrator and Mettler-Toledo fluoride ISE. The main organic impurities found were diethyl carbonate and dimethyl carbonate, which are products of transesterification of EMC. The main inorganic impurities were water and HF. No significant trace metal impurities were found in the electrolyte.

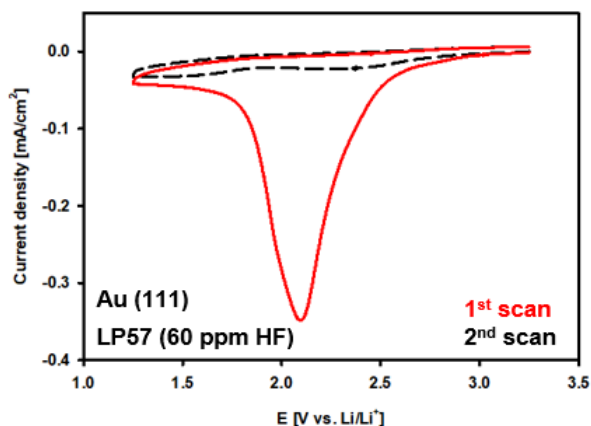
In order to support the XPS analysis of the passive film on Au(111), we dissolved the film in water and tested the obtained solution with ICP-MS for Li⁺ and with the ISE for F⁻. The amounts of Li⁺ and F⁻, which are summarized in Supplementary Table 1, were close to a 1:1 ratio, which supports the XPS data for LiF as the main component of the SEI. Considering the film from a 0.2826 cm² electrode was dissolved in 400 μL of TISAB, we calculate the film thickness to be around 2.5 nm if compact, slightly less than that calculated from integration of the charge under the reduction peak (2.8 nm). Note that the amount of charge passed through the interface in a single sweep corresponds to less than 0.1% of the total HF concentration in the cell. To underline this, we measured the HF concentration in the cell before and after experiment and it remained unchanged.

Supplementary Table 1: Results of analysis of as received LP57, SEI film on Au(111) dissolved in water.

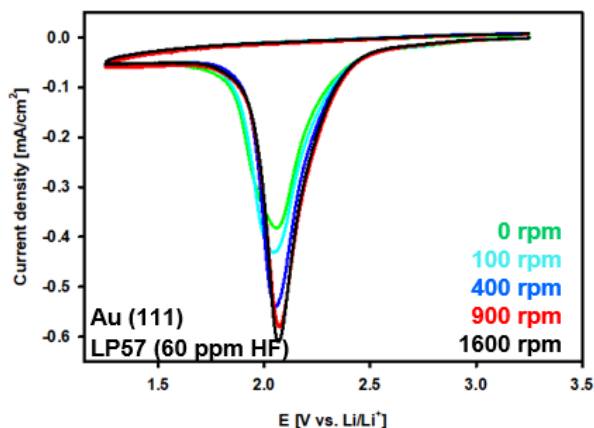
Component	Sample	Detection Method	Concentration	Comments
LiPF ₆	LP57-BASF	Vendor spec	12.7 wt %	
EC	LP57-BASF	Vendor spec	26.2 wt %	
EMC	LP57-BASF	Vendor spec	61.1 wt%	
DEC	LP57-BASF	GC-MS	0.4 wt%	
DMC	LP57-BASF	GC-MS	0.2 wt%	
H ₂ O	LP57-BASF	Karl-Fischer	1-5 ppm	Depending on batch
HF	LP57-BASF	ISE	30-60 ppm	Depending on batch
Metals	LP57-BASF	ICP-MS	below 1ppm	Other than Li
Li ⁺	SEI on Au(111)	ICP-MS	1.83 10 ⁻⁵ mol/L	Corresponding to 2.5
F ⁻	SEI on Au(111)	ISE	1.80 10 ⁻⁵ mol/L	nm of compact film

Electrochemical measurements:

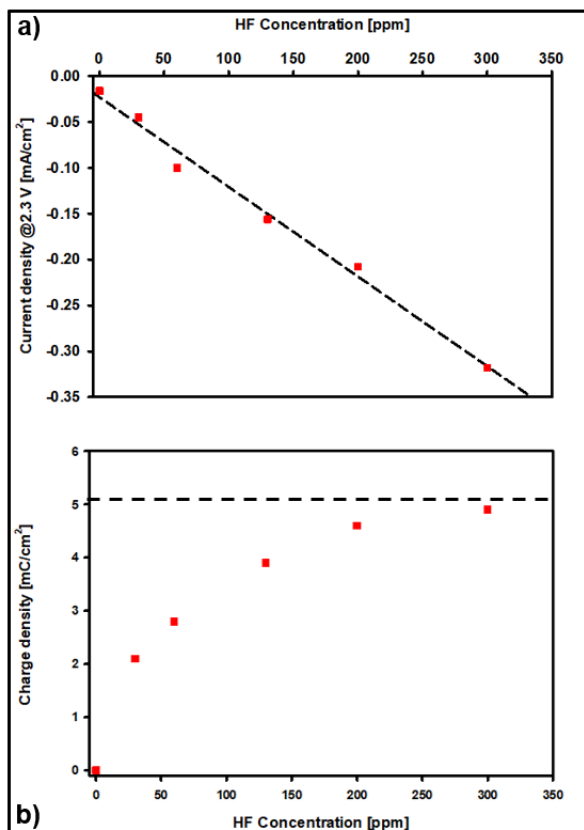
All electrochemical measurements were performed inside a glovebox using a three-electrode electrochemical cell. Au wire was used as a counter electrode, separated from the working electrode compartment by a frit. Ag/AgNO₃ electrode was used as a reference electrode. All potentials are given vs. Li/Li⁺ electrode. All single crystal electrodes were annealed and transferred to the electrochemical cell inside the glovebox. First scans are reported for all the electrodes, unless stated otherwise.



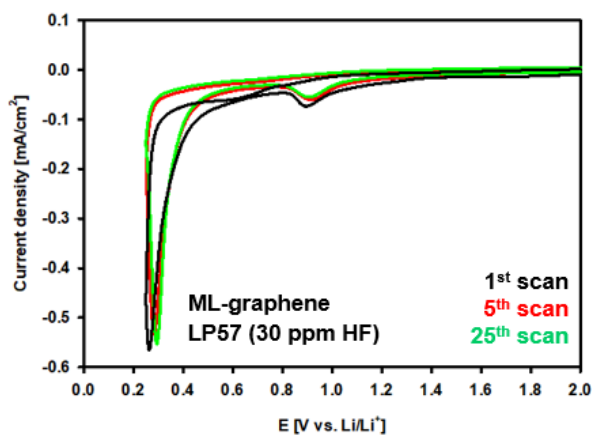
Supplementary Figure 2: First and second scan of Au(111) electrode in LP57 containing 60 ppm of HF. Scans are performed at 50 mV/s. Almost a complete passivation of the electrode is observed in the first scan as by the substantially diminished currents in the second scan.



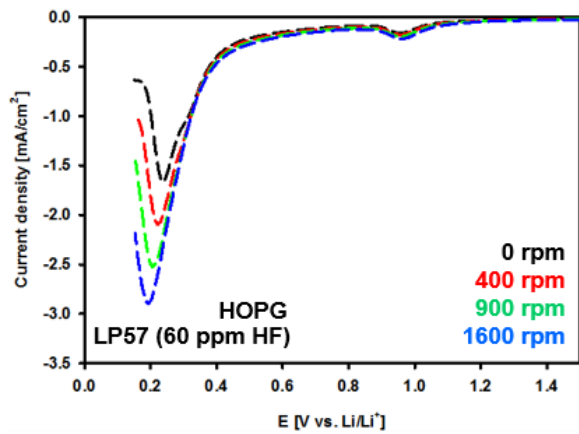
Supplementary Figure 3: Rotation rate dependence of the main reduction peak on Au(111) electrode. As can be seen, the peak current shows a significant dependency at lower rotation rates and lesser at higher rotation rates, typical of a passivation process that requires a certain amount of charge to pass (product to form) in order to passivate the electrode completely. In addition, this result demonstrates that the reactant is not present in abundance, signaling that we might be observing the reduction of an impurity rather than a main component of the electrolyte.



Supplementary Figure 4: Plots of a) the kinetic current density values and b) total charge density values taken from the curves in Figure 2f. A linear dependence of the kinetic current density on the concentration of HF is observed while the total charge approaches a constant value, consistent with a passivation process.



Supplementary Figure 5: Electrochemical response of multilayer graphene in LP57 shows no passivation with subsequent scans despite evidence from XPS measurements of thickening of LiF with additional scans.



Supplementary Figure 6: Rotation rate dependence of the main reduction peak on a basal HOPG electrode. In contrast with Au single crystal surface, the electrode does not passivate upon deposition of the LiF film, hence the linear increase of peak current with $\omega^{1/2}$.

XPS Measurements:

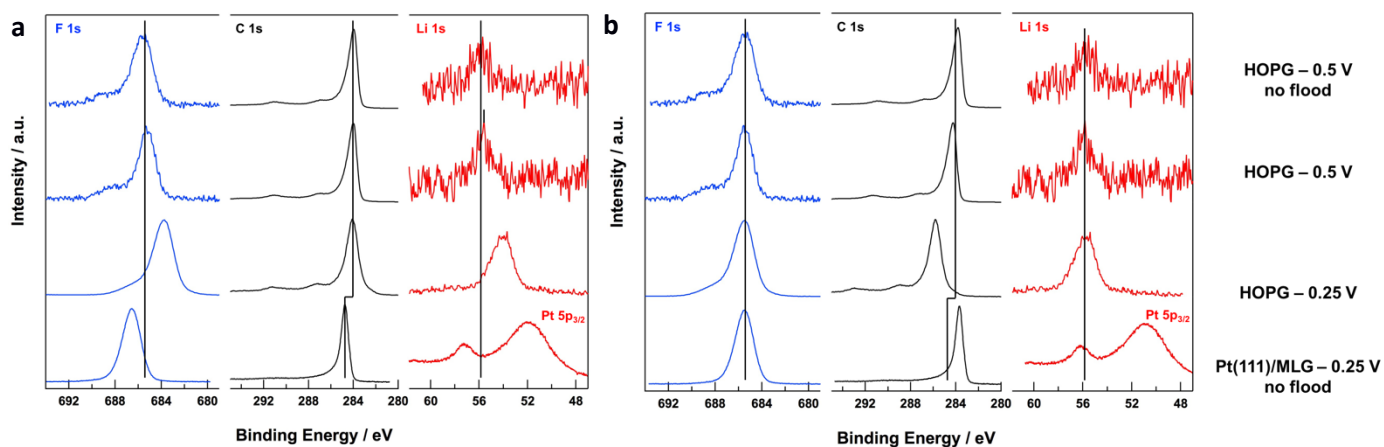
XPS measurements were performed using a Specs PHOIBOS 150 hemispherical energy analyzer using a monochromated Al K α X-ray source. The load-lock of the analytical UHV system is connected directly to an Ar-filled glove box, enabling the loading of samples without any exposure to ambient atmosphere. Survey spectra were measured using a pass energy of 40 eV at a resolution of 0.2 eV/step and a total integration time of 0.2 sec/point. Core level spectra were measured using a pass energy of 20 eV at a resolution of 0.05 eV/step and a total integration time of 0.5 sec/point. A charge neutralizing electron flood gun was used for some samples to attempt to address differential charging between highly insulating LiF and conductive substrates. Deconvolution was performed using CasaXPS software with a Shirley-type background and 70-30 Gaussian-Lorentzian peak shapes. In general, spectra were charge referenced using the position of the Au 4f_{7/2} at 84.0 eV, Pt 4f_{7/2} at 71.2 eV and C 1s at 284.0 eV for Au, Pt-MLG and HOPG samples, respectively. A detailed discussion of charge referencing, differential charging and charge compensation is given below.

Assignment of LiF from XPS Analysis

There is significant spread in literature values for the position of LiF in the F 1s core level. Examining the NIST database¹ provides 6 values for the LiF peak position, yielding an average binding energy (BE) of 685.5 ± 0.7 eV. Our observation of the main F 1s peak on Au(111) at 686.3 ± 0.2 eV, although at the high end, falls within this range of peak positions for LiF. This uncertainty is further reflected in a comprehensive review cited in the manuscript [Verma et al. – ref 8], which lists the LiF peak position as 685.0-686.4 eV and is also consistent with our peak assignment. No data is available for LiPF₆ on the NIST database, but Ref 8 in the main text identifies this peak position as 688 eV, which is lower than the peak position observed on Au(111) but within experimental error if there is a similar degree of uncertainty as that found on the NIST database for LiF (± 0.7 eV). As we discuss below, it is likely that the higher BE location of both peaks is due to differential surface charging. It is also possible that the peak we assign to LiPF₆ could correspond to a LiP_xO_yF_z-type compound; however, the absence of any measurable P signal on this sample makes it impossible to distinguish which species dominates. As PF₆ is present in significant concentration in the electrolyte (1.2M) and there is a significantly higher fraction of F in PF₆ than any LiP_xO_yF_z-type compound, the assignment of PF₆ seems far more likely than an oxyfluorophosphate species given the lack of measurable P signal. Nevertheless, this peak represents 8.5% of the total F signal and 1.8% of the total surface signal (see quantification discussion below), and as a result this peak does not represent a majority surface species that can account for the electrochemistry reported in the paper.

One likely explanation for the high BE F 1s peak locations is differential surface charging due to the highly insulating nature of LiF relative to the highly conductive Au(111) substrate. The data in Figure 2d for Au(111) was acquired without the use of an electron flood gun to compensate for surface charging; however, the use of a low energy flood gun during the analysis of a variety of other samples failed to provide adequate matching of the LiF surface potential to that of the underlying substrate, again likely due to the large difference in conductivity between the LiF and the substrate. This effect is particularly pronounced when comparing between samples of differing LiF film thickness and/or homogeneity across the surface (i.e. Pt(111)/MLG vs. HOPG). Figure

S7a illustrates this phenomenon, where a significant spread in the LiF peak positions in both the F 1s and Li 1s core levels is observed when using the C 1s peak position as a charge reference (284.0 eV for HOPG and 284.4 eV for graphene, calibrated separately using the Pt 4f_{7/2} peak at 71.2 eV). Spectra acquired both with and without the use of a charge compensating electron flood gun are shown to illustrate that the flood gun is unable to completely compensate for differential charging on these samples, instead shifting the LiF peaks to lower binding energy with respect to the underlying conductive substrate. If we charge reference the data such that the main F 1s peak is located at 685.5 eV (consistent with the NIST database value for LiF, Supplementary Figure 7b), we find that the main Li 1s peaks are also similarly aligned at 56.1 ± 0.2 eV, exactly matching the NIST database value for LiF in the Li 1s of 56.1 ± 0.6 eV (or 55.1 ± 2.6 eV if a significant outlier in the database is included).



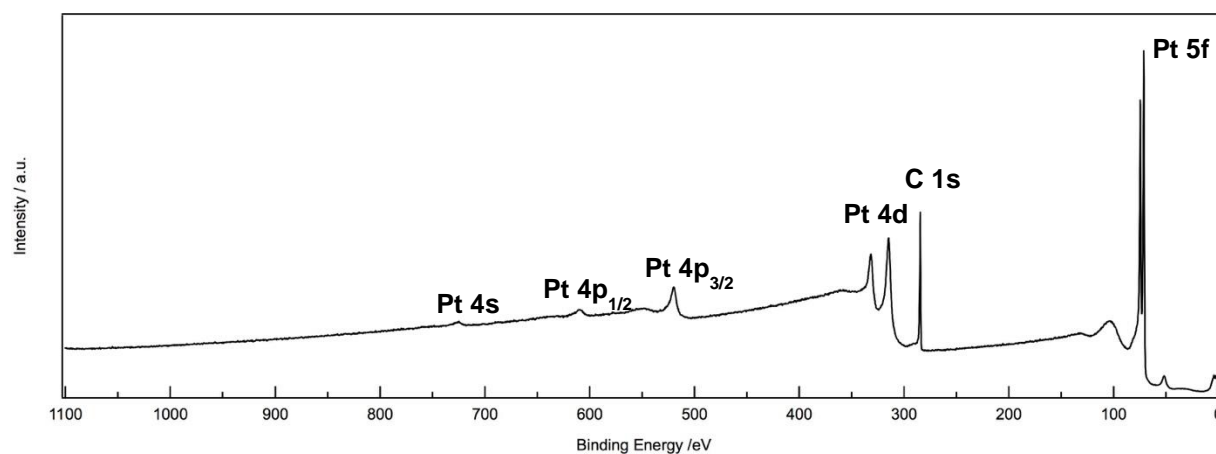
Supplementary Figure 7: XPS analysis of F 1s, C 1s and Li 1s core level spectra charge referenced using (a) C 1s at 284.0 eV (HOPG) and 284.4 eV (graphene), and (b) F 1s at 285.5 eV (NIST value for LiF). Note also that significant LiF formation does not take place on HOPG surfaces until after the potential is swept through the feature at 0.25 V vs. Li/Li⁺ (see Supplementary Table 2 below for quantification).

However, in light of the issues with differential surface charging on these samples, we do not make our assignment of LiF based solely on peak position, but instead also rely on quantitative analysis of survey spectra taken on the same sample surfaces. Supplementary Table 2 summarizes the quantification of the survey spectra shown in Supplementary Figure 9a, clearly demonstrating that Li and F are present in a 1:1 ratio on Pt(111)/MLG surfaces, and that there is negligible concentration of other surface species. Deviation from the 1:1 Li:F ratio on Au(111) surfaces is due to the fact that the Li 1s is completely overlapped by the Au 5p_{3/2} (Supplementary Figure 9c). The very large sensitivity factor for the Li 1s, in combination with this overlap, results in significant error in the quantification, as small changes in the Li 1s intensity derived from deconvolution of the lower resolution survey spectrum results in large variation in the apparent surface concentration. Nevertheless, the results on Pt(111)/MLG, taken together with the above analysis of differential charging and the ICP-MS and fluoride ISE measurements on Au(111) summarized in Supplementary Table 1, we can say with certainty that the primary surface species on all samples analyzed in this work is LiF.

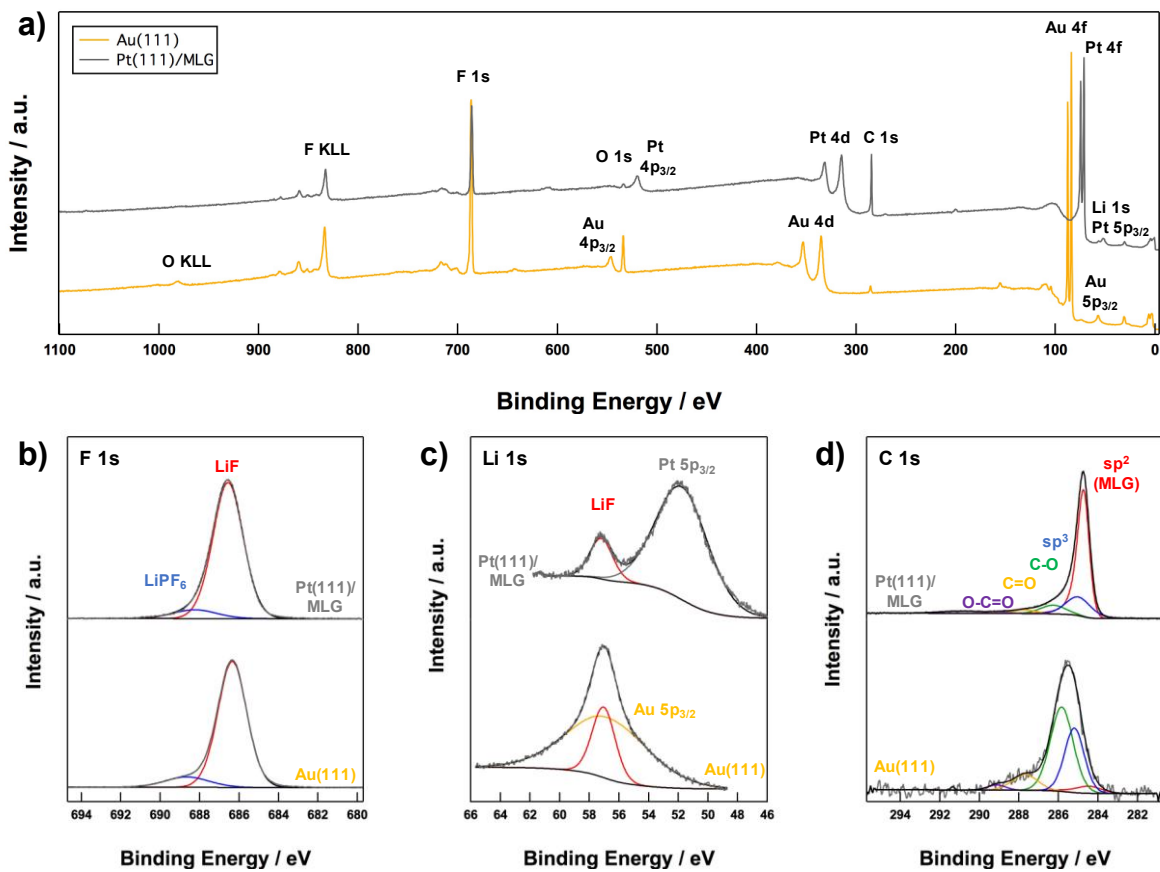
Supplementary Table 2: XPS quantification of survey spectra in Supplementary Figure 9 and basal HOPG surfaces analyzed in Supplementary Figure 7. The potentials given along with each surface indicate the negative vertex potential applied during the voltammetric sweep.

Species	Concentration (at%)			
	Au(111) (1.25 V)	Pt(111)/MLG (0.25 V)	Basal HOPG (0.5 V)	Basal HOPG (0.25 V)
Li	50.0	24.2	0.0*	35.2
F	29.7	22.4	1.5	28.6
O	7.4	1.4	4.6	3.8
C	3.4	37.3	93.9	31.6
Au/Pt	9.5	14.8	0.0	0.0
P	0.0	0.0	0.0	0.9

* Due to low signal in the survey spectrum, reliable quantification of Li was not possible; however, high resolution core level spectra (Supplementary Figure 7) reveal the presence of a measurable Li peak, consistent with the presence of R-OCO₂Li species noted in Figure 4d, as well as with the slight Li excess measured on HOPG samples cycled to lower potentials.



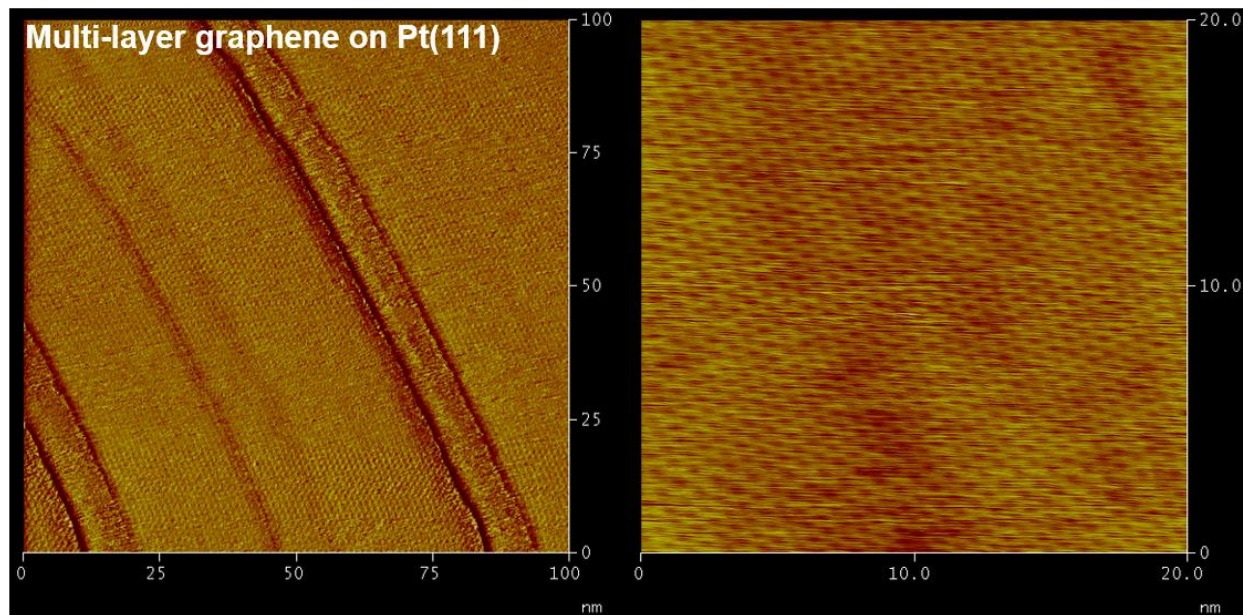
Supplementary Figure 8: XPS survey spectrum of a Pt(111)/MLG electrode cycled to 1.25 V vs. Li/Li⁺ in 1M LiPF₆, clearly demonstrating that there is no LiF deposited on the surface in the absence of electrochemical reactions.



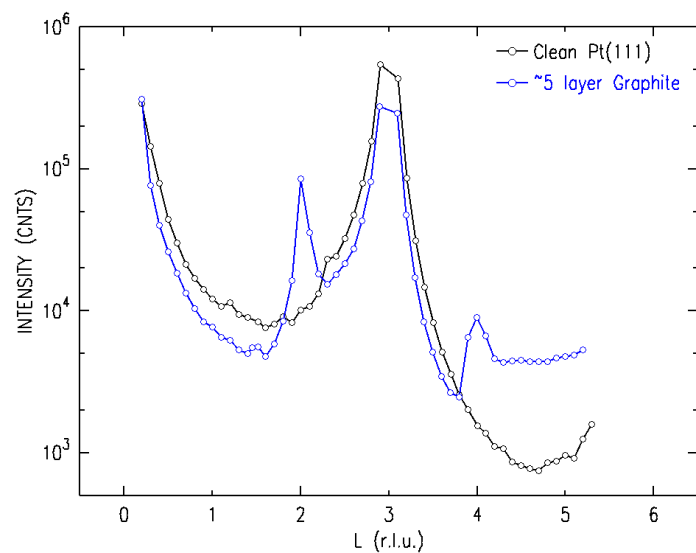
Supplementary Figure 9: (a) XPS Survey spectra comparing Au(111) and Pt(111)/MLG after sweeping potential to 1.25 V and 0.25 V, respectively, to form LiF. Signal from Au substrate is significantly more attenuated relative to signal from Pt/MLG, indicating Au surface is covered in a thicker/more continuous LiF film. (b) F 1s, (c) Li 1s and (d) C 1s core level spectra confirm the presence of LiF, with no evidence of carbonate species.

STM and CTR measurements:

The model carbon surface was graphene grown by CVD on Pt (111) crystal. We report here the STM images and crystal truncation rod (CTR) data testifying to the quality of the surface as well as to the graphitic nature of the multilayer graphene.



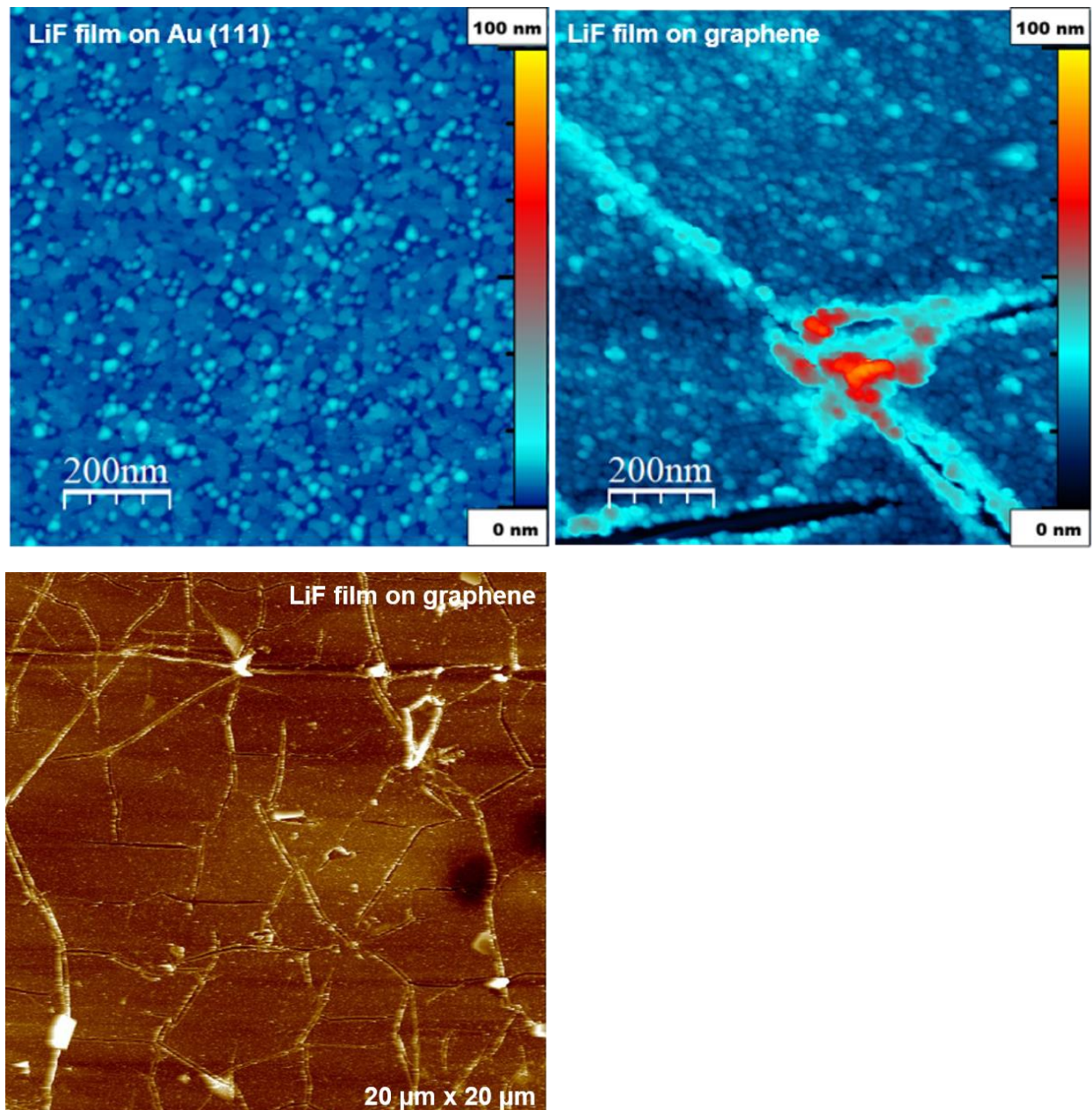
Supplementary Figure 10: STM images of the multi-layer graphene grown on Pt(111) surface.



Supplementary Figure 11: CTR for Pt(111) and Pt(111) with 5 layers of graphene.

AFM measurements:

After electrochemical measurements, the samples were taken out of the glovebox and transferred to a Bruker Dimension Icon AFM in a vibration isolation enclosure for imaging. A Si TESPA-V2 tapping tip was used to obtain the images.



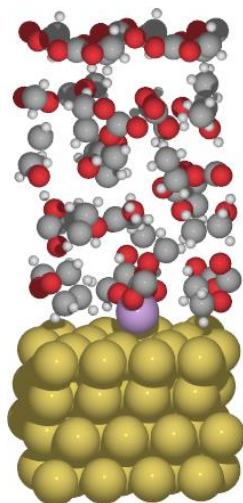
Supplementary Figure 12: AFM images of LiF film on Au(111) and graphene showing extensive cracking on graphene sample. The LiF film structure on graphene is much rougher than films analyzed on Au(111) (see Supplementary Table 3). The porous, granular structure of the film, along with the many cracks, enables access of electrolyte to the graphene surface.

Supplementary Table 3: Roughness analysis of the LiF films on Au(111) and graphene

Results	LiF film on graphene	Results	LiF film on Au (111)
Image Raw Mean	556.329 nm	Image Raw Mean	-233.412 nm
Image Mean	0.294 nm	Image Mean	-0.262 nm
Image Z Range	130 nm	Image Z Range	20.0 nm
Image Surface Area	1388286 nm ²	Image Surface Area	1112427 nm ²
Image Projected Surface Area	1000000 nm ²	Image Projected Surface Area	1000000 nm ²
Image Surface Area Difference	38.8 %	Image Surface Area Difference	11.2 %
Image Rq	11.5 nm	Image Rq	2.20 nm
Image Ra	7.87 nm	Image Ra	1.62 nm

DFT calculations:

We use Density Functional Theory (DFT) to investigate the trends that have been seen in the electrochemical response. To do so, we performed ab-initio molecular dynamics simulations in which we combine molecular dynamics (at room temperature) where each step is calculated at the DFT level. The calculations are done using the GPAW code^{2,3} and the structures as well as the molecular dynamics is run by means of the ASE package⁴. The calculations are performed using RPBE as exchange-correlation functional⁵, a single k-point (Gamma), and we apply the dipole correction to handle the electrostatic potential in the z-direction at the periodic boundary condition. The characteristic time for the Berendsen thermostat was set to 2000 fs and the time step to 1 fs. This procedure has been previously applied by Hansen and Rossmeisl to water⁶.

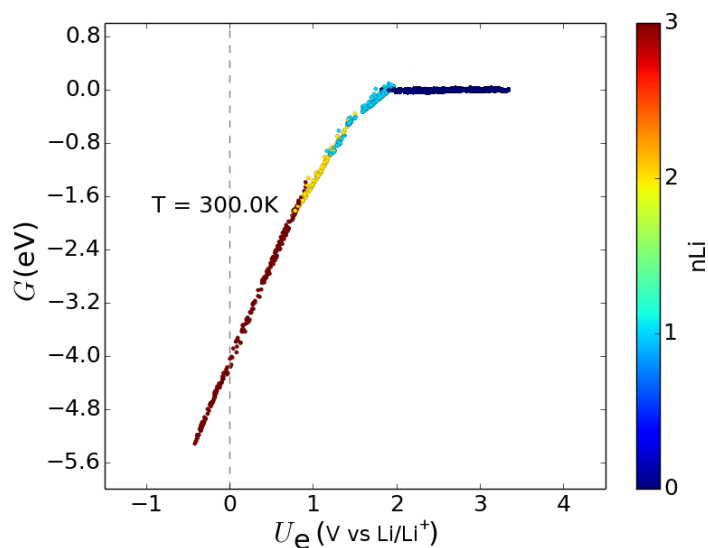


Supplementary Figure 13: Structure of the simulation (in yellow: gold, in purple: lithium, in red: oxygen, in gray: carbon, in white: hydrogen atoms, respectively). The metal slab and the top layer of the electrolyte are kept frozen, while the electrolyte is allowed to move.

The structure of the 1M LiPF₆ electrolyte on Au(111) is shown in Supplementary Figure 13. We can distinguish three different regions: (i) fixed metal slab (Au in this case), (ii) electrolyte, and (iii) fixed top layer. As fixed top layer, we use the ice structure of ethylene carbonate (EC)⁷, with the total dipole along the direction normal to the surface equal to zero. The top layer has the function of confining the electrolyte at the correct experimental density and of mimicking the bulk structure of the electrolyte. In addition, to not affect the orientation of the molecules in the electrolyte, the dipole in the normal direction should be zero. The 1M LiPF₆ electrolyte is composed of ethylene carbonate (EC) and ethyl methyl carbonate (EMC) with a ratio 3:7 in weight. This corresponds, in our simulations, to 8 molecules of EMC and 4 of EC. Different concentrations of lithium atoms, which can be placed both dissolved in the electrolyte and on the metal slab, and of the salt (hexafluorophosphate, PF₆), as well as additives, is added to investigate the phase

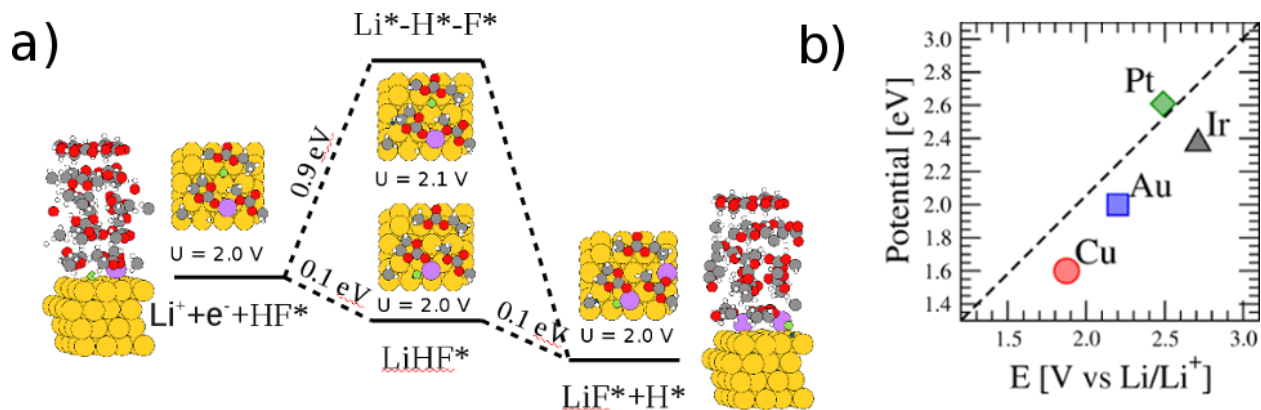
diagram of 1M LiPF₆ with Li. For this purpose, we use an equivalent for Li of the generalized computational hydrogen electrode^{6,8}. In this methodology, the Gibbs free energy, G , is calculated as a function of the enthalpy of the system, ΔE , and of the electronic work function (the calculated work function in the z-direction of each image of the molecular dynamics), U_e , with respect to the Li/Li⁺ potential, Φ . In formula: $G = \Delta E - n_{Li}(\Phi - U_e)$, where n_{Li} is the number of Li atoms in the configuration. In addition, to ensure the same probability of every state to be visited, we perform a quantum Monte Carlo simulation at 300 K before calculating the phase diagram.

Supplementary Figure 14 shows the phase diagram of LP57 with Li on Au(111) at 300 K. At high chemical potential, the most stable configurations have no Li atoms at the interface. Reducing the chemical potential, however, Li atoms become more stable and are found non-specifically adsorbed. We note that the regions of stability for the different configurations are very well defined and a rather large change in potential is needed to explore different concentrations of Li. In other words, the presence of Li atoms is necessary to screen a change in the potential in a combination with a reorientation of the dipoles of the LiPF₆/EC/EMC molecules. This situation is different from liquid water, where a reorientation of the water molecules is enough to screen a change in the potential. On the other hand, we are in a situation different from solid oxide electrolytes, where the potential is screened mainly by vacancies and oxygen ions.



Supplementary Figure 14: Phase diagram of LP57 without salt and Li atoms. The concentration of Li atoms (which adsorbs non-specifically as Li⁺) increases when the electrochemical potential decreases.

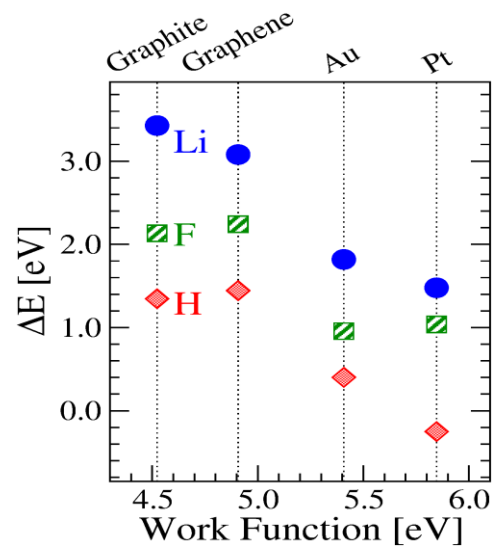
Similar phase diagrams are obtained for the other metals investigated. The main difference is the potential at which Li starts to be non-specifically adsorbed. These values are reported in Supplementary Figure 15b, and scale with the measured first electrochemical response. The structure of the electrolyte used to calculate the reaction path of Supplementary Figure 15a has been taken from these simulations.



Supplementary Figure 15: a) Proposed reaction pathways for HF splitting and LiF formation on Au (white: H, purple: Li, grey: C, red: O, green: F, gold: Au, blue: H from the HF molecule). b) Correlation between the calculated potential where Li starts to be “non-specifically adsorbed” on the y-axis and the measured first electrochemical response (on the x-axis).

A significant difference between the HER in Figure 2a and 2b is that, in contrast to OH^- in alkaline solution, F^- ions readily react with Li^+ ions in LP57, resulting in the formation of $\text{LiF}_{(s)}$ that precipitates on the metal surface. In addition, the full reaction $2\text{Li}_{(s)} + 2\text{HF} \rightarrow 2\text{LiF} + \text{H}_{2(g)}$ is exothermic ($\Delta G \approx -3.5$ eV). By considering the adsorption energies of reactants (H, Li, F), as well as the dissociation energy of HF and the LiF formation energy, we find that the dissociation of HF is enhanced in the presence of Li^+ in the double layer. Supplementary Figure 15a shows two different possible reaction pathways for the HF dissociation step and the concomitant formation of $\text{LiF}_{(s)}$ on Au(111). Briefly, the dissociation of HF in the absence of Li^+ is energetically unfavorable (ca. +0.9 eV), indicating that the dissociation of HF is quite difficult. On the other hand, the dissociation energy is exothermic (ca. -0.2 eV) if HF interacts with Li^+ – presumably via similar non-covalent forces similar to those discussed for the $\text{PtNi}(\text{OH})_2 \cdots \text{Li}^+ \cdots \text{H}_2\text{O}$ system⁹. As schematically depicted in Figure 3, Li^+ positioned close to the metal surface (2.7 Å) plays a dual role: to facilitate HF dissociation and to react with F^- and produce $\text{LiF}_{(s)}$ (eq. 7). It is therefore not surprising that the observed activity trend is strongly correlated with the onset of Li^+ “non-specific adsorption” (Supplementary Figure 15b)

$$\Delta E > 0 \Delta E \approx 0$$



Supplementary Figure 16: Adsorption energies of H, Li and F as functions of the work function with respect to H_2 , $\text{Li}_{(s)}$, and F_2 at a potential $U_{\text{RHE}}=0$ V.

Supplementary Figure 16 reports the adsorption energy of H, Li, and F in vacuum for Au(111), Pt(111) and two different carbon systems (graphene on Pt(111) and graphite). The work function of the two carbon systems is smaller than the ones of Au and Pt and the adsorption energy of Li is also smaller.

OEMS measurements:

The graphite electrodes for the OEMS measurements were prepared by mixing SLP30 graphite powder (TIM-REX by Imerys Graphite & Carbon, Switzerland, BET surface area $\sim 7 \text{ m}^2/\text{g}$) and polyvinylidene fluoride binder (PVdF, Kynar, HSV 900, Arkema, France) at a 90:10 weight ratio with N-methyl-2-pyrrolidone (NMP, anhydrous, chemical purity 99.5%, Sigma-Aldrich, Germany; solid content 30 wt%) in a planetary orbital mixer (Thinky, USA) at 2000 rpm and 50 mbar for 10 min. The resulting ink was blade-coated onto a 20 μm thick porous Celgard separator (H2013, Celgard, USA) at a wet-film thickness of 250 μm using an automatic coater (RK Print, UK). For further details please refer to Metzger et al.¹⁰. This configuration allows for a reasonably short diffusion time for gases produced by the graphite electrode to the flow-restricting capillary (on the order of several minutes) which connects the OEMS cell with the mass spectrometer, which is a requirement for measurements with the OEMS system¹¹.

After drying the graphite coated separator in an oven at 55 °C, 15 mm diameter electrodes were punched out and dried overnight at 95 °C under dynamic vacuum in a glass oven (Büchi B585, Switzerland). The dried electrodes were transferred into an Ar-filled glove box ($<0.1 \text{ ppm O}_2$ and H_2O , MBraun, Germany) without exposure to ambient air. The average graphite loading was $4.7 \pm 0.2 \text{ mg}/\text{cm}^2$ (equivalent to $1.7 \pm 0.1 \text{ mAh}/\text{cm}^2$ calculated with a theoretical specific capacity of $370 \text{ mAh}/\text{g}_{\text{SLP30}}$); the total amount of graphite mass in the cell is thus $8.3 \pm 0.35 \text{ mg}/\text{cm}^2$ which corresponds to a total graphite surface area of $580 \pm 25 \text{ cm}^2_{\text{BET}}$.

All OEMS measurements were performed with two glass fiber separators (VWR, 22 mm diameter) and 320 μl electrolyte. As counter electrode for the OEMS measurements, high areal capacity LiFePO_4 electrodes ($3.5 \text{ mAh}/\text{cm}^2$; from Customcells, Germany) were used, which provide a stable potential at 3.55 V vs. Li/Li^+ , a potential at which the investigated electrolytes are stable. Note that metallic lithium could not be used in this study, as it would react with residual H_2O forming additional H_2 .

After assembling the cell and attaching the cell to the OEMS system, the cell was purged with argon and subsequently kept at open circuit voltage (OCV) for 4 h in order to obtain stable OEMS background signals. After this, a potential scan from OCV to -3.5 V vs. LiFePO_4 was performed (this is equal to +0.05 V vs. Li/Li^+) with a scan rate of 0.2 mV/s. All potentials shown are referenced vs. Li/Li^+ . To quantify the amount of evolved gases, the ion currents at different m/z values (I_z) were normalized by the signal for the ^{36}Ar isotope and calibrated with calibration gases containing 2000 ppm of CO , C_2H_4 , and H_2 in pure argon (further details can be found in Metzger et al.¹⁰).

Supplementary references

1. Naumkin, A. V., Kraut-Vass, A., Gaarenstroom, S. W. & Powell, C. J. NIST X-ray Photoelectron Spectroscopy Database, Version 4.1. Available at: <http://srdata.nist.gov/xps/>.

2. Enkovaara, J. *et al.* Electronic structure calculations with GPAW: a real-space implementation of the projector augmented-wave method. *J. Phys. Condens. Matter* **22**, 253202 (2010).
3. Mortensen, J. J., Hansen, L. B. & Jacobsen, K. W. Real-space grid implementation of the projector augmented wave method. *Phys. Rev. B - Condens. Matter Mater. Phys.* **71**, 1–11 (2005).
4. Hjorth Larsen, A. *et al.* The atomic simulation environment—a Python library for working with atoms. *J. Phys. Condens. Matter* **29**, 273002 (2017).
5. Hammer, B., Hansen, L. & Nørskov, J. Improved adsorption energetics within density-functional theory using revised Perdew-Burke-Ernzerhof functionals. *Phys. Rev. B* **59**, 7413–7421 (1999).
6. Hansen, M. H. & Rossmeisl, J. pH in Grand Canonical Statistics of an Electrochemical Interface. *J. Phys. Chem. C* **120**, 29135–29143 (2016).
7. Bunn, C. W. The crystal structure of ethylene. *Trans. Faraday Soc.* **40**, 23 (1944).
8. Rossmeisl, J., Chan, K., Ahmed, R., Tripković, V. & Björketun, M. E. pH in atomic scale simulations of electrochemical interfaces. *Phys. Chem. Chem. Phys.* **15**, 10321–5 (2013).
9. Subbaraman, R. *et al.* Enhancing hydrogen evolution activity in water splitting by tailoring Li⁺-Ni(OH)₂-Pt interfaces. *Science* **334**, 1256–60 (2011).
10. Metzger, M., Strehle, B., Solchenbach, S. & Gasteiger, H. A. Origin of H₂ Evolution in LIBs: H₂O Reduction vs. Electrolyte Oxidation. *J. Electrochem. Soc.* **163**, A798–A809 (2016).
11. Tsiouvaras, N., Meini, S., Buchberger, I. & Gasteiger, H. A. A Novel On-Line Mass Spectrometer Design for the Study of Multiple Charging Cycles of a Li-O₂ Battery. *J. Electrochem. Soc.* **160**, A471–A477 (2013).

7. Results and Discussion Section 4 – Cathode Surface Layers – Oxidation of Ethylene Carbonate on Li Metal Oxide Surfaces

Status Published online, 23 April 2018
Journal The Journal of Physical Chemistry C, 2018, Volume 122, 10442–10449
Publisher ACS Publications, American Chemical Society.
DOI 10.1021/acs.jpcc.8b01713
Authors Østergaard, Thomas M.; Giordano, Livia; Castelli, Ivano E.; Maglia, Filippo; Antonopoulos, Byron K.; Shao-Horn, Yang; Rossmeisl, Jan

Contributions: T.Ø. and L.G. designed and performed the calculations. T.Ø., L.G., I.E.C., F.M., B.K.A., Y.S.-H. and J.R. discussed the results and wrote the paper.

Content

The electrolyte oxidation reaction in Li ion batteries is initiated at increasing potentials, where the Li content decreases. Experimental studies report that shifting to late 3d transition metals lowers the onset potential. In this work, density functional theory is applied to investigate the oxidative decomposition of the electrolyte component, ethylene carbonate (EC), on layered Li_xMO_2 oxide surfaces. We show that the reactivity of the oxygen sites of Li_xMO_2 ($10\bar{1}4$) surfaces follows the same trend, whereas the reactivity of the metal sites does not. The EOR must therefore involve reactions with the oxygen sites, which is in agreement with previously reported EOR pathways, where an H transfer from EC to O_{surf} is the rate-determining step. We find that the hydrogen adsorption energy on surface oxygen, ΔE_H , is a descriptor for both the thermodynamic driving force and the kinetic barrier of the EOR. ΔE_H correlates with the O-2p band center, and the resulting shift in charge can be understood in a simple Lewis diagram. This study leads us to propose a coating design principle, where (1) ΔE_H of the material must be low and comparable to surfaces known not to oxidize EC, such as LiMnO_2 or LiCoO_2 , and (2) oxygen release should be unfavorable, so as to have a stable coating. Simple guidelines could aid design strategies of high throughput studies for cathode coatings. Low ΔE_H can be achieved using early 3d transition metals in LiMOs, or perhaps by replacing O with a different anion. Li_xMnO_2 has been demonstrated as a coating in $\text{Li}_x\text{Mn}_2\text{O}_4$ - Li_xNiO_2 core-shell nanoparticle cathodes, improving the capacity retention and suppressing oxygen evolution.

Oxidation of Ethylene Carbonate on Li Metal Oxide Surfaces

Thomas M. Østergaard,[†] Livia Giordano,^{‡,§} Ivano E. Castelli,^{||,†} Filippo Maglia,[⊥]
Byron K. Antonopoulos,[⊥] Yang Shao-Horn,^{‡,#,∇} and Jan Rossmeisl^{*,†}

[†]Nano-Science Center, Department of Chemistry, University of Copenhagen, DK-2100 Copenhagen, Denmark

[‡]Department of Mechanical Engineering, [#]Department of Materials Science & Engineering, and [∇]Research Laboratory of Electronics, Massachusetts Institute of Technology, 77 Massachusetts Avenue, Cambridge, Massachusetts 02139, United States

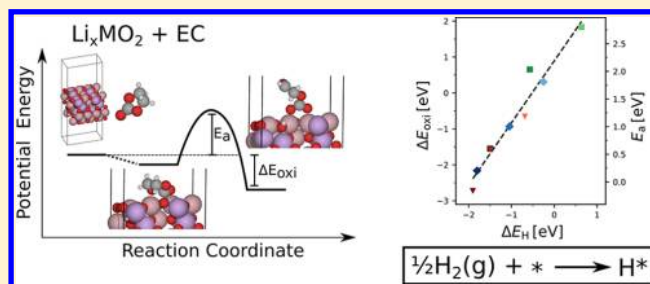
[§]Department of Material Science, Università di Milano-Bicocca, Via Cozzi 55, 20136 Milano, Italy

^{||}Department of Energy Conversion and Storage, Technical University of Denmark, Building 309, DK-2800 Kgs. Lyngby, Denmark

[⊥]Battery Cell Technology, BMW Group, 80788 München, Germany

S Supporting Information

ABSTRACT: Understanding the reactivity of the cathode surface is of key importance to the development of batteries. Here, density functional theory is applied to investigate the oxidative decomposition of the electrolyte component, ethylene carbonate (EC), on layered Li_xMO_2 oxide surfaces. We compare adsorption energy trends of atoms and small molecules, on both surface oxygen and metal sites, as a function of the Li content of the surface. The oxygen sites are identified as the reactive site for the electrolyte oxidation reaction (EOR). We report reaction energies and NEB-calculated kinetic barriers for the initial oxidative decomposition of EC, and correlate both with the reaction energy of hydrogen adsorption on oxygen. The hydrogen adsorption energy scales with the distance between the Fermi level and the O-2p band center. We expect this model of the EOR to be valid for other organic electrolytes and other Li metal oxide surfaces, due to its simplicity, and the model leads to simple design principles for protective coatings.



INTRODUCTION

Li ion batteries (LiBs) are widely used for powering portable electronics and electric vehicles. Although significant development of the LiBs has been achieved, better cell energy-density is still necessary for the wide deployment of battery powered electric vehicles.^{1–3} This requires both larger capacity and higher open-circuit voltage of the cell.^{4,5} The cell voltage is practically limited by the stability of the electrolyte, which depends on the energy gap between the highest occupied molecular orbital (HOMO) and the lowest unoccupied molecular orbital (LUMO) of the electrolyte.⁶ During the charge of the cell, the Fermi level of the negative electrode (anode) moves above the LUMO of the electrolyte, which causes electrolyte reduction and the formation of the solid electrolyte interphase (SEI).^{7–12} The picture of LUMO alignment describes an upper limit to the stability, as electronic states may be formed inside the HOMO–LUMO gap by catalytic or polaronic effects upon reduction reactions.¹³ The SEI is electrically insulating and protects the electrolyte from further reduction, while maintaining cell operation as it allows for Li ion transport. On the positive electrode (cathode), the Fermi level is lowered during charging, and oxidation reactions of the organic electrolyte can occur. This results in a cathode electrolyte interphase (CEI) that consists of electrolyte degradation products, including organics, and LiF .^{9,14,15}

Oxidation products are observed at lower cell potential than expected from predicted HOMO–LUMO gaps⁹ (>5.5 V vs Li/Li^+ for carbonate electrolytes), and the chemistry of the CEI formation is not understood to a degree where it can be designed and optimized. The CEI generally does not passivate the electrode, and therefore, the voltage, upon charging, is limited to avoid capacity loss and thermal runaway from electrolyte decomposition.⁹ The cathode surface reactivity has been linked to the oxidative electrolyte decomposition in various reports. By online electrochemical mass spectrometry (OEMS), oxidation products are observed at 4.7 V vs Li/Li^+ on inactive carbon electrodes,¹⁶ at 4.5 V vs Li/Li^+ on NMC-111 cathodes,¹⁷ and at 4.2 V vs Li/Li^+ on LiNiO_2 and 4.8 V vs Li/Li^+ on LiCoO_2 and LiMnO_4 cathodes,¹⁸ whereas no oxidation products are observed up until 5.0 V vs Li/Li^+ for the $\text{LiNi}_{0.43}\text{Mn}_{1.57}\text{O}_4$ (LNMO) spinel cathode.¹⁹ Understanding at the atomic scale the catalytic effect of the Li metal oxide (LiMO) surfaces is essential for understanding the CEI formation on novel cathode materials, and for determining design principles for coating materials.^{20–24} Trend studies of well-defined surfaces have been useful in understanding the

Received: February 19, 2018

Revised: April 10, 2018

Published: April 23, 2018

formation mechanism of LiF in the SEI at the atomic scale.²⁵ Here we present a trend study of the physical origins of the oxidation mechanism, resulting from the electrolyte–cathode interaction at high voltages. We consider layered Li_xMO_2 ($10\bar{1}4$) surfaces with varied metal M and Li content, shown in Figure 1a–c, and a widely used electrolyte solvent, ethylene carbonate (EC), shown in Figure 1d.

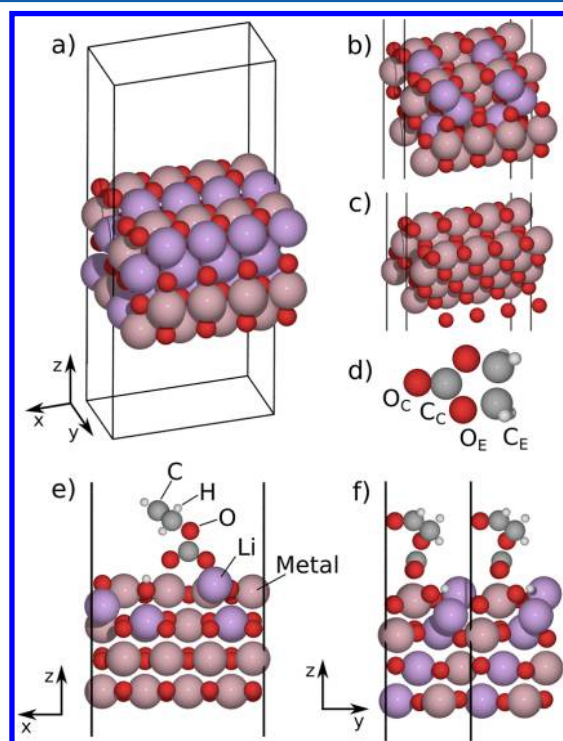


Figure 1. Layered Li_xMO_2 ($10\bar{1}4$) surface model of (a) LiMO_2 , (b) $\text{Li}_{0.5}\text{MO}_2$, and (c) MO_2 with 4 layers. Periodic boundary conditions are imposed in the x and y directions; the two bottom layers are kept fixed. (d) Labeling scheme for ethylene carbonate, indicating carbonyl oxygen, O_C , carbonyl carbon, C_C , ethylene coordinated oxygen, O_E , and ethylene carbon, C_E . (e) Front view and (f) side view of the oxidized configuration of EC that is considered in this work, shown here on $\text{Li}_{0.5}\text{CoO}_2$. One H is transferred to surface oxygen and an oxygen vacancy is formed in the surface.

The EC oxidation reaction (EOR) has been studied theoretically on different LiMO surfaces. EC can interact with a surface in many ways, due to the polar nature of the molecule and the complexity of the LiMO surfaces. Density functional theory (DFT) studies of $\text{Li}_{0.6}\text{Mn}_2\text{O}_4$ spinel (100) suggested that EC initially binds through the carbonyl carbon (C_C) and carbonyl oxygen (O_C) to the surface oxygen (O_{surf}) and surface metal (M_{surf}), respectively.²⁶ The chemisorption of EC through the C_C was studied for a layered $\text{Li}(\text{Ni}_{0.5}\text{Mn}_{0.3}\text{Co}_{0.2})\text{O}_2$ ($10\bar{1}4$) surface, where the reaction was found to be facilitated by nearby Li^+ in the electrolyte.²⁷ The partially negative O_C of EC has also been proposed to bind to M_{surf} on a wide range of layered Li_xMO_2 ($10\bar{1}4$) surfaces in an electrophilic attack,^{28,29} and to Li surface atoms of spinel $\text{Li}_x\text{Mn}_2\text{O}_4$ (111), when no M_{surf} sites are exposed.³⁰ Nudged elastic band (NEB) barrier calculations of the initial EC–cathode interaction show that the oxidation reaction is a two step process,^{26,30} where the first step could be one of those mentioned above. The second step of the EOR can include breaking of the $\text{C}_C\text{--O}_E$ bond (also called a ring opening reaction²⁹), transferring of a H (H abstraction),

and/or EC possibly taking up an O_{surf} and forming an oxygen vacancy (O_{vac}).^{26,28} Oxidized EC with a H transfer and a surface O_{vac} is shown in Figure 1e,f. The energy barrier for a H transfer was found to decrease with decreasing Li content of spinel $\text{Li}_x\text{Mn}_2\text{O}_4$ (111).³⁰ The H-abstraction reaction energy was proposed as a descriptor for the solvent stability in nonaqueous Li– O_2 batteries³¹ and was found to correlate with its $\text{p}K_a$.^{32–34} The role of the Li content and the transition metal of the cathode was studied for Li_xCoO_2 and LiMO_2 ($x = [1.0, 0.5, 0]$ and $\text{M} = [\text{Mn}, \text{Fe}, \text{Co}, \text{Ni}]$), where the stability of four different adsorption configurations was compared.²⁸ In the most stable adsorption state, a H is transferred to O_{surf} and EC binds to a neighboring O_{surf} through the exposed C_E . This adsorption state is shown in Figure S1 (the final state). The adsorption energy was found to correlate with the bulk O-2p band center relative to the Fermi level.²⁸

This work studies the EOR on layered Li_xMO_2 ($10\bar{1}4$) surfaces for $x = [1.0, 0.5, 0.0]$ and $\text{M} = [\text{Mn}, \text{Co}, \text{Ni}]$, shown in Figure 1a–c, and focuses on the oxidation state, shown in Figure 1e,f. The ($10\bar{1}4$) surface is the most stable nonpolar surface³⁵ for layered Li_xMO_2 and has exposed Li channels. The real cathode particles are multifaceted, and the terminations depend on the environmental conditions.^{36,37} We report oxidation reaction energy trends and identify the H adsorption energy on O_{surf} atoms ΔE_{H} , as a descriptor for both the reaction barrier, E_a , and the oxidation reaction energy, ΔE_{oxi} . We relate ΔE_{H} to the O-2p band model,²⁸ and conclude that ΔE_{H} is a measure for the oxidative strength of LiMOs. We organize the results in two subsections. In the first part we report the H transfer pathway that is considered in this work, on $\text{Li}_{0.5}\text{CoO}_2$ in vacuum. We study the surface reactivity in terms of adsorption energies and identify O_{surf} as the active site for the EOR. We report trends in oxidation reaction energy and energy barrier for several surfaces, as a function of ΔE_{H} . The reactivity trends are related to the electronic structure of the oxides. Both the energy barrier and the thermodynamic driving force for EOR are correlated to the Fermi level and the O-2p band center of the cathode. In the second part, we study an 8-electron oxidation of EC into $2\text{CO}_2 + \text{CO}$ and discuss the final state of the reduced Li_xMO_2 surface. In the conclusion, we summarize the work into a design requirement for cathode coatings, and the computational details are reported below.

METHODS

Total energy calculations for structure optimization and climbing image nudged elastic band (NEB)³⁸ are performed with the GPAW code^{39,40} using the ASE simulation package.⁴¹ Projector augmented wave potentials (PAW) are used to replace the inner core electrons, and the electronic wave functions are represented on a uniform real-spaced grid with 0.18 Å grid-spacing. All calculations are performed in grid-mode, and the revised Perdew–Burke–Ernzerhof functional (RPBE)⁴² is used to treat the exchange–correlation energy. The RPBE functional and other standard GGA functional tend to stabilize delocalized over localized electronic states, due to the self-interaction of the electrons in DFT.⁴³ This can lead to errors in band gaps and in absolute Li-intercalation potentials for Li_xMO_2 systems.⁴⁴ The self-interaction error is usually improved upon with the DFT+U approach. However, wide ranges of effective U (U_{eff}) values are reported in the literature, and redox reaction energies can depend significantly on the value of the U_{eff} .^{45,46} Applying a U-correction would not affect the conclusions of this work, because they are based on trends.

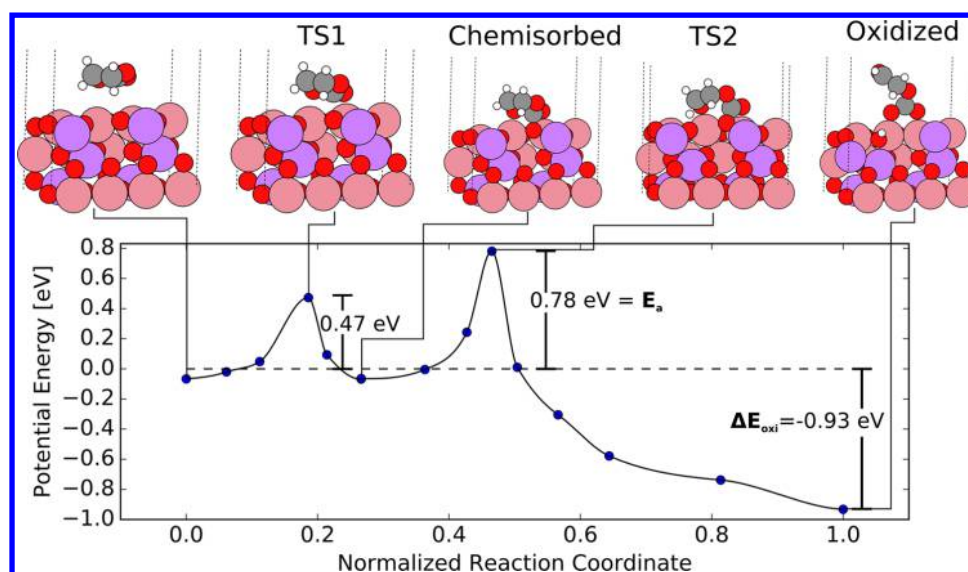


Figure 2. Potential energy diagram for the oxidation reaction pathway on $\text{Li}_{0.5}\text{CoO}_2$. EC chemisorbs to O_{surf} in the first step; in the second transition state a H is transferring, and in the final state an oxygen vacancy has been formed. The H transfer step has the highest barrier, E_a . The reaction energy for the entire oxidation reaction, ΔE_{oxi} is shown.

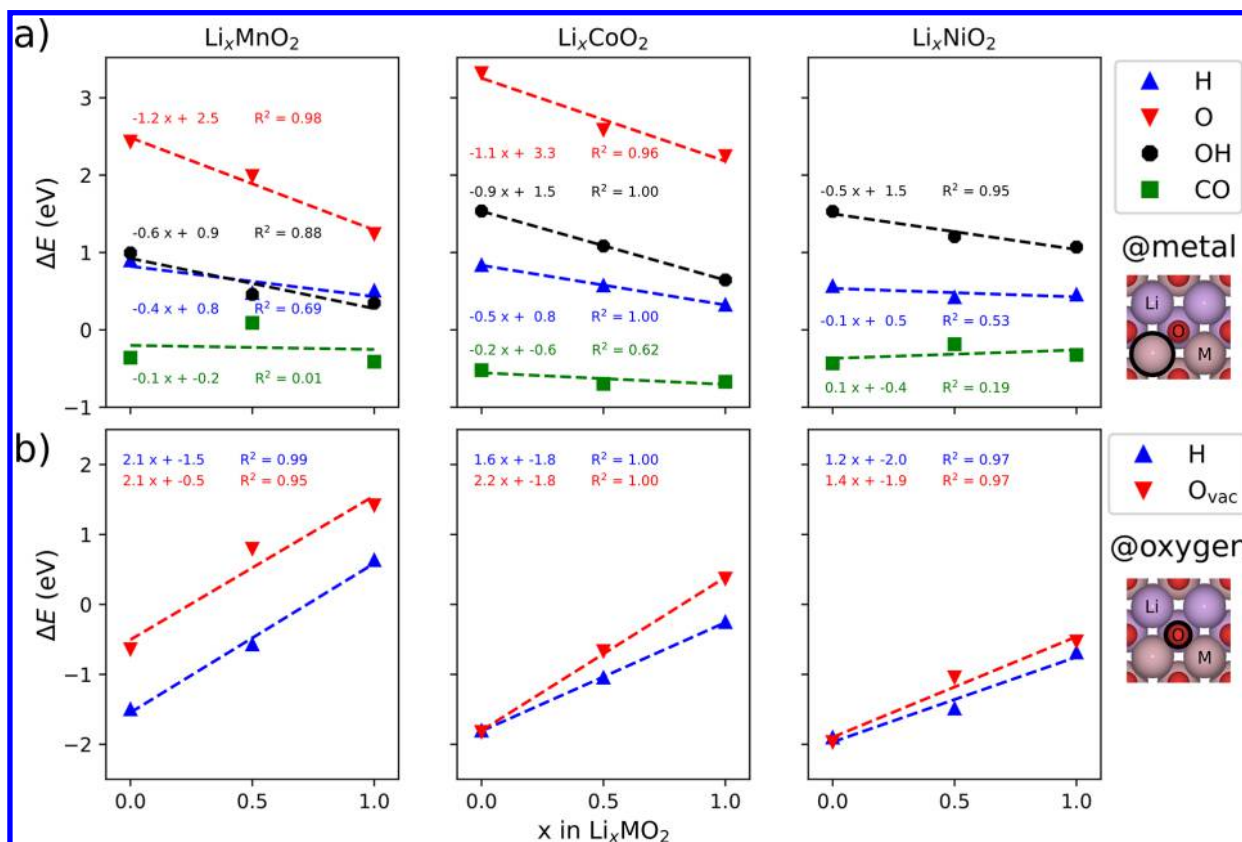


Figure 3. Adsorption energies as a function of the Li content, for atoms and small molecules adsorbing on M_{surf} (a) and O_{surf} (b) for Li_xMO_2 ($10\bar{1}4$) surfaces (Mn, Co, and Ni). The adsorbates are specified by symbol and color and are shown in the legend. The dashed lines are the corresponding linear best fit. The adsorption energies of O, OH, and H and the formation of O_{vac} are referred to $\text{H}_2\text{O}(\text{g})$ and $\text{H}_2(\text{g})$, and CO is referred to as $\text{CO}(\text{g})$. (a) For the metal site the adsorption energy is either unaffected or increasing as x decreases, and the metal atoms are becoming less reactive with increasing potential. (b) For the oxygen site the adsorption energies are decreasing with decreasing x , and the oxygen atoms become more reactive.

For these reasons we employ standard GGA-DFT, and vary the state of charge (SOC) instead of the potential. The Li_xMO_2 ($10\bar{1}4$) surfaces with space group $R\bar{3}m$ are modeled with 4 metal atoms in the x direction, with 1 metal and Li atom in in

the y direction, and with 4 layers in the direction perpendicular to the surface. The two bottom layers are constrained to the calculated lattice parameter of the bulk structure. It was found unnecessary to passivate metal dangling bonds on the bottom

layer. By passivation with H on the bottom metal, the H adsorption energy on top layer O_{surf} changed by less than 0.05 eV for LiMnO_2 , $\text{Li}_{0.5}\text{CoO}_2$, and NiO_2 . The Brillouin zone of the surfaces is sampled using a $2 \times 4 \times 1$ k-point mesh. Electron spins are treated separately, and the ferromagnetic state is considered in all cases. At least 14 Å of vacuum is included in the nonperiodic z direction, perpendicular to the slab. A dipole correction is applied to ensure flat potentials in the vacuum region, and a Fermi-level smearing of 0.1 eV width is used. The structure is optimized until the forces on the nonconstrained atoms are below 0.05 eV/Å. All barriers and reaction energies for EC are referred to the clean surface and gas-phase EC, and vibrational corrections are not included. Structures, total energies, scripts to run calculations, and plotting methods are collected in the KatlaDB database available at this link: <http://nano.ku.dk/english/research/theoretical-electrocatalysis/katlabdb/>.

RESULTS AND DISCUSSION

Energetics, Barriers, and Trends of the Initial EC Oxidation Reaction. The reaction profile for EC oxidation, as reported in Leung,²⁶ is shown for $\text{Li}_{0.5}\text{CoO}_2$ in Figure 2. The reaction path has two steps and two barriers. EC adsorbs in the nucleophilic attack where C_C binds to O_{surf} and the $C_C=O_C$ double bond becomes a single bond. The oxidation reaction proceeds with a subsequent H transfer, and EC undergoes a ring opening. An O_{vac} is formed along with the H transfer. The $\text{Li}_{0.5}\text{CoO}_2$ structure is the charging limit of the LiCoO_2 cathode (~ 4 V),⁴ and a CEI layer is known to form.^{29,47,48} In the first transition state (TS1), the O_C coordinates to the surface Co atom, and EC is slightly bent as the carbonate group dihedral angle goes from 180° in the initial state to 153° in TS1 and ends up at 124° in the chemisorbed state with an elongated O_E-C_C bond. In the second transition state (TS2), the O_E-C_C bond is broken, and the transferred H is shared between C_E and O_{surf} . From TS2 to the final state, a Li atom is moved to a subsurface layer and an O_{vac} is formed. The barrier for TS1 and TS2 is 0.47 and 0.78 eV, respectively. With the assumption of a fast equilibrium between the initial state and the chemisorbed state, it is the energy barrier of TS2, relative to the initial state, that determines the overall rate of the oxidation reaction.

As reviewed in the Introduction, the adsorption of EC on Li metal oxide (LiMO) cathode surfaces is not restricted to the pathway shown in Figure 2. However, only few adsorption configurations are relevant for describing the EOR onset potential. To identify the relevant adsorption reactions, we identify the active site for the EOR by studying adsorption energy trends of Li_xMO_2 ($10\bar{1}4$) surfaces. We consider $x = [1.0, 0.5, 0.0]$ and $M = [\text{Mn}, \text{Co}, \text{Ni}]$. Adsorption energies for CO, H, OH, and O atoms, on the M_{surf} sites, are reported in Figure 3a as a function of the Li content. For all surfaces, a linear relation with a negative slope is observed between the Li content and the adsorption energies of H, OH, and O. Thus, the M_{surf} sites become weaker reducing agents with decreased Li content, in line with the Fermi level (Figure S8), E_F , and the Bader charge on Co atoms (Table S1), decreasing with Li content. No correlation is observed for the CO adsorption energy. Energies of H adsorption on O_{surf} and for O_{vac} formation are reported in Figure 3b. Here, the slope is positive as O_{surf} becomes a stronger oxidizing agent at lower Li content. The effect of changing the transition metal is most pronounced in the adsorption trends of the O site, where the reactivity follows the order of the 3d metal series. The EOR occurs at an

onset potential, which reflects that a rate-determining intermediate is becoming active. We find that the metal sites become less reactive as the Li content is decreased, and the O atoms become more reactive. The intermediate involved in the rate-determining step must therefore involve chemical bonds to the O atoms, and cannot solely interact with the metal atoms.

There are only two ways that EC can go through reaction intermediates with O_{surf} . Pathway 1²⁶ was presented for $\text{Li}_{0.5}\text{CoO}_2$ in Figure 2. Pathway 2³⁰ is a direct H transfer from the physisorbed state, shown in Figure S1. The direct H transfer was found to be kinetically inaccessible as the deprotonated EC is highly unstable in vacuum, which is discussed in the Supporting Information. Here, only pathway 1 is considered, that goes through a chemisorbed intermediate before the H transfer. We note that pathway 2 has been reported for $\text{Li}_x\text{Mn}_2\text{O}_4$ spinel (111), where it is stabilized by Li surface atoms.³⁰ However, regardless of the pathway, the transfer of a H is rate-limiting for the EOR. The barrier calculations are extended to Li_xCoO_2 with $x = [0.0, 0.5, 1.0]$, and LiNiO_2 in Figure 4, where only the rate-determining H

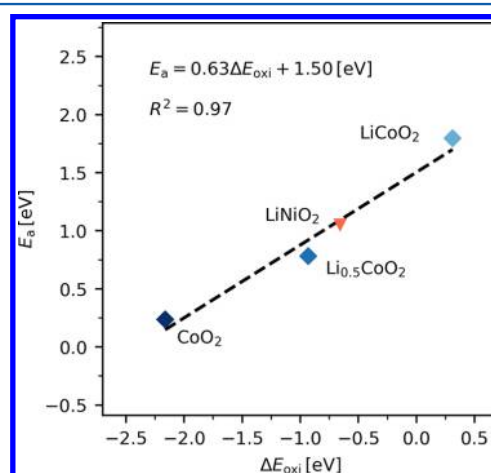


Figure 4. Linear relation between the activation energy for H transfer from EC (TS2), E_a , and the reaction energy for the oxidation, ΔE_{oxi} . The slope is close to 0.5, reflecting that both a H transfer and an O_{vac} formation have occurred in the oxidized state. The barriers are obtained by NEB calculations.

transfer step is considered (TS2 in Figure 2). The pathways are shown in Figures S2–S4. We find that the activation energy barrier, E_a , is a linear function of the oxidation energy, ΔE_{oxi} , from which the activation energy on all the surfaces is obtained by extrapolation, E_a^{extr} .

In Figure 5, ΔE_{oxi} and E_a^{extr} are plotted as a function of the H adsorption energy on O_{surf} , ΔE_{H} . A linear relation is found between E_a^{extr} and ΔE_{H} , with a slope close to 1. Thus, the trend in the energy barrier is determined by the H transfer, rather than by stabilization of the $\text{C}_3\text{O}_3\text{H}_3$ product. ΔE_{oxi} scales with $\sim 2\Delta E_{\text{H}}$, since the thermodynamic driving force also depends on the O_{vac} formation energy and stabilization of the product. Therefore, both the kinetics and the thermodynamics of the initial EOR can be described by ΔE_{H} . We note that if ΔE_a^{extr} is close to zero or negative, it might be the barrier for chemisorption (TS1) that determines the overall energy barrier of the EOR. The $\text{p}K_a$ ^{32–34} and the energy for H removal,³¹ as descriptors for the oxidation of aprotic solvents, fit well with ΔE_{H} as being a descriptor for the EOR. We observe the trend that Li_xNiO_2 (in red) is the most reactive surface and Li_xMnO_2

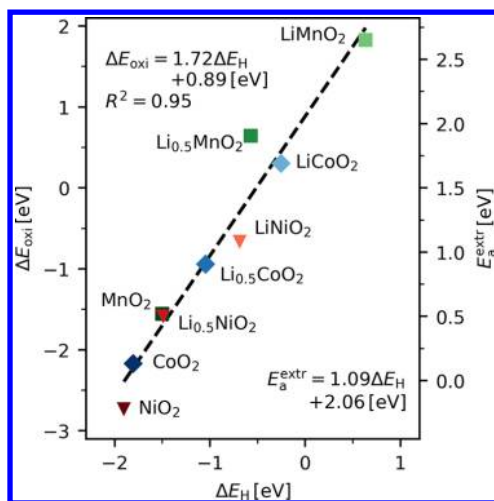


Figure 5. Reaction energy, ΔE_{oxi} , and extrapolated energy barrier, $E_{\text{a}}^{\text{extr}}$, as a function of ΔE_{H} . ΔE_{H} decreases with lower Li content and with moving to the right in the 3d metal series, causing a more exothermic EOR with lower kinetic barrier.

(in blue) is the least reactive, following the 3d series of the periodic table, Ni > Co > Mn, in agreement with the adsorption trends in Figure 3, and experimental trends.¹⁸ The reaction energies reported here differ from previous studies of the EC oxidation on oxide surfaces,^{26,28} where the DFT+U methodology is employed. Increasing U_{eff} makes an oxide surface more reactive toward H abstractions by as much as 2 eV (depending on the U_{eff}).⁴⁵ The reactivity of LiMnO₂, LiCoO₂, and LiNiO₂ layered (10 $\bar{1}$ 4) surfaces was reported with $U_{\text{eff}} = 4.0, 3.3,$ and 6.4 for Mn, Co, and Ni, in Giordano et al.²⁸ Here LiMnO₂ was found to be slightly more reactive than LiCoO₂, and LiNiO₂ is most reactive. We emphasize that the scaling with ΔE_{H} does not depend on the choice of U_{eff} . The surface undergoes reduction as EC is oxidized, which can be monitored by a change in the transition metal ion spin state, shown in Table S2.

With ΔE_{H} as a descriptor, the initial EOR on Li_xMO₂ surfaces has been significantly simplified. It has been shown that the thermodynamics of the EOR are correlated to the band center of the bulk O-2p states for Li_xMO₂ surfaces.²⁸ The bulk O-2p band center has also been correlated to the overall activity for the oxygen reduction reaction (ORR) of solid oxide fuel cell (SOFC) perovskite-type cathode materials.^{49,50} For the SOFC cathodes, the bulk O-2p band center was correlated to the O_{vac} formation energy, a correlation that we observe as well for the Li_xMO₂ surfaces (Figure S6). Here, we demonstrate a close correlation between ΔE_{H} and the O-2p center of the active O_{surf} as shown in Figure 6. As E_{F} moves down into the O-2p band, ΔE_{H} decreases with a slope of -1.4 . (The slope is 1.1 for the bulk O-2p band in Figure S5.)

The correlation between ΔE_{H} and the O-2p band center can be understood through a simple Lewis diagram, shown in Figure 7a. Before H adsorption, the O_{surf} can be represented as sharing a single bond to two metal atoms each, and after H adsorption, the O_{surf} requires only one single bond distributed between the two metal atoms. Two electrons transferred: one forms the O–H bond, and one moves to the metal atoms and reduces the oxidation state partially. This corresponds to one electron transferring from the O-2p band to the M-3d band at the Fermi level, and one electron transferring from the O-2p band to the O–H bond state, as illustrated in Figure 7b. The

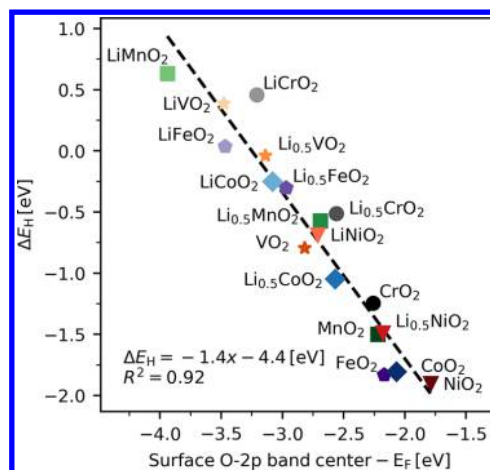


Figure 6. Linear relation between ΔE_{H} and the O-2p band center relative to the Fermi level, E_{F} , for the O_{surf} on which H adsorbs. The band center is measured for the clean surface. The surface becomes more reactive as E_{F} is lowered, and the scaling relation holds for a wide range of metals (V to Ni) and Li contents $x = [0, 0.5, 1]$.

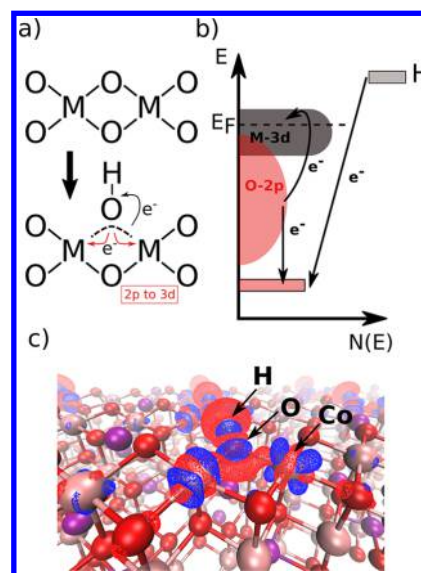


Figure 7. Electron transfers upon H adsorption. (a) A diagram showing the change in Lewis bonds. M, O, and H are metal, oxygen, and hydrogen, respectively. (b) Schematic showing the change in density of states. (c) Change in charge density for Li_{0.5}CoO₂, showing charge depletion in red, and accumulation in blue. Charge accumulates on O, and depletes in between the O and Co (Bader charge analysis in Table S1).

O-2p band center has been demonstrated as a descriptor for the oxidative strength of Li_xMO₂ surfaces.²⁸ Here we find that the oxidative strength is related to ΔE_{H} , and Figure 7b draws the connection between the two pictures. On an absolute energy scale, the position of the M-3d band and the Fermi level varies by several electronvolts between different transition metals, whereas the position of the O-2p band and the O–H state is approximately constant (Figures S7–S12). Therefore, the O_{surf} 2p band center relative to E_{F} correlates well to ΔE_{H} for a wide range of Li_xMO₂ surfaces. We also find a correlation between ΔE_{H} and the position of the Fermi level (Figure S8), showing that the change in E_{F} contains the largest contribution to the change in ΔE_{H} . A similar electronic structure model was used to explain the correlation between the O-2p band center and

the O_{vac} formation energy for SOFC perovskite cathode materials.⁴⁹ The picture from of the Lewis diagram can be visualized by the charge difference upon H adsorption, shown in Figure 7c for $\text{Li}_{0.5}\text{CoO}_2$, and in Figure S10 for LiCoO_2 , $\text{Li}_{0.5}\text{CoO}_2$, and CoO_2 . Charge is depleted (in red) between the active O_{surf} and the two nearest Co atoms, reducing the covalent character of the bond, and charge accumulates (in blue) on the O atom and on both of the Co atoms. Bader charge analysis of the active O_{surf} and the two nearest Co atoms shows that electron charge from H adsorption accumulates more on the O atom rather than on the Co atoms (Table S1). This effect is pronounced with lower Li content.

Gas Evolution and Reduction of the Surface. So far, we have studied the thermodynamics and kinetics of the initial EC–surface interaction. In experiments, the oxidation of EC can be measured by detection of gas species released in the reaction. The quantitative release of 2:1 CO_2/CO has been detected upon overcharging of different NMC cathodes,¹⁹ in a proposed reaction where EC reacts with $4O_{\text{surf}}$: $\text{EC} + * \rightarrow 2\text{CO}_2 + \text{CO} + 2\text{H}_2\text{O} + 4O_{\text{vac}}$. During the EOR, H atoms are transferred and O_{vac} 's are formed. Therefore, we suggest an intermediate to the reaction $2\text{CO}_2 + \text{CO} + 4\text{H}^* + 2O_{\text{vac}}$. The potential energy diagram of the gas evolution reaction of $2\text{CO}_2 + \text{CO}$ follows three steps:

- Oxidation state 1. Gases evolved: $2\text{CO}_2 + \text{CO}$. State of the surface: $4\text{H}^* + 2O_{\text{vac}}$ calculated in the same cell.
- Oxidation state 2. Same as state 1, except that each H and O_{vac} is calculated in separate simulation cells. This corresponds to a low coverage.
- Oxidation state 3. Gases evolved: $2\text{CO}_2 + \text{CO} + 2\text{H}_2\text{O}$. State of the surface: $4O_{\text{vac}}$. The H adsorbates reacted with O_{surf} to H_2O and formed two additional O_{vac} calculated in separate cells.

The reaction involves 8 electron transfers and leaves the surface reduced. Since the H atoms and O_{vac} 's repel each other, oxidation state 1 is an upper limit to the reaction energy, compared to oxidation state 2 where the species are treated in separate simulation cells. The potential energy diagram is shown in Figure 8. The reaction energy, ΔE , becomes more exothermic from Mn to Ni and upon delithiation.

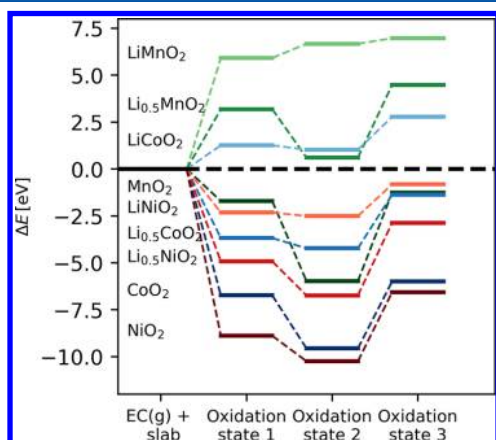


Figure 8. Potential energy diagram for the evolution of $2\text{CO}_2 + \text{CO}$ from EC. The oxidation states are described in the main text, and the last step is the evolution of H_2O from H^* .

For the more reactive surfaces, $\Delta E(\text{state 1})$ is exothermic (< -2 eV). In general, oxidation state 2 with the lower coverage is more stable than state 1. Oxidation state 3 where the H adsorbates react with O_{surf} to H_2O is highly unstable compared to both state 1 and state 2. The reaction energy from either states is uphill by several electronvolts for all surfaces. The presence of surface hydroxyl groups has been proposed to affect the energetics of the EOR.^{26,27,29} We conclude that adsorbed H does not form H_2O on any battery relevant Li_xMO_2 surfaces. This result is considered robust toward thermodynamic corrections. The Gibbs free energy of water stabilizes by 0.67 eV per molecule, when going from 0 K in the gas phase, to water at room temperature. Thus, the energy of oxidation state 3 could be stabilized by up to 1.3 eV from thermodynamic corrections. This is an upper estimate of the error, since the water molecule is less stable upon solvation in an organic solution. We report the scaling between ΔE_{H} and $\Delta E(\text{state 1})$ in Figure S13, from which the slope of the fit is 5.1 for Co and Ni, and 3.5 for Li_xMnO_2 . The oxidation into $2\text{CO}_2 + \text{CO}$ does not result in any CEI products and is therefore not consistent with experimental observations of organic CEI fragments.⁹ The results clearly show a thermodynamic driving force for the full oxidation, but some metastable organic fragment must exist in between the initial H abstraction and oxidation state 1.

CONCLUSION

The electrolyte oxidation reaction in Li ion batteries is initiated at increasing potentials, where the Li content decreases. Experimental studies report that shifting to late 3d transition metals lowers the onset potential.¹⁸ In this work, we have shown that the reactivity of the oxygen sites of Li_xMO_2 ($10\bar{1}4$) surfaces follows the same trend, whereas the reactivity of the metal sites does not. The EOR must therefore involve reactions with the oxygen sites, which is in agreement with previously reported EOR pathways, where a H transfer from EC to O_{surf} is the rate-determining step.^{26,30} We find that the hydrogen adsorption energy on surface oxygen, ΔE_{H} , is a descriptor for both the thermodynamic driving force and the kinetic barrier of the EOR. ΔE_{H} correlates with the O-2p band center, and the resulting shift in charge can be understood in a simple Lewis diagram. In effect, an electron is transferred to the Fermi level of the surface, and therefore, we expect the trend to hold more generally for other Li metal oxide surfaces, rather than for the ($10\bar{1}4$) layered Li_xMO_2 surfaces. In the final state of the EOR pathway we consider here (Figure 2), the oxidized product of EC is in a ring-opened state with the $\text{R}-\text{CH}_2\text{CHO}$ group pointing away from the surface. From this position many different reactions can occur. EC can react with electrolyte salts or with other electrolyte molecules^{27,29} or decompose further on the surface, reacting with Li or O or forming protonated species.¹⁷ In the full oxidation of EC to 2CO_2 and CO , four H atoms are transferred to the surface. We find that the H atoms are too strongly bound on the surface to be released as water, for the surfaces that are reactive enough to abstract H from EC. This study leads us to propose a coating design principle, where (1) ΔE_{H} of the material must be low and comparable to surfaces known not to oxidize EC, such as LiMnO_2 or LiCoO_2 , and (2) oxygen release should be unfavorable, so as to have a stable coating. Simple guidelines could aid design strategies of high throughput studies for cathode coatings.^{22–24} Low ΔE_{H} can be achieved using early 3d transition metals in LiMO s (see Figure 6), or perhaps by replacing O with a different anion. Li_xMnO_2 has been demonstrated as a coating in $\text{Li}_x\text{Mn}_2\text{O}_4$ –

Li_xNiO_2 core-shell nanoparticle cathodes, improving the capacity retention and suppressing oxygen evolution.⁵¹

■ ASSOCIATED CONTENT

5 Supporting Information

The Supporting Information is available free of charge on the ACS Publications website at DOI: 10.1021/acs.jpcc.8b01713.

Additional calculation details on projected density of states and Bader analysis; discussion of oxidation reaction pathway 2; data on NEB-calculated reaction pathways, scaling relations between adsorption energies, and electronic properties; data on change in charge transfers, charge densities, and in density of states, upon hydrogen adsorption; scaling relation between oxidation state 2 and ΔE_{H} ; and change in magnetic moment for the metal ions upon EC oxidation (PDF)

■ AUTHOR INFORMATION

Corresponding Author

*E-mail: jan.rossmeisl@chem.ku.dk.

ORCID

Thomas M. Østergaard: 0000-0002-8687-7211

Livia Giordano: 0000-0002-6879-9424

Ivano E. Castelli: 0000-0001-5880-5045

Yang Shao-Horn: 0000-0001-8714-2121

Notes

The authors declare no competing financial interest.

■ ACKNOWLEDGMENTS

The research was supported by BMW Technology Corporation and the Carlsberg Foundation (Grant CF15-0165).

■ REFERENCES

- (1) Armand, M.; Tarascon, J.-M. Building Better Batteries. *Nature* **2008**, *451*, 652–657.
- (2) Gröger, O.; Gasteiger, H. A.; Suchsland, J.-P. Review—Electromobility: Batteries or Fuel Cells? *J. Electrochem. Soc.* **2015**, *162*, A2605–A2622.
- (3) Opitz, A.; Badami, P.; Shen, L.; Vignarooban, K.; Kannan, A. Can Li-Ion Batteries be the Panacea for Automotive Applications? *Renewable Sustainable Energy Rev.* **2017**, *68*, 685–692.
- (4) Goodenough, J. B.; Kim, Y. Challenges for Rechargeable Li Batteries. *Chem. Mater.* **2010**, *22*, 587–603.
- (5) Andre, D.; Kim, S.-J.; Lamp, P.; Lux, S. F.; Maglia, F.; Paschos, O.; Stiaszny, B. Future Generations of Cathode Materials: An Automotive Industry Perspective. *J. Mater. Chem. A* **2015**, *3*, 6709–6732.
- (6) Goodenough, J. B.; Park, K.-S. The Li-Ion Rechargeable Battery: A Perspective. *J. Am. Chem. Soc.* **2013**, *135*, 1167–1176.
- (7) Verma, P.; Maire, P.; Novák, P. A Review of the Features and Analyses of the Solid Electrolyte Interphase in Li-Ion Batteries. *Electrochim. Acta* **2010**, *55*, 6332–6341.
- (8) Peled, E.; Menkin, S. Review—SEI: Past, Present and Future. *J. Electrochem. Soc.* **2017**, *164*, A1703–A1719.
- (9) Gauthier, M.; Carney, T. J.; Grimaud, A.; Giordano, L.; Pour, N.; Chang, H.-H.; Fenning, D. P.; Lux, S. F.; Paschos, O.; Bauer, C.; et al. Electrode-Electrolyte Interface in Li-Ion Batteries: Current Understanding and New Insights. *J. Phys. Chem. Lett.* **2015**, *6*, 4653–4672.
- (10) Xu, K. Nonaqueous Liquid Electrolytes for Lithium-Based Rechargeable Batteries. *Chem. Rev.* **2004**, *104*, 4303–4418.
- (11) Wang, Y.; Nakamura, S.; Ue, M.; Balbuena, P. B. Theoretical Studies To Understand Surface Chemistry on Carbon Anodes for Lithium-Ion Batteries: Reduction Mechanisms of Ethylene Carbonate. *J. Am. Chem. Soc.* **2001**, *123*, 11708–11718.
- (12) Balbuena, P. B.; Wang, Y. X. *Lithium-ion Batteries: Solid-Electrolyte Interphase*; Imperial College: London, 2004.
- (13) Leung, K.; Soto, F.; Hankins, K.; Balbuena, P. B.; Harrison, K. L. Stability of Solid Electrolyte Interphase Components on Lithium Metal and Reactive Anode Material Surfaces. *J. Phys. Chem. C* **2016**, *120*, 6302–6313.
- (14) Aurbach, D.; Levi, M. D.; Levi, E.; Teller, H.; Markovsky, B.; Salitra, G.; Heider, U.; Heider, L. Common Electroanalytical Behavior of Li Intercalation Processes into Graphite and Transition Metal Oxides. *J. Electrochem. Soc.* **1998**, *145*, 3024–3034.
- (15) Dedryvère, R.; Martinez, H.; Leroy, S.; Lemordant, D.; Bonhomme, F.; Biensan, P.; Gonbeau, D. Surface Film Formation on Electrodes in a LiCoO₂/Graphite Cell: A Step by Step XPS Study. *J. Power Sources* **2007**, *174*, 462–468. 13th International Meeting on Lithium Batteries.
- (16) Metzger, M.; Marino, C.; Sicklinger, J.; Haering, D.; Gasteiger, H. A. Anodic Oxidation of Conductive Carbon and Ethylene Carbonate in High-Voltage Li-Ion Batteries Quantified by On-Line Electrochemical Mass Spectrometry. *J. Electrochem. Soc.* **2015**, *162*, A1123–A1134.
- (17) Metzger, M.; Strehle, B.; Solchenbach, S.; Gasteiger, H. A. Origin of H₂ Evolution in LIBs: H₂O Reduction vs. Electrolyte Oxidation. *J. Electrochem. Soc.* **2016**, *163*, A798–A809.
- (18) Imhof, R.; Novák, P. Oxidative Electrolyte Solvent Degradation in Lithium-Ion Batteries: An In Situ Differential Electrochemical Mass Spectrometry Investigation. *J. Electrochem. Soc.* **1999**, *146*, 1702–1706.
- (19) Jung, R.; Metzger, M.; Maglia, F.; Stinner, C.; Gasteiger, H. A. Oxygen Release and Its Effect on the Cycling Stability of LiNi_{0.8}Mn_{0.2}Co_{0.2}O₂ (NMC) Cathode Materials for Li-Ion Batteries. *J. Electrochem. Soc.* **2017**, *164*, A1361–A1377.
- (20) Loftager, S.; Garcia-Lastra, J. M.; Vegge, T. A Density Functional Theory Study of the Carbon-Coating Effects on Lithium Iron Borate Battery Electrodes. *Phys. Chem. Chem. Phys.* **2017**, *19*, 2087–2094.
- (21) Loftager, S.; García-Lastra, J. M.; Vegge, T. A Density Functional Theory Study of the Ionic and Electronic Transport Mechanisms in LiFeBO₃ Battery Electrodes. *J. Phys. Chem. C* **2016**, *120*, 18355–18364.
- (22) Aykol, M.; Kim, S.; Hegde, V. I.; Snyder, D.; Lu, Z.; Hao, S.; Kirklín, S.; Morgan, D.; Wolverton, C. High-Throughput Computational Design of Cathode Coatings for Li-Ion Batteries. *Nat. Commun.* **2016**, *7*, 13779.
- (23) Aykol, M.; Kirklín, S.; Wolverton, C. Thermodynamic Aspects of Cathode Coatings for Lithium-Ion Batteries. *Adv. Energy Mater.* **2014**, *4*, 1400690.
- (24) Borodin, O.; Olguin, M.; Spear, C. E.; Leiter, K. W.; Knap, J. Towards High Throughput Screening of Electrochemical Stability of Battery Electrolytes. *Nanotechnology* **2015**, *26*, 354003.
- (25) Strmcnik, D.; Castelli, I. E.; Connell, J. G.; Haering, D.; Zorko, M.; Martins, P.; Lopes, P. P.; Genorio, B.; Østergaard, T.; Gasteiger, H. A.; et al. Electrocatalytic Transformation of HF Impurity to H₂ and LiF in Lithium-Ion Batteries. *Nat. Catal.* **2018**, *1*, 255.
- (26) Leung, K. First-Principles Modeling of the Initial Stages of Organic Solvent Decomposition on Li_xMn₂O₄(100) Surfaces. *J. Phys. Chem. C* **2012**, *116*, 9852–9861.
- (27) Xu, S.; Luo, G.; Jacobs, R.; Fang, S.; Mahanthappa, M. K.; Hamers, R. J.; Morgan, D. Ab Initio Modeling of Electrolyte Molecule Ethylene Carbonate Decomposition Reaction on Li(Ni,Mn,Co)O₂ Cathode Surface. *ACS Appl. Mater. Interfaces* **2017**, *9*, 20545–20553.
- (28) Giordano, L.; Karayaylali, P.; Yu, Y.; Katayama, Y.; Maglia, F.; Lux, S.; Shao-Horn, Y. Chemical Reactivity Descriptor for the Oxide-Electrolyte Interface in Li-Ion Batteries. *J. Phys. Chem. Lett.* **2017**, *8*, 3881–3887.
- (29) Tebbe, J. L.; Fuerst, T. F.; Musgrave, C. B. Degradation of Ethylene Carbonate Electrolytes of Lithium Ion Batteries via Ring Opening Activated by LiCoO₂ Cathode Surfaces and Electrolyte Species. *ACS Appl. Mater. Interfaces* **2016**, *8*, 26664–26674.

- (30) Kumar, N.; Leung, K.; Siegel, D. J. Crystal Surface and State of Charge Dependencies of Electrolyte Decomposition on LiMn_2O_4 Cathode. *J. Electrochem. Soc.* **2014**, *161*, E3059–E3065.
- (31) Feng, S.; Chen, M.; Giordano, L.; Huang, M.; Zhang, W.; Amanchukwu, C. V.; Anandakathir, R.; Shao-Horn, Y.; Johnson, J. A. Mapping a Stable Solvent Structure Landscape for Aprotic Li-Air Battery Organic Electrolytes. *J. Mater. Chem. A* **2017**, *5*, 23987–23998.
- (32) Khetan, A.; Pitsch, H.; Viswanathan, V. Solvent Degradation in Nonaqueous Li- O_2 Batteries: Oxidative Stability versus H-Abstraction. *J. Phys. Chem. Lett.* **2014**, *5*, 2419–2424.
- (33) Khetan, A.; Pitsch, H.; Viswanathan, V. Identifying Descriptors for Solvent Stability in Nonaqueous Li- O_2 Batteries. *J. Phys. Chem. Lett.* **2014**, *5*, 1318–1323.
- (34) Khetan, A.; Luntz, A.; Viswanathan, V. Trade-Offs in Capacity and Rechargeability in Nonaqueous Li- O_2 Batteries: Solution-Driven Growth versus Nucleophilic Stability. *J. Phys. Chem. Lett.* **2015**, *6*, 1254–1259.
- (35) Kramer, D.; Ceder, G. Tailoring the Morphology of LiCoO_2 : A First Principles Study. *Chem. Mater.* **2009**, *21*, 3799–3809.
- (36) Warburton, R. E.; Iddir, H.; Curtiss, L. A.; Greeley, J. Thermodynamic Stability of Low- and High-Index Spinel LiMn_2O_4 Surface Terminations. *ACS Appl. Mater. Interfaces* **2016**, *8*, 11108–11121.
- (37) Kim, S.; Aykol, M.; Wolverton, C. Surface Phase Diagram and Stability of (001) and (111) LiMn_2O_4 Spinel Oxides. *Phys. Rev. B: Condens. Matter Mater. Phys.* **2015**, *92*, 115411.
- (38) Henkelman, G.; Uberuaga, B. P.; Jónsson, H. A Climbing Image Nudged Elastic Band Method for Finding Saddle Points and Minimum Energy Paths. *J. Chem. Phys.* **2000**, *113*, 9901–9904.
- (39) Mortensen, J. J.; Hansen, L. B.; Jacobsen, K. W. Real-Space Grid Implementation of the Projector Augmented Wave Method. *Phys. Rev. B: Condens. Matter Mater. Phys.* **2005**, *71*, 035109.
- (40) Enkovaara, J.; Rostgaard, C.; Mortensen, J. J.; Chen, J.; Dulak, M.; Ferrighi, L.; Gavnholt, J.; Glinsvad, C.; Haikola, V.; Hansen, H. A.; et al. Electronic Structure Calculations with GPAW: a Real-Space Implementation of the Projector Augmented-Wave Method. *J. Phys.: Condens. Matter* **2010**, *22*, 253202.
- (41) Larsen, A. H.; Mortensen, J. J.; Blomqvist, J.; Castelli, I. E.; Christensen, R.; Dulak, M.; Friis, J.; Groves, M. N.; Hammer, B.; Hargus, C.; et al. The Atomic Simulation Environment—a Python Library for Working with Atoms. *J. Phys.: Condens. Matter* **2017**, *29*, 273002.
- (42) Hammer, B.; Hansen, L. B.; Nørskov, J. K. Improved Adsorption Energetics within Density-Functional Theory using Revised Perdew-Burke-Ernzerhof Functionals. *Phys. Rev. B: Condens. Matter Mater. Phys.* **1999**, *59*, 7413–7421.
- (43) Heaton, R. A.; Harrison, J. G.; Lin, C. C. Self-Interaction Correction for Density-Functional Theory of Electronic Energy Bands of Solids. *Phys. Rev. B: Condens. Matter Mater. Phys.* **1983**, *28*, 5992–6007.
- (44) Urban, A.; Seo, D.-H.; Ceder, G. Computational Understanding of Li-Ion Batteries. *npj Comput. Mater.* **2016**, *2*, 16002.
- (45) Capdevila-Cortada, M.; Łodziana, Z.; López, N. Performance of DFT+U Approaches in the Study of Catalytic Materials. *ACS Catal.* **2016**, *6*, 8370–8379.
- (46) Tripkovic, V.; Hansen, H. A.; Garcia-Lastra, J. M.; Vegge, T. Comparative DFT+U and HSE Study of the Oxygen Evolution Electrocatalysis on Perovskite Oxides. *J. Phys. Chem. C* **2018**, *122*, 1135–1147.
- (47) Kong, W.; Li, H.; Huang, X.; Chen, L. Gas Evolution Behaviors for Several Cathode Materials in Lithium-Ion Batteries. *J. Power Sources* **2005**, *142*, 285–291.
- (48) Kim, Y. J.; Lee, E.-K.; Kim, H.; Cho, J.; Cho, Y. W.; Park, B.; Oh, S. M.; Yoon, J. K. Changes in the Lattice Constants of Thin-Film LiCoO_2 Cathodes at the 4.2 V Charged State. *J. Electrochem. Soc.* **2004**, *151*, A1063–A1067.
- (49) Lee, Y.-L.; Kleis, J.; Rossmeis, J.; Shao-Horn, Y.; Morgan, D. Prediction of Solid Oxide Fuel Cell Cathode Activity with First-Principles Descriptors. *Energy Environ. Sci.* **2011**, *4*, 3966–3970.
- (50) Grimaud, A.; Hong, W.; Shao-Horn, Y.; Tarascon, J.-M. Anionic Redox Processes for Electrochemical Devices. *Nat. Mater.* **2016**, *15*, 121.
- (51) Cho, Y.; Lee, S.; Lee, Y.; Hong, T.; Cho, J. Spinel-Layered Core-Shell Cathode Materials for Li-Ion Batteries. *Adv. Energy Mater.* **2011**, *1*, 821–828.

Supporting information for: Oxidation of Ethylene Carbonate on Li Metal Oxide Surfaces

Thomas M. Østergaard,[†] Livia Giordano,^{‡,¶} Ivano E. Castelli,[§] Filippo Maglia,^{||}
Byron K. Antonopoulos,^{||} Yang Shao-Horn,^{‡,⊥, #} and Jan Rossmeisl^{*,†}

[†]*Nano-Science Center, Department of Chemistry, University of Copenhagen, DK-2100
Copenhagen, Denmark*

[‡]*Department of Mechanical Engineering, Massachusetts Institute of Technology, 77
Massachusetts Avenue, Cambridge, Massachusetts 02139, United States*

[¶]*Department of Material Science, Università di Milano-Bicocca, Via Cozzi 55, 20136
Milano, Italy*

[§]*Department of Energy Conversion and Storage, Technical University of Denmark,
Building 309, DK-2800, Kgs. Lyngby, Denmark*

^{||}*Battery Cell Technology, BMW Group, 80788 München, Germany*

[⊥]*Department of Materials Science & Engineering, Massachusetts Institute of Technology,
77 Massachusetts Avenue, Cambridge, Massachusetts 02139, United States*

[#]*Research Laboratory of Electronics, Massachusetts Institute of Technology, 77
Massachusetts Avenue, Cambridge, Massachusetts 02139, United States*

E-mail: jan.rossmeisl@chem.ku.dk

The supporting information is organized in 5 sections. The 1st section presents a NEB barrier calculation of the direct H transfer, pathway 2, on $\text{Li}_{0.5}\text{CoO}_2$. The 2nd section presents NEB barrier calculations of pathway 1 of the main text, on LiCoO_2 , CoO_2 and LiNiO_2 . The 3rd section presents the scaling relations between the bulk O-2p band and ΔE_{H} and the O_{vac} formation energy. The 4th section presents supporting information for figure 7 in the main text. It contains Bader charge analysis of the H adsorption reaction, density of states analysis, plots of the change in charge density and projected density of states upon H adsorption. This section shows that the position of the O-2s state can be used as a measure for the relative position of the E_{F} between the different Li_xMO_2 materials. The scaling relation between ΔE_{H} and E_{F} is also presented. The 5th section contains the scaling relation between ΔE_{H} and the reaction energy for oxidation state 2 in section 2 of the main text. The 6th section contains the change in magnetic moment for the transition metal ions upon EC oxidation.

The spin states are summed for the reported projected density of states (pdos) band centers. The Bader partitioning scheme was used to estimate electronic charges on individual atoms.^{S1,S2}

Direct Hydrogen Transfer Reaction Pathway

The second reaction pathway begins with a H transfer to O_{surf} with subsequent binding of C_{E} to O_{surf} . EC does not undergo a ring opening and no O_{vac} is formed. Since this pathway includes a transfer of a charged H atom across an interface, the reaction path is particularly sensitive to the electrochemical environment. For a realistic reaction pathway calculation, other electrolyte molecules should be included, and the workfunction of the surface should be kept constant to ensure a well-defined potential.^{S3-S5} Figure S1 is a simple NEB calculation in vacuum. The energy barrier is 1.15 eV, whereas it was 0.78 eV in pathway 1 in the main text (figure 2). Thus the direct H transfer is kinetically inaccessible as the deprotonated EC

is unstable in vacuum. Including electrolyte, one could imagine that other solvents molecules could facilitate the direct H transfer via H bonding and/or proton shuttling processes, as in the case of water. However, the battery electrolyte consists of an aprotic solvent and we therefore consider such processes to be prohibited.

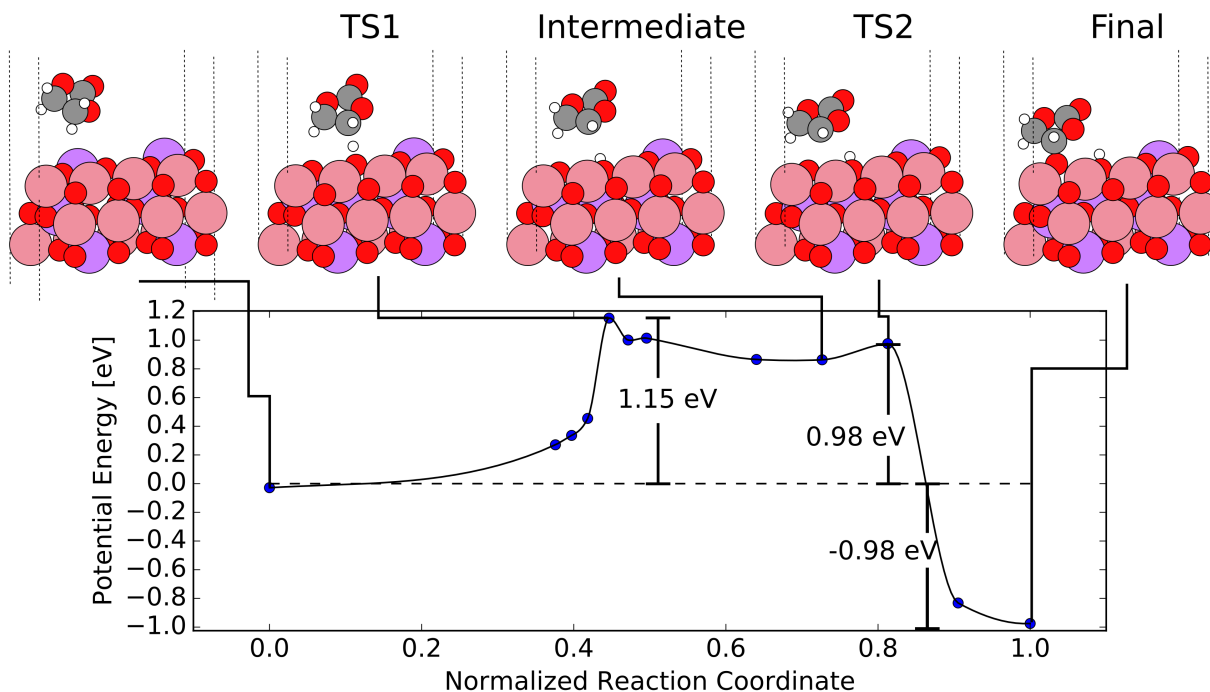


Figure S1: Potential energy diagram for oxidation reaction where a H is directly transferred. A Li ion moves to a subsurface layer before the proton transfer. The reaction energy is comparable to the two-step reaction pathway presented in the main paper, but the energy barrier is 0.37 eV higher. This corresponds to a rate which is 6×10^{-7} times lower at room temperature.

NEB Calculations of Pathway 1 for LiCoO_2 , CoO_2 and LiNiO_2

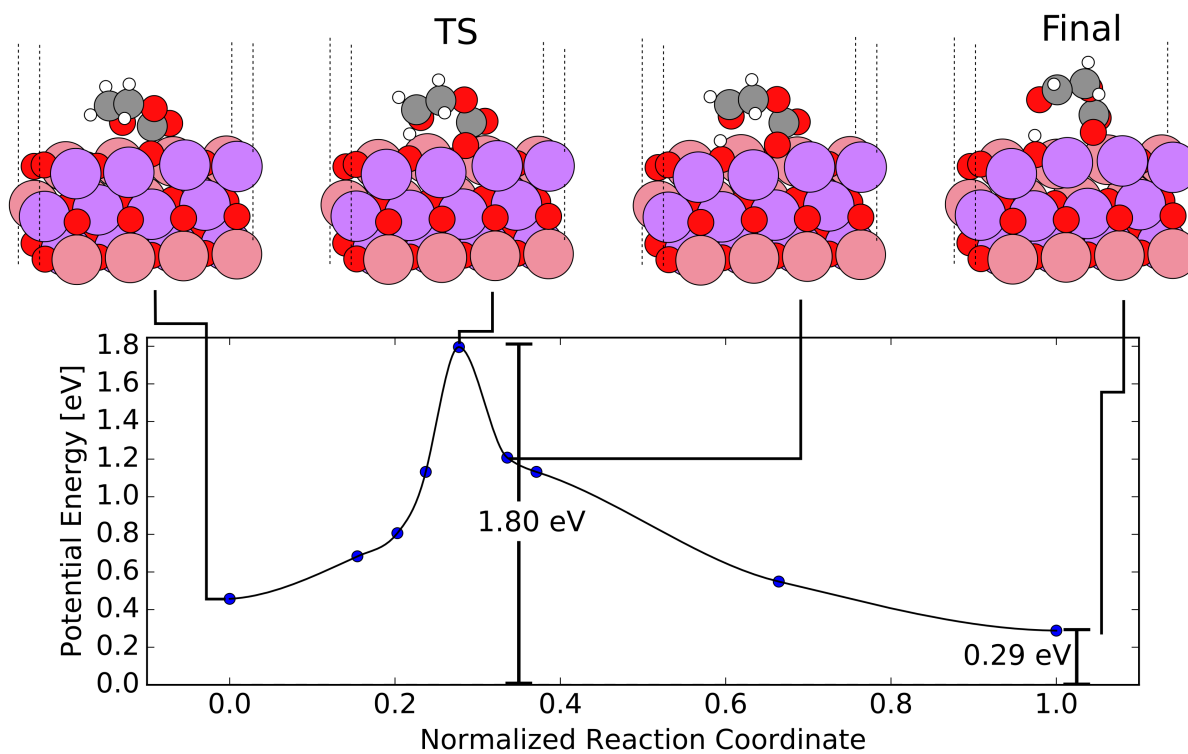


Figure S2: Potential energy diagram for the oxidation reaction on LiCoO_2 .

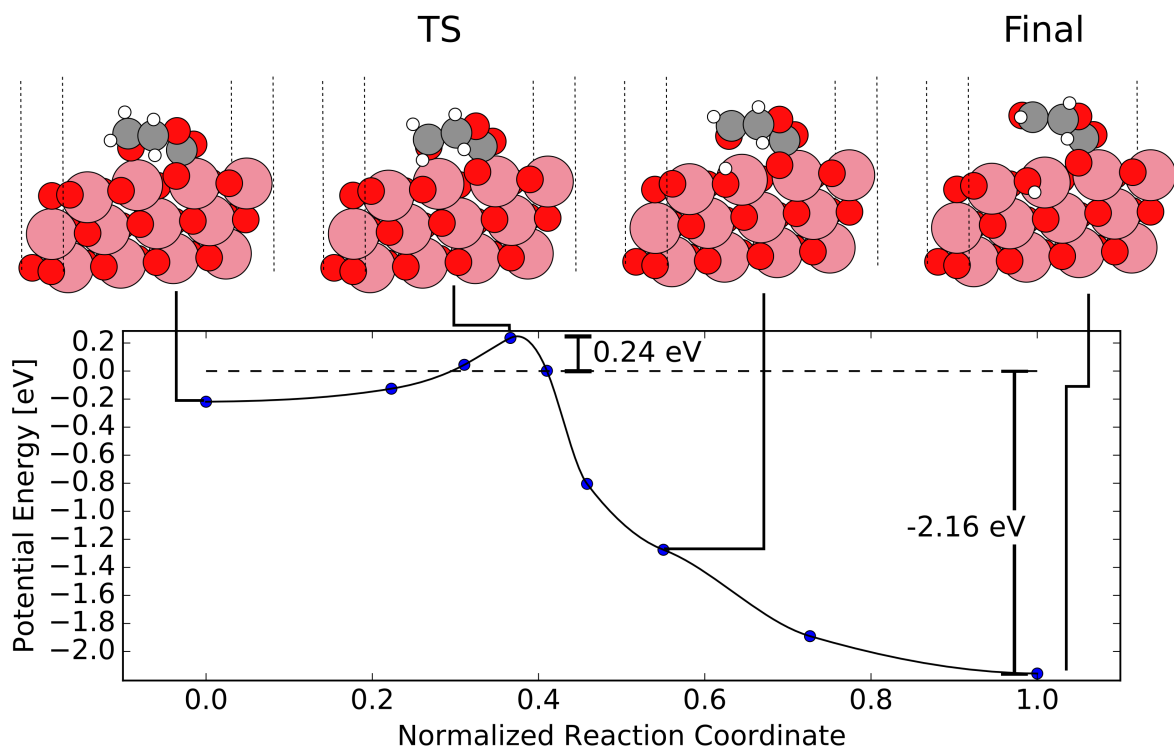


Figure S3: Potential energy diagram for the oxidation reaction on CoO_2 . The transferring H is already bonded the O_{surf} , and not shared with C_E , in the transition state.

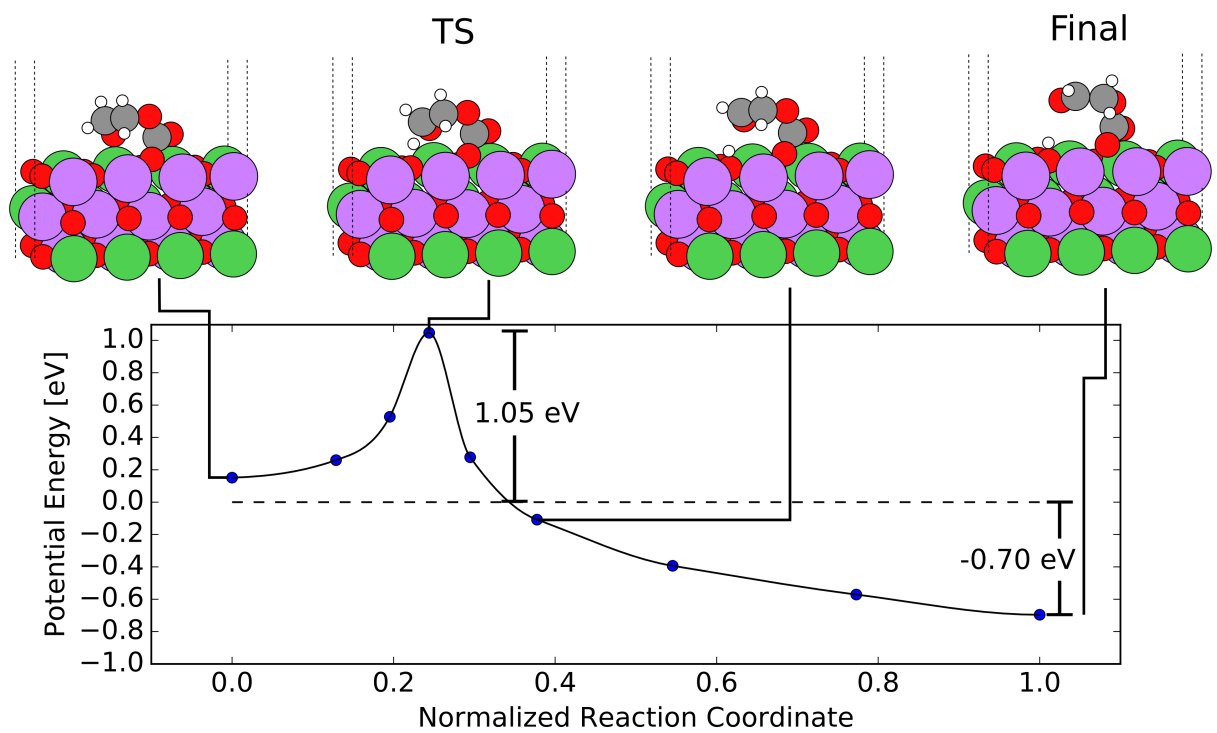


Figure S4: Potential energy diagram for oxidation reaction on LiNiO_2 .

Scaling Relations with the Bulk O-2p Band

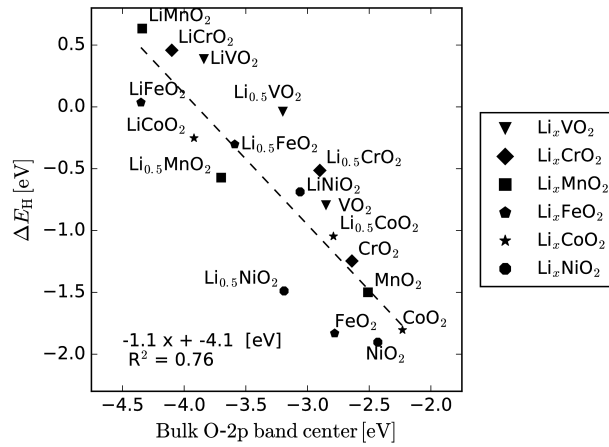


Figure S5: ΔE_H as function of the bulk O 2p-band center relative to the Fermi level.

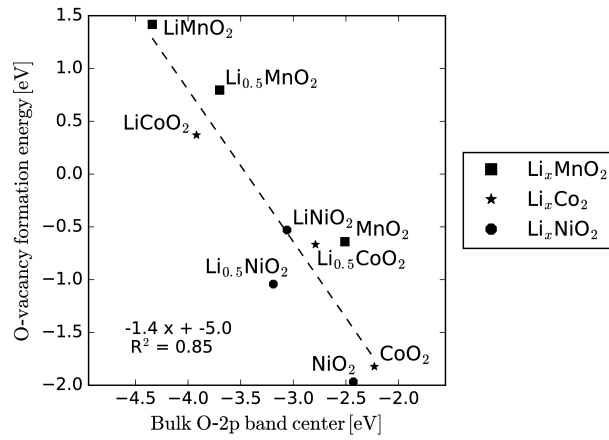


Figure S6: O_{vac} formation energy as function of the bulk O 2p-band center relative to the Fermi level.

Change in Electronic Structure Upon Hydrogen Adsorption

Table S1: Bader charge analysis of H adsorption on an O_{surf} atom, for Li_xCoO_2 , $x = [1, \frac{1}{2}, 0]$. The Bader net charge is reported for the H, O and two Co atoms, before and after H adsorption, as well as the change in charge Δq . Δq becomes more negative on the O atom, as the Li content decreases. The sum of Δq is about 0.2, reflecting that 80% ($1 - 0.2$) of the charge, from adsorbing a H, is localized to these four atoms.

	Atom	Clean surface	With H	Δq
LiCoO ₂	H		+0.54	+0.54
	O	-1.07	-1.17	-0.11
	Co _a	+1.32	+1.22	-0.10
	Co _b	+1.32	+1.22	-0.10
	Sum of Δq			+0.23
Li _{0.5} CoO ₂	H		+0.59	+0.59
	O	-0.82	-1.11	-0.29
	Co _a	+1.44	+1.39	-0.04
	Co _b	+1.45	+1.40	-0.05
	Sum of Δq			+0.21
CoO ₂	H		+0.61	+0.61
	O	-0.65	-1.01	-0.36
	Co _a	+1.50	+1.48	-0.02
	Co _b	+1.50	+1.47	-0.03
	Sum of Δq			+0.20

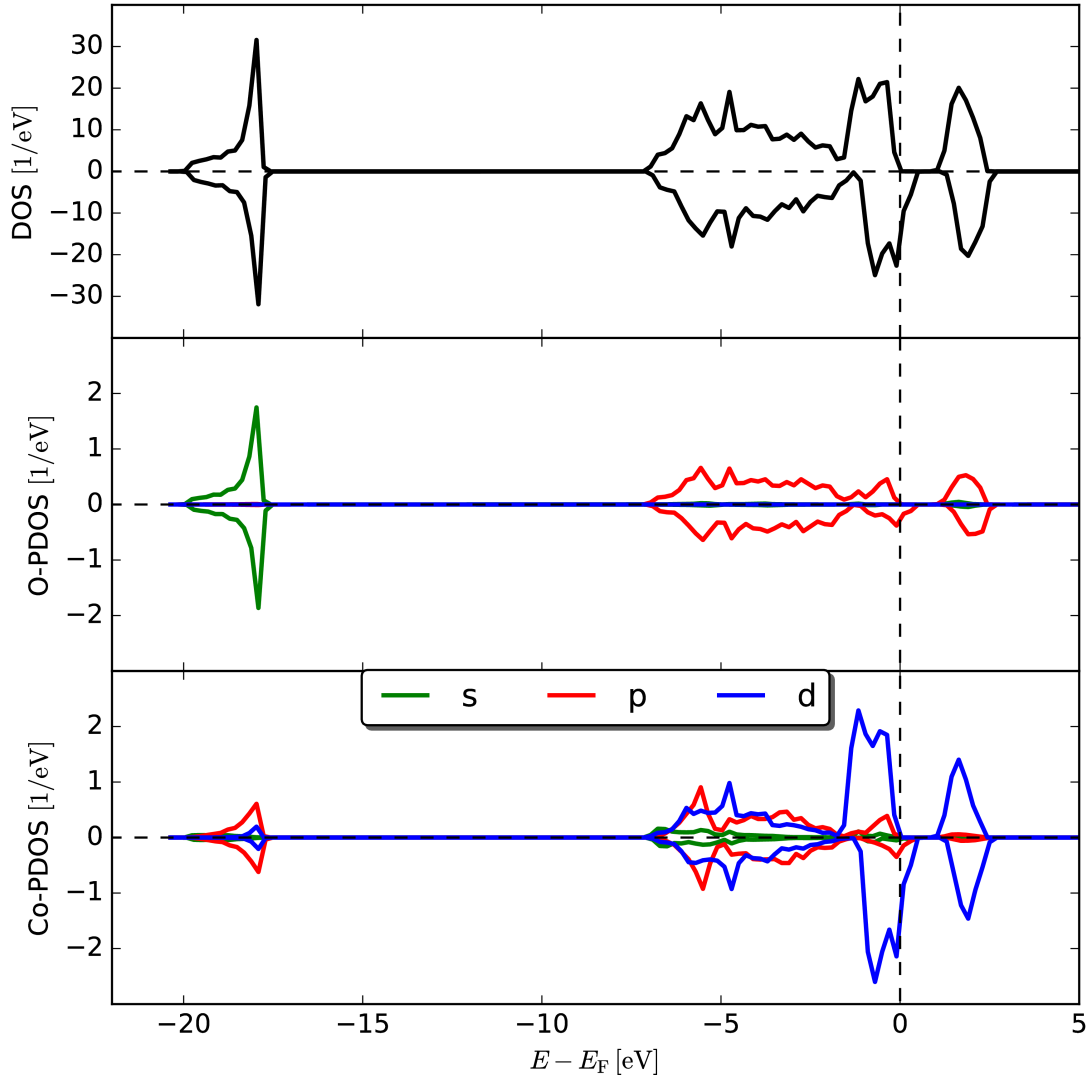


Figure S7: Density of states (DOS) and projected-DOS (PDOS) for bulk $\text{Li}_{0.5}\text{CoO}_2$. Positive and negative values corresponds to spin-up and spin-down states respectively. The DOS is calculated for the whole unit-cell, whereas O-PDOS is projected onto one O atom, and the Co-PDOS is projected onto one Co atom. The main contribution to the peak at about -18 eV, comes from the O 2s-state. The O-2s state is a narrow peak located at such deep energy levels, that it does not participate in chemical reactions. Therefore we use the position of the bulk O-2s peak as an approximate measure, of the relative position of the Fermi level between the different Li_xMO_2 surfaces.

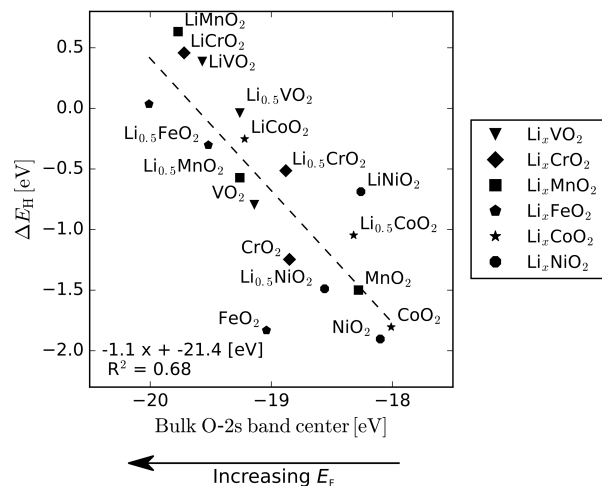


Figure S8: ΔE_H as function of the bulk O-2s band center, relative to the Fermi level. The Fermi level increases from right to left, and ΔE_H correlates linearly with a slope of one. The scaling holds for a wide range of 3d metals, from V to Ni.

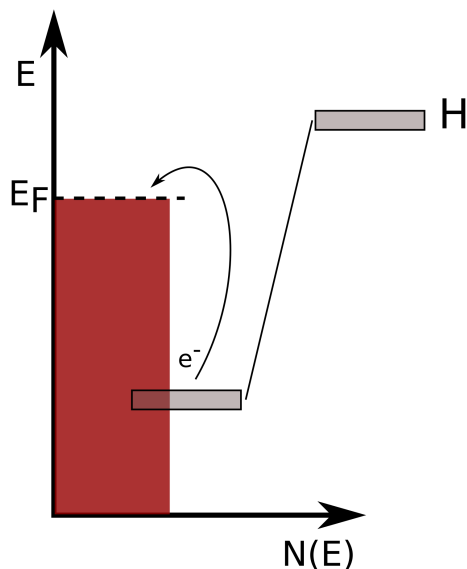


Figure S9: A simpler picture, than in the main paper, of the electronic structure of the H adsorption reaction. As shown in figure S8, ΔE_H correlates to the Fermi level. The figure shows an electron transfer to the Fermi level, which is the net effect of the mechanism in the main paper, assuming that the energy of the OH state and the distribution of the O-2p band are constant on an absolute scale. This assumption is investigated in figure S11.

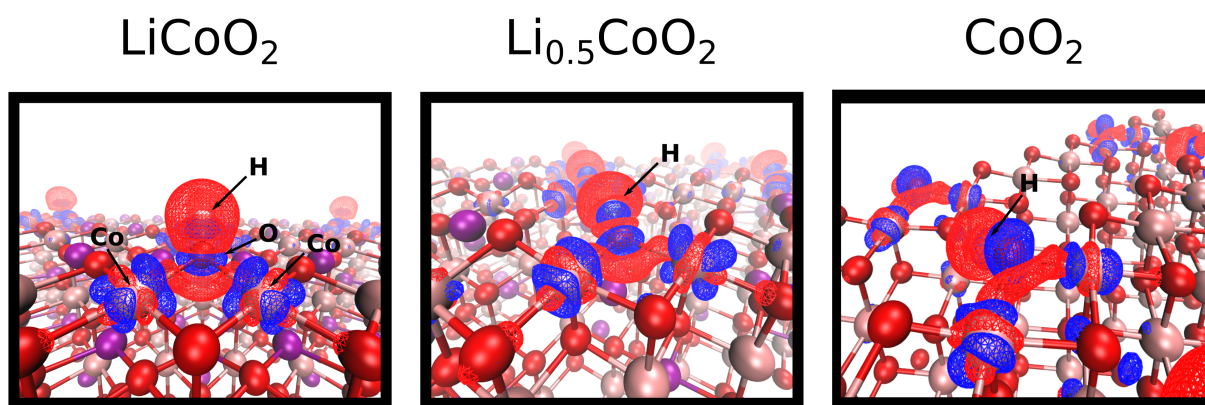


Figure S10: Change in charge density upon H adsorption for Li_xCoO_2 , $x = [1, \frac{1}{2}, 0]$. The change in charge density, ρ , is calculated as $\rho(\text{H}^*) - \rho(\text{H}) - \rho(*)$, where H^* is the surface with a proton adsorbed, H is the free proton in vacuum and $*$ is the clean surface. The charge depletion is shown in red, and accumulation in blue. For all surfaces, charge accumulates on O, and depletes in between the O and Co. Charge rearranges on the Co sites. This is in agreement with a reduced overlap between the pdos on the O and the metal atoms (see figure S11 and S12), and reflects a decrease in the covalent character of the M-O bond.

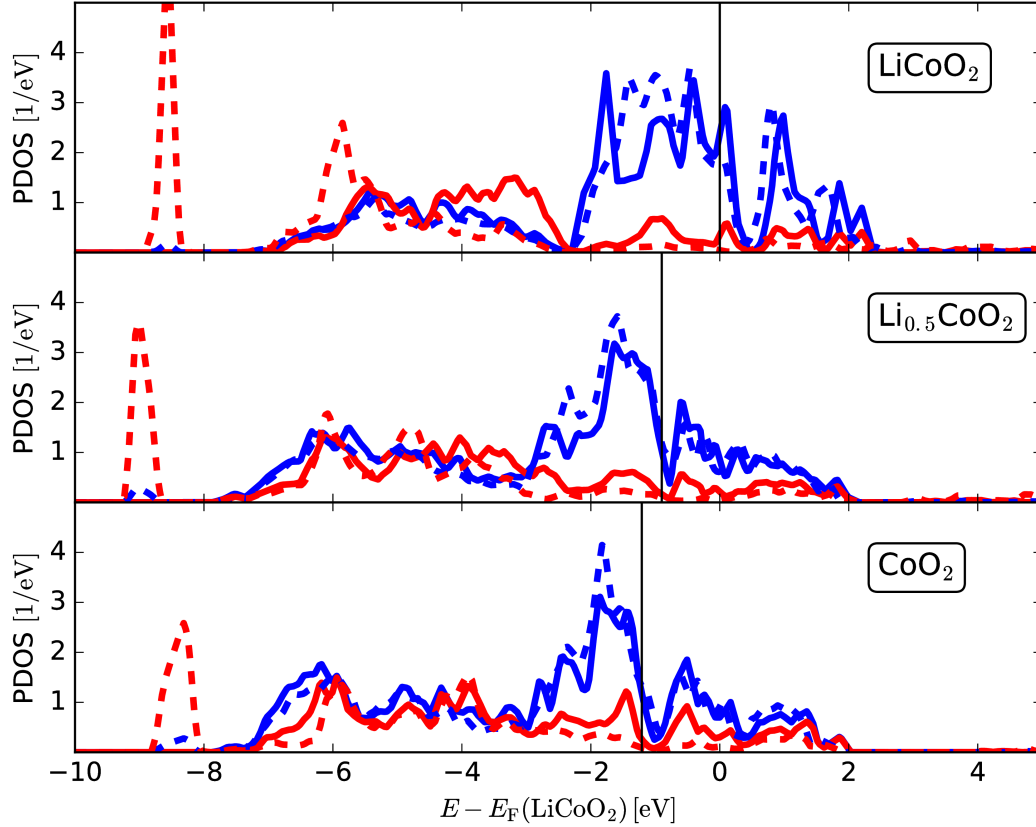


Figure S11: Projected density of states (PDOS) for Li_xCoO_2 $x = [1, \frac{1}{2}, 0]$ surfaces, before and after H adsorption, indicated by solid and dashed lines respectively. Spin-up and spin-down states are summed. The O-2p band is shown in red for the active O_{surf} and the Co-3d band is shown in blue for Co_{surf} . For $\text{Li}_{0.5}\text{CoO}_2$ the Co-3d PDOS is averaged between the two non-equivalent Co sites. The Fermi level is indicated with vertical black line. The energies for $\text{Li}_{0.5}\text{CoO}_2$ and CoO_2 are shifted by the difference in Fermi level with respect to LiCoO_2 , which is measured by the difference in the bulk O-2s band center. Upon H adsorption, a peak appears at about -8.5 eV, related to the formation of the O-H bond. The span of the O-2p band is constant between the surfaces. Upon H adsorption, the 3d-PDOS tends to increase, and the 2p-PDOS tends to decrease at higher energies.

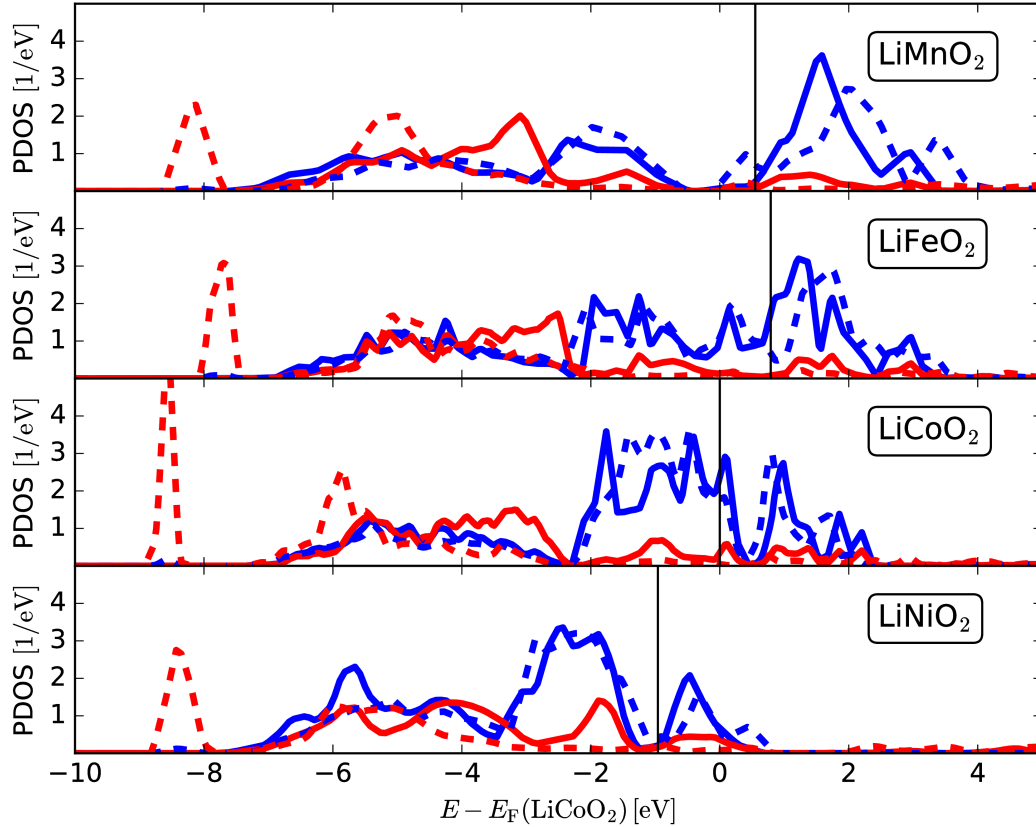


Figure S12: Projected density of states (PDOS) for LiMO_2 $M = [\text{Mn}, \text{Fe}, \text{Co}, \text{Ni}]$ surfaces, before and after H adsorption, indicated by solid and dashed lines respectively. The O-2p band is shown in red for the active O_{surf} and the M-3d band is shown in blue for M_{surf} . The Fermi level is indicated with vertical black line, and the energies are shifted by the difference in Fermi level with respect to LiCoO_2 , which is measured by the difference in the bulk O-2s band center. Upon H adsorption, a peak appears at about -8.5 eV, related to the formation of the O-H bond. The on-set of the O-2p band is at about -7 eV for the surfaces. Upon H adsorption, the 3d-PDOS tends to increase and the 2p-PDOS tends to decrease at higher energies.

Scaling Relation of Oxidation State 2

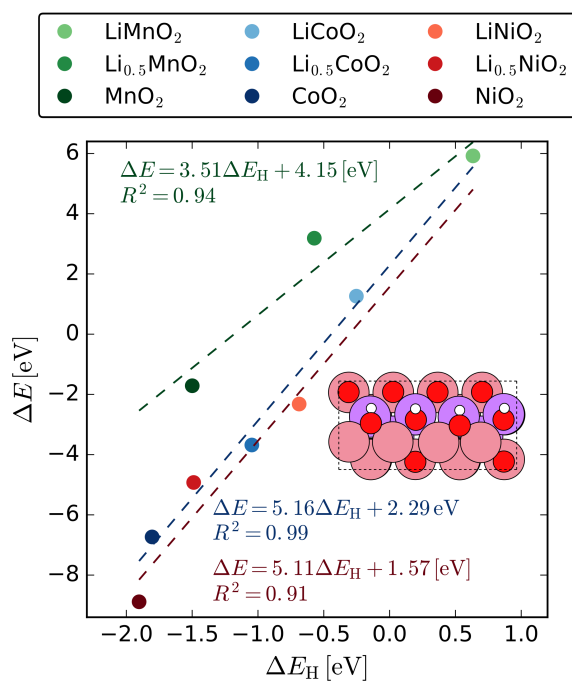


Figure S13: The reaction energy for oxidation state 2 as function of ΔE_H . Inset with the final state of the oxide surface with 4 H atoms and 2 oxygen vacancies.

Surface Transition Metal Spin States Before and After EC Oxidation

Table S2: Magnetic moment for the four surface transition metal ions in units of μ_B , before and after the EC oxidation. The metal ions are all equivalent for the LiMO_2 and MO_2 clean surfaces, whereas two non-equivalent surface sites are present for the $\text{Li}_{0.5}\text{MO}_2$ surfaces. Upon the oxidation reaction, EC adsorbs, an O_{vac} is formed and a H is abstracted. Therefore all four surface metal ions are non-equivalent and are all reported. An increase in the magnetic moment may indicate the reduction of a metal ion, as the redox state changes from n to $n - 1$.

	Clean surface		EC oxidized			
	Site 1	Site 2	Site 1	Site 2	Site 3	Site 4
LiMnO_2	3.73		3.74	4.51	4.44	4.29
$\text{Li}_{0.5}\text{MnO}_2$	3.74	3.78	3.74	3.91	4.37	3.74
MnO_2	2.95		2.96	2.93	3.76	3.69
LiCoO_2	1.61		1.6	2.73	2.53	1.46
$\text{Li}_{0.5}\text{CoO}_2$	0.54	1.88	0.35	1.3	0.23	1.73
CoO_2	0.85		0.86	0.46	0.39	0.59
LiNiO_2	0.81		0.79	0.19	1.53	0.81
$\text{Li}_{0.5}\text{NiO}_2$	0.82	0.84	0.8	0.75	1.54	0.64
NiO_2	0.14		0.88	-0.18	0.72	0.8

References

- (S1) Bader, R. F. W. A Quantum Theory of Molecular Structure and its Applications. *Chem. Rev.* **1991**, *91*, 893–928.
- (S2) Tang, W.; Sanville, E.; Henkelman, G. A Grid-Based Bader Analysis Algorithm Without Lattice Bias. *J. Phys.: Condens. Matter* **2009**, *21*, 084204.
- (S3) Rossmeisl, J.; Skúlason, E.; Björketun, M. E.; Tripkovic, V.; Nørskov, J. K. Modeling the Electrified Solid-Liquid Interface. *Chem. Phys. Lett.* **2008**, *466*, 68 – 71.
- (S4) Skúlason, E.; Tripkovic, V.; Björketun, M. E.; Gudmundsdóttir, S.; Karlberg, G.; Rossmeisl, J.; Bligaard, T.; Jónsson, H.; Nørskov, J. K. Modeling the Electrochemical Hydrogen Oxidation and Evolution Reactions on the Basis of Density Functional Theory Calculations. *J. Phys. Chem. C* **2010**, *114*, 18182–18197.
- (S5) Chan, K.; Nørskov, J. K. Electrochemical Barriers Made Simple. *J. Phys. Chem. Lett.* **2015**, *6*, 2663–2668.

8. General Conclusions

The experiments on model electrode surfaces showed, that the chemical and physical properties of SEIs formed at different potentials can vary significantly, although all SEIs are passivating regarding electrolyte decomposition. While the differences of SEI properties are not surprising, the passivation nature of all SEIs leads to an important conclusion: The major part of the SEI is already formed at high potentials, though those high-potential SEI species are further reduced at lower potentials. Furthermore, impurities like HF can play a significant role in the formation of the SEI by forming themselves a semi-passivating layer. This means that the composition of the final SEI formed at low potentials strongly depends on the physical and chemical properties of the high-potential SEI. While this fact appears trivial, it discloses a whole new field of SEI optimization research in terms of step-like SEI formation in high purity electrolytes. While typical formation approaches investigate formation protocols with a single constant current rate, the presented work strongly suggests the importance of individual formation parameters in the upper and lower potential regions, respectively. In order to provide a springboard, three advanced formation approaches applicable to real composite carbon electrodes were presented. None of them was optimized in terms of their single parameters or was verified in commercial full cells. Nonetheless, they successfully demonstrate that there are several options how the high-potential SEI can be treated individually, leading to improved electrode performance properties in laboratory type half-cells. Furthermore, it could be shown how surface physics significantly affect electrolyte oxidation on the positive electrode of Li-ion cells and how this know-how can help with the development of passivating coating materials.

The model electrode surfaces allowed forming a set of SEIs whose physical and chemical properties could be described in detail. This property awareness allowed the investigation of the deposition mechanism of transition metal cations on anodes. While the deposition mechanism was studied only on model electrode surfaces and the experiments were not performed on commercial-like electrodes, the results are expected to be transferable for the following reasons. First, the deposition of the two investigated cations Mn and Ni appeared to be similar from the electrochemical point of view. Since several chemical and electrochemical properties of the transition metal cations (e.g. diffusion coefficient, ion charge, electrochemical standard potential) are similar particularly from the Li⁺-ion point of view, a similar deposition mechanism can be assumed. However, the metal containing species which are formed may vary. While the exact identification of the formed species was out of the scope of this study, first steps in this direction were made by other research groups, who analyzed in detail the deposition of Mn²⁺-ions. The author nevertheless believes that the deposition mechanism of Mn, Ni, Co and even Fe and Al cations does not vary significantly, so that the results obtained by this work should be transferable to all commercially used cell chemistries. The author is furthermore convinced, that a combination of cations (e.g. in Ni-rich NMC cathode systems) will lead to separated metal containing sectors in the SEI as the metals are probably deposited preferably on their kind (e.g. Mn on existing Mn clusters). If the anode

surface reaches a severe coverage of metal containing species, the deposition mechanism may be affected. However, commercial systems cells will be declared “dead” much earlier due to the decrease of reactive surface area and the resulting increase of the inner cell resistance. It is important to mention that, while this work considers only cation deposition experiments on model electrode surfaces, the results are in accordance to literature. Furthermore, in this work it was presented how the results of model electrode surfaces in neat electrolyte are transferable to commercial-like systems. Therefore it is presumed, that the cation deposition mechanism concluded from HOPG is applicable also to commercial-like electrodes.

This work demonstrates, how simplified model experiments can support the progress of understanding complicated commercial-like systems. While using fundamental techniques to analyze the model electrodes, the results could be well coupled to data obtained by other research groups. As pointed out, there are numerous parameters which can affect the transferability of model system results to application. However, model systems can provide helpful trends, so that the chemical and physical mechanisms on the electrodes can be understood and steered. Furthermore, in this study it was possible to identify significant similarities between aqueous and carbonate solvent-based environments, which should encourage the research community to respectively transfer know-how and experiences from decades of aqueous electrochemistry to Li-ion chemistry.

9. Outlook

As clearly stated in chapter 5, the results obtained on composite graphite electrodes do not provide applicable formation protocols, but serve as a springboard for a broad field of formation research. The results indicate, how important it is to treat the initial SEI formed at high potentials individually. This can be done either by several current rate steps, by high frequency stimulation or by other uninvestigated external influences like external magnetic fields. It appears particularly promising to combine or superposition the investigated methods in the first half cycle, which is schematically shown for a full cell setup in Figure 21. The low voltage region, where the anode is at high potentials, is passed with a high current, which is interrupted at an appropriate point in order to stimulate the cell with a high frequency electric field. The high voltage regions, where the SEI formation is finalized, is passed with a lower current.

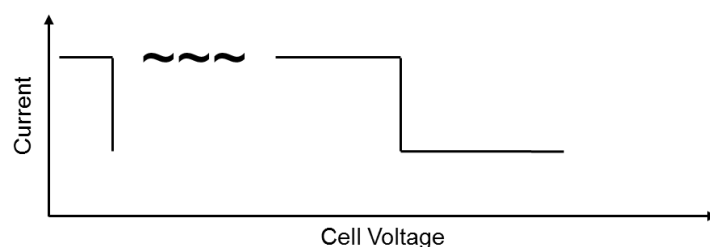


Figure 21: Combination of the investigated high-potential SEI engineering approaches, schematically shown for the first half cycle of a full cell.

Despite the possibility of combining the suggested methods, the single parameters like current rates and stimulation frequencies have to be optimized. They are expected to strongly depend on the cell chemistry and format, electrode balancing and several other features. Therefore, for the development of commercially applicable formation protocols it is inevitable to investigate the full parameter room using different current rates, stimulation frequencies, open circuit phases etc. This demands a respective systematic experiment matrix, ideally performed on both laboratory type three electrode full cells and commercially manufactured cells. Combining the electrochemical matrix with *post-mortem* analyses like surface spectroscopy (e.g. XPS, FTIR, TOF-SIMS) and other methods (e.g. electrolyte analysis) will strongly support the understanding of formation reactions and thus the SEI optimization process. A very promising derived artificial SEI concept study is on the way and is expected to be finished and published soon.

On the field of transition metal dissolution a large research effort is necessary to better understand the ongoing mechanisms. Once understood, appropriate measures can be taken in order to avoid drawbacks from transition metal deposition on the anode if transition metal dissolution cannot be suppressed on the cathode side. While thinking of state-of-the art cell chemistries the issue might not be that relevant, future cathode compositions and operation conditions will increase the dissolution from the actual point of view. Therefore, it is important to put more effort in understanding not only the deposition mechanism, which was investigated in this work, but also to dig deeper in terms of transition metal chemical

species, surface coverage, physical damage and safety issues of metal covered anodes. It is particularly necessary to gain a better understanding of the chemical state of the deposited metals on both charged and discharged electrode states. Furthermore, while the present work suggests a flat (uniform) electrode coverage, under certain conditions the transition metal might cause dendrites growth which can cause internal shorts. Promising methods to investigate those white spots are advanced techniques like neutron scattering or XAS, which can be used *in-situ*. Respective time-resolved results during operation are fundamental tools for a better understanding of the transition metal deposition and its effects on the anode. From the industry point of view, it is most likely inevitable to suppress the cation dissolution in the first place (e.g. by using a reference electrode and control the cathode half-cell potential), so that both electrodes can provide a long and safe cell life.

10. References

- [1] D. Andre, S.-J. Kim, P. Lamp, S.F. Lux, F. Maglia, O. Paschos, B. Stiaszny, *J. Mater. Chem. A* 3 (2015) 6709–6732.
- [2] M. Winter, W.K. Appel, B. Evers, T. Hodal, K.-C. Möller, I. Schneider, M. Wachtler, M.R. Wagner, G.H. Wrodnigg, J.O. Besenhard, *Monatsh. Chem.* 132 (2001) 473–486.
- [3] J. Vetter, P. Novak, Wagner, C. Veit, K.-C. Möller, J.O. Besenhard, M. Winter, M. Wohlfahrt-Mehrens, C. Vogler, A. Hammouche, *J. Power Sources* 147 (2005) 269–281.
- [4] J.-K. Park (Ed.), *Principles and Applications of Lithium Secondary Batteries*, 1st ed., Wiley-VCH Verlag GmbH & Co. KGaA, 2012.
- [5] B.K. Antonopoulos, C. Stock, F. Maglia, H.E. Hoster, *Electrochim. Acta* 269 (2018) 331–339.
- [6] D. Strmcnik, I.E. Castelli, J.G. Connell, D. Haering, M. Zorko, P. Martins, P.P. Lopes, B. Genorio, T. Østergaard, H.A. Gasteiger, F. Maglia, B.K. Antonopoulos, V.R. Stamenkovic, J. Rossmeisl, N.M. Markovic, *Nat. Catal. (Nature Catalysis)* 1 (2018) 255–262.
- [7] A.M. Andersson, M. Herstedt, A.G. Bishop, K. Edström, *Electrochim. Acta* 47 (2002) 1885–1898.
- [8] K. Xu, *Chem. Rev.* 104 (2004) 4303–4418.
- [9] D. Aurbach, A. Zaban, A. Schechter, Y. Ein-Eli, E. Zinigrad, B. Markovsky, *J. Electrochem. Soc.* 142 (1995) 2873–2882.
- [10] D. Aurbach, A. Zaban, Y. Ein-Eli, I. Weissman, O. Chusid, B. Markovsky, M. Levi, E. Levi, A. Schechter, E. Granot, *J. Power Sources* 68 (1997) 91–98.
- [11] H. Ota, Y. Sakata, A. Inoue, S. Yamaguchi, *J. Electrochem. Soc.* 151 (2004) A1659-A1669.
- [12] H. Ota, K. Shima, M. Ue, J.-i. Yamaki, *Electrochim. Acta* 49 (2004) 565–572.
- [13] D. Aurbach, E. Zinigrad, Y. Cohen, H. Teller, *Solid State Ionics* 148 (2002) 405–416.
- [14] D. Aurbach, K. Gamolsky, B. Markovsky, Y. Gofer, M. Schmidt, U. Heider, *Electrochim. Acta* 47 (2002) 1423–1439.
- [15] D. Aurbach, *J. Power Sources* 89 (2000) 206–218.
- [16] V. Eshkenazi, E. Peled, L. Burstein, D. Golodnitsky, *Solid State Ionics* 170 (2004) 83–91.
- [17] M. Herstedt, D.P. Abraham, J.B. Kerr, K. Edström, *Electrochim. Acta* 49 (2004) 5097–5110.
- [18] K. Edström, M. Herstedt, D.P. Abraham, *J. Power Sources* 153 (2006) 380–384.
- [19] A.M. Andersson, K. Edström, N. Rao, Wendsjö, *J. Power Sources* 81 (1999) 286–290.
- [20] F.M. Kindermann, P.J. Osswald, S. Klink, G. Ehlert, J. Schuster, A. Noel, S.V. Erhard, W. Schuhmann, A. Jossen, *J. Power Sources* 342 (2017) 638–643.
- [21] Y. Li, M. Bettge, B. Polzin, Y. Zhu, M. Balasubramanian, D.P. Abraham, *J. Electrochem. Soc.* 160 (2013) A3006-A3019.
- [22] K. Amine, J. Liu, I. Belharouak, *Electrochem. Commun.* 7 (2005) 669–673.
- [23] Z. Chen, J.R. Dahn, *Electrochem. Solid-State Lett.* 7 (2004) A11-A14.

- [24] D. Aurbach, B. Markovsky, G. Salitra, E. Markevich, Y. Talyossef, M. Koltypin, L. Nazar, B. Ellis, D. Kovacheva, *J. Power Sources* 165 (2007) 491–499.
- [25] I. Buchberger, S. Seidlmayer, A. Pokharel, M. Piana, J. Hattendorff, P. Kudejova, R. Gilles, H.A. Gasteiger, *J. Electrochem. Soc.* 162 (2015) A2737-A2746.
- [26] J. Wandt, A. Freiberg, R. Thomas, Y. Gorlin, A. Siebel, R. Jung, H.A. Gasteiger, M. Tromp, *J. Mater. Chem. A* 4 (2016) 18300–18305.
- [27] D. Aurbach, *J. Power Sources* 119 (2003) 497–503.
- [28] A.V. Plakhotnyk, L. Ernst, R. Schmutzler, *J. Fluorine Chem.* 126 (2005) 27–31.
- [29] H.-H. Chang, H.-C. Wu, N.-L. Wu, *Electrochem. Commun.* 10 (2008) 1823–1826.
- [30] H. Tsunekawa, Tanimoto, a, Satoshi, R. Marubayashi, M. Fujita, K. Kifune, M. Sano, *J. Electrochem. Soc.* 149 (2002) A1326-A1331.
- [31] S. Komaba, N. Kumagai, Y. Kataoka, *Electrochim. Acta* 47 (2002) 1229–1239.
- [32] Y. Lai, Z. Cao, H. Song, Z. Zhang, X. Chen, H. Lu, M. Jia, J. Li, *J. Electrochem. Soc.* 159 (2012) A1961-A1966.
- [33] C. Delacourt, A. Kwong, X. Liu, R. Qiao, W.L. Yang, P. Lu, S.J. Harris, V. Srinivasan, *J. Electrochem. Soc.* 160 (2013) A1099-A1107.
- [34] B. Markovsky, A. Rodkin, G. Salitra, Y. Talyosef, D. Aurbach, H.-J. Kim, *J. Electrochem. Soc.* 151 (2004) A1068-A1076.
- [35] M. Ochida, Y. Domi, T. Doi, S. Tsubouchi, H. Nakagawa, T. Yamanaka, T. Abe, Z. Ogumi, *J. Electrochem. Soc.* 159 (2012) A961-A966.
- [36] M. Bettge, Y. Li, B. Sankaran, N.D. Rago, T. Spila, R.T. Haasch, I. Petrov, D.P. Abraham, *J. Power Sources* 233 (2013) 346–357.
- [37] K. Osawa (Ed.), *Lithium Ion Rechargeable Batteries: Materials, Technology, and New Applications*, 1st ed., Wiley-VCH Verlag GmbH & Co. KGaA, 2009.
- [38] T.M. Østergaard, L. Giordano, I.E. Castelli, F. Maglia, B.K. Antonopoulos, Y. Shao-Horn, J. Rossmeisl, *J. Phys. Chem. C* 122 (2018) 10442–10449.
- [39] P. Verma, P. Maire, P. Novak, *Electrochim. Acta* 55 (2010) 6332–6341.
- [40] S.S. Zhang, *J. Power Sources* 162 (2006) 1379–1394.
- [41] D. Aurbach, Y. Talyosef, B. Markovsky, E. Markevich, E. Zinigrad, L. Asraf, J.S. Gnanaraj, H.-J. Kim, *Electrochim. Acta* 50 (2004) 247–254.
- [42] D. Aurbach, B. Markovsky, M.D. Levi, E. Levi, A. Schechter, M. Moshkovich, Y. Cohen, *J. Power Sources* 81 (1999) 95–111.
- [43] E. Peled, D. Golodnitsky, G. Ardel, *J. Electrochem. Soc.* 144 (1997) L208-L210.
- [44] E. Peled, D. Golodnitsky, A. Ulus, V. Yufit, *Electrochim. Acta* 50 (2004) 391–395.
- [45] M. Tang, J. Newman, *J. Electrochem. Soc.* 159 (2012) A1922-A1927.
- [46] W. Märkle, C.-Y. Lu, P. Novak, *J. Electrochem. Soc.* 158 (2011) A1478-A1482.

- [47] E. Peled, D. Bar Tow, A. Merson, A. Gladkikh, L. Burstein, D. Golodnitsky, *J. Power Sources* 97 (2001) 52–57.
- [48] J. Ma, L. Seidl, W. Ju, E. Mostafa, L. Asen, S. Martens, U. Stimming, O. Schneider, *ECS Trans.* 64 (2014) 407–423.
- [49] M. Tang, K. Miyazaki, T. Abe, J. Newman, *J. Electrochem. Soc.* 159 (2012) A634-A641.
- [50] P. Lu, C. Li, E.W. Schneider, S.J. Harris, *J. Phys. Chem. C* 118 (2014) 896–903.
- [51] O. Matsuoka, A. Hiwara, T. Omi, M. Toriida, T. Hayashi, C. Tanaka, Y. Saito, T. Ishida, H. Tan, S.S. Ono, S. Yamamoto, *J. Power Sources* 108 (2002) 128–138.
- [52] K. Tasaki, A. Goldberg, J.-J. Lian, M. Walker, A. Timmons, S.J. Harris, *J. Electrochem. Soc.* 156 (2009) A1019-A1027.
- [53] A. Zaban, D. Aurbach, *J. Power Sources* 54 (1995) 289–295.
- [54] P. Novák, F. Joho, M. Lanz, B. Rykart, J.-C. Panitz, D. Alliata, R. Kötz, O. Haas, *J. Power Sources* 97-98 (2001) 39–46.
- [55] A. Mukhopadhyay, A. Tokranov, X. Xiao, B.W. Sheldon, *Electrochim. Acta* 66 (2012) 28–37.
- [56] P. Niehoff, S. Passerini, M. Winter, *Langmuir* 29 (2013) 5806–5816.
- [57] B.K. Antonopoulos, F. Maglia, F. Schmidt-Stein, J.P. Schmidt, H.E. Hoster, *Batteries & Supercaps* 1 (2018) 110–121.
- [58] A.v. Cresce, S.M. Russell, D.R. Baker, K.J. Gaskell, K. Xu, *Nano Letters* 14 (2014) 1405–1412.
- [59] M. Tang, J. Newman, *J. Electrochem. Soc.* 158 (2011) A530-A536.
- [60] M. Tang, J. Newman, *J. Electrochem. Soc.* 159 (2012) A281-A289.
- [61] A.M. Andersson, A. Henningson, H. Siegbahn, U. Jansson, K. Edström, *J. Power Sources* 119 (2003) 522–527.
- [62] G. Zampardi, F. La Mantia, W. Schuhmann, *Electrochem. Commun.* 58 (2015) 1–5.
- [63] M. Winter, J.O. Besenhard, M.E. Spahr, P. Novák, *Adv. Mater.* 10 (1998) 725–763.
- [64] M.B. Pinson, M.Z. Bazant, *J. Electrochem. Soc.* 160 (2013) A243-A250.
- [65] J.Q. Xu, *Dynamic Formation Protocol for Lithium-Ion Battery*, 2015.
- [66] P.-C.J. Chiang, M.-S. Wu, J.-C. Lin, *Electrochem. Solid-State Lett.* 8 (2005) A423.
- [67] M. Winter, G.H. Wrodnigg, J.O. Besenhard, W. Biberacher, P. Novák, *J. Electrochem. Soc.* 147 (2000) 2427.
- [68] V.A. Sethuraman, Winkle, N. Van, D.P. Abraham, A.F. Bower, P.R. Guduru, *J. Power Sources* 206 (2012) 334–342.
- [69] U. Kasavajjula, C. Wang, A.J. Appleby, *J. Power Sources* 163 (2007) 1003–1039.
- [70] M.A. Danzer, V. Liebau, F. Maglia, in: *Advances in Battery Technologies for Electric Vehicles*, Elsevier, 2015, pp. 359–387.
- [71] C.H. Hamann, A. Hammnett, W. Vielstich, *Electrochemistry*, 2nd ed., Wiley-VCH Verlag GmbH & Co. KGaA, 2007.

- [72] A.J. Bard, L.R. Faulkner, *Electrochemical methods: Fundamentals and applications*, 2nd ed., Wiley, New York, 2001.
- [73] M. Nie, D. Chalasani, D.P. Abraham, Y. Chen, A. Bose, B.L. Lucht, *J. Phys. Chem. C* 117 (2013) 1257–1267.
- [74] A. Xiao, L. Yang, B.L. Lucht, S.-H. Kang, D.P. Abraham, *J. Electrochem. Soc.* 156 (2009) A318-A327.
- [75] S.-H. Kang, D.P. Abraham, A. Xiao, B.L. Lucht, *J. Power Sources* 175 (2008) 526–532.
- [76] F. German, A. Hintennach, A. LaCroix, D. Thiemig, S. Oswald, F. Scheiba, M.J. Hoffmann, H. Ehrenberg, *J. Power Sources*.
- [77] L. Bodenes, R. Dedryvere, H. Martinez, F. Fischer, C. Tessier, J.-P. Peres, *J. Electrochem. Soc.* 159 (2012) A1739-A1746.
- [78] D.P. Abraham, J. Liu, C.H. Chen, Y.E. Hyung, M. Stoll, N. Elsen, S. MacLaren, R. Twesten, R. Haasch, E. Sammann, I. Petrov, K. Amine, G. Henriksen, *J. Power Sources* 119–121 (2003) 511–516.
- [79] E. Markevich, M.D. Levi, D. Aurbach, *J. Electrochem. Soc.* 152 (2005) A778-A786.
- [80] M.D. Levi, C. Wang, D. Aurbach, *J. Electrochem. Soc.* 151 (2004) A781-A790.
- [81] T. Tsujikawa, K. Yabuta, T. Matsushita, M. Arakawa, K. Hayashi, *J. Electrochem. Soc.* 158 (2011) A322-A325.
- [82] D. Lu, M. Xu, L. Zhou, A. Garsuch, B.L. Lucht, *J. Electrochem. Soc.* 160 (2013) A3138-A3143.
- [83] B. Stiaszny, J.C. Ziegler, E.E. Krauß, J.P. Schmidt, E. Ivers-Tiffée, *J. Power Sources* 251 (2014) 439–450.
- [84] S.F. Lux, I.T. Lucas, E. Pollak, S. Passerini, M. Winter, R. Kostecki, *Electrochem. Commun.* 14 (2012) 47–50.
- [85] L. Terborg, S. Weber, F. Blaske, S. Passerini, M. Winter, U. Karst, S. Nowak, *J. Power Sources* 242 (2013) 832–837.
- [86] H. Zheng, Q. Sun, G. Liu, X. Song, V.S. Battaglia, *J. Power Sources* 207 (2012) 134–140.
- [87] C. Zhan, J. Lu, A. Jeremy Kropf, T. Wu, A.N. Jansen, Y.-K. Sun, X. Qiu, K. Amine, *Nat. Commun.* 4 (2013) 2473.
- [88] I.A. Shkrob, A.J. Kropf, T.W. Marin, Y. Li, O.G. Poluektov, J. Niklas, D.P. Abraham, *J. Phys. Chem. C* 118 (2014) 24335–24348.
- [89] S.R. Gowda, K.G. Gallagher, J.R. Croy, M. Bettge, M.M. Thackeray, M. Balasubramanian, *Phys. Chem. Chem. Phys.* 16 (2014) 6898.
- [90] L. Boulet-Roblin, M.E. Kazzi, P. Novak, C. Villevieille, *J. Electrochem. Soc.* 162 (2015) A1297-A1300.
- [91] G. Amatucci, A. Du Pasquier, A. Blyr, T. Zheng, J.-M. Tarascon, *Electrochim. Acta* 45 (1999) 255–271.

- [92] X. Xiao, Z. Liu, L. Baggetto, G.M. Veith, K.L. More, R.R. Unocic, *Phys. Chem. Chem. Phys.* 16 (2014) 10398–10402.
- [93] K. Amine, Z. Chen, Z. Zhang, J. Liu, W. Lu, Y. Qin, J. Lu, L. Curtis, Y.-K. Sun, *J. Mater. Chem.* 21 (2011) 17754.
- [94] T. Joshi, K. Eom, G. Yushin, T.F. Fuller, *J. Electrochem. Soc.* 161 (2014) A1915-A1921.
- [95] A. Blyr, C. Sigala, G. Amatucci, D. Guyomard, Y. Chabre, J.-M. Tarascon, *J. Electrochem. Soc.* 145 (1998) 194–209.
- [96] K. Amine, J. Liu, S. Kang, I. Belharouak, Y. Hyung, D. Vissers, G. Henriksen, *J. Power Sources* 129 (2004) 14–19.
- [97] S. Zhang, M.S. Ding, K. Xu, J. Allen, T.R. Jow, *Electrochem. Solid-State Lett.* 4 (2001) A206-A208.
- [98] M. Tang, S. Lu, J. Newman, *J. Electrochem. Soc.* 159 (2012) A1775-A1785.
- [99] K. Xu, *Chem. Rev.* 114 (2014) 11503–11618.
- [100] J.-M. Tarascon, M. Armand, *Nature* 414 (2001) 359–367.
- [101] O.K. Park, Y. Cho, S. Lee, H.-C. Yoo, H.-K. Song, J. Cho, *Energy Environ. Sci.* 4 (2011) 1621–1633.
- [102] D. Bar-Tow, E. Peled, L. Burstein, *J. Electrochem. Soc.* 146 (1999) 824–832.
- [103] Y. Ji, Y. Zhang, C.-Y. Wang, *J. Electrochem. Soc.* 160 (2013) A636-A649.
- [104] T.L. Kulova, A.M. Skundin, E.A. Nizhnikovskii, A.V. Fesenko, *Russ. J. Electrochem.* 42 (2006) 259–262.
- [105] C.D. Rahn, C.-Y. Wang, *Battery Systems Engineering*, 1st ed., John Wiley & Sons Inc, 2013.
- [106] M. Park, X. Zhang, M. Chung, G.B. Less, A.M. Sastry, *J. Power Sources* 195 (2010) 7904–7929.
- [107] T. Brülle, U. Stimming, *J. Electroanal. Chem.* 636 (2009) 10–17.
- [108] J. Maruyama, C. Baier, H. Wolfschmidt, P. Bele, U. Stimming, *Electrochim. Acta* 63 (2012) 16–21.
- [109] Innovative Solutions Bulgaria Ltd., HOPG, spmtips.com/test-structures-HOPG.html, accessed 4 March 2014.
- [110] T. Rinken (Ed.), *State of the Art in Biosensors - General Aspects*, InTech, 2013.
- [111] K. Murase, I. Sasaki, A. Kitada, Y. Uchimoto, T. Ichii, H. Sugimura, *J. Electrochem. Soc.* 160 (2013) D453-D458.
- [112] J.L. Gómez-Cámer, P. Novák, *Electrochem. Commun.* 34 (2013) 208–210.
- [113] A.M. Andersson, K. Edström, *J. Electrochem. Soc.* 148 (2001) A1100-A1109.
- [114] A.M. Andersson, K. Edström, J.O. Thomas, *J. Power Sources* 81 (1999) 8–12.
- [115] A. Augustsson, M. Herstedt, J.-H. Guo, K. Edström, G.V. Zhuang, P.N. Ross Jr, J.-E. Rubensson, J. Nordgren, *Phys. Chem. Chem. Phys.* 6 (2004) 4185–4189.
- [116] B.K. Antonopoulos, C. Kirdar, F. Maglia, H.E. Hoster, Manuscript in preparation.

- [117] B.K. Antonopoulos, *Journal Technik Up2date* (2013).
- [118] B.K. Antonopoulos, F. Maglia, F. Schmidt-Stein, J.P. Schmidt, H.E. Hoster, *Batteries & Supercaps* 1 (2018) 96.
- [119] B.K. Antonopoulos, F. Maglia, F. Schmidt-Stein, J.P. Schmidt, H.E. Hoster, *Batteries & Supercaps* 1 (2018) 95.
- [120] B.K. Antonopoulos, A.-C. Gentschev, F. Maglia, H.E. Hoster, Manuscript in preparation.
- [121] I.E. Castelli, D. Strmcnik, M. Zorko, T.M. Østergaard, P. Martins, P.P. Lopes, B.K. Antonopoulos, F. Maglia, N.M. Markovic, J. Rossmeisl, in preparation.

11. Publication Overview

11.1. Journal Publications

- B.K. Antonopoulos, F. Maglia, F. Schmidt-Stein, J.P. Schmidt, H.E. Hoster, Formation of the Solid Electrolyte Interphase at Constant Potentials: a Model Study on Highly Oriented Pyrolytic Graphite, *Batteries & Supercaps* 1 (2018) 110-121 [57]
- B.K. Antonopoulos, C. Stock, F. Maglia, H.E. Hoster, Solid Electrolyte Interphase: Can faster formation at lower potentials yield better performance? *Electrochim. Acta* 269 (2018) 331–339 [5]
- D. Strmcnik, I.E. Castelli, J.G. Connell, D. Haering, M. Zorko, P. Martins, P.P. Lopes, B. Genorio, T. Østergaard, H.A. Gasteiger, F. Maglia, B.K. Antonopoulos, V.R. Stamenkovic, J. Rossmeisl, N.M. Markovic, Electrocatalytic transformation of HF impurity to H₂ and LiF in lithium-ion batteries, *Nat. Catal.* 1 (2018) 255–262 [6]
- T.M. Østergaard, L. Giordano, I.E. Castelli, F. Maglia, B.K. Antonopoulos, Y. Shao-Horn, J. Rossmeisl, Oxidation of Ethylene Carbonate on Li Metal Oxide Surfaces, *J. Phys. Chem. C* 122 (2018) 10442–10449 [38]

11.2. Conference Contributions

- B.K. Antonopoulos, F. Maglia, H.E. Hoster, The Solid Electrolyte Interphase on model electrode surfaces, German-Israeli Battery School (2014) Tel-Aviv/Israel, Oral Presentation
- B. K. Antonopoulos, C. Kirdar, F. Maglia, F. Schmidt-Stein, H. E. Hoster, Chemical, Electrochemical and Physical Properties of the Solid Electrolyte Interphase on HOPG Surface: Mechanisms of Formation and Transition Metal Deposition, 228th Meeting of the Electrochemical Society (2015), Phoenix/USA, Oral Presentation
- B.K. Antonopoulos, F. Maglia, F. Schmidt-Stein, H.E. Hoster, The two-step SEI formation mechanism on HOPG and the applicability and benefits on commercial composite carbon electrodes, ABAA (2015), Bilbao/Spain, Poster Presentation

11.3. Patent Applications

- B.K. Antonopoulos, D. Most; DE102012221072: Redox flow battery for supplying electrical power, has cell that is composed of electrode frame for receiving felt or fleece-electrodes on which electrolyte is supplied for generating electrical power
- B.K. Antonopoulos, M.S. Lepiorz; DE102012222236: Method for electrical protection of redox flow battery stack through single cell monitoring, involves detecting operation voltage on single cell by battery management system, for electrical protecting redox flow battery

- B.K. Antonopoulos, M.S. Lepiorz; DE10201222235: Method for magnifying efficiency of redox flow battery stack of redox flow battery, involves adjusting manipulated variable by battery management system based on current value such that efficiency of stack is maximized
- B.K. Antonopoulos, B. Stiaszny; DE102014216466: Determination of the water content of materials
- B.K. Antonopoulos, C. Stock; DE102015212590: Rapid forming of an electrode
- B.K. Antonopoulos; DE102015212591: Forming an Electrode
- B.K. Antonopoulos; DE102016212736: Method for producing a solid state electrolyte, solid state electrolyte and lithium ion battery
- B.K. Antonopoulos; DE102016212735: Method and device for producing an anode of a lithium-ion battery and a lithium-ion battery cell
- B.K. Antonopoulos, S. Lupart, S. Zugmann; DE102016220726: Reference Electrode of the second type for use in Li-ion cells
- D. Andre, B.K. Antonopoulos, S. Lupart, D. Schünemann, B. Stiaszny, S. Zugmann; DE102016222004: Herstellung dünner Folien auf Metallbasis

11.4. Other

- B.K. Antonopoulos, Kanalelektrode für Redox-Flow-Batterien, Journal Technik Up2date (2013), doi 10.4421/PAPDEOTT001256 [117]
- B.K. Antonopoulos, F. Maglia, F. Schmidt-Stein, J.P. Schmidt, H.E. Hoster, Formation of the Solid Electrolyte Interphase at Constant Potentials: a Model Study on Highly Oriented Pyrolytic Graphite, Batteries & Supercaps 1 (2018), Cover Profile [118]
- B.K. Antonopoulos, F. Maglia, F. Schmidt-Stein, J.P. Schmidt, H.E. Hoster, Formation of the Solid Electrolyte Interphase at Constant Potentials: a Model Study on Highly Oriented Pyrolytic Graphite, Batteries & Supercaps 1 (2018), Cover Picture [119]

11.5. In Preparation/Unpublished

- B.K. Antonopoulos, A.-C. Gentschev, F. Maglia, H.E. Hoster, The Dynamic Impedance Properties of Solid Electrolyte Interphase on HOPG, Manuscript in preparation [120]
- B.K. Antonopoulos, C. Kirdar, F. Maglia, H.E. Hoster, New Insights on the Deposition Mechanism and Location of Transition Metal Cations on the Negative Electrodes of Li Ion Batteries, Manuscript in preparation [116]
- I.E. Castelli, D. Strmcnik, M. Zorko, T. Østergaard, P. Martins, P.P. Lopes, B.K. Antonopoulos, F. Maglia, N. Markovic, J. Rossmeisl, The Role of Interface in Stabilizing Reaction Intermediates for Hydrogen Evolution and SEI Formation in Aprotic Electrolyte [121]
- 5 patent applications filed but not published yet

